Investigation of ultrasound-measured blood flow related parameters in radial and ulnar arteries

Xiaowei Zhou

Supervisors:

Prof Zhihong Huang
Prof Peter Hoskins
Prof George Corner
Prof Faisel Khan

School of Science and Engineering
University of Dundee

A thesis submitted for the degree of
Philosophy doctor (PhD)
University of Dundee
Jan 2017

Contents

List of figures

List of tables

Acronyms and abbreviations

AWM	Arterial wall motion
AVF	Arteriovenous fistula
A-mode	Amplitude mode
B-mode	Brightness mode
BMF	Blood mimicking fluid
CT	Computerised tomography
CVDs	Cardiovascular diseases
CW	Continuous-wave
CVS	Cardiovascular system
CFD	Computational fluid dynamics
DI	Deionised water
DICOM	Digital Imaging and Communications in Medicine
ESRD	End stage renal disease
FFT	Fast Fourier transform
FTM	Failure to mature
FV	Flow velocity
FR	Flow rate
GUI	Graphic user interface
IEC	International Electrotechnical Commission
LPF	Low pass filter
MRI	Magnetic resonance imaging

PW	Pulsed-wave
PRF	Pulse repetition frequency
PVA-c	polyvinyl alcohol cryogel
PC	Personal computer
ROI	Region of Interest
RP	Raynaud’s phenomenon
RF	Radio frequency
RAVF	Radiocephalic arteriovenous fistula
RI	Resistive index
SSc	Systemic sclerosis
SNR	Signal-noise ratio
SBP	Systolic blood pressure
SD	Standard deviation
STL	Stereolithography
TMM	Tissue mimicking material
TDI	Tissue Doppler Imaging
US	Ultrasound
VMM	Vessel mimicking material
VFI	Vector flow imaging
WSS	Wall shear stress
WSR	Wall shear rate
WE	Womersley equation
1D	One directional
2D	Two directional
3D	Three directional

Glossary of terms

A	Arterial vessel area	[m^2]
A_d	Diastolic blood vessel area	[m^2]
A_s	Systolic blood vessel area	[m^2]
A_{motion}	Motion amplitude in the simulation with Field II	[m]
Amp_s	Signal amplitude with test sample	[V]
Amp_w	Signal amplitude with water	[V]
α_w	Attenuation coefficient of water	[$dB.cm^{-1}.MHz^{-1}$]
α_s	Attenuation coefficient of test sample	[$dB.cm^{-1}.MHz^{-1}$]
α_k	the Womersley number for the k-th harmonic	
β	Arterial wall rigidity coefficient	
c	Speed of sound	[$m.s^{-1}$]
c_w	Speed of sound in water	[m.s-1]
c_s	Speed of sound in test sample	[m.s-1]
D_b	Arterial baseline diameter	[m]
$DiaW$	Arterial diameter waveform	[m]
D	Vessel diameter	[m]
f_{motion}	Motion frequency in the simulation with Field II	[Hz]
f_t	Transmitted sound frequency	[Hz]
f_d	Doppler shift frequency	[Hz]
f_c	Central frequency of the RF signal	[Hz]
f_{dem}	Demodulation frequency	[MHz]
f_s	Sampling frequency	[Hz]

k	Component order in Fourier transform	
p	Blood pressure	[Pa]
p_d	Diastolic blood pressure	[Pa]
p_s	Systolic blood pressure	[Pa]
$p_{m,Brachial}$	Mean blood pressure in the brachial artery	[Pa]
$p_{m,radial}$	Mean blood pressure in the radial artery	[Pa]
ρ	Density	[$kg.m^{-3}$]
Q	Flow rate	[$m^3.s^{-1}$]
Q_k	The k-*th* order component of the flow rate	[$m^3.s^{-1}$]
$\Phi_{mean,k}$	phase of the k-*th* harmonic component of mean velocity	[rad]
$\Phi_{centre,k}$	phase of the k-*th* harmonic component of centreline velocity	[rad]
Φ_k	phase of the k-*th* harmonic component of flow rate	[rad]
θ	Beam-vessel angle	[rad]
R_{ref}	acoustical reflection coefficient	
R	Radius	[m]
r	Polar coordinate distance	[m]
λ	Wavelength	[m]
rf_i	Simulated RF signal from the simple model	
$s(t)$	RF signal	
Th	Sample thickness	[mm]
T_s	sampling period of the RF signal	[s]
t	Time	[s]
τ_w	Wall shear stress	[Pa]
τ_i	Time delay in the wall motion simulation model	[s]

μ	Dynamic viscosity	[Pa.s]
v	Blood Velocity	[m.s^{-1}]
$V_{centre,k}$	Centreline maximum velocity of the k-*th* velocity component	[m.s-^{1}]
$v(r,t)$	Velocity profile	[m.s^{-1}]
$v_k(r,t)$	The k-*th* component of the velocity profile	[m.s^{-1}]
v_0	The constant component of the mean velocity waveform	[m.s^{-1}]
v_{mean}	Mean velocity in the blood vessel	[m.s^{-1}]
$V_{mean,k}$	Mean velocity of the k-*th* velocity component	[m.s^{-1}]
W_{motion}	Wall motion waveform in simulation with Field II	[m]
wsr	Wall shear rate	[s^{-1}]
w_s	The size of transducer element group in Field II	[m]
ω_0	Fundamental angle frequency	[rad.s^{-1}]
ω_m	Central angular frequency of simulated RF signal in the simple model	[rad]
ω_k	The k-*th* order frequency component	[rad]
z_s	Acoustical impedance of the test sample	[Kg.m^{-2}.s^{-1}]
z_w	Acoustical impedance of the water	[Kg.m^{-2}.s^{-1}]
ΔD	displacement of tissue or vessel wall	[m]
ΔD_p	Posterior wall motion	[m]
ΔD_a	Anterior wall motion	[m]
$\Delta\theta$	Phase delay	[rad]
Δt_m	Time delay in measuring speed of sound	[μs]
$\Delta t_{d,s}$	Time delay in test sample	[μs]
$\Delta t_{d,w}$	Time delay in water	[μs]
ΔT_p	Pulse length	[s]

Acknowledgements

I would like to give my great thanks to my first supervisor Prof Zhihong Huang for her giving me this opportunity to do this project, for her consistent efforts to take this project forward, and for her indispensable support during my PhD time. I also have to stress the incomparable role played by Prof Peter R. Hoskins from University of Edinburgh; he contributed the determinant suggestions to my project, kept me on the track and provided technical supervisions throughout my thesis. Undoubtedly, I cannot hide my deep gratitude to Prof George A. Corner whose uncountable support, encouragement and patience, both in academic and in life, are very important factors that helped me through my PhD life successfully. I also appreciate the help from Dr Faisel Khan for his input in the clinical part of my thesis, and for his suggestions in volunteer recruitment and data collection.

Additionally, I would like to thank Dr David Kenwright from Edinburgh University for his help with making flow phantoms at the early time, and Dr Efstratios Kokkalis for his suggestions on phantom fabrication, hands-on experience on CFD simulation, as well as volunteer data collection from MRI. Thanks to Dr Noel Conlisk from Edinburgh University for his useful guidance to the CFD simulation in Abaqus. I also need to thank Duncan Kirkcaldy, Ian Rutherford, Patrick Carena and John Anderson from Medical Physics and School of Science and Engineering.

Furthermore, I sincerely thank my colleagues whom I have been working with for these years in our big group. Particular gratitude needs to be given to my flatmates during my PhD time. All these friends, including colleagues and flatmates, made my life wonderful and unforgettable, and help me through the difficult time. Thank you all for being with me.

I always thank my parents for their unconditional support in all aspects during my study abroad. Without them, I will never be able to finish my thesis. Other family members also deserve my great thank you to them.

One very important person that I have to express my deepest gratitude is my wife Mingming Chen who is amazing and is the most important person that help me through my tough time in the pursuit of my PhD degree. I could not thank her enough. Of course,

I really need to thank my daughter little Anna who just arrived a few days after I finish my thesis draft. I give my thanks to her for her coming into my life and encouraging me to finish my thesis (as a gift for her as well). Obviously, I need to thank Mingming again for her great work on this.

Lastly, I have to thank the Chinese Scholarship Council (CSC) which funded me for these 42 months. Without this support, I would never be able to finish this thesis.

Declaration of originality

I hereby declare that I am the author of this thesis; that, unless otherwise stated, all references cited have been by myself; that the work of which the thesis is a record has been done by myself except due acknowledgement is made in the text and that it has not been previously accepted for another degree or qualification of this university or any other universities or institute of learning.

.....

Xiaowei Zhou

Supervisor’s declaration

This is to certify that Xiaowei Zhou has done this research under my supervision and that I have read this thesis. Also, to certify that he has fulfilled the conditions of Ordinance 39 and relevant Regulations of the University of Dundee, so that he is qualified to submit for the Degree of Doctor of Philosophy.

.....

Prof Zhihong Huang

Abstract

The incidence of disease of the cardiovascular system is very high and increasing worldwide, especially in the developing world. The radial and ulnar arteries are implicated in some important ailments where blood flow related parameters such as flow rate (FR), wall shear rate (WSR), arterial wall motion (AWM) and pressure, all of which can be measured using ultrasound techniques, are useful in diagnosis and patient management. However these measurements are prone to error due to the manner of image formation and the complex flow conditions within the vessels. In this thesis, the errors in ultrasound-measured parameters in the radial and ulnar arteries are investigated using experimental phantoms, computer simulation and on volunteers.

Using the Womersley theory, FR and WSR were estimated using a clinical ultrasound scanner with the pulsed wave (PW) mode and B mode. Experimental flow phantoms were designed to evaluate those measurements under different circumstances. A simulation technique which combined image-based computational fluid dynamics and ultrasound simulation was also used to evaluate ultrasound estimation of these parameters. A case study was then conducted on healthy volunteers to evaluate the method of measuring FR and WSR *in-vivo*. For the AWM in the radial artery, an auto-correlation method was used based on the radio-frequency (RF) data and validations were done by a flow phantom, simulation, and *in-vivo* trial. The blood pressure waveform in a volunteer's radial artery was derived from the ultrasound measured AWM and compared with the waveform from a tonometry.

FR and WSR were both found to be overestimated by up to 50%, mainly due to the beam-vessel angle in the PW Doppler ultrasound. Measurement of the vessel diameter and assumption of the blood flow direction can also influence the estimations. Other factors, such as flow amplitude, vessel size, imaging depth and flow waveforms, do not seem to affect the estimation of these two parameters. Results taken from the flow phantoms agree with those from simulation and the estimations from the *in-vivo* case study also agree with the published data. The auto-correlation method for the AWM was validated from the phantom and simulation. It is able to detect motion amplitude of about tens of micrometres. The trial on volunteers proved the feasibility of this motion detection

method. Blood pressure waveforms at the radial artery of a volunteer, derived from this ultrasound-measured wall motion and from the tonometry, were very similar.

The Womersley-based method is able to estimate the FR and WSR in the radial and ulnar arteries with high accuracy. Sources of the error and their magnitudes in estimation of the two parameters by ultrasound pointed out in this thesis are beam-vessel angle, vessel diameter measurement and flow direction assumption. Researchers and clinicians using these measurements in practice and research should be aware. The capability of ultrasound imaging to measure arterial AWM in the radial artery is demonstrated and it is found that the blood pressure waveform can also be derived from the arterial AWM.

Chapter 1

1. Introduction

This chapter will give a brief introduction of this study, regarding to the radial and ulnar arteries in the cardiovascular system, measurements of flow related parameters that are of interest, aims of this thesis, and outline of the thesis structure.

1.1 Radial and ulnar arteries

Radial and ulnar arteries are located in the wrist, generally dividing from the brachial artery around the elbow. These are the two main arteries in the lower arm as shown in Figure 1.1, forming a dual blood supply network in the hand. The radial artery runs distally on the anterior part of the forearm and is connected with the deep palmar arch. Ulnar artery also arises from the brachial artery and terminates in the superficial palmar arch, which joins with the superficial branch of the radial artery (Ali and Srivastava 2008).

These two arteries are peripheral arteries and lie very close to the skin, especially the radial artery which passes the front of the distal end of the radius, only about 5 mm from the skin. It is here that clinician commonly takes the radial pulse for assessing the heart rate and cardiac rhythm. The diameters of these two arteries are approximately 2.0-3.0 mm and no strong association was found between diameters and age, weight, height and body surface area (Habib et al. 2012; Velasco et al. 2012).

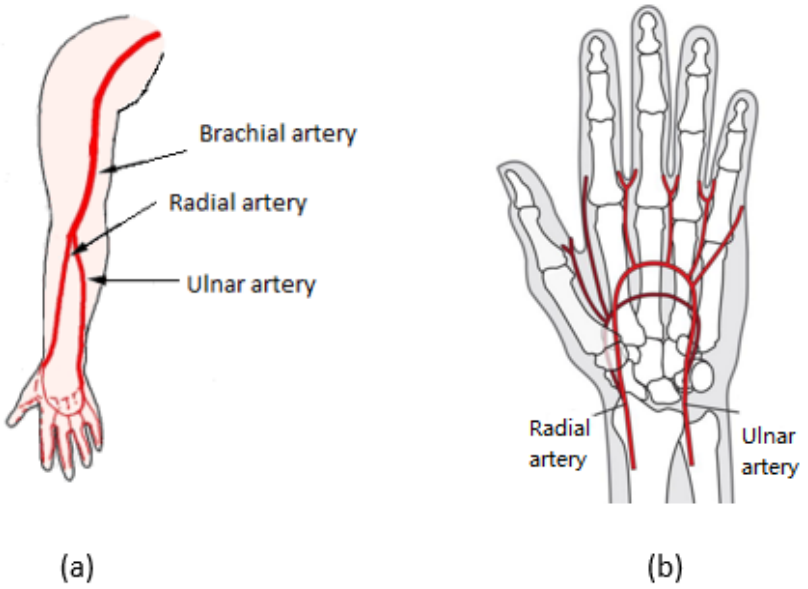

Fig. 1. 1. Radial and ulnar arteries.

1.2 Measurement of flow related parameters

In the radial and ulnar arteries some flow related parameters, such as flow velocity, volumetric flow rate, wall shear rate and arterial wall motion, are closely involved in some specific diseases and clinical procedures both in clinical practice and research. For example, clinical studies have measured velocity related quantities (flow velocity, flow rate and wall shear rate) in these two arteries in relation to the creation of arteriovenous fistula (AVF) for patients with renal diseases, as shown in Figure 1.2. The created AVF is a lifeline for receiving the hemodialysis for those patients. However this AVF is likely to fail and 40% of the AVFs were reported as failure after 12 months (Brahmbhatt et al. 2016). Flow related parameters in the radial and ulnar arteries are being used to pre-operatively analyze the outcome and to post-operatively assess the vessel remodeling for the AVF creation (Malovrh 2002; Ene-Iordache et al. 2003; Masengu et al. 2016).

In addition, prior to preparation for radial artery harvesting for coronary bypass surgery, where the radial artery is harvested and placed to the coronary arteries as a bypass graft as shown in Figure 2.3, the flow velocity and volumetric flow rate in the radial and ulnar arteries are measured to assess the risks of ischemia in patient's hand and fingers after the receiving surgery (Abu-Omar et al. 2004; Manabe et al. 2005; Royse et al. 2008; Habib et al. 2012).

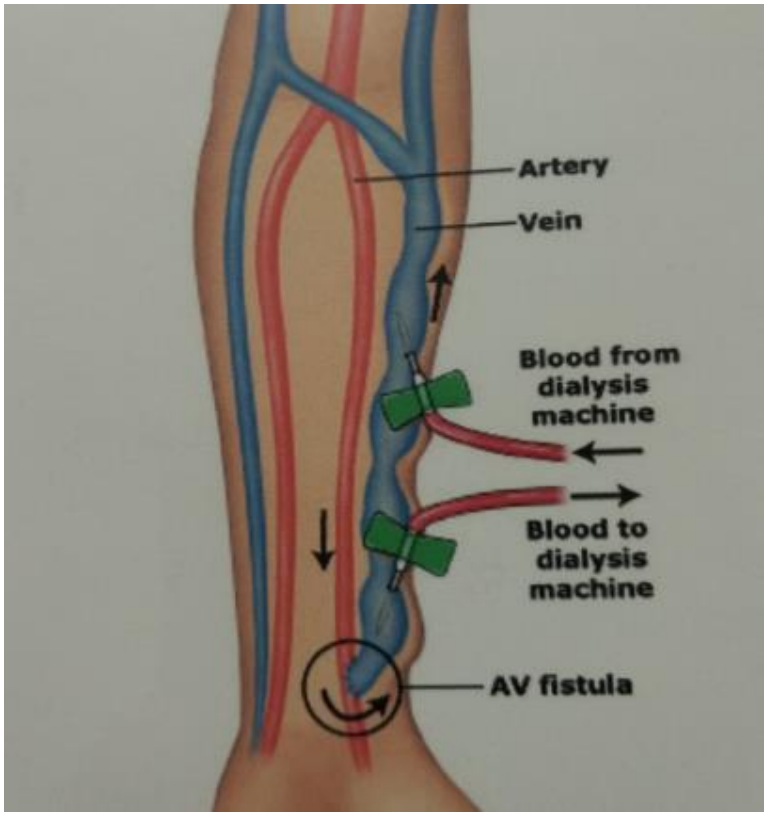

Fig. 1. 2. Arteriovenous fistula by connecting the radial artery and its surrounding vein

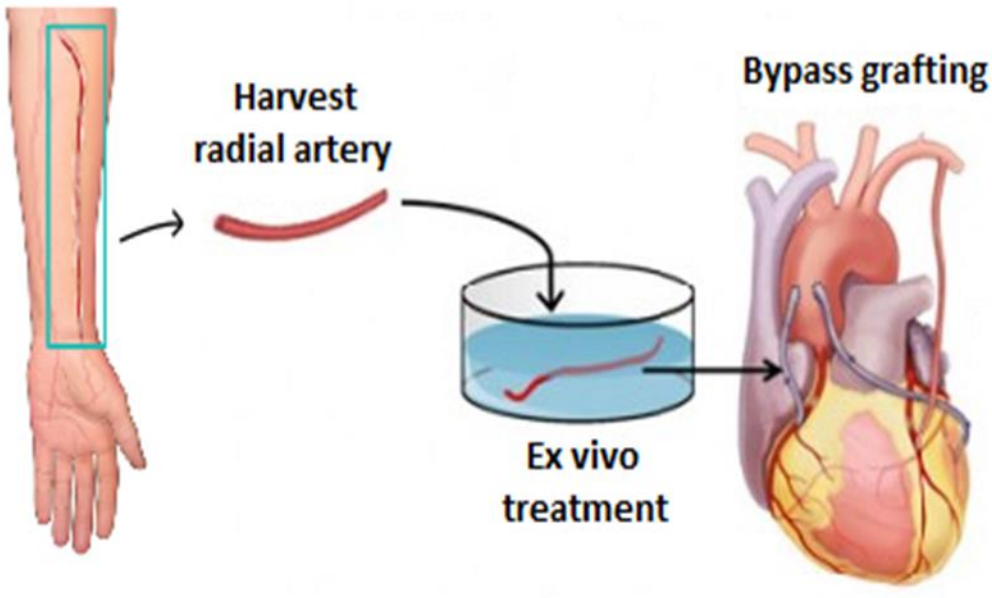

Fig. 1. 3. Radial artery harvesting for coronary arteries as a bypass graft

Furthermore, the flow parameters in the radial and ulnar arteries have been chosen to study the Raynaud's phenomenon (RP) which could cause the cease of blood supply in fingers while the patients are exposed to cold, anxiety or other emotional stress (Mcilory 1985; Chikui et al. 1999). For clinical management, it is important to distinguish the primary RP and secondary RP because the latter is more crucial and dangerous (Herrick 2013).

The arterial wall motion in the radial and ulnar arteries has not been reported to be directly involved in clinical studies, but its derivative the blood pressure waveform in the radial artery is of great interest for the pulse wave analysis (Cohn et al. 1995; Duprez et al. 2004). In fact, the radial artery blood pressure waveform can be used to derive the central blood pressure (the aortic artery) through mathematical transfer function (Chen 1997; Hope et al. 2002), which is useful in clinical practice (Safar et al. 2002; Roman et al. 2007).

As for measurements of the aforementioned flow related parameters in these two arteries, ultrasound is the imaging modality that is chosen in most cases in the clinical practice and research because of its low-cost, real-time and non-invasive imaging procedure when comparing to the MRI and CT imaging. The advantage of real-time imaging makes ultrasound, especially the Doppler ultrasound, the optimal choice to investigate those flow-related movements. However, ultrasound based measurements are prone to errors in estimating those parameters due to the manner of image formation and the complex flow conditions within the vessels. To understand the potential error magnitudes and the error sources, it is necessary to conduct the evaluation of these ultrasound based measurements. This evaluation can avoid misinterpretation while researchers and clinicians are using those flow related parameters in clinical practice and research.

1.3 Aims of this thesis

This thesis aims to investigate the flow related parameters measured by ultrasound in the radial and ulnar arteries, including methodologies to estimate parameters and evaluations of these estimations. More specifically, it includes:

- Measurement of blood flow velocity, volumetric flow rate and wall shear rate in

the radial and ulnar arteries using clinical ultrasound scanners; and evaluation of those measurements using experimental phantom and computational simulation;

- Measurement of radial artery's arterial wall motion; validation of this measurement through flow phantom, simulations and *vivo* trial; and trial on estimation of blood pressure waveform through arterial wall motion in the radial artery;
- Acquisition of data from healthy volunteers to trial on the established methodologies to study correlation between flow related parameters and hand perfusion in digits by looking into the flow and wall shear rates in these two arteries.

1.4 Thesis structure

Chapter 1 gives a brief introduction to this study, aims and the thesis structure.

Chapter 2 has reviewed the literature with regard to clinical applications and relevant flow related parameters involved in the radial and ulnar arteries in the cardiovascular system (CVS), and has explained the ultrasound imaging and its limitations on measuring flow related parameters. The necessity of validating these parameters with experimental or computational phantom system was highlighted.

Chapter 3 applies the methodology based on the Womersley theory to estimate the blood flow rate and wall shear rate in the radial and ulnar arteries using a clinical ultrasound scanner. The experimental flow phantom is designed to validate those measurements under different circumstances by changing a series of parameters so as to study their influences on blood flow rate and wall shear rate estimations.

Chapter 4 adopts a coupling technique to combine image-based CFD modelling of blood flow and ultrasound simulation together to further validate the estimation of blood flow rate and wall shear rate in these two arteries. Maximum velocity in the arteries is also studied through this computational simulation method.

Chapter 5 establishes the methodology to detect the arterial wall motion in the radial artery using ultrasound. The established methodology is validated, not only through the experimental flow phantom but also through computational simulations. Volunteers are

also recruited to test this arterial wall motion detection method in *vivo*. Based on the data from a single volunteer's radial artery, a trial was made to test the blood pressure waveform estimation which is derived from ultrasound measured wall motion waveform.

Chapter 6 presents data collected from healthy volunteers as a case study to test the ultrasound methodologies for estimating the flow rate and wall shear rate *in-vivo*.

Chapter 7 concludes this thesis and sets out suggestions for future work.

Chapter 2

2. Background

This chapter will provide a detailed background about this study. Firstly the cardiovascular system (CVS) and diseases related to this system are briefed. The significance of radial and ulnar arteries in clinical applications is then highlighted. Next, the requirement to measure flow related parameters in those two arteries is explained. The ultrasound imaging technologies used to estimate those parameters are discussed, along with the validation strategies. Finally, the gaps in the literature and explanation of the novelties and challenges are concluded.

2.1 Cardiovascular system

The CVS, also known as the circulatory system, is an organ system that circulates blood so as to transport nutrients and oxygen, and to pick up carbon dioxide and waste products in the body. Diseases related to the CVS have become the leading cause of millions of deaths worldwide (Davidson et al. 2016). Clinical management is needed to improve patents' quality of life and reduce mortality and morbidity.

2.1.1 Components of cardiovascular system

The complete CVS consists of the heart, blood vessels and blood. Performing as the power source, the heart pumps blood out each cardiac cycle body-wide to the blood vessels. It has four chambers, two atria as receiving chambers and two ventricles as discharging chambers, working under two alternate phases called systole and diastole. During systole, both left and right ventricles contract to pump blood out of the heart. Conversely, blood flows into the left and right atria during the diastolic phase. The atria and ventricles work in together to ensure blood is circulating efficiently.

The blood first passes through arteries, capillaries, then into veins and finally flows back to the heart. The heart muscle receives its own blood supply through the coronary arteries. The diameter of blood vessel varies from 5-10 μm for capillaries to around 25 mm for large arteries and veins. Vessel walls have three primary layers, the intima, the media and the adventitial layer, directly or indirectly interacting with the blood flow and regulating the functionality of the vessel organ (Humphrey 2002).

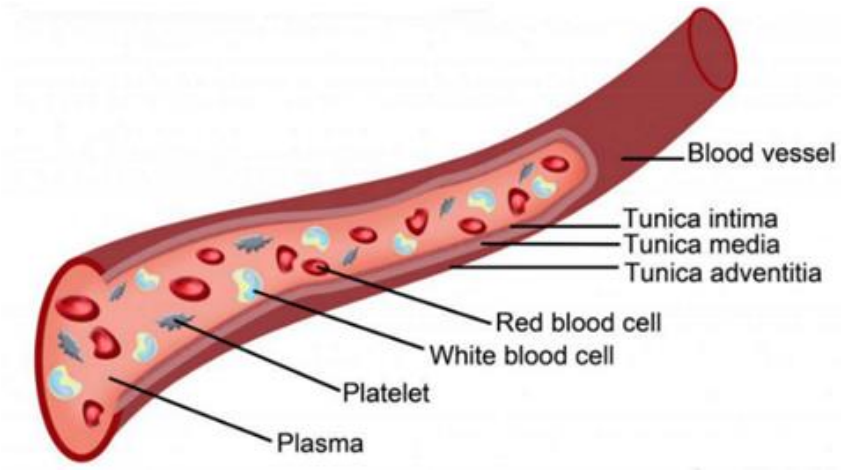

Fig. 2. 1. Blood vessel and its blood constituent

Blood carries and delivers necessary materials to cells, and transport metabolic waste products away from cells. It accounts for 7% of human body weight with an average density of approximately 1050 $kg.m^{-3}$, and is composed of plasma, red cells, white cells and platelets as indicated in Figure 2.1. The red cells are the most abundant (with about 45% by volume) while white cells account for only about 0.7% and the plasma about 54.3%.

2.1.2 Diseases related to CVS

The incidences of diseases developing related to the CVS are very high amongst the world population and the mortality and morbidity continue to increase, especially in the developing world (Mendis et al. 2011). A wide range of diseases may occur at various sites due to the malfunction of the CVS in specific sites (Yusuf et al. 2001). Some clinical events are directly caused by the diseases in the CVS itself, which are called cardiovascular diseases (CVDs), such as heart-attacks (relevant to coronary arteries) and stroke (relevant to cerebrovascular arteries). It was reported in 2008 that heart attacks are responsible for 7.3 million deaths and strokes for 6.2 million deaths (Heron 2012). Some

other diseases, which may not be directly related to CVS, involve CVS in treatment. For example, haemodialysis (a means of artificially replacing functions of the kidney) is a treatment for patients with end stage renal disease (ESRD). Here reliable vascular access is required. It was reported that there are more than 1 million patients receiving this treatment worldwide (Couser et al. 2011).

Diagnosis and intervention of those diseases can reduce the mortality and morbidity, and improve the patients' quality of life (Levi et al. 2009). Different medical imaging modalities, such as ultrasound (US), magnetic resonance imaging (MRI) and computerized tomography (CT), play an important role in diagnosis and treatment planning. Flow related parameters obtained from medical imaging technologies can be useful indicators in clinical practice and research. Since disease occurs at different sites throughout the CVS, measuring the flow related parameters in many specific sites has been studied in the literature (Dodge et al. 1992; Kehrer et al. 2002; Grant et al. 2003; Mynard et al. 2013). This thesis will focus on measuring some important flow related parameters in the radial and ulnar arteries using ultrasound imaging.

2.2 Clinical conditions related to radial and ulnar arteries

The radial and ulnar artery are closely involved in some specific diseases and clinical procedures both in clinical practice and research. Generally, involvement of these two arteries can be classified into these three categories: study of CVDs occurring at hand arteries, clinical procedures with respect to these two arteries, and blood pressure estimation from the radial artery.

2.2.1 Diseases

The radial and ulnar arteries are two main arteries supplying blood to hand as shown in Figure 1.1. Abnormalities of blood flow occurring in the hand may be related to the biomechanical parameters in these two arteries. A common example of circulation related problems in the hand is Raynaud's disease.

Raynaud's disease, also called *Raynaud's Phenomenon* (RP), is characterized by transient cessation of blood flow to the digits of the extremities, such as fingers and toes (Cooke and Dzau 1996). The prevalence of symptoms of Raynaud's phenomenon in general practice was 11% and 19% respectively in men and women (Silman et al. 1990). RP is usually manifested as colour changes along with pain, sensations of cold or

numbness when the patients are exposed to cold, anxiety or other emotional stress (Cooke and Marshall 2005), as shown in Figure 2.2. This causes the affected area to change colour to white, then blue and then red as the blood flow returns. These symptoms can last from a few minutes to several hours. Nietert et al. (2015) reported that RP was independently associated with mortality among older adults in a 20+ years' follow-up study. RP is considered to be primary RP if it is related to a functional dysregulation of autonomous nervous system with evidence of any associated disorders, and the reason for this type of RP is still unknown. In comparison, secondary RP is associated with connective tissue diseases such as systemic sclerosis (SSc) or other related diseases (Lally 1992).

Herrick (2013) proposed that the first principle of management of RP is to establish the diagnosis to distinguish secondary RP from primary RP. The underlying reasons for primary RP and secondary RP are quite different, and usually the secondary RP are more severe. For example, the SSc-related RP, which results from structural as well as functional vascular change, frequently progresses to digital ulceration and/or critical digital ischemia (Tiev et al. 2009; Khimdas et al. 2011). In this case, it is important to diagnose it at early stage so that the patient can receive proper management.

The diagnosis of RP is based mainly on clinical criteria (Wigley 2002), and it is often difficult to differentiate between primary RP and secondary RP, especially in patients with underlying connective tissue disorders (Lee et al. 2006; Kim et al. 2008). Although many different techniques were used to diagnosis these two types of RP (Wigley 2002), there is still no reliable single method.

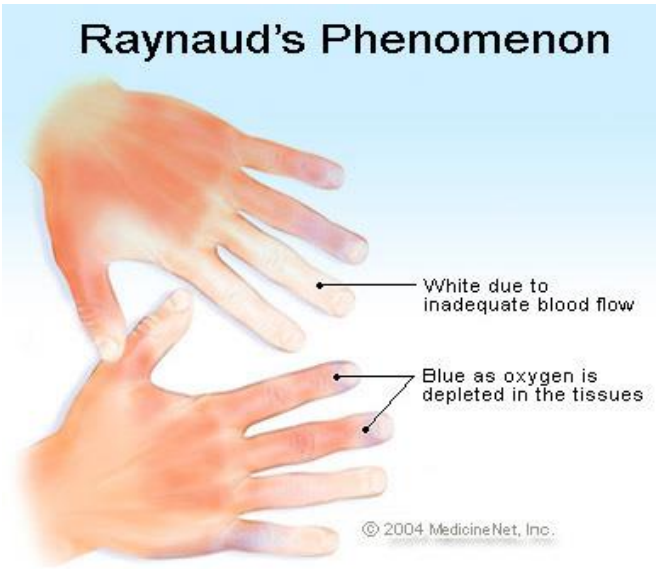

Fig. 2. 2. Raynaud's phenomenon shown in hand.

2.2.2 Clinical procedures

Ease of accessibility, as well as the collateral circulation in radial and ulnar arteries, makes the radial artery a popular site for conducting some clinical procedures.

One of the procedures involving the radial artery is harvest for cardiac surgery, where the radial artery is harvested and used as a bypass graft to replace a severely stenosised coronary artery. The radial artery is now the third most commonly used arterial conduit in myocardial revascularization and its popularity is growing rapidly (Iaco et al. 2001; Abu-Omar et al. 2004; Achouh et al. 2012; Gaudino et al. 2015). The reason for radial artery as a good option on this is that it can be harvested easily, has handling characteristics superior to other conduits, and a suitable length can be harvested (Taggart 1999). An assessment of the adequacy of the ulnar collateral hand circulation before harvesting is necessary to allow the safe harvesting of the radial artery.

Another involvement of the radial artery in clinical practice is the radiocephalic arteriovenous fistula (RAVF), where the radial artery is accessed to construct a connection with the nearby cephalic vein at the wrist to allow diverting blood flow from radial artery to the vein for the hemodialysis (Van Tricht et al. 2005). Permanent vascular access is the lifeline for the end stage renal disease (ESRD) patient. It was recommended by UK Renal Association that all patients with ESRD who commence hemodialysis or are on long-term hemodialysis should be dialysed with arteriovenous fistula (AVF) as first choice (Kumwenda 2015). Due to it minimizing of complications, revisions and interventions, RVAF was recommended as the first choice when compared to other AVF creations (Tordoir et al. 2007). However, the high rate of failure to mature (FTM) is the major disadvantage of this technique, which makes it essential to evaluate preoperatively the practicality to use this RAVF access. Follow-up care is also important for the fistula to maintain functional during the postoperative arterial remodelling (Brahmbhatt et al. 2016).

2.2.3 Estimation of blood pressure

Blood pressure is an independent cardiovascular risk factor, especially the peak systolic blood pressure (SBP) commonly used in clinical practice. The blood pressure waveform has been used to analyse the CVS in many arteries, giving an insight into the effects of aging and of vasoactive drugs on the arterial pressure wave (Wilkinson et al. 1998; Nichols 2005).

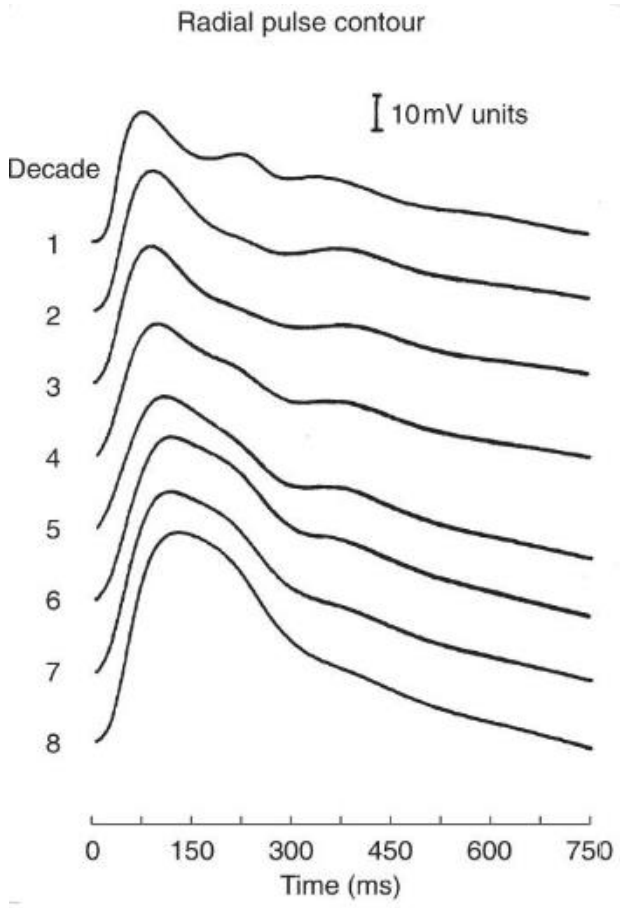

Fig. 2. 3. Change in contour and amplitude of pressure waves recorded in the radial artery in normal subjects between the first and eighth decade of life. Data are ensemble averaged into decades from 1005 different subjects (O'Rourke et al. 2001).

The radial artery is a suitable site for measuring the blood pressure waveform due to its superficial location. The blood pressure waveform analysis, also called the pulse wave analysis, in the radial artery has been used to investigate diseases in the CVS for many years. For example, the changing pressure waveform contours of subjects from different ages were reported by (Kelly et al. 1989) and O'Rourke et al. (2001) as shown in Figure 2.3. Change in radial artery waveform could indicate change in the wall stiffness of the whole CVS (Nichols 2005). In addition, Cohn et al. (1995) proved that pulse wave analysis is useful in screening subjects for early evidence of vascular disease such as hypertension and coronary artery disease and in monitoring the response to therapy. It was also used by Duprez et al. (2004) to evaluate the risk of CVS by correlating diastolic and systolic indices of pulse waveform with traditional risk factors in asymptomatic population. Furthermore, the radial artery pressure waveform can be used to estimate

central blood pressure through mathematical transfer function (Chen 1997; Hope et al. 2002). This was proved to useful in clinical practice (Safar et al. 2002; Roman et al. 2007).

2.3 The importance of flow related parameters

As explained in last section, radial and ulnar arteries in the CVS are implicated in assessment of peripheral artery disease in the hand (the Raynaud's phenomenon), clinical procedures (radial artery harvesting and radiocephalic arteriovenous fistula), and estimation of blood pressure waveform. All these clinical applications require measuring flow related parameters. In this section, measurement of some flow related parameters using ultrasound for clinical applications in these two arteries is reviewed.

2.3.1 Blood flow velocity and volumetric flow rate

Values of flow velocity and flow rate have proven useful in these clinical applications. These are linked with each other since flow rate can be estimated by measuring the flow velocity and the arterial area. The flow rate in this study always refers to the volumetric flow rate.

Raynaud's phenomenon

Knowledge of flow velocity and volumetric flow rate in the radial and ulnar artery is useful for investigating RP. Preliminary study by Mcilory (1985) pointed out that Doppler ultrasound can differentiate patients with RP from normal subjects by investigating the blood flow velocity in the hand arteries at different temperatures. Chikui et al. (1999) found that the blood flow rate in the deep radial arch is statistically higher in healthy controls than that in patients with RP using Doppler ultrasound. The flow differences between RP patients and healthy controls in hand arteries were also shown by Toprak et al. (2009). A further study by Toprak et al. (2011) showed that the blood flow rate both at baseline and after cold provocation provided a clue to distinguish primary RP and secondary RP, with flow rate lower in the radial and ulnar arteries in patients with secondary RP.

Harvesting of radial artery

Prior to harvesting radial arteries for coronary bypass grafts, assessment of adequacy of the collateral ulnar circulation to the hand is necessary to avoid ischemia. Although severe ischemia after radial artery harvest is rare, several cases (including leading to death)

have been reported (Manabe et al. 2005). Modest symptoms such as sensory abnormalities and exercise intolerance were mentioned in some studies (Verma et al. 2004; Manabe et al. 2005). Preoperative exclusion of these risks before radial artery harvest is considered essential to avoid complications, especially to avoid severe hand ischemia which is more dangerous. The Allen test is the most popular current preoperative screening method for radial artery harvest, but this test is considered far from ideal because of considerable numbers of both false-positive and false-negative results (Manabe et al. 2002; Abu-Omar et al. 2004).

Doppler ultrasound has been proposed to evaluate the feasibility of radial artery harvest and has proved able to predict safer radial artery harvest more accurately in general than the Allen test (Abu-Omar et al. 2004). Agrifoglio et al. (2005) suggested to exclude patients from radial artery harvest when the radial artery peak systolic flow velocity is less than 20 $cm.s^{-1}$. An increase in ulnar artery peak systolic velocity less than 20% from baseline with radial artery compression was considered abnormal, and the radial artery should be excluded for harvest (Rodriguez et al. 2001). Patients possessing low ulnar flow levels (less than 40 $ml.min^{-1}.m^{-2}$ during compression of the radial artery) have a higher risk of ischemia after the radial artery harvest even with a negative Allen test (Manabe et al. 2002).

Therefore, accurate measurement of blood flow velocity and flow rate in the radial and ulnar arteries is clearly an important preoperative assessment of hand circulation for radial artery harvest in coronary bypass graft.

RAVF for haemodialysis

As explained before, creation of a wrist radiocephalic arteriovenous fistula (RAVF) is a recommended option for the haemodialysis procedure among end stage renal disease (ESRD) patients. However RAVF has the problem of high rates of thrombosis and failure to mature (FTM). This FTM can be defined as a surgically created AVF that failed to properly grow to become usable for the purpose of haemodialysis. Such failure is manifest as difficult cannulation, inadequate AVF flow characteristics or both (Nassar 2008). Therefore consideration is required to be taken to evaluate the suitability of RAVF when choosing a patient's preferred access type.

Blood flow velocity and flow rate in the radial artery have been studied in the literature to predict the outcome of RAVF. Masengu et al. (2016) stated that a radial artery flow rate less than 50 $ml.min^{-1}$ was associated with a sevenfold increased risk of FTM in

RAVF. Similar reports also demonstrated that flow rate in radial artery, over 54.5 ml.min^{-1} and 40 ml.min^{-1} respectively, was associated with better AVF outcomes (Yerdel et al. 1997; Malovrh 2002). Peak systolic flow velocity in the radial artery was found to be significantly lower in patients who had FTM, and at the same time the radial artery resistive index (RI) was higher (Gibyeli Genek et al. 2015). Non-invasive blood flow velocity measured in the radial artery 24h after the operation has proved capable of predicting the fistula success or failure at an early stage (Wong et al. 2011).

2.3.2 Wall shear stress and wall shear rate

Wall shear stress (WSS) is the tangential shearing force exerted by the blood flow on the arterial vessel wall, as illustrated in Figure 2.4. Compared to the blood pressure (10 000 Pa) in the radial direction, WSS is less than 10 Pa in the normal artery (Malek et al. 1999). WSS is sensed within the endothelium and thought to be part of a control mechanism in the regulation of arterial structure, remodelling, and the localization of atherosclerotic lesions in the arterial wall (Davies 1995), having attracted great interest over the years (Hoeks et al. 1995; Malek et al. 1999; Gnasso et al. 2001; Blake et al. 2008; Mynard et al. 2013). The stress is calculated by eqn. 2.1 as follows:

$$\tau_w = \mu \cdot \frac{\partial v}{\partial r}\Big|_{r=R} \tag{2.1}$$

where μ is the dynamic viscosity, v is the velocity in the vessel, r is the variable for position in the vessel, $\partial v / \partial r$ is the velocity gradient, also called shear rate, and R is the radius of the vessel. The $\partial v / \partial r|_{r=R}$ is called the wall shear rate (WSR).

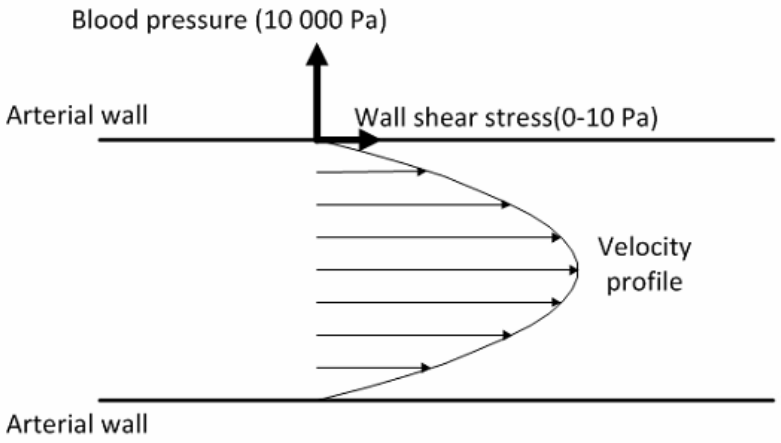

Fig. 2. 4. Tangent forces on the arterial wall arising from blood. The horizontal force is wall shear stress and the vertical force is blood pressure.

Experimental studies suggest that low WSS promotes plaque development and high WSS is associated with plaque destabilization. Investigations on this have been conducted in different locations, such as coronary artery, carotid artery and aortic artery (Gnasso et al. 1996; Spring et al. 2006; Samady et al. 2011).

In the case of the radial artery, the WSS or WSR is a biomarker for evaluating the remodelling of radial artery after RAVF for haemodialysis access. The most important thing after the RAVF surgery is for the fistula to mature so that it can be used as a routine vascular access. However, the patency rate within 12 months is only 60% (Brahmbhatt et al. 2016). Many studies have been working to find the responsible mechanism leading to the fistula failure during the radial artery's remodelling, including investigating the WSS or WSR in the radial artery. The main reason is that the tractive force acting on the arterial wall influences the endothelial cell function which, as explained above, is believed to be part of a control mechanism in the regulation of arterial structure, remodelling, and the localization of atherosclerotic lesions in the arterial wall.

Some studies looked into the radial artery wall remodelling by directly estimating the WSS in this artery. Girerd et al. (1996) measured WSS in radial artery with ultrasound, and found the WSS was maintained at a similar level although blood flow internal diameter increase during the process of remodelling. Compared to Girerd's study, Remuzzi et al. (2003) improved the methodology of estimating WSS and did find an increase in WSS after surgical creation of RAVF. Ene-lordache (2003) pointed out that after surgery the radial artery diameter adapts to keep peak pulsatile WSS nearly constant (only with a small increase), but the mean WSS increased over sevenfold. Ene-Iordache and Remuzzi (2012) also stated that low WSS occurs in the sites where luminal reduction and stenosis are found. In order to investigate the relationship between WSS and radial artery remodelling in the event of RAVF, some simulation studies on estimating WSS in radial artery were also conducted (Kharboutly et al. 2010; Manini et al. 2014).

From eqn. 2.1, it should be noted that shear stress and shear rate are related by the dynamic viscosity μ. For most simple fluids, also known as Newtonian fluids, viscosity is independent of shear rate. However, human blood is a non-Newtonian fluid and exhibits a change in viscosity with shear rate, especially at lower shear rates and in small vessels. Fortunately this anomalous effect is not significant in blood vessels with diameters of 0.1 mm or more and it is possible to assume the blood as a Newtonian fluid in major arteries when it comes to use the viscosity in calculations of blood flow (Nichols

2005). Based on this assumption, only one of these two parameters need to be calculated, either the shear rate or the shear stress.

In this study, the radial and ulnar arteries have the diameter in the range of 2 – 3 mm and therefore it is safe to regard the blood as a Newtonian fluid and the dynamic viscosity of blood is considered to have a typical value of 3.5 mPa.s (Stewart et al. 2012). Because of the linear relationship, the wall shear rate and wall shear stress are regarded with no difference when mentioned in this thesis.

2.3.3 Arterial wall motion

As explained in section 2.2.3, the value out of measuring blood pressure waveform in the radial artery is that it can be used as an important biomarker in assessment of the CVS. Normally this pressure waveform is measured by an applanation tonometry. However, it can also be derived from the arterial wall motion (AWM) based on the correlation between arterial cross-section area and pressure in a healthy artery (Hayashi et al. 1980). The underlying reason is that arterial wall motion is caused by the variation of blood pressure in the lumen. A number of studies have focused on estimating the blood pressure waveform from its corresponding AWM in the carotid artery using ultrasonic methods (Watanabe et al. 1998; Beulen et al. 2011).

In theory, blood pressure waveform in the radial artery could also be estimated from its corresponding AWM measured by the ultrasonic method. This ultrasonic method has a potential to be an alternative way to estimate blood pressure waveform in the radial artery.

2.4 Ultrasound imaging of arteries

The aforementioned blood flow related parameters have been widely studied with ultrasound imaging techniques over the past decades (Hoskins et al. 1998; Eklund C 2012). Ultrasound application in the CVS involves different means, such as B-mode, spectral Doppler, Colour Doppler, and sometimes even beam forming and radio frequency (RF) data. The basic principles of ultrasound imaging and its limitations are explained in this section.

2.4.1 Transmitting and receiving ultrasound signals

During ultrasound imaging high frequency compression wave pulses from a transducer are transmitted and sound waves are partially scattered back to the transducer; these are converted into measurable electrical voltages for reconstructing the anatomical and motion information in body.

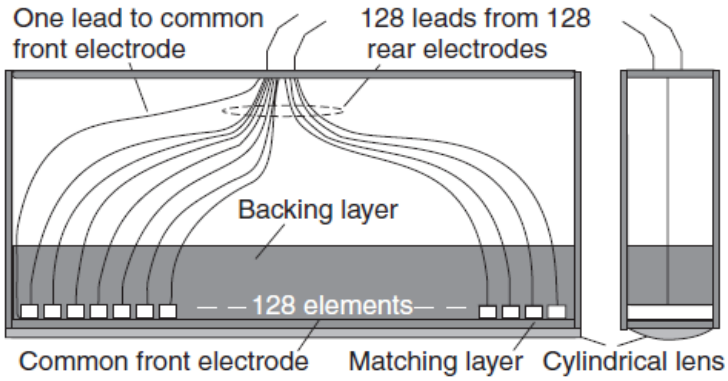

Fig. 2. 5. Section through a linear-array transducer (reproduced with permission of Cambridge University Press, from Hoskins 2010a).

Modern transducers are composed of many individual elements as shown in Figure 2.5, sending and receiving sound waves by converting signals between electrical form and mechanical pressure using piezoelectric material. Each of those elements can be turned on or off in a pre-programmed sequence by the manufacturers according to different modes. Some research systems allow reprogramming of the sequence.

Generally for each single scan line, a group of elements (as shown in Fig. 2.6a) in the array will be activated, transmitting high frequency short pulses according to a well-controlled time sequence, forming a transmitting aperture. The returning signal is treated in analogous way when a receive aperture is formed. Beam-forming techniques are used to control the transmitting and receiving processes, allowing setting focal regions at different depths and also steering the beam to different directions as shown in Figure 2.6b and Figure 2.6c. Based on the electrical signals from reflected sound waves, a series of signal processing techniques are applied to multiple elements simultaneously to obtain the RF data, as shown in Figure 2.6c.

In practice, many parameters need to be carefully considered, such as transducer bandwidth, element size, pulse central frequency, pulse length and shape, apodization, using a lens to focus in the elevation plane, and RF signal formation. Although those

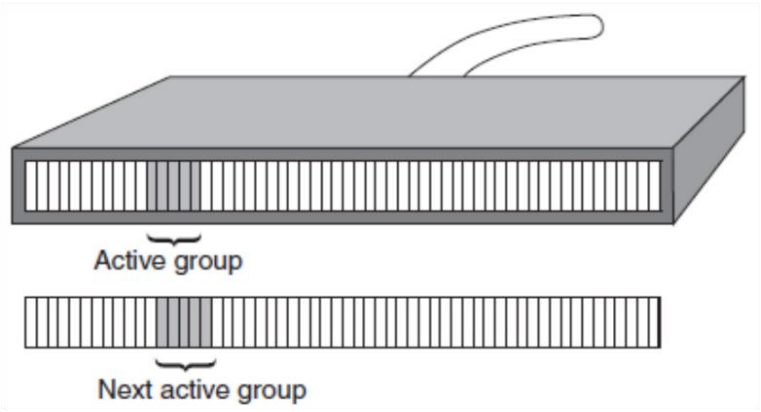

a

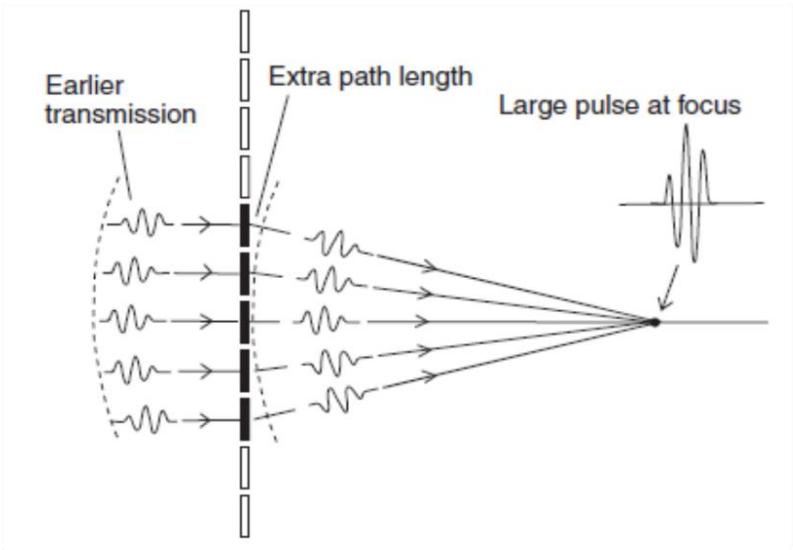

b

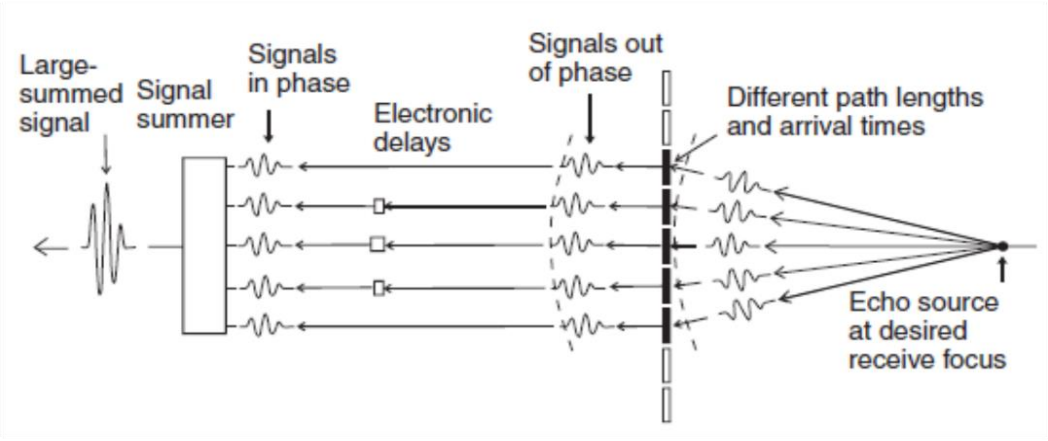

c

Fig. 2. 6. Beam forming technique. (a) The active element group is stepped along the array by dropping an element from one end and adding a new on to the other. In reality, the group would contain at least 20 elements rather than the five shown here. (b) Creating a transmission focus for a linear array transducer by arranging a delay time of the pulse from each element. (c) Creating a receive focus for a linear-array transducer by introducing a delay time before the scan converter (reproduced with permission of Cambridge University Press, from Hoskins 2010a).

techniques vary slightly among different situations, the basic transmitting and receiving procedure explained here applies to most current transducers, including phase-type transducer or other advanced transducers like 3D transducer (Hoskins et al. 2010a).

2.4.2 Different modes in ultrasound imaging

As explained in last section, a number of elements are involved in transmitting and receiving of one scan line. In practice, the scan line is swept along the transducer incrementally to build a 2D image as shown in Figure 2.6a. Usually the position of the central element within the active element group is defined as the origin of the scan line. Different timing sequences for obtaining the RF data with different active elements forming the aperture in the transducer, together with different signal processing methods, determine the imaging mode in the ultrasound imaging. The most basic modes in modern scanners are explained in this section.

Greyscale imaging

In brightness mode (B-mode), the scan line moves incrementally from one end of the transducer to the other end, advancing forward one element at a time in the beam centre. The RF data from usually over 100 scan lines is then used all together to form one frame of the 2D B-mode image. The same procedure is repeated commonly more than 30 times per second to give a flicker-free moving image. In order to obtain the practical B-mode images, techniques like demodulation, envelope detection and log compression are applied to those RF data. Images from B-mode provide a cross-sectional view of the body structure. The brightness of the image at each pixel represents intensity of returned echo from that position in the tissue. Depth information of this 2D B-mode image is derived based on the known speed of sound (usually 1540 $m.s^{-1}$) in soft tissue and the time between transmission and reception.

Doppler ultrasound

In Doppler ultrasound, the reflected sound waves have shifted frequencies caused by the movements of targets in the insonating area. The velocity information could be estimated based on Doppler Effect as explained in eqn. 2.2,

$$f_d \triangleq \frac{2 \cdot f_t \cdot v \cdot \cos(\theta)}{c} \tag{2.2}$$

where f_d is the Doppler shift frequency, f_t represents the frequency of transmitted sound waves, θ is the angle between sound beam and blood velocity, and c represents

the velocity of sound wave in the tissue (usually assumed as 1540 $m.s^{-1}$).

There are different types of modes determined by the ways of beam-forming. Early Doppler devices applied two transducers simultaneously, one for transmitting sound signals and the other for receiving. The sound waves transmitted and received are continuous, and this is therefore called the continuous wave (CW) Doppler mode. The frequency spectrum of the received continuous wave is estimated through signal processing to extract the velocity information according to eqn. 2.2. Since the continuous system is unable to provide the information on the depth from which the blood flow signal has returned, it is not as popular as its later counterpart the pulsed wave (PW) Doppler which is commonly used in the modern Doppler system.

The PW Doppler system transmits a sound pulse and receives the reflected signal with the same transducer as shown in Figure 2.7. From the measured time lag between transmission and reception in the same transducer, the PW Doppler system can differentiate depth. After transmitting a pulse, the transducer waits for the reflected signal and the depth information is encoded in the receiving time sequence as the speed of sound is known. With the help of the grayscale image or colour mode (explained later), the reflected signal is gated within the artery of interest (also called the sample volume as shown in Figure 2.8) and only the movements within this gate will be derived by signal processing. This PW Doppler mode allows to detect the velocity information at a specific site.

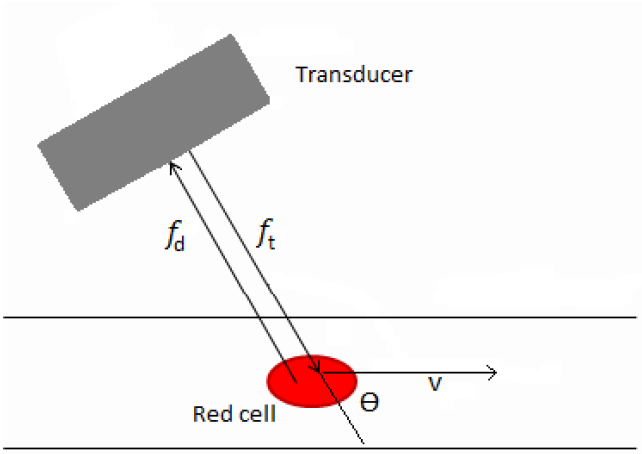

Fig. 2. 7. A simple diagram for demonstrating Doppler ultrasound.

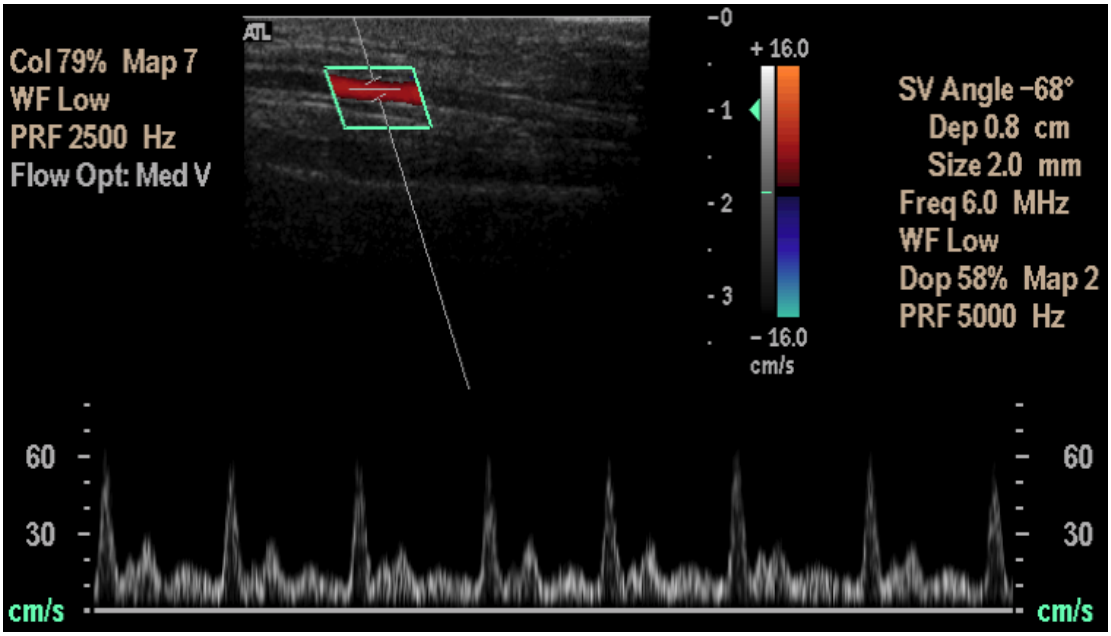

Fig. 2. 8. Triplex ultrasound system for scanning CVS.

Another Doppler mode is the colour Doppler ultrasound. This is able to provide the 2D colour-mapped images to illustrate the movement of the blood in a chosen area (a box as shown in Figure 2.8) and normally red and blue are adopted by most manufacturers to represent the blood flow in two directions. The beam is generated along the transducer elements using beam-forming technique to form a 2D planar image. For each scan line, normally a certain number of pulsed-waves (8-10 pulses) are transmitted and received to implement the correlation algorithm used in estimating shifted frequency in colour mode. This means the frame rate of colour imaging will be reduced in accordance with the number of pulses needed (also called "ensemble length"). The correlation algorithm, unlike the whole frequency spectrum estimation in Spectral Doppler system, estimates the mean frequency shift in a specific area called volume sample (Kasai et al. 1985). With the correlation or its variants, three quantities with respect to blood velocities could be given: power, mean blood velocity and variance.

Doppler mode is combined with B-mode in modern scanners. Two modes combined together is called a duplex system where PW mode or colour mode is superimposed on the B-mode image that visualize the structure or architecture of the region of interest. PW mode, colour mode and the B-mode could all be mixed together to form the Triplex ultrasound system where 2D colour mapping of blood vessel, flow velocity sonogram of a specific sample volume and B-mode structural image are processed and shown on the screen at the same time as shown in Figure 2.8. In Duplex and Triplex system, the timing

of transmission and reception of sound pulses is well-designed to coordinate the scan procedure. Inevitably, the combined mode decreases the frame rate of the imaging since only one transducer is used both for sound transmission and reception.

2.4.3 Limitations of ultrasound measurements

What has been described so far assumes an ideal imaging system operating in an ideal medium. The real imaging system has limitations at each stage of the image formation. For example, the beam from each scan line has finite dimensions changing with position in the ultrasonic field, as shown in Figure 2.9. The beam structure and dimension directly affect the spatial resolution of the system. Actually resolution is determined by many factors, such as the pulse duration, pulse wave frequency, transducer bandwidth, element sizes in transducer and beam-forming methods. The contrast resolution and dynamic range of an ultrasound system can also influence the scanning. Further, detecting moving objects needs high temporal resolution, especially for Doppler ultrasound in the CVS.

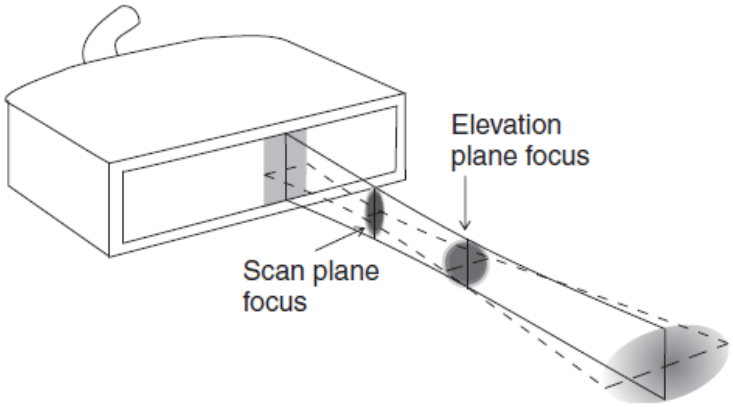

Fig. 2. 9. The shape of a typical ultrasound beam (reproduced with permission of Cambridge University Press, from Hoskins 2010a).

Factors affecting spatial resolution, temporal resolution and contrast resolution play their roles in affecting the performance of an ultrasound system in different and sometimes conflicting ways. Compromises always have to be made to achieve an overall performance. Moreover, the speed of sound is not constant in all tissues and the sound wave attenuates heavily as it travels along the tissue. All these lead to imperfections in the images.

For ultrasound imaging in the CVS, one more important factor significantly affecting Doppler-based measurements is the blood flow pattern. Blood flow is pulsatile and can develop to extremely complicated situations due to bifurcating structures, stenosis or curvature of the arteries. In each cardiac cycle, the complex flow condition under these circumstances will result in the blood cells moving in different directions at various velocities in a pulsatile way.

Red cells (accounting for nearly 95% of cells in blood) are responsible for scattering most of the insonating energy. The amplitude of scattered signal from red cells is much weaker than that from surrounding tissue. Although microbubbles can be used as a contrast agent in ultrasound imaging to increase the Doppler signal intensity and signal-noise ratio (SNR) in cardiovascular applications (Stride and Saffari 2003; Tang et al. 2011a) and it has been expanding markedly in recent years (Leow et al. 2015b; Ma et al. 2015) , it is still under development and has only been partially adopted in clinical practice under some specific circumstances(Tang et al. 2011b; Appis et al. 2015). It also adds greatly to the cost and complexity of a scan because the microbubbles have to be injected into the region of interest *in-vivo* and they are not stable under a long period of time.

Typical Doppler ultrasound in modern scanners only detects one dimensional movement in the propagating direction of sound beam. Only velocity components projected to this beam travelling direction can be detected. In this case, the angle between moving cells and beam direction must be known to calculate the magnitude of the velocities of the blood cells. This angle is hard to measure, especially when the flow condition is complicated. In addition, the Doppler ultrasound estimates the frequency shifts caused by thousands of moving cells in the beam travelling direction within one volume sample where blood cells are not just moving in one direction. Usually it is assumed the blood flow is parallel to the blood vessel and the beam-vessel angle is used to estimate the flow velocity in the vessel direction. The difference between the beam-vessel angle and true beam-flow angles (angles between sound beam and moving red cells) may cause error in estimating blood velocity (Hoskins 1999a; Van Canneyt et al. 2013)

Since the flow condition in the arteries is complex and Doppler ultrasound system only detects the velocity component in the direction of sound beam, the estimated velocities from Doppler ultrasound does not fully capture the flow condition. PW and colour Doppler also have the problem with aliasing when the blood cells are moving a

very high speed. The pulse repetition frequency (PRF) has to be at least twice the maximum frequency shift caused by Doppler Effect.

The errors in measuring maximum velocity (maximum frequency shift) and mean velocity (mean frequency shift) in arteries with ultrasound have been reported by Hoskins in a series of studies using flow and string phantom (Hoskins 1996; Hoskins 1997; Hoskins 2011). In Hoskins' studies, it is stated that both maximum velocity and mean velocity is prone to overestimation as a result of geometric spectral broadening and small sample volume size respectively. The extent and causes of maximum velocity estimation errors using linear-array Doppler ultrasound transducers have been investigated by Steinman (Steinman et al. 2001). Researchers in several other groups also reported inaccuracies in measurements relating to blood velocities in the arteries (Gill 1985; Logason et al. 2001; Lui et al. 2005). Among clinical studies, discrepancies were found in the maximum velocity measured from patients using different ultrasound scanners and variations from the same scanner at different vessel-beam angles (Fillinger et al. 1996; Tola and Yurdakul 2006).

In order to tackle the limitations of 1D velocity measurement in a typical ultrasound scanner, some advanced methods for blood velocity vector flow imaging (VFI) are of great interest in recent years. The ultrasound imaging methodologies for reconstructing vector flow can be broadly summarized into two categories: conventional sequential data acquisition and parallel systems (Jensen et al. 2016a; Jensen et al. 2016b). In the conventional sequential data acquisition, a focused field is emitted in one direction and received beamforming is performed before estimating the velocity vector along this direction, which includes multi-beam methods (Dunmire et al. 2000), speckle tracking (Bohs et al. 2000; Poelma 2017), transverse oscillation (Jensen 2015), colour flow mapping derived VFI (Garcia et al. 2010), directional beamforming (Jensen and Nikolov 2004), and variants of these(Jensen et al. 2016a).

In the parallel systems, the spherical or plane sound waves are transmitted and received in each sequence and can achieve much higher frame rate than the conventional ultrasound imaging (Udesen et al. 2005; Jensen et al. 2006). Parallel systems allow very fast and sensitive velocity estimators, capable of acquiring thousands of images per second for fast moving flow as well as yielding the estimates of low velocity flow. It also provides the possibility of assessing highly complex flow with transitory vortices, moving tissues, as well as functional ultrasound imaging (Jensen et al. 2016b).

Ultrasound contrast agent (Microbubbles) can be integrated with those VFI techniques, responsible for enhancing reflected ultrasound signals (Leow et al. 2015a; Poelma 2017). Although a large number of research studies have been done on 2D or 3D flow imaging, using either the conventional sequencing techniques or the parallel system, these techniques are still under development and have not yet become an accepted clinical standard. The amount of clinical studies is still very limited and restricted to smaller patient populations. Reasons may include lack of robustness, limitations in acquisition and high demanding in calculation for real-time imaging, which could cause limited practical applicability (Ekroll et al. 2012; Jensen et al. 2016b; Jensen et al. 2016a).

Since VFI techniques have not reached a wide clinical application, the conventional pulsed waved (PW) Doppler ultrasound is still the routine approach for detecting blood flow velocity in clinical practice in spite of the inevitable biasness in estimating flow velocity. Biased measurements of blood velocity lead to the inaccuracies in measuring other parameters which are based on the blood velocity. The most relevant parameter is the flow rate which is usually derived using blood velocities and arterial diameter. Current clinical scanners only provide quantitative blood velocity (frequency shifts) with PW Doppler mode from a single small area called the sample volume. In order to obtain the flow rate in an artery which is much bigger than Doppler sample volume, assumptions on the velocity profile within the cross section of the vessel have to be made. For example, the most commonly used Hagen-Poiseuille law assumes that the flow is steady, the artery is a straight rigid cylindrical tube, and the velocity profile in the artery is parabolic in a well-developed domain (Schlichting 1987). Bias could be caused due to these assumptions when deriving velocity profile based on one sample volume in clinical practice.

Due to the difficulties in direct measurements, wall shear rate is derived from the measured blood velocities as explained in eqn. 2.1. Normally velocity profile within the artery and arterial diameter are used together to calculate the velocity gradient at the vessel wall (Blake et al. 2008; Mynard et al. 2013). Errors in measuring blood velocities with Doppler ultrasound and assumptions made for deriving the velocity profile have a direct influence on the estimation of the wall shear rate.

The arterial diameter is required for estimating the flow rate and wall shear rate. Some errors also exist when measuring arterial diameter with ultrasound under B-mode or A-mode due to the limited spatial resolution with the frequency of ultrasound used (Gemignani et al. 2007; Brum 2011). Increasing ultrasound frequency could improve the

spatial resolution but at the expense of penetration depth. Bearing in mind that the wavelengths of ultrasound of frequencies 3 MHz, 5 MHz and 10 MHz are 0.5 mm, 0.3 mm and 0.15 mm respectively, the error in the area estimation, especially on small vessels of a few millimetres diameter, can be very high (Li et al. 1993b). This error in diameter is squared when it is used for estimating the volumetric flow rate. Errors in diameter can also cause problems in locating the vessel wall which consequently lead to further errors in estimating the wall shear rate.

2.5 Validation of measurements from ultrasound imaging

Errors in ultrasound-measured parameters make it necessary to validate those measurements before they are applied clinically. The validation enables us to learn the sources of error, error ranges, and limitations in those measurements. Often, for validation a phantom is used. This provides simulated arterial ultrasound images and allows various measurements to be obtained. Phantoms can be classified into two categories: experimental phantom and computer-based (simulated) phantom.

2.5.1 Experimental flow phantom

An experimental flow phantom system was built using various materials to mimic the physical properties of human tissue and blood in an ultrasound beam. To give simulated images very similar to those from the body, it is necessary that relevant physical properties of the phantom be as close to properties of human tissue as possible. A variety of phantoms have been developed for arterial ultrasound. A review on simulation and validation of arterial ultrasound imaging with the help of phantoms was made by Hoskins (2008) in which a variety of phantoms were described such as flow, string, belt and rotating phantoms and electronic injection phantoms. To investigate the flow-related parameters with ultrasound, fluid motion has to be simulated and the most popularly phantom for this is the flow phantom.

A flow phantom is composed of basically four components, a pump, blood vessel mimic, blood fluid mimic and surrounding tissue mimic as shown in Figure 2.10. Some accessories are also needed to complete the whole system, including pipes, connectors, tissue container and blood fluid mimic container. The flow phantom attempts to mimic physiologically realistic flow condition in the CVS from the perspective of ultrasound

imaging. All these four components have to be made with close similarity to their counterparts in the human CVS with respect to their mechanical and acoustic properties.

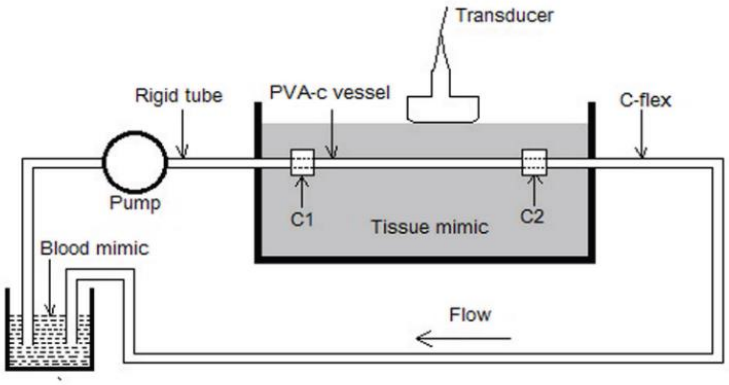

Fig. 2. 10. The diagram of a flow phantom.

The arterial wall motion caused by the pulsatile flow also needs to be mimicked to test techniques and algorithms in estimating arterial wall motion or wall strain. Phantoms designed to generate arterial wall motion were reported in various studies (Dineley et al. 2007; Hammer et al. 2007; Hasegawa and Kanai 2008). The flow phantom (Fig. 2.10) discussed above can also be used to mimic the motion of the arterial wall by pumping pulsatile flow in the loop. Its limitation is that it is difficult to know the real motion of the wall in this flow phantom.

In order to have the correlation between the human body and phantom, great care has to be taken at each step while designing and fabricating the phantom. It is extremely difficult to create a blood vessel with realistic anatomical geometry (Poepping et al. 2004; Meagher et al. 2007). This means it is hard to obtain exact physiological flow conditions in the phantom. In addition, the experimental phantom is not geometrically adjustable. If any sizes need to be adjusted, a new phantom has to be made. Another limitation on experimental phantom is knowing the true value of parameter of interest. For example, if the velocity in the flow phantom is being investigated with ultrasound, the absolute velocity has to be measured with another technique as a reference. This is usually not easy to implement.

2.5.2 Computer-based phantom

Despite these limitations, the experimental phantom is still widely being used in ultrasound imaging research and is the main technique for validation. Concurrently, there have been researchers seeking a computational simulation method for validation, the in-silico simulation. The in-silicon models were extremely helpful in understanding the Doppler process and have led to insights into the factors affecting the Doppler spectrum. Because of its flexibilities, simulation also can be used as the platform to test and improve the practical ultrasound-based measurements and assess signal process algorithms.

A range of toolkits have been developed to simulate ultrasound imaging by a computer (Jensen 1996; Hergum et al. 2009; Varray et al. 2013). The underlying theory in these simulators is mathematic algorithms for solving wave equation. The scanning object for these simulators is called the "synthetic phantom" where tissue-mimicking scatterers are defined with position and amplitude information. This scatterers-based tissue has homogeneous and isotropic acoustic properties. A well-known ultrasound simulator is Field-II developed by Jensen (1996). The Filed-II is widely used for ultrasound simulation and accepted by many researchers, from which simulated RF data with high accuracy could be realized.

In order to use a simulator, such as Field II, the scanned target with modelled point scatterers has to be created. For Doppler ultrasound, modelled point scatterers in the insonating domain change their positions spatially and temporally. In early times, the trajectory of those moving scatterers were determined according to analytical derivation of the flow field in the simulated domain (Kerr and Hunt 1992; Jensen and Munk 1997). These analytically-derived flow fields were not able to describe the realistic flow conditions, leading to discrepancies between simulated RF signals and the physiological situation.

In recent years computational fluid dynamics (CFD) has made it possible to estimate velocity flow field in patient-specific situations with the help of various imaging modalities. This image-based CFD technique has been extensively reviewed (Steinman and Taylor 2005; Sui et al. 2015). It provides an indirect approach to derive flow data, spatially and temporally by modelling the region of interest as a set of differential equations, in which the geometry of the domain and the boundary conditions are obtained from medical imaging, such as CT, MRI, or ultrasound, or other physiological data (De Santis et al. 2011b).

As the flow field and ultrasound data can be obtained through CFD and the ultrasound simulator respectively, Swillens et al. (2009b) coupled these two techniques together by inputting CFD results to the ultrasound simulator. This enables the simulator to have scatterers moving based on a realistic CFD velocity field, rather than a simplified analytical derivation. The meshed geometry from CFD was transformed into a 3D grid where moving scatterers were accurately-fitted and their positions changed spatially and temporally according to the CFD velocity field. A series of studies by Swillens have proved the feasibility of coupling CFD with Field II to acquire high-quality ultrasound RF signals from realistic blood flow (Swillens et al. 2009a; Swillens 2010; Swillens et al. 2010).

Compared to the experimental phantom, the computational simulation of Doppler imaging in blood flow has three advantages: more realistic flow conditions; more flexibility; and true values of parameters of interest are easily obtained from CFD result which consequently can be compared with the ultrasound result.

2.6 Conclusion

What has been discussed so far relates to the radial and ulnar arteries in the CVS, specifically the clinical relevance of these two arteries and their important flow related parameters. Ultrasound is being used widely to measure flow related parameters to help clinicians in diagnosis and treatment. The problem is that ultrasound imaging is prone to bias in estimation due to the means of image formation and the complex flow condition in the vessel. Validation, either experimentally or in simulation, is therefore required. In this section, the gaps in the literature regarding investigation of flow related parameters in radial and ulnar arteries are explained.

Validation of ultrasound measured flow related parameters, such as flow velocity, flow rate, wall shear rate and arterial wall motion, is a necessary task before these parameters are eventually used in clinical practice. This has been done for many sites of the CVS and extensive studies are published in the literature, such as in the brachial artery (Leguy et al. 2009a; Leguy et al. 2009b), carotid artery (Fillinger et al. 1996; Deane and Markus 1997; Samijo et al. 1997; Hammer et al. 2007; Papaioannou et al. 2009; Thorne et al. 2009), aortic artery (Maier et al. 1989; Ponzini et al. 2010), femoral artery(Vergara et al. 2010), coronary artery (Doucette et al. 1992; Ferrari et al. 2006), renal artery (King et al. 2010; King et al. 2011) and others (Savader et al. 1997; Hoskins et al. 2010b).

Unlike in the case for these big arteries, there has been no specific in-depth investigation of errors in these flow related parameters in the radial and ulnar arteries although those parameters in these two arteries are involved in a variety of clinical applications (discussed in section 2.2).

Methodologies applied for estimating flow rate and wall shear rate in these two arteries have been much less investigated than those in other arteries. For example, the advanced Womersley theory is used and evaluated in measurement of flow and wall shear rates in the carotid and brachial arteries (Blake et al. 2008; Ponzini et al. 2010). By contrast, the flow rate in the radial and ulnar arteries was simply obtained by multiplying 1D maximum or mean velocity with blood vessel cross-sectional area in several studies (Ozcan et al. 2011; Toprak et al. 2011; Tiftik et al. 2014). Although a tiny number of studies also used the Womersley theory to estimate the flow and wall shear rates in the radial artery (Remuzzi et al. 2003; Van Canneyt et al. 2013), there are very few studies evaluating those measurements. Considering the value of the flow and wall shear rates in clinical practice and research, it is felt necessary to assess this Womersley theory in these two arteries.

As explained in section 2.3.3, arterial wall motion in the radial artery has the potential to allow us to derive the blood pressure waveform which can be used for pressure waveform analysis. Although applanation tonometry provides a non-invasive way to measure pressure waveform at the radial artery, it was reported that this technology needs to be improved further for routine use in morbidly obese patients (Dueck et al. 2012; Greiwe et al. 2016). The ultrasonic echo-tracking method provided a way to estimate the blood pressure waveform in carotid artery through the arterial wall distension (Papaioannou et al. 2009; Millasseau and Agnoletti 2015). The limitations of tonometry are it can only access superficial sites and it requires underlying stiff or bony structures to flatten the artery wall. They are also fairly uncommon (only one in Ninewells hospital, Dundee) Ultrasound imaging scanners are more common in the clinical environment and can be applied to a wide range of sites in the arterial tree (Haluska et al. 2007). However, this ultrasonic echo-tracking method for deriving the pressure information has only been used to estimate the blood pressure waveform in the carotid artery (Papaioannou et al. 2009; Millasseau and Agnoletti 2015). It is worth investigating this method in the radial artery, thus providing an alternative method to obtain this pressure information.

Compared to large arteries such as carotid and femoral arteries having diameters in the range of 4-8 mm, radial and ulnar arteries have a diameter of 2-3 mm (Habib et al.

2012) and have a lower flow rate of 50 ml min^{-1} (Manabe et al. 2005). As a result, all the flow related parameters in these two arteries have lower amplitude. This leads to challenges in estimating these parameters due to the limited ultrasound imaging resolution. Methodologies used in large arteries have not been investigated when estimating these flow related parameters in the radial and ulnar arteries.

Chapter 3

3. Investigation of ultrasound-measured flow related parameters with flow phantoms

3.1 Introduction

The importance of estimating and validating the ultrasound measured flow parameters in the radial and ulnar arteries has been explained in the previous chapter. This chapter establishes feasible methods to measure those parameters in the two arteries, including the flow rate (FR) and wall shear rate (WSR), with a clinical ultrasound scanner. More importantly, validation of these estimations is done using flow phantoms.

Although there has been interest in measuring flow related parameters in arteries for many years, routine clinical ultrasound scanners only provide quantitative blood velocity (frequency shifts) with PW Doppler mode from a single small sample volume. Other flow related parameters, such as flow rate and wall shear rate, have to be derived based on the velocity data obtained from this single point. Consequently, attempts have been made to derive the velocity profile from which the flow rate and the wall shear rate can be calculated. This single-point method relies strongly on mathematical models for reconstructing the cross-sectional velocity distribution. As discussed before in last chapter (section 2.4.3), the Hagen-Poiseuille law was adopted initially to derive the velocity profile within cross-sectional plane of the blood vessel. However, the Hagen-Poiseuille law assumes the flow in arteries is steady, which is of course not realistic.

The more advanced Womersley theory was introduced to derive the velocity profile within the vessel during pulsatile flow. This assumes that the blood is a Newtonian fluid

and the artery is a rigid pipe. Then sinusoidal components of the pulsatile flow waveform can be linearly superimposed. In the original theory, it was the relation between pressure gradient and volume flow that was derived (Womersley 1955). Evans (1982) has shown that it is possible to calculate the velocity profile for the steady-state pulsatile flow by extending the Womersley theory using the mean velocity. Holdsworth et al. (1999) adapted the Womersley equations so that the centre-line velocity could be input instead of the mean velocity.

Since its capability of deriving velocity profile, the Womersley theory has been used in many arteries to estimate flow related parameters with clinical ultrasound scanners and accuracies have been evaluated (Kirpalani et al. 1999; Struijk et al. 2005; Stroev et al. 2007; Fraser et al. 2008; Leguy et al. 2009a). However, there are few studies using the Womersley theory to estimate flow rate and wall shear rate in the radial and ulnar arteries (Remuzzi et al. 2003; Van Canneyt et al. 2013). Most importantly, the validation of these estimations in these two arteries remains to be done.

The aim of this chapter is to estimate the flow rate and wall shear rate using clinical ultrasound scanners based on the Womersley theory, and consequently evaluate these estimations. Errors in these estimations are investigated under various circumstances using carefully-designed flow phantoms. This allows understanding of the sources and size of these errors when measured for clinical applications.

3.2 Methods

3.2.1 Overall

Flow phantoms were designed to simulate the flow conditions under various circumstances in the radial and ulnar arteries. A clinical scanner HDI 5000 (Bothell, USA) was used to scan the phantoms and, the centreline maximum velocity waveform and vessel diameter were measured from the PW and B-mode image respectively. These data could be obtained from the digital image without the need for RF data. The Womersley theory was used to estimate the flow rate and wall shear rate, where the maximum velocity waveform and vessel diameter were taken as inputs. The output of the Womersley equations is the time-varying velocity profile from which the flow rate waveform and the wall shear rate waveform are calculated.

The time-averaged flow rate and wall shear rate estimated from Womersley equations were compared with the known reference values in the flow phantoms to evaluate their accuracies.

3.2.2 Theory

The Womersley equation is used to derive the time-varying velocity profile of the pulsatile flow in a long, rigid walled pipe (Womersley 1955). When the flow is in a stable pulsatile condition (well-developed), its pattern can be resolved into a series of sinusoidal components which can then be superimposed to obtain the velocity variation in time and space. The blood is assumed to be a Newtonian fluid allowing linear superimposition. The Womersley equation describes the relation between a single sinusoidal component of the mean velocity waveform and the corresponding velocity profile associated with this single component. The overall velocity profile is obtained by superimposing these individual profiles. The relation between the velocity profile and the mean volumetric flow waveform is given by,

$$v(r,t) = \sum_{k=0}^{\infty} \mathrm{Re}\left\{ V_{mean,k} e^{j(k\omega_0 t - \Phi_{mean,k})} \psi_k(r,\tau_k) \right\}$$

$$\psi_k(r,\tau_k) = \frac{J_0(\tau_k) - J_0(\tau_k r)}{J_0(\tau_k) - 2J_1(\tau_k)/\tau_k}$$

$$\tau_k = \alpha_k j^{3/2}$$

$$\Phi_{mean,k} = \angle V_{mean,k}$$

$$\alpha_k = R\sqrt{\frac{\rho k \omega_0}{\mu}} \qquad (3.1)$$

where $\mathrm{Re}\{.\}$ represents the real part of a complex function; J_0 and J_1 are the zero and first order Bessel functions of the first kind; j is the imaginary number, r is the normalized radial coordinate; ω_0 is the fundamental angular frequency of the mean velocity waveform; t is time; $\Phi_{mean,k}$ represents the phase of each harmonic; α_k the Womersley number for each harmonic; and ρ is the fluid density. $V_{mean,k}$ is the amplitude of k-*th* sinusoidal component of the mean velocity waveform.

As seen in eqn. 3.1, the Womersley theory uses the mean velocity waveform as input to calculate the velocity profile. However, in practice it is difficult to obtain the mean

velocity directly with routine clinical ultrasound scanners (Hoskins 2011). Holdsworth et al. (1999) modified the Womersley equations so that the centreline velocity could be input instead of the mean velocity.

$$V_{mean,k} \cdot e^{-j\Phi_{mean,k}} = V_{centre,k} e^{-j\Phi_{centre,k}} \left[\frac{J_0(\tau_k) - 2J_1(\tau_k)/\tau_k}{J_0(\tau_k) - 1} \right]$$

$$\Phi_{centre,k} = \angle V_{centre,k} \tag{3.2}$$

Combining the eqn. 3.1 and eqn. 3.2 yields an expression relating the centre line velocity directly to the velocity profile,

$$v(r,t) = \sum_{k=0}^{\infty} \mathrm{Re}\left\{ V_{centre,k} e^{j(k\omega_0 t - \Phi_{centre,k})} \frac{\left[J_0(\tau_k) - J_0(\tau_k r)\right]}{\left[J_0(\tau_k) - 1\right]} \right\} \tag{3.3}$$

Generally, the centreline velocity corresponds to the maximum velocity. This formulation then allows the maximum velocity waveform obtained from spectral Doppler to be used as input to the Womersley equations. Vessel radius R can be measured using B-mode imaging. The first eight orders of the sinusoidal components of the maximum velocity waveform are used in this thesis to represent the maximum velocity information because higher order components have very small contributions to the waveform.

After obtaining the time-varying velocity profile, the flow rate $Q(t)$ can be derived using eqn. 3.4:

$$Q(t) = 2\pi \int_0^R v(r,t) r \partial r \tag{3.4}$$

Wall shear rate $wsr(t)$, is calculated using eqn. 3.5. In order to help conceptualize the procedure, the schematic for estimating flow rate and wall shear rate using the Womersley equations is given in Figure 3.1.

$$wsr(t) = \frac{\partial v(r,t)}{\partial r}\Big|_{r=R} \tag{3.5}$$

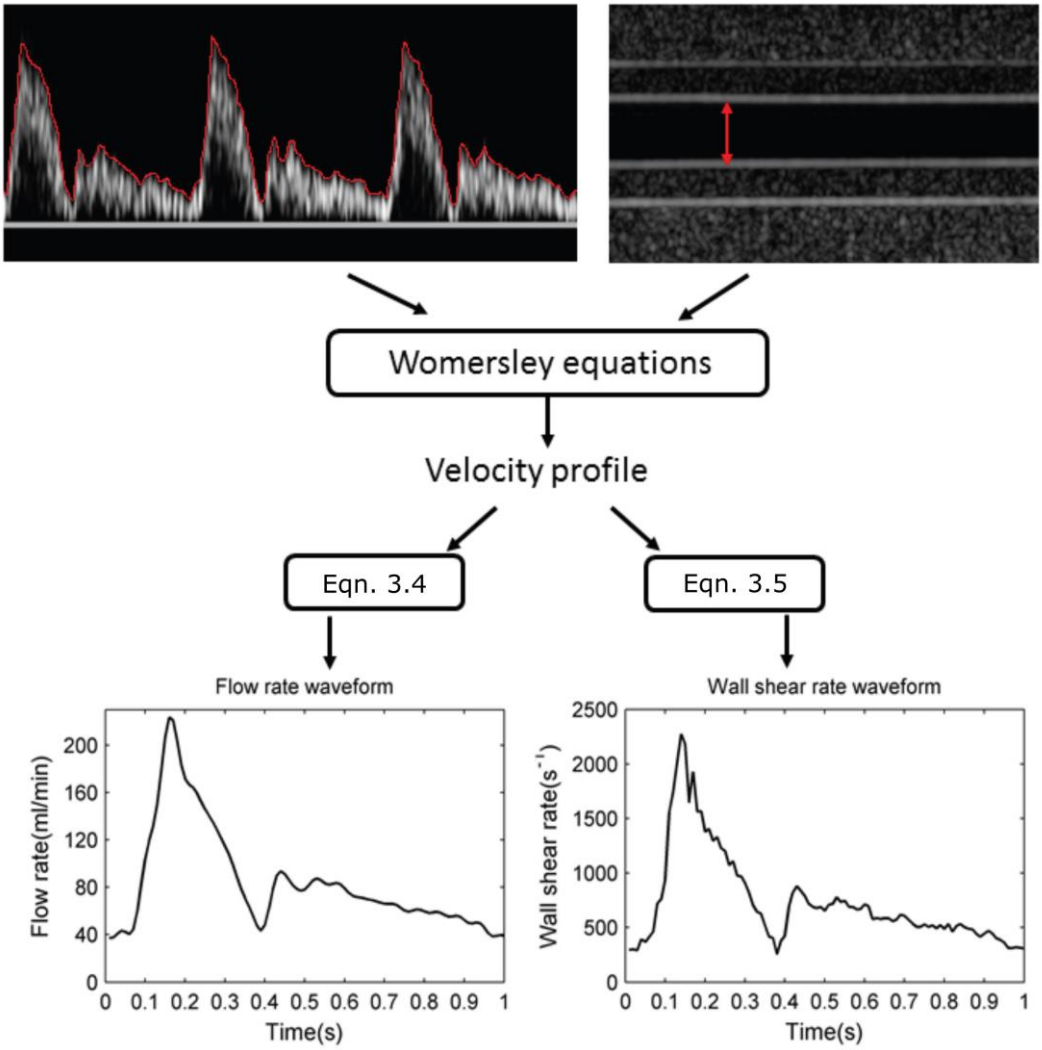

Fig. 3. 1. Estimation of volumetric flow and wall shear rate waveforms using the Womersley theory where the maximum velocity waveform and the diameter are used. The resulting velocity profile is then used to calculate the FR and WSR waveforms. In this example, the flow rate was 40 ml.min^{-1}, and the diameter was 2.89 mm.

3.2.3 Flow phantom

Flow phantoms were designed and fabricated to simulate flow conditions in the radial and ulnar arteries. In a flow phantom for ultrasound imaging the most critical thing is to ensure the materials closely mimic the acoustic properties of human tissue. A wide range of mimicking materials have been tried attempting to match the realistic properties of the human arterial system, and a review on this was given by (Hoskins 2008). In 2001 the specifications of a standard flow phantom were defined in International Electrotechnical Commission (IEC) 61685 (IEC 2001). In a flow phantom there are usually three main mimicking materials: the vessel mimicking material (VMM), the blood mimicking fluid (BMF) and the tissue mimicking materials (TMM). In this thesis careful attention was

paid to meet the standard defined by IEC when choosing the recipes for these mimicking materials.

Overall design

The flow phantom consists of the main components as shown in Figure 3.2. A straight blood vessel mimic made from polyvinyl alcohol cryogel (PVA-c) subject to 6 freeze-thaw cycles (Dineley et al. 2006) was embedded at a known depth within the agar-based tissue mimic (Teirlinck et al. 1998). A blood mimic including nylon particles was used with acoustic properties and viscosity matched to blood (Ramnarine et al. 1998).

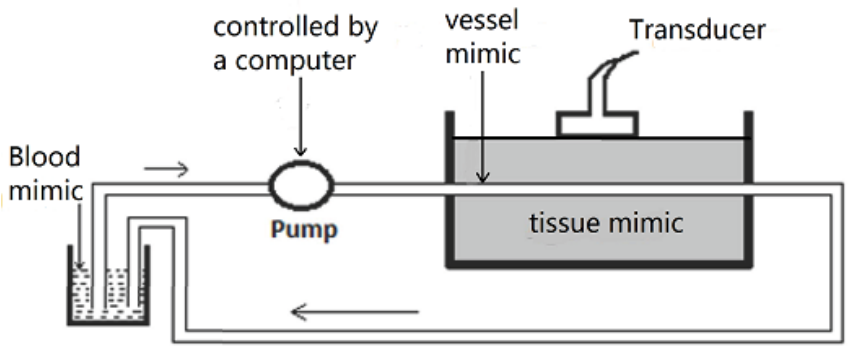

Fig. 3. 2. The diagram of a flow phantom.

Pulsatile flow patterns were achieved through connecting a gear pump (Micropump® Series GA-X21, Vancouver, WA, USA) to the inflow of the phantom loop. The pump was controlled by LabVIEW 2010 (National Instruments, Austin, TX, USA) to generate different flow waveforms.

Mimicking material preparation

Agar-based TMM. The recipe for making the agar-based TMM is listed in Table 3.1 and the manufacturing procedure is as follows: (1) measure out the required amount of all the materials in the Table 3.1 (except the glycerol) into a metal beaker and whisk for 2 minutes; (2) degas the mixed solution for half an hour with a vacuum pump to remove the bubbles involved from whisking; (3) put the beaker containing the solution into a controllable water bath (with a lid) and set the temperature to about 96 ^{o}C. At the same time, an overhead stirrer is placed above the water bath, stirring the solution while heating. The water bath's lid has a hole on it to let the overhead stirrer go through; (4) keep heating and stirring the solution for one hour after the temperature reaches 96 ^{o} C. During this

step, make sure the water bath is well-covered to avoid water vaporization. During the last five minutes, add in the glycerol; (5) take the beaker out from the water bath and let it cool down. This cooked solution can be poured into a mould before solidifying below 40 ^{o} C.

Table 3. 1. Recipe for making TMM

Component	**Weight (%)**	**Component**	**Weight (%)**
DI water	82.4	0.3 μm Aluminum oxide powder	0.88
Glycerol (99%)	11.32	Benzalkonium chloride	0.92
Silicon carbide (400 grain)	0.53	Agar	3
3 μm Aluminium oxide powder	0.94	----	----

PVA-c VMM. The recipe for making the PVA-c VMM is listed in Table 3.2 and the manufacturing procedure is as follows: (1) measure out all the ingredient as in the Table 3.2 and put into a container. Whisk for two minutes; (2) put the container into a water bath. Set the temperature to 96 ^{o} C and cook the mixture for 3-4 hours until the mixture turns to a clear gel; (3) take the container out from the water bath and wait until the hot PVA solution cools down to around 50 ^{o} C; (4) while waiting for the PVA solution, a vessel mould is prepared. The mould consists of three parts, a stainless-steel straight tube, a stainless-steel rod and a flange, as shown in Figure 3.3. The mould size can be changed to model vessels of different sizes. The cooked PVA solution is injected into the mould through a hole near one end of the mould. After injection, the ends of the mould are sealed with tape. Leave the mould at room temperature (22 ± 0.5 °C) for 10 h in an upright position (with the hole at the upper end) to let air bubble come out; (5) the mould is then placed in a freezer at -20°C for 14 h, after which time the mould is taken out from the freezer and left for 10 h at room temperature (22 ±0.5 °C). This freeze-thaw cycle is repeated five times; (6) after the freeze-thaw cycles, carefully extract from the mould. The PVA vessel mimic is ready now for use but must be kept immersed water to prevent it from drying out.

Table 3. 2. Recipe for making PVA-c vessel mimic.

Component	Weight (%)	Component	Weight (%)
DI water	88.79	Benzalkonium chloride	0.46
Polyvinyl alcohol	10	Silicon carbide (400 grain)	0.75

Blood fluid mimic. The recipe for making the BFM is listed in Table 3.3 and the manufacturing procedure is as follows: (1) measure out all the ingredients listed in Table 3.3 and put it into a plastic beaker; (2) put a magnetic stirrer bar into a plastic beaker and place the beaker onto a magnetic stirrer plate. Stir for approximately 3 hr for the powder to become wetted and held in suspension; (3) filter the BFM with the 38 μm sieve and then degas it with a vacuum pump. This BFM is then ready to use.

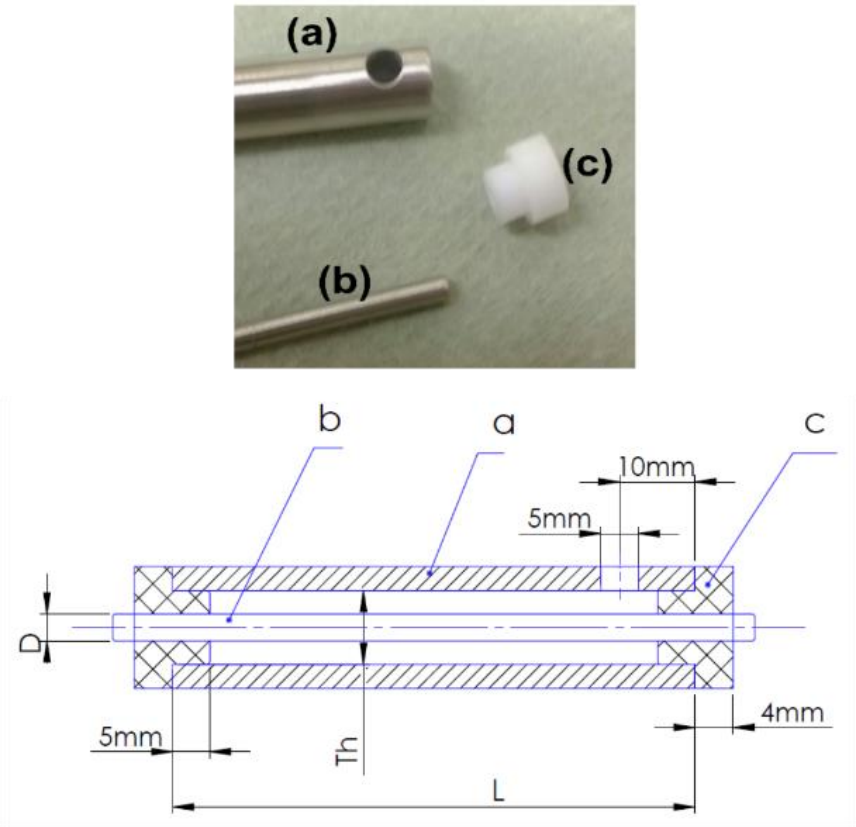

Fig. 3. 3. The parts of the vessel mould and assembly diagram.

Table 3. 3. Recipe for making BFM.

Component	Weight (%)	Component	Weight (%)
DI water	83.86	Dextran	3.36
Glycerol (99%)	10.06	Synperonic N	0.9
5 µm orgasol particles	1.82%	Benzalkonium chloride 50% solution	1-2 drops

Properties of mimicking materials

The original recipes of these mimicking materials are widely used in the literature and the BFM was even cited by the IEC 2001 standard. While making these mimicking materials in this study, their original recipes and manufacturing procedures were strictly adhered. To further confirm that the mimicking materials used in this study were consistent with the original published ones and to meet the IEC standards, some key properties, such as density, speed of sound and attenuation coefficients, were measured by the methods described by (Zell et al. (2007)).

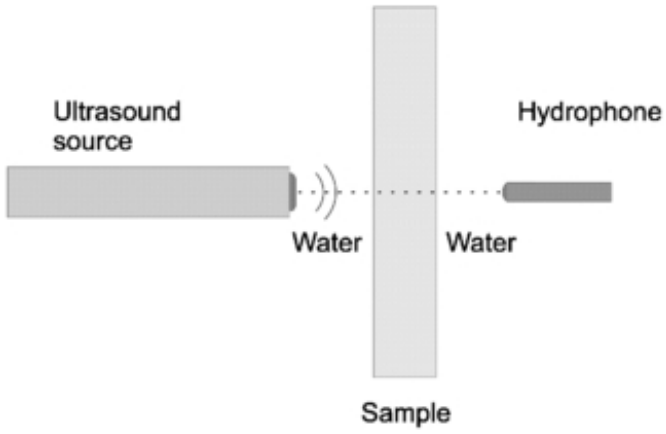

Fig. 3. 4. The schematic design for measuring acoustic properties.

The experimental design for measuring speed of sound and attenuation coefficient is presented schematically in Figure 3.4. It is a relative measurement method, using water as the reference to study the transmission of longitudinal ultrasonic waves through solid

media inserted in an aqueous environment. The speed of sound c_s in the test sample can be calculated as

$$c_s = \left(\frac{1}{c_w} - \frac{\Delta t_d}{Th}\right)^{-1} \tag{3.6}$$

where c_w is the speed of sound in water; Δt_d is the sound transmission time delay difference between having sample in the middle and without sample in the middle; and Th is the thickness of the test sample. The attenuation coefficients α_s are calculated from the following equation:

$$\alpha_s = \alpha_w - \frac{1}{Th}\left[\ln Amp_s - \ln Amp_w - 2\ln(1 - R_{ref})\right] \tag{3.7}$$

where α_w is the attenuation coefficient of water; Amp_s and Amp_w are the amplitude of the received ultrasonic pulse with and without samples respectively. R_{ref} is the acoustic reflection coefficient at the water-sample interface. The R_{ref} is determined by the impedance of these two materials:

$$R_{ref} = \frac{z_w - z_s}{z_w + z_s} \tag{3.8}$$

The acoustic impedance (z_w and z_s) can be derived from the density and the speed of sound by $z = \rho c$. Therefore, the density ρ of two materials, thickness Th of sample, amplitude of received sound pulse Amp_s and Amp_w, attenuation coefficient of water α_w, and speed of sound of water c_w are required to be measured to derive the speed of sound and attenuation coefficient of the sample according to the eqn. 3.6, eqn. 3.7 and eqn. 3.8. Among them, the density, speed of sound and attenuation coefficient of water are known based on the literature (Hoskins et al. 2010a).

In this study, an ultrasound transducer was driven by a signal generator at 2.25 MHz to send out the ultrasonic pulse. A hydrophone receiver was placed towards the transducer with a short distance to allow fitting the sample in the middle. Both the hydrophone and the transducer were connected to a multi-channel oscilloscope receiving the ultrasonic signals from the hydrophone and the signal generator (as references) as shown in Figure 3.5. A mould was designed to help fit the sample in the middle between the transducer

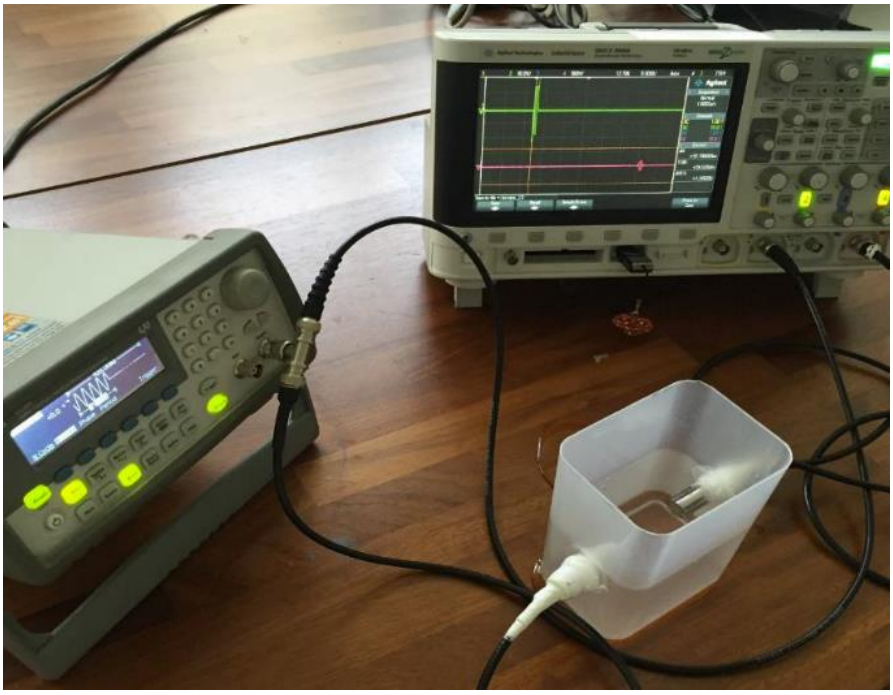

Fig. 3. 5. The experimental setup for measuring acoustic properties.

and the hydrophone. For determination of phantom material densities, the mass of the samples was scaled and their volumes were recorded using a cylinder with water (record the volumes before and after putting the sample in). The densities were measured as 1058.7 kg.m^{-3} and 1037 kg.m^{-3} for agar-based TMM and PVA-c VMM respectively.

The measurements were first taken without the sample in the middle. Two values were recorded, the time delay $\Delta t_{d,w}$ (between the received signal and reference signal) and the received signal amplitude Amp_w. Figure 3.6 demonstrates how these two values were recorded in the oscilloscope. The $\Delta t_{d,w}$ was recorded by reading the start point of the green wave (reference wave directly from signal generator) and the pink wave (wave received from the hydrophone) in Figure 3.6, and the Amp_w was obtained by reading the peak-peak value of the pink wave. The measurements were repeated after inserting the sample, and the time delay $\Delta t_{d,s}$ and signal amplitude Amp_s recorded. The thickness of the sample Th was measured using a Vernier calliper. All measurements were repeated three times and the results are shown in Table 3.4 and Table 3.5 for agar-based TMM and PVA-c VMM.

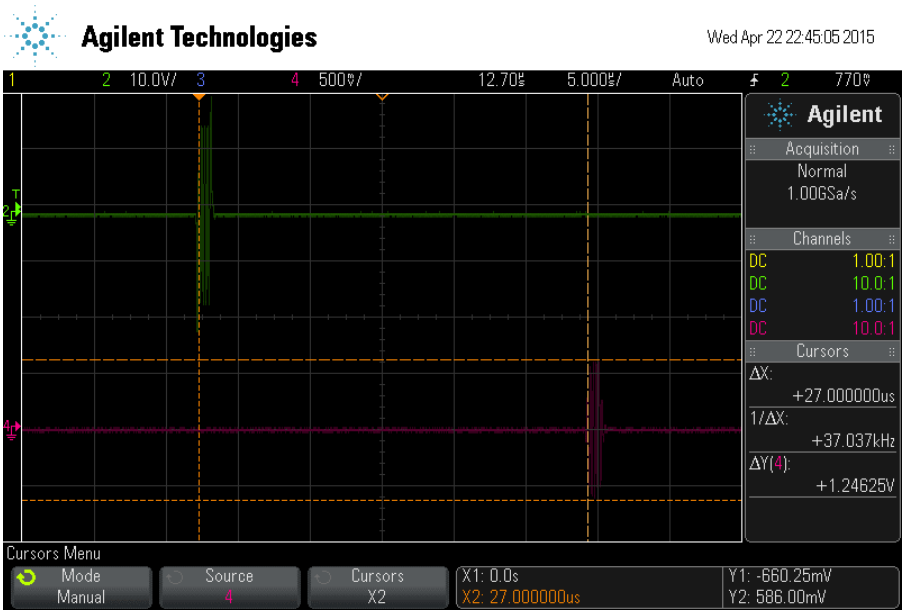

Fig. 3. 6. The signal from the hydrophone obtained by the oscilloscope.

Table 3. 4. Experiment records from the sample of the Agar-based TMM.

Th (±0.02 mm)	Amp_s (± 0.002 V)	Amp_w (± 0.002V)	$\Delta t_d = \Delta t_{d,w} - \Delta t_{d,s}$ (μs) (±0.02 μs)
9.58	1.090	1.900	0.25
9.90	0.422	0.748	0.30
9.87	0.355	0.620	0.28

Table 3. 5. Experiment records from the sample of the PVA-c TMM.

Th ((±0.02 mm)	Amp_s (± 0.002 V)	Amp_w (± 0.002 V)	$\Delta t_d = \Delta t_{d,w} - \Delta t_{d,s}$ (±0.02μs)
4.50	0.430	0.580	0.15
9.68	0.550	0.980	0.26
9.75	0.675	1.150	0.27

Based on the eqn. 3.6 and 3.7, the speed of sound and attenuation coefficient of agar-based TMM and PVA-c VMM were calculated. The detailed results of these two mimicking materials and the IEC 2001 standard for flow phantom are listed in Table 3.6. It can be seen that the Agar-based TMM and PVA-c VMM are in good agreement with

the IEC 2001 standard in terms of their density, sound velocity and attenuation (IEC 2001).

Table 3. 6. The measured properties of the TMM, the VMM and the IEC standard.

Property	**Density** ($kg.m^{-3}$)	**Sound velocity** ($m.s^{-1}$)	**Attenuation coefficient** ($dB.cm^{-1}.MHz^{-1}$)
Agar-based TMM	1058.7	1546.8+-4.81	0.48+-0.01
PVA-c VMM	1037	1551+-7.24	0.529+-0.06
IEC 2001 standard	1040+-100	1540+-15	0.5+-0.05

Phantom fabrication

A Perspex box was used to contain the main part of the phantom. Pipe connectors were attached through holes in either end of the container so that they were aligned horizontally and fixed in place with the fast setting glue (Araldite). The connector protruded into the phantom and the flexible tubing was connected to the outside end.

Due to dehydration of PVA-c vessel, only the tubing segment within the phantom container will be made of PVA-c vessel. The PVA-c vessel mimic is surrounded by agar-based tissue mimic and filled with water or 9% glycerol solution inside when not in use to prevent the dehydration. Thick walled flexible C-flex tubing was used to form the rest of the complete circular circuit. Connectors (Cole-Parmer) are required to connect the PVA-c vessel and the connecting tubes. The PVA-c vessel was at a known height in the Perspex container as shown in Figure 3.7.

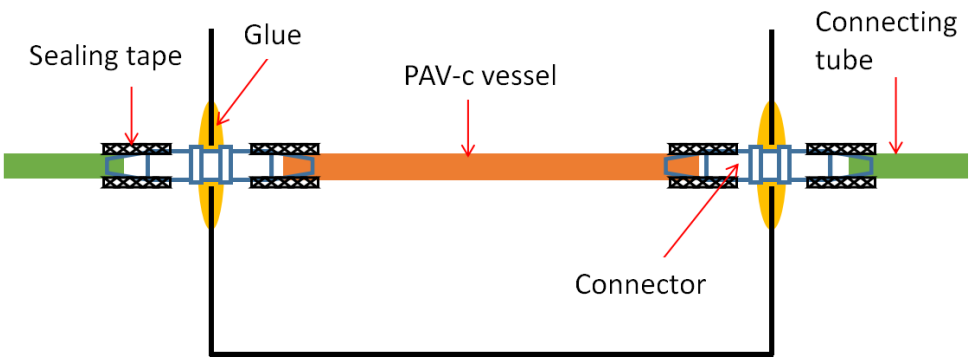

Fig. 3. 7. Diagram to mount the PVA-c VMM onto the phantom container.

After the PVA-c vessel mimic was fixed onto the Perspex phantom container at a desired height, the next step is to pour the previously prepared agar-based TMM into this container to form the surrounding tissue mimic. Before pouring the liquid agar-based TMM, the PVA-c vessel was filled with water and sealed at both ends to prevent the vessel from being pressed into non-circular shape. The agar-based TMM (at about 42 ^{o}C, and higher temperature might destroy the PVA-c vessel) was poured into the container slowly to bury the vessel at required depth.

Phantoms were fabricated with different vessel depths and diameters to mimic realistic situations for the radial and ulnar arteries.

In order to generate the flow in the phantom, a pump system was required, functioning similarly to the heart in the cardiovascular system. A gear pump, controlled by LabView (Fig. 3.8), was used to generate the pulsatile flow. Variations of the control signals were designed on a computer where LabVIEW software was installed so that different custom waveform can be achieved in the flow phantom. The programme for outputting arbitrary flow waveform in the LABVIEW is given in the appendix I.

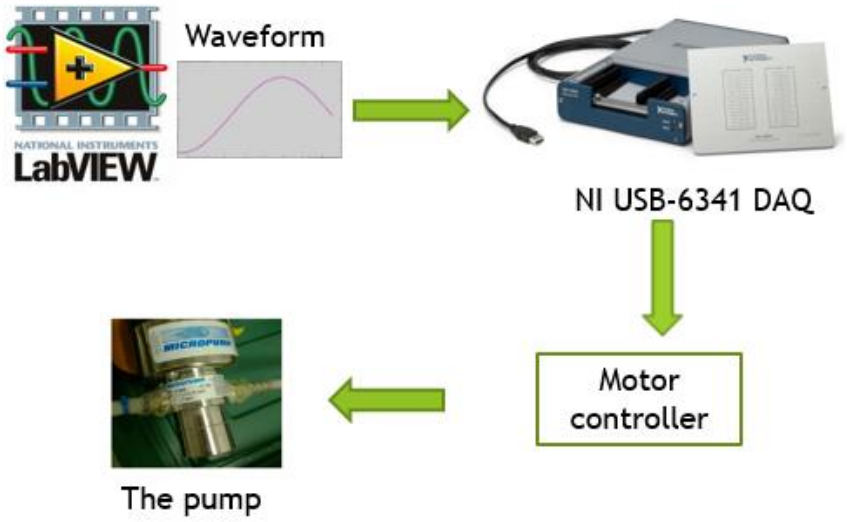

Fig. 3. 8. The diagram for assembling the pump system.

The complete assembly, including the pump, fabricated phantom container, connecting tubing and BFM reservoir, is shown in Figure 3.9. An ultrasound transducer was held in place on the top of the phantom to scan the generated flow.

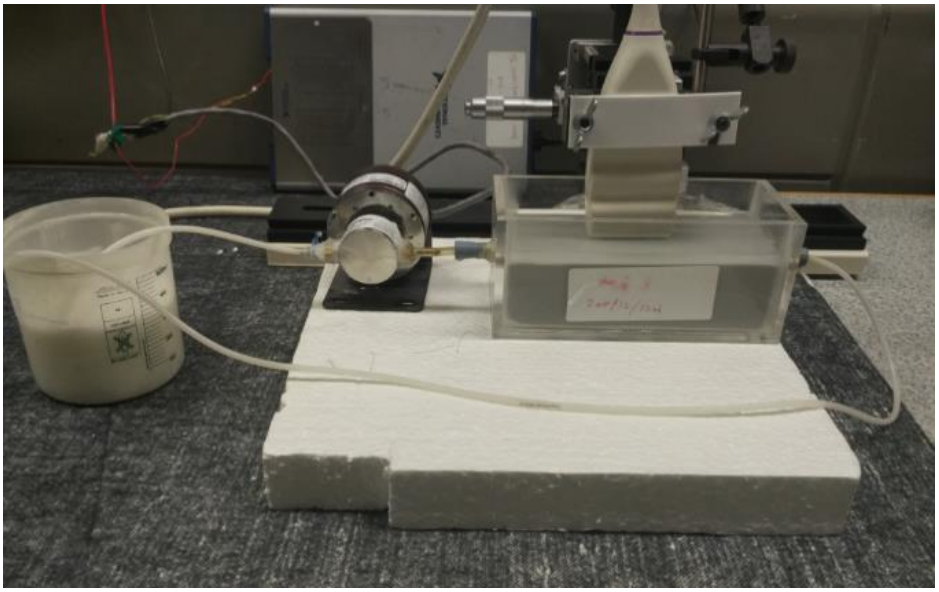

Fig. 3. 9. The completed flow phantom system.

3.2.4 Experimental protocol

Vessel depths, beam-vessel angles (see the angle θ in Fig 2.7), flow rates, vessel diameters and flow waveforms were investigated to evaluate their effects on the flow rate and wall shear rate estimations. The ranges of these variables were based on published data and a preliminary set of measurements which were made on 15 normal volunteers to help inform the choice of diameter, depth, flow rate and waveform. These are shown in Table 3.7 and Figure. 3.10.

Spectral velocity waveforms from the radial or ulnar artery were quite different among the 15 volunteers. Therefore, an averaged waveform from 15 volunteers' spectral Doppler velocity outlines in both radial and ulnar arteries was adopted as the typical centreline velocity waveform in the experiment, which was indicated in waveform 1 in Figure 3.10. The depth of the blood vessel was chosen to be around 6 mm. The thickness of the vessel wall was 2 mm. For each assembled phantom, 9% glycerol was added on top of the agar-based tissue mimic in the Perspex box to provide ultrasound coupling while allowing depth and angle to be adjusted. The depth at which the vessel was positioned within the ultrasound image could be varied by adjusting the position of the transducer relative to the vessel. Four flow phantoms of different vessel diameter (Table 3.7) were constructed and labelled phantoms 1 to 4.

Table 3. 7. The details of these five variables used in the flow phantoms.

Variables	**1**	**2**	**3**	**4**	**5**
Depth(mm)	6	8	10	12	14
Angle(°)	38	48	58	68	----
Diameter(mm)	1.86	2.6	2.89	3.49	----
Flow rate(ml.min-^{1})	20	40	60	80	100
Waveform	Waveform 1	Waveform 2	Waveform 3	Waveform 4	----

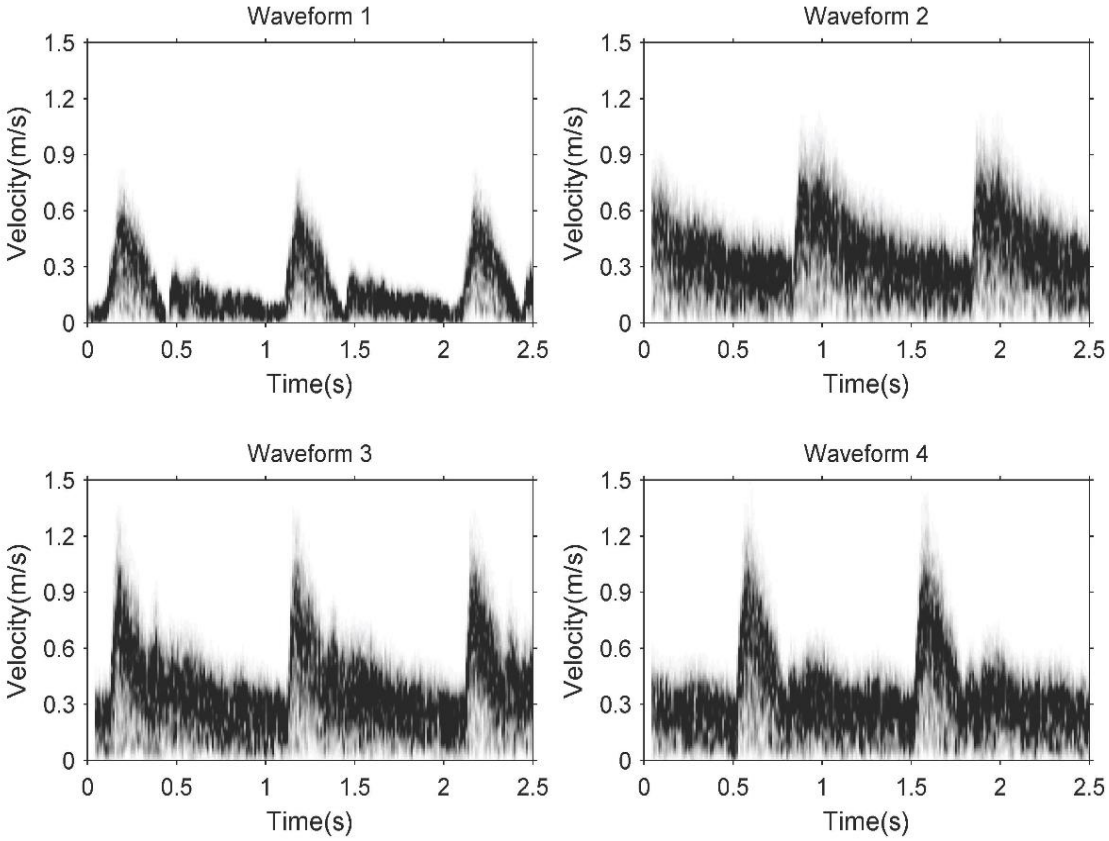

Fig. 3. 10. Four different waveforms generated in the flow phantom.

To allow full consideration of different waveforms of radial and ulnar arteries in practice, waveforms in the radial artery from different stages of a flow mediated experiment in a healthy volunteer were used, as shown in waveform 2, 3 and 4 in Figure 3.10. The brachial artery was blocked for five minutes with a pressure cuff. The dynamics

of the downstream flow was then studied from the moment the cuff is released. Waveforms in this case will be quite non-typical and the corresponding flow rates are usually higher than normal.

All volunteers who were involved in this study were told not to consume any food other than water 2 hours before the experiment and asked to take a rest for at least five minutes. The room temperature was about 22 ±1ºC. The experimental protocol for these measurements was reviewed and approved by the Research Ethics Committee of Dundee University and all volunteers gave their written informed consent to participate.

A typical value for each variable was chosen. This was 10mm for vessel depth, 68° for beam-vessel angle, 2.60 mm for the diameter, 40 ml.min^{-1} for the flow rate and the waveform 1 (Fig. 3.10) for the waveform. In the experiments, only one variable was altered at a time in turn while the others were set at their typical value.

3.2.5 Data acquisition and processing

Data acquisition

A Philips HDI 5000 clinical ultrasound scanner was used to collect all the data from the phantom and volunteers. A L12-5 transducer with B-mode frequency10 MHz and Doppler frequency 6 MHz was used. The diameters from each frame of the B-mode were averaged through several cardiac cycles. The centreline velocity was obtained from the PW Doppler mode with the sample volume placed centrally in the vessel. In order to achieve accurate measurements both for diameter and centreline velocity, the transducer was adjusted to get the clearest view of the vessel in the longitudinal orientation (Fig. 3.11). The wall filter was set to low and Doppler gain was adjusted to give spectral Doppler traces with consistent brightness. The sample gate size was 2.0 mm, enough to cover the centreline of the vessel and record maximum velocity. The measurements were repeated six times with the transducer repositioned between each.

While collecting the data, the true average volumetric flow rate was measured using timed-collection with a measuring cylinder and stopwatch. The reference average wall shear rate was estimated using eqn. 3.9 (Hoskins 2011), where Q_{mean} represents mean flow rate over time and R is the arterial diameter.

$$\frac{dv}{dr} = \frac{4Q_{mean}}{R} \tag{3.9}$$

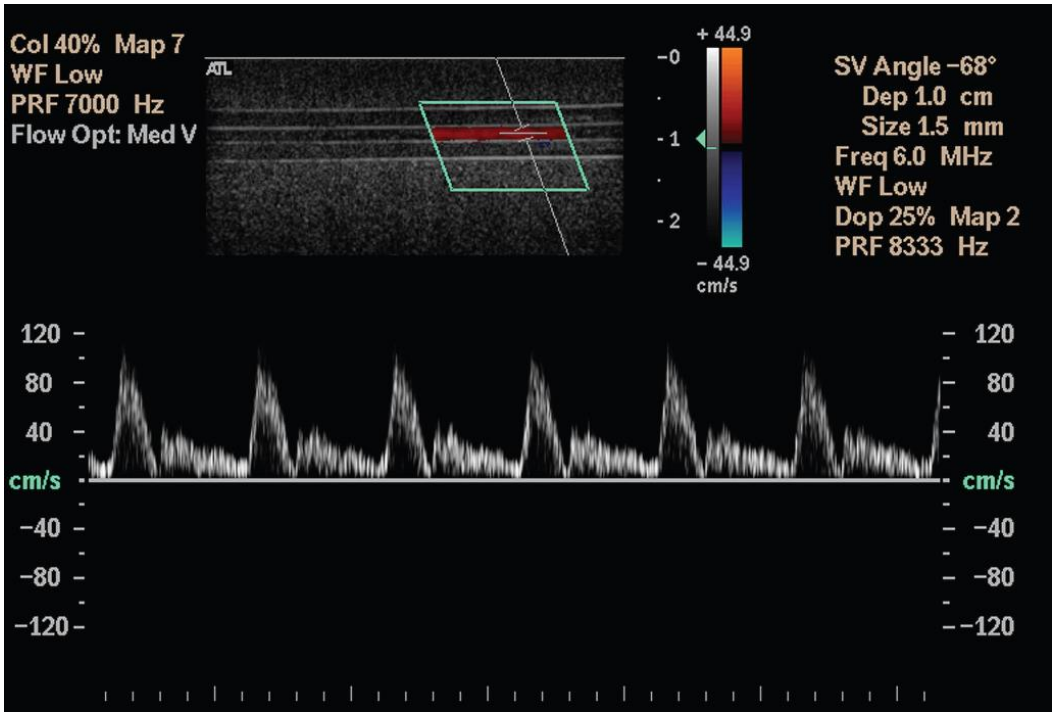

Fig. 3. 11. Image from which data were collected with ultrasound scanner.

Data processing

The data from the ultrasound machine was processed in MATLAB R2013b (MathWorks, Natick, MA, USA). An in-house developed MATLAB code was used to read the binary files generated from the cine loop memory of the ultrasound scanner. The diameter of the blood vessel within the phantom was measured using the distance-intensity method (Blake et al. 2008). The distance-intensity method uses the intensity differences of the reflected B-mode signal between lumen and tissue to estimate the vessel diameter. As shown in Figure 3.12, each frame of B-mode images was used to obtain the vessel diameter with the pixel-level resolution by searching the peak points on the distance-intensity curve resulting from the strong reflection from both inner surfaces of blood vessel. The diameter was obtained by averaging the time-varying diameter waveform over whole number multiples of the cardiac cycle.

For the centreline velocity, over 5 cycles of the peak Doppler velocity waveform were averaged into a single cycle. The average diameter and velocity waveform were processed as indicated in Figure 3.1 to calculate flow rate and wall shear rate waveforms over one cardiac cycle. Finally the time-averaged flow rate and wall shear rate were calculated from their waveforms. With the estimated time-averaged values (repeated six times under each setting), the errors in the form of mean ± standard deviation were

calculated based on the true reference flow rate from timed-collection and true reference wall shear rate from eqn. 3.9.

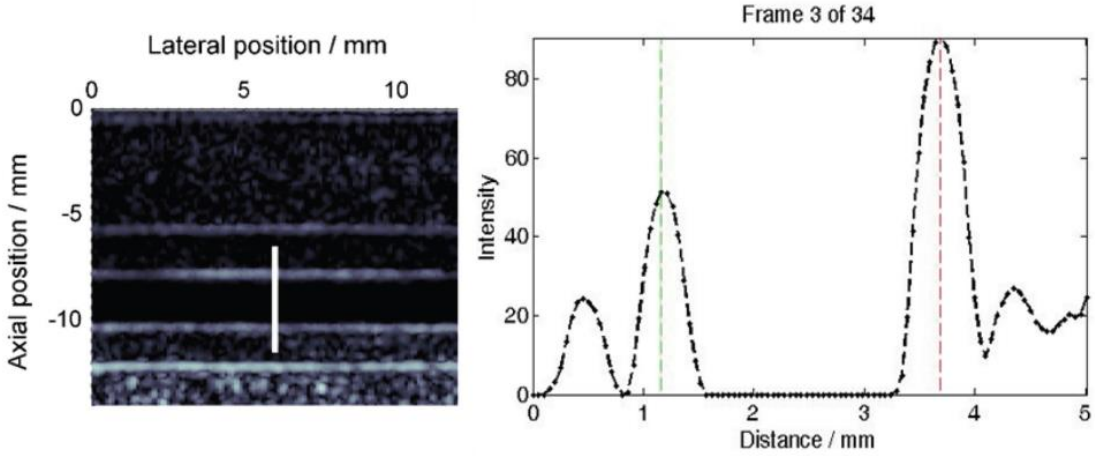

Fig. 3. 12. Distance-intensity method used to measure the diameter of the vessel. The white line in image on the left indicates the measurement position. On the right picture are the corresponding distance-intensity curves.

3.3 Results

3.3.1 Diameter measurement

Figure 3.13 shows the diameter waveform of the vessel in phantom 2 over two cardiac cycles when the average flow rate is 40 ml.min^{-1}. The vessel diameter in the phantom is not constant. It changes with the pulsatile flow in the vessel.

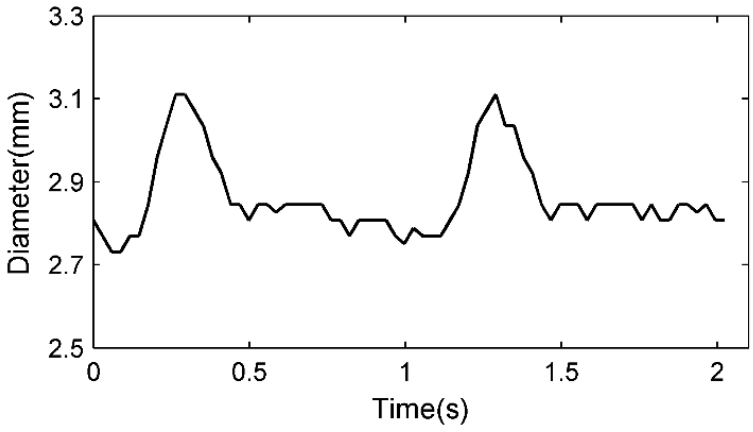

Fig. 3. 13. Pulsatile diameter over two cardiac cycles measured with the distance-intensity method.

Table 3.8 lists the diameters of phantom 1 to 4, measured in both static and pulsatile conditions. The diameters of blood vessel in phantom 1 to phantom 4 under static condition were at 1.86±0.02 mm, 2.60±0.03 mm, 2.89±0.03 mm and 3.49±0.04 mm. The mean diameter of vessel in the pulsatile condition was greater than the diameter in static condition.

Table 3. 8. The diameters of blood vessels in phantoms under static condition and different flow rates.

Flow rate ($ml.min^{-1}$)	**Diameter** (mm), mean±SD			
	Phantom 1	**Phantom 2**	**Phantom 3**	**Phantom 4**
0	1.86±0.02	2.60±0.03	2.89±0.03	3.49±0.04
20		2.72±0.03		
40	1.99±0.04	2.89±0.03	3.00±0.03	3.70±0.02
60		3.06±0.03		
80		3.17±0.05		
100		3.25±0.04		

3.3.2 FR and WSR from Womersley equations

The Womersley equations can estimate the time-varying waveforms of flow rate and wall shear rate over the cardiac cycle in the flow phantom. Since only the time-averaged flow rate and wall shear rate are available as reference values based on the timed-collection method and eqn. 3.9, the ultrasound-measured waveforms were averaged within one cardiac cycle and then compared with the reference values.

Figure 3.14 to Figure 3.18 show the estimation errors of flow and wall shear rates with different vessel depths, beam-vessel angles, flow rates, vessel diameters and waveforms. From these figures, it can be seen that all results, both for flow rate and wall shear rate, are overestimated in a range of 13% to nearly 50%. In Figure 3.14 and 3.18, with different vessel depths and flow waveforms the overestimations remain nearly constant, indicating that different vessel depths and waveforms do not have an obvious effect on flow rate and wall shear rate estimations. Statistical confidence was analysed to support the conclusion that vessel depth (Fig 3.14) does not affect the estimation of

ultrasound measured flow and wall shear rates, with the correlation coefficient and the corresponding p-value shown in Table 3.9.

For the flow rates in the phantom (Fig 3.16), it seems that bigger flow rate in the flow phantom could cause less overestimations of flow rate and wall shear rate by ultrasound. In this case, the correlation coefficient between flow rate in the phantom and the ultrasound-estimated flow rate is -0.70 with a p-value less than 0.0001, which strengthens the confidence of drawing this conclusion. The statistical confidence for the wall shear rate in this case are also shown in Table 3.9.

However, vessel diameter and beam-angle do effect these estimations. When the beam-vessel angle increased from 38° to 68° (Fig. 3.15), the overestimations of both parameters shifted from around 14% to 35%, with high correlation coefficient and very low p-value as shown in Table 3.9. Similarly for the vessel diameter, the overestimation was only about 13% for a vessel of diamete1.86mm, but around 35% at 2.60 mm and 2.89 mm, going up dramatically to nearly 50% at a diameter of 3.49 mm (Fig. 3.17). Very high correlation coefficients and low p-values can be seen in Table 3.9 for this situation.

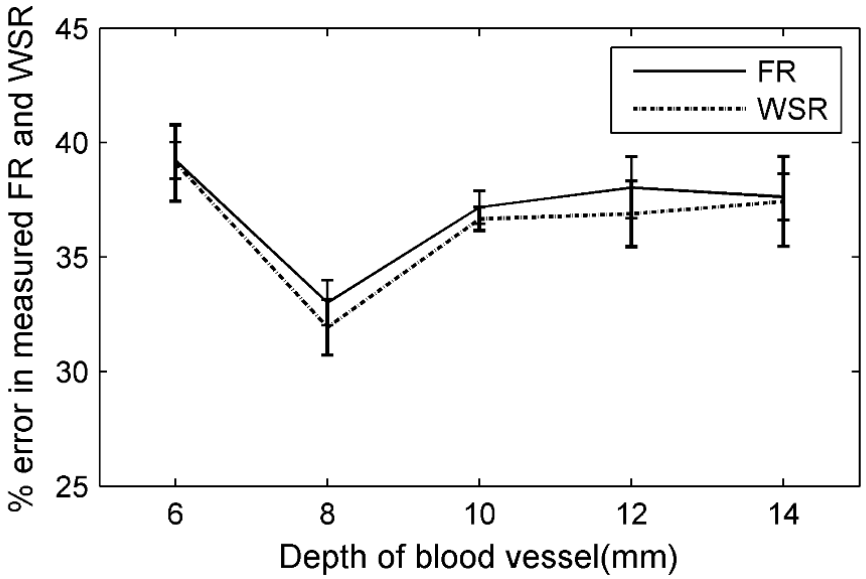

Fig. 3. 14. Percentage error (mean ± standard deviation) in measured FR and WSR at different vessel depths.

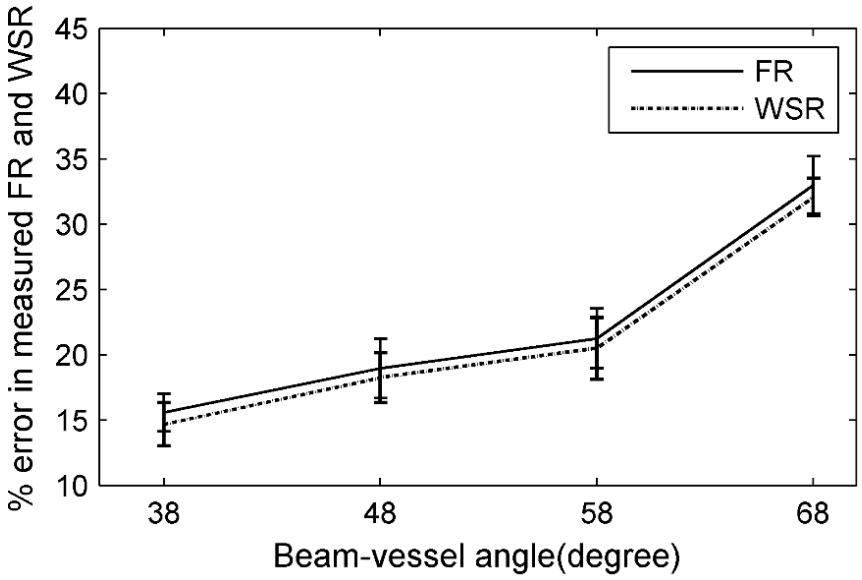

Fig. 3. 15. Percentage error (mean ± standard deviation) in measured FR and WSR at different beam-vessel angles.

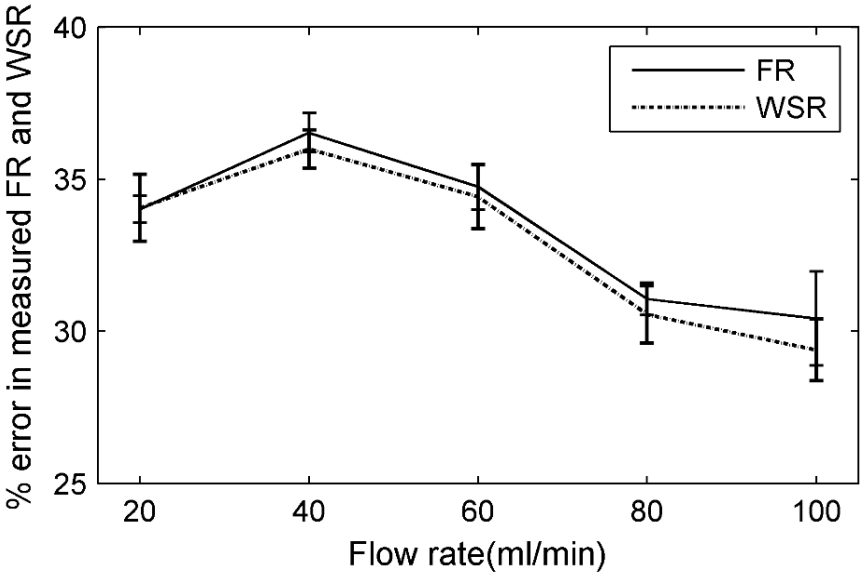

Fig. 3. 16. Percentage error (mean ± standard deviation) in measured FR and WSR at different flow rates.

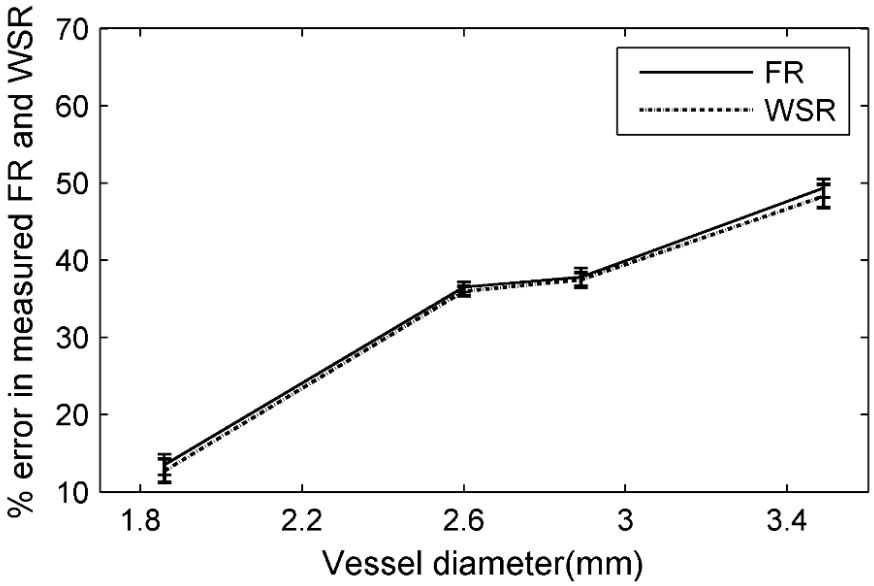

Fig. 3. 17. Percentage error (mean ± standard deviation) in measured FR and WSR at different vessel diameters.

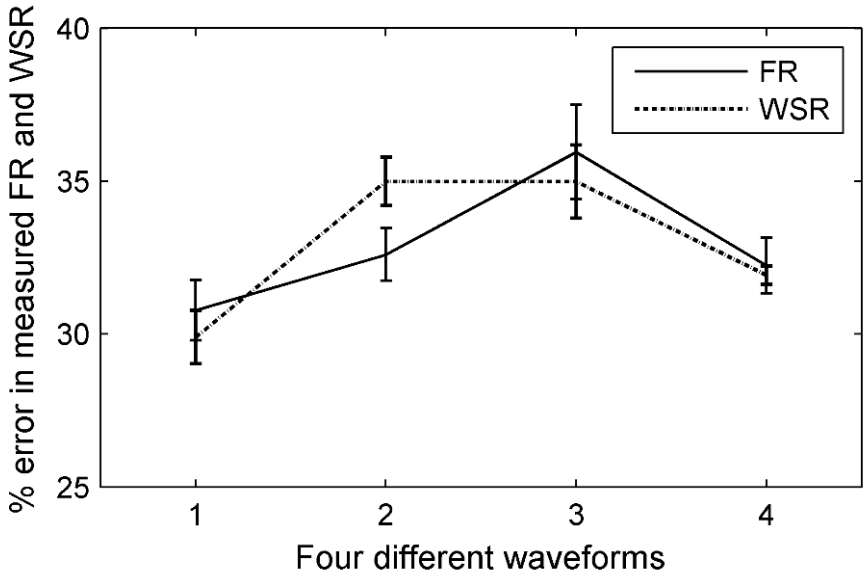

Fig. 3. 18. Percentage error (mean ± standard deviation) in measured FR and WSR at different flow waveforms.

Table 3. 9. The correlation coefficients and p-values between estimated flow parameters and scanning variables.

Estimated parameters / Scanning factor	Flow rate	Wall shear rate
Vessel depth (Fig 3.14)	Correlation: 0.11 P-values: 0.55	Correlation: 0.09 P-values: 0.88
Beam-vessel angle (Fig 3.15)	Correlation: 0.89 P-values: < 1e-3	Correlation: 0.93 P-values: 0.06
Flow rate (Fig 3.16)	Correlation: -0.70 P-values: < 1e-3	Correlation: -0.84 P-values: 0.07
Vessel diameter (Fig 3.17)	Correlation: 0.97 P-values: 0.023	Correlation: 0.97 P-values: 0.025

3.4 Discussion

This study used PVA-c VMM coupled with agar-based TMM in the flow phantoms. It was found that the vessel was slightly compressed into an elliptical shaped cross-section due to the pressure generated by the weight of the tissue mimic above the vessel. The non-circular vessel may lead to an underestimate of the vessel diameter, and may also have an effect on the estimation of velocity profile based on the Womersley theory and on estimations of flow and wall shear rates. Despite measures taken to minimise the non-circular effect, including burying the vessel at only a shallow depth within tissue mimic, making the PVA-vessel wall thicker and filling the vessel with water while pouring the tissue mimic, a difference between the horizontal and vertical directions (less than 0.1 mm) within the cross-section plane of the vessel still existed.

Both flow and wall shear rates were derived from the maximum velocity measured from Doppler ultrasound. Their errors ranged from 14% to 35% depending on beam-vessel angle (between 38° to 68°). The estimation errors in this study were consistent with the previously reported errors caused by geometric spectral broadening in the estimation of maximum velocity (Hoskins 1996; Hoskins 1999b; Steinman et al. 2001). It may be

that the angle-dependent errors in maximum velocity led to the corresponding errors in estimations of flow rate and wall shear rate.

In this study, 68° was chosen as a typical beam-vessel angle, because, in most cases, the angle was near 68° when placing the linear array transducer on the surface of the wrist to which the radial and ulnar arteries lie parallel. As a result, the flow and wall shear rates were obviously overestimated when studying all other variables, shown in Figure. 3.14, 3.16, 3.17 and 3.18. As proposed in published studies, angle corrections can be made to reduce the inaccuracies in estimating the maximum velocity (Hoskins 1996; Hoskins 2008). This should also reduce the inaccuracies of estimation in flow and wall shear rates.

Errors in measurements of vessel diameter have a crucial effects on the estimate of flow and wall shear rates (Hoskins et al. 2010b; Vergara et al. 2010). Accurate measurement is very important in three areas in particular. The Womersley theory for deriving the velocity profile (shown in eqn. 3.3) is sensitive to the measurement of vessel diameter (Ponzini et al. 2010). As indicated in eqn. 3.4 and 3.5, the calculations of flow and wall shear rates depend on vessel diameter. Further, the mean wall shear rate calculated by eqn. 3.9 is based on the estimated vessel diameter. However, for this work there was no way to know the true diameter of the vessels after fabrication of the phantom. In clinical practice, visualizing the radial and ulnar arteries with ultrasound will not be as easy as on the flow phantom. A high frequency transducer is necessary to measure the diameter accurately but since the depth of the radial and ulnar arteries is small, attenuation in using a high frequency transducer should not be a problem in clinical practice.

The overestimate was less at flow rates above 40 $ml.min^{-1}$. This is explained by the average diameter of the blood vessel being underestimated at high flow rates. Higher flow rates in the tube could increase the amplitude of vessel wall motion, leading to a higher velocity of blood vessel wall in radial direction. Therefore, if the B-mode frame rate were too low, it may not be fast enough to capture the motion of the vessel wall, causing the the diameter to be underestimated. Frame rates of 17 Hz and 34 Hz in B-mode were used to measure the diameter during this study. It was found that the estimated diameters of vessel at the flow rate over 40 $ml.min^{-1}$ with 17 Hz were indeed smaller than at 34 Hz. 34 Hz was the upper limit frame rate at this depth for the HDI5000 scanner and even this may not be enough to capture the fast-moving vessel motion when the flow rate is over 40 $ml.min^{-1}$. According to eqn. 3.4 and eqn. 3.5, the underestimation of vessel diameter could reduce overestimation of flow and wall shear rates. A higher frame rate is desirable to capture the fast motion when measuring vessel diameter in B-mode.

Although a high flow rate up to 100 ml.min^{-1} was applied within the vessel made of PVA-c shown in Table 3.7, the vessel diameter would return to its original size 2.60 ± 0.03 mm once the flow rate reduced. The greatest extension of the PVA-c was comfortably less than 30% in the radial direction (about 25%, from 2.60 mm to 3.25 mm).

When the flow rate was kept at 40 ml.min^{-1} (Fig. 3.17), the overestimate increased as the diameter of the vessel changed from 1.86 mm to 3.49 mm. This may be attributed to a larger non-circularity of the PVA-c vessel mimic when the vessel diameter is bigger but the fluid rate is the same, which could cause the invalidity of the Womersley theory in estimating the velocity profile. Another possibility is that the vessel diameter had an effect on the estimation of flow rate and wall shear rate when the true flow rate in the flow loop was kept at the same level.

It was seen that the waveforms did not influence the estimations. However only a single flow direction was investigated with no reverse flow. The fact is that the reverse flow was found in the radial and ulnar arteries of very few volunteers. However, reverse flow may have an effect on the Womersley-based calculations.

The same velocity profile calculated by inputting diameter and centreline velocity into Womersley equations was used to derive both flow and wall shear rates. The reference values of mean flow rate and mean wall shear rate in the phantoms were estimated based on the timed-collection and the Hagen–Poiseuille approach respectively. Despite the difference in collection of reference value data, the percentage errors of flow and wall shear rates were nearly at the same level in all cases, which suggests that the derived velocity profile based on the Womersley equations was reliable. However, the flow phantoms fabricated in this study only simulated the flow condition in the straight tube-like vessel where the flow is most likely well-developed. This well-developed flow condition meets the requirement of using the Womersely theory which neglects the influence of curvature or tapering in the real arteries. The radial and ulnar arteries are not a near perfect a circular tube as the flow phantoms and the Womersley theory may give a further estimation error when it was used in the arteries. This will be investigated further through simulation in next chapter where more realistic flow conditions will be studied.

This chapter is the first attempt to validate the measurements of volumetric flow rate and wall shear rate in the settings of radial and ulnar arteries (with flow phantoms) using a clinical ultrasound scanner. This Womersley equations can be readily applied in clinical practice providing the scanner can give PW Doppler mode and B-mode image data.

3.5 Conclusion

In this chapter, the measurement and validation of flow and wall shear rates in the radial and ulnar arteries using ultrasound were described using soundly-designed flow phantoms which mimicked these two arteries in depth, diameter, flow rate, flow waveform and also the beam-vessel angle.

Generally, the flow and wall shear rates were both overestimated from around 13% to 50%. Beam-vessel angle and vessel diameter appeared to affect the estimations while vessel depth, flow rate and flow waveform did not. Overestimate of flow and wall shear rates may be caused by the overestimation of maximum velocity when using the PW Doppler ultrasound.

Since errors in those measurements can lead to misinterpretation, this study should raise the awareness of researchers and clinicians who need to use these measurements in these two arteries, such as in preoperative assessment of adequacy of the collateral ulnar circulation for coronary bypass surgery, in evaluation of the radial artery remodelling after creation of arteriovenous fistula for haemodialysis access, and to distinguish the types of Raynaud's syndrome for clinical management.

Chapter 4

4. Investigation of ultrasound-measured flow related parameters with computational simulation

4.1 Introduction

While the traditional approach to evaluating velocity measurement errors uses experimental flow phantoms as chapter 3, a less commonly used method, but with potentially more flexibility, is computer simulation of the ultrasound measurement process. In this chapter, simulations will be applied to provide more realistic flow conditions in the radial and ulnar arteries, aiming at further evaluating the flow related parameters measured with ultrasound in these arteries.

The simulation method in this chapter involves simulation of the ultrasound system and also simulation of the flow-field. For the ultrasound system the beam-forming and scattering from seeded particles are simulated, followed by construction and processing of RF data (Kerr and Hunt 1992; Jensen and Munk 1997). To simulate ultrasound signals, the flow-field has to be known to help establish the trajectory of moving scatterers which mimic the movement of blood cells. At earlier date, the flow-field was obtained by approximated analytical equations to derive the trajectory.

Computational fluid dynamics (CFD) provides 3D time varying flow-field data using an iterative modelling approach. This has been developed for simulation of patient-specific blood flow since the late 1990s (Milner et al. 1998; Taylor and Figueroa 2009; Malkawi et al. 2010) and there is now a growing community using these techniques (Steinman and Taylor 2005; Hoskins and Hardman 2009; Sui et al. 2015). Most recently,

Swillens et al coupled ultrasound simulation with CFD in the investigation of velocity measurement errors in arteries (Swillens et al. 2009a; Swillens et al. 2009b; Swillens et al. 2010). The meshed geometry from CFD was transformed into a 3D grid where moving scatterers were fitted spatially and temporally according to the CFD velocity field. Based on the CFD velocity field, realistic RF data can be obtained from the ultrasound simulation.

In this chapter the ultrasound-measured flow velocity (FV), flow rate (FR) and wall shear rate (WSR) were investigated with computational simulations to understand the underlying errors in these estimations in the radial and ulnar arteries. The same strategy as used in the flow phantoms in chapter 3 was adopted but now all flow and ultrasound scan data were generated through simulations.

4.2 Methods

4.2.1 Overall

The basic simulation procedure to investigate the ultrasound-measured flow parameters in the radial and ulnar arteries is explained below and a schematic for this procedure is shown in Figure 4.1 to help conceptualise this computational simulation method.

- The MRI dataset and the tonometry data from a volunteer's arm was obtained to reconstruct the 3D geometry of the radial and ulnar arteries, and provide necessary boundary conditions for CFD simulation.
- CFD simulation was used to calculate the blood velocity field within the 3D geometry.
- Based on the CFD-calculated velocity field, simulated moving scatterers within the 3D geometry was virtually scanned by an ultrasound simulator to obtain realistic RF data.
- The RF data was used to estimate the flow velocity by applying typical signal processing strategies that are commonly used in clinical ultrasound imaging, and the flow and wall shear rates were derived based on the Womersley theory.
- Flow related parameters estimated from ultrasound were compared with the CFD reference values, giving an objective assessment of ultrasound estimations

and the performance of Womersley equation in estimating flow rate and wall shear rate in these two arteries.

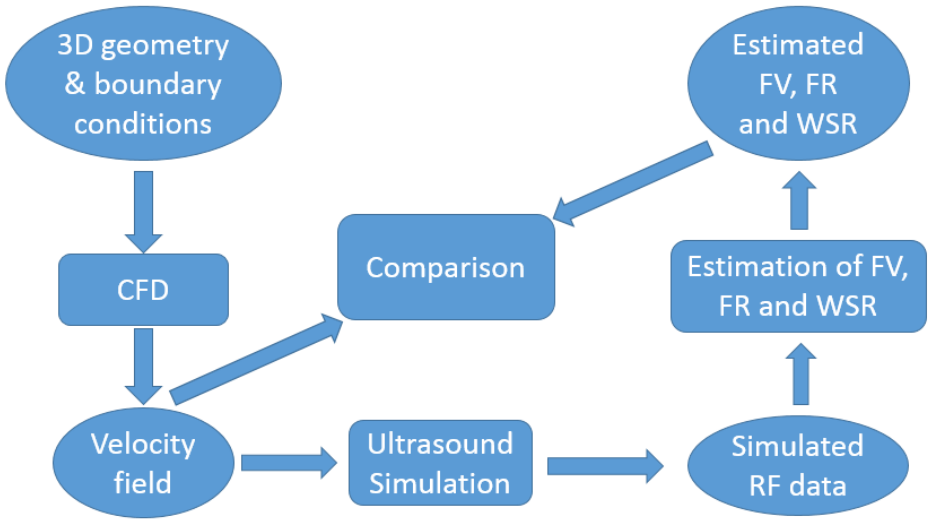

Fig. 4. 1. The procedure of simulation method.

4.2.2 Image-based CFD simulation

The image-based CFD simulation used medical images to reconstruct the 3D geometry of vasculature and obtain the boundary conditions for solving the Navier–Stokes equations *via* computational methods. Since the modelling is created based on data from a specific person, the blood flow field can be simulated in the patient-specific situation. In this study, MRI imaging data of a healthy male's left arm was accessed through the Clinical Research Centre at Dundee Ninewells Hospital and Medical School of NHS Tayside, including the images for reconstructing 3D vascular geometry and for blood flow rate waveforms. The volunteer data acquisition procedure was subject to Dundee University ethical approval and written informed consent was given by the volunteer.

3D surface geometry

The MRI dataset was exported in DICOM (Digital Imaging and Communications in Medicine) format. The 3D geometry of the blood vessels in the arm was then obtained through segmentation with Amira (Amira 5.4.3, FEI, Hillsboro, Oregon, USA) by extracting the boundaries between the lumen and vessel walls in each image (Fig. 4.2a). The bright sections in the grey-scale MRI image indicated the lumen area in the blood

vessels. As the signal magnitude in the lumen area was not consistent in MRI scanning, automatic segmentation did not work well and manual segmentation was used.

After extracting the lumen area from surrounding tissue, 224 images with thickness of 1.06 mm were stacked in sequence to reconstruct the vascular geometry as shown in Figure 4.2b. 3D geometry originating from 40 mm above the bifurcation in the brachial artery down to the point 30 mm above end of the radial artery was obtained and used as the CFD simulation domain. Surface smoothing was applied on the primitive surface in Amira to achieve the refined 3D surface geometry (Fig. 4.2c). The smoothing tools in Amria are based on averaging the height of adjacent surface elements. Harsh smoothing might cause decreased geometric diameter and lead to loss of surface detail. Limited smoothing was applied to provide a surface free of sharp edges with the minimum loss of original surface topography. An STL (stereolithography) format surface file of the 3D geometry was exported from Amira. In order to achieve a fully-developed flow in CFD, both the inlet and outlet sections were extended in Solidworks 2014 (Dassault Systemes, Massachusetts, USA).

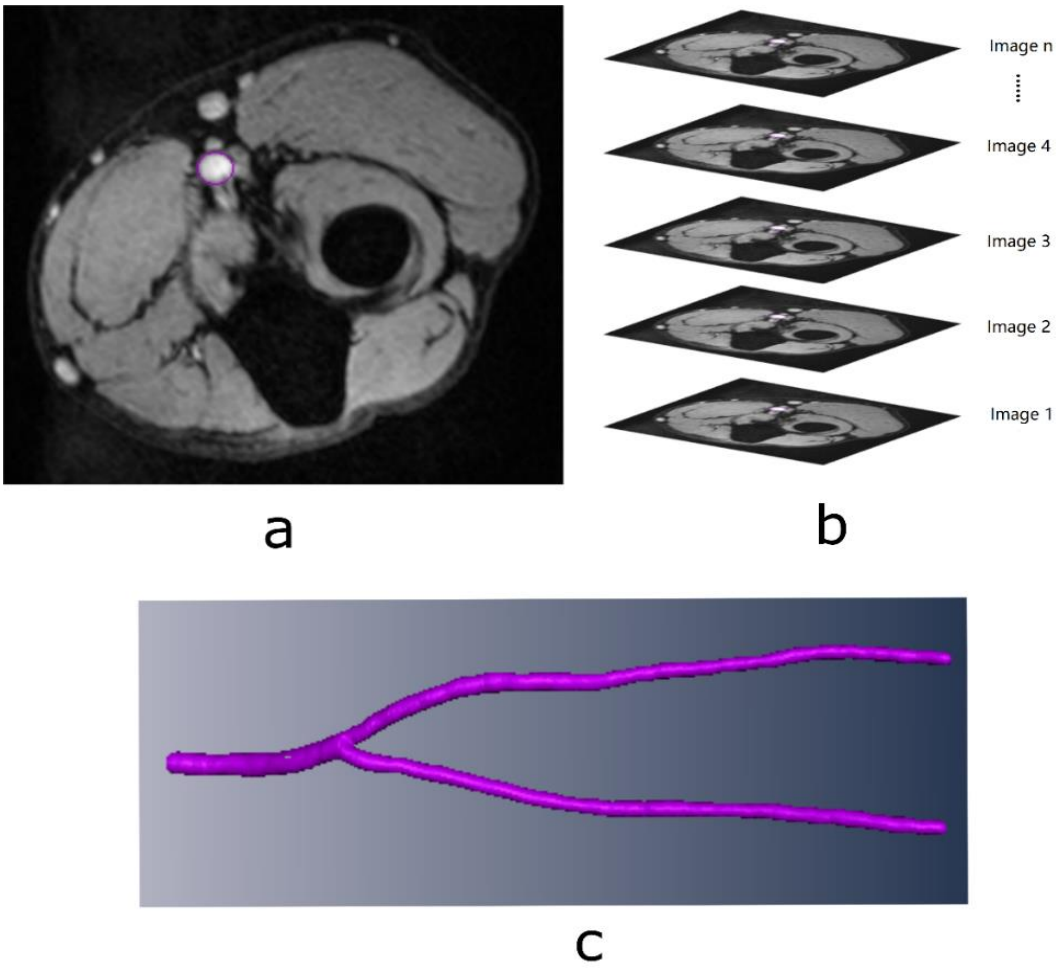

Fig. 4. 2. Reconstruction of 3D geometry of the radial and ulnar arteries.

Volume meshing

CFD provides a way to predict fluid flows by means of computer based mathematical modelling (partial differential equations) and numerical methods (discretization and solution techniques). In order to solve the mathematical models throughout the flow domain, strategies are taken to split the domain into smaller regular-shaped subdomains (such as tetrahedral, hexahedra or pyramid), also called cells or elements, so that the Navier-Stokes equations (governing the conservation of mass, momentum and energy of a moving fluid) can be solved in each single subdomain separately.

The procedure to split the flow domain is called meshing and is an important step having direct influence on simulation time, convergence and accuracy (Prakash and Ethier 2001; Steinman 2002). Practically, a mesh is the collection of points, lines and cells that occupy the space around a body in a fluid flow. It is required before the CFD can be solved. Meshing with structured hexahedral elements was proved to have better performance than that with unstructured tetrahedral elements in terms of the simulation time and accuracy (Viceconti et al. 1998; Longest and Vinchurkar 2007).

Owing to the geometrical complexity of the STL surface of vascular vessels, hexahedral elements are more difficult to be produced than tetrahedral elements in CFD simulations of the cardiovascular system. De Santis et al. (2011a) proposed a method for generating the structured hexahedral elements during the meshing of vascular vessels. In order to achieve high accuracy in this study, the hexahedral elements were generated by De Santis' method. The STL 3D geometry file was imported into a toolkit pyFormex (http://pyformex.org) as shown in Figure 4.3a. pyFormex is open source software for generating, manipulating and transforming large geometrical models of 3D structures by sequences of mathematical transformations. The meshed 3D geometry is shown in Figure 4.3b, with two locally enlarged illustrations shown in Figure. 4.3c and 4.3d. The meshing procedure in pyFormex is briefly described below and detailed procedure can be found in study by De Santis et al. (2011a),

- The central line of the geometry was calculated based on the user-defined helper line and the 3D surface; a central point was also defined to help the partition at the bifurcating area;
- The triangulated surface was cut into 6 semi-branches, and longitudinal Bezier splines were created to represent the vessel surface;

- The vertices defined for the spline division were longitudinally sorted into sections; isoparametric transformation, which maps a planar quadrilateral surface into a cubic surface, was applied to each section; a sweeping operation was conducted along the longitudinal direction to produce the cubic surface for all the sections.

The mesh density can be set easily in the longitudinal direction by adjusting the number of elements in each section and in the radial direction by changing the element distribution in the cross-sectional plane. The flow condition is more complex near the vessel wall and its velocity is lower. Therefore, three layers were defined in the cross-sectional plane to allow finer and finer meshes from the centre to the wall (Fig. 4.3d).

Boundary conditions

In addition to the 3D geometry, CFD simulation requires boundary condition inputs. To simulate the flow in blood vessels, three boundary conditions are needed: inlet, outlet and arterial wall (no-slip). In this study, values of these were measured from the same person whose 3D geometry data was previously obtained.

The inlet is at the brachial artery, 40 mm above the bifurcation (after extension). A flow waveform for the inlet boundary condition was obtained from the slice at the original inlet location although the geometry has been extended. One frame of the phase-contrast MRI images coming from the inlet location is shown in Figure 4.4a. Each frame contains two images, on the left the magnitude image and on the right the phase image, allowing derivation of blood flow perpendicular to this imaging plane. Open source software, Segment version 1.9 (http://segment.heiberg.se), was used to extract the flow rate waveform from these phase-contrast images in a chosen region of interest (Heiberg et al. 2010). The lumen of the brachial artery was manually chosen in Segment. The flow rate waveform at the inlet location is shown in Figure 4.4b. Similar procedure was applied to the ulnar artery to obtain the outlet boundary condition. The resultant flow rate waveform in the ulnar artery is shown in Figure 4.5.

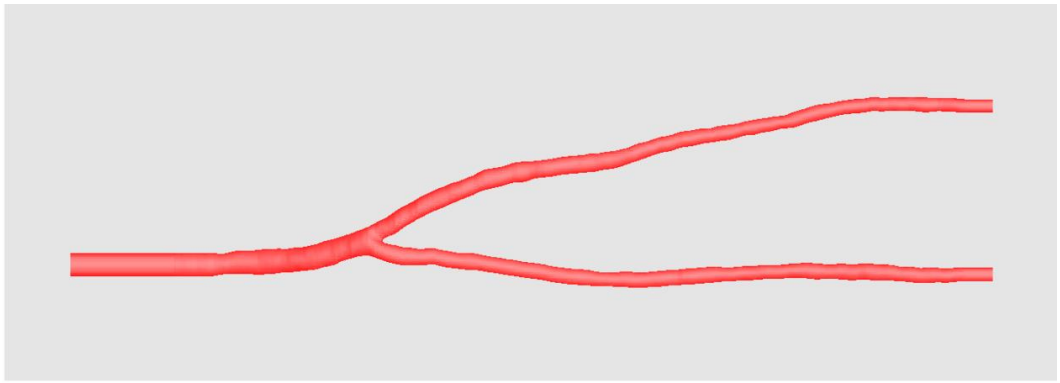

a

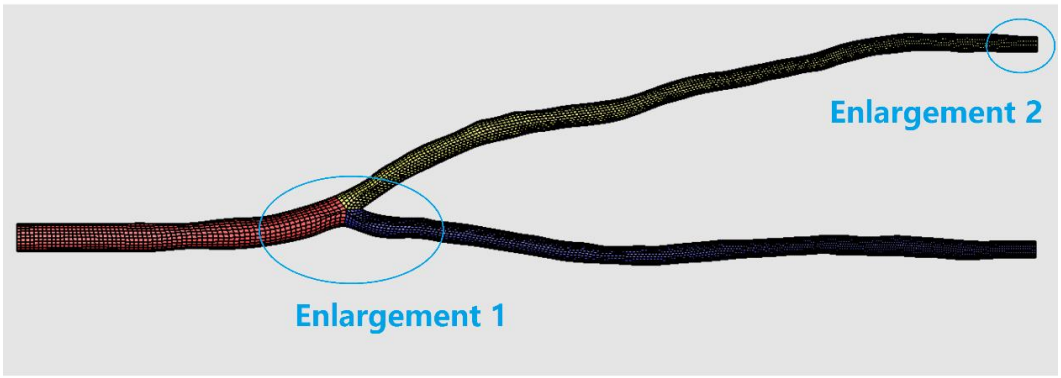

b

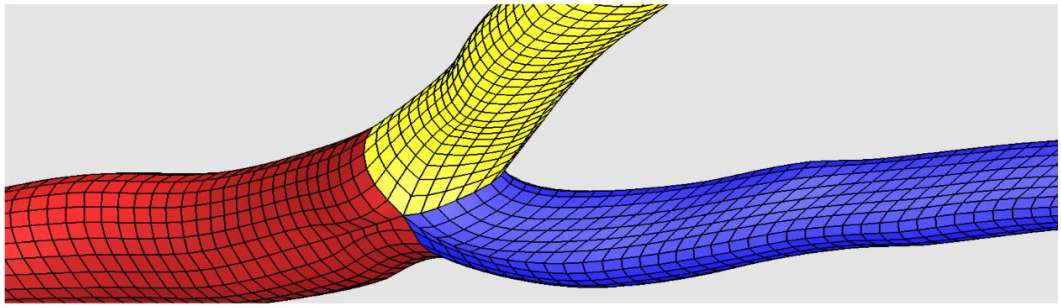

c

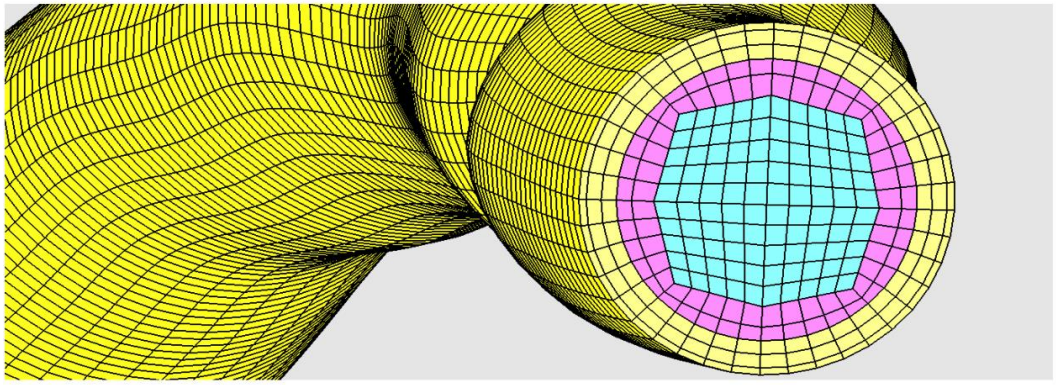

d

Fig. 4. 3. Generation of hexahedral elements using pyFomrex. (a) The 3D surface geometry of the arteries. (b) The well meashed geometry of the arteries. (c) The enlargement 1 from b. (d) The enlargement 2 from b.

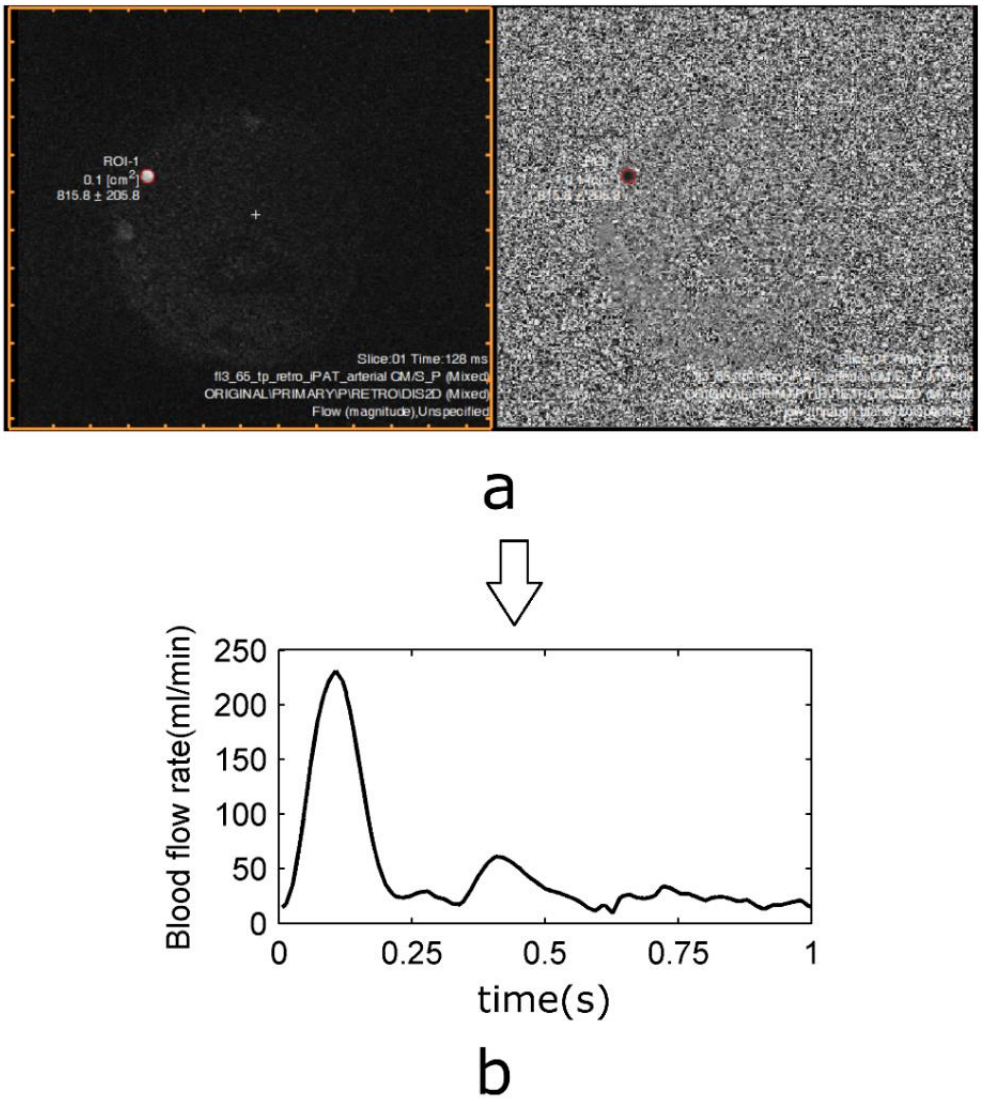

Fig. 4. 4. Extracting the flow waveforms in the brachial artery from MRI data.

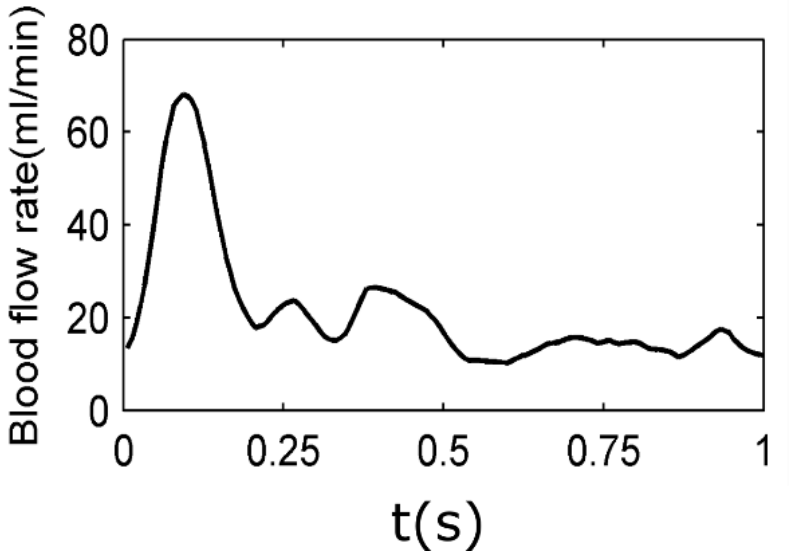

Fig. 4. 5. The flow rate waveform for the ulnar artery outlet boundary condition.

The boundary condition for the outlet of the radial artery was set to the blood pressure waveform which was measured by applanation tonometry (SphygmoCor device, AtCor Medical, Sydney, Australia) from the same volunteer. The volunteer was asked to sit still and relax for 5 minutes. To record the pressure waveform, a pencil-like pressure transducer connected to a PC was attached at the position around the wrist where the pulse signal is strongest. The blood pressure waveform was scaled to 80-120mmHg in the radial outlet (Fig. 4.6).

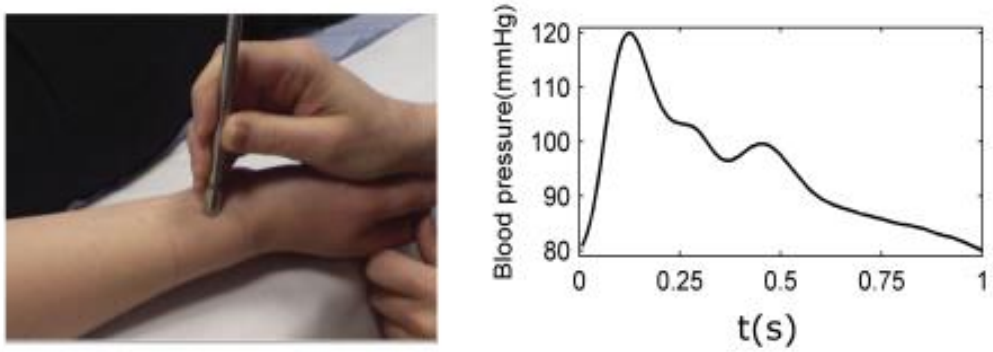

Fig. 4. 6. Acquisition of the blood pressure waveform in the volunteer's radial artery.

All waveforms were scaled to one second with respect to time for consistency although the real cardiac cycles obtained at different sites from flow and pressure are not exactly one second. Based on the waveforms in Figure 4.4b and 4.5, the time-averaged flow rate is 47.2 $ml.min^{-1}$ in the brachial inlet and 21.4 $ml.min^{-1}$ in the ulnar artery outlet within one cardiac cycle. The 3D geometry was assumed to have rigid walls and the "no-slip" condition was applied at the walls. A parabolic velocity profile was assumed when using flow rate waveforms as boundary conditions (Xiang et al. 2014). The overall 3D geometry and boundary conditions are shown in Figure 4.7.

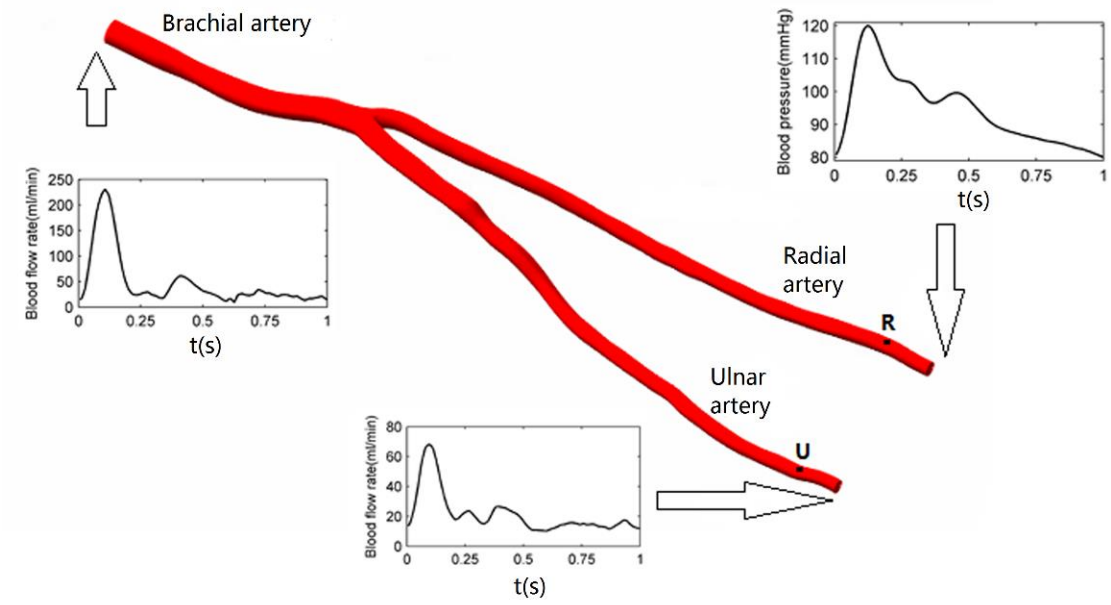

Fig. 4. 7. 3D geometry and boundary conditions for CFD.

CFD model properties and calculation

In this simulation, blood was assumed to be an incompressible Newtonian fluid having the typical properties of normal healthy human blood, with density of 1050 $kg.m^{-3}$ and dynamic viscosity of 3.5 mPa.s (Stewart et al. 2012). Abaqus (Simula, Inc. Providence, RI, USA) was chosen to solve the Navier-Stokes equations in the 3D geometric domain for this transient analysis. A projection method in Abaqus/CFD was used to enable segregation of pressure and velocity fields for efficient solution, and a second-order least-squares gradient estimation was used for the numerical solution. The time step for outputting results was set to 5 ms, giving 200 values within one cardiac cycle which was scaled to one second.

Mesh independence tests were conducted to determine the optimum number of mesh elements. The number of elements needs to be adequate to provide reliable results but not excessive so as to keep a reasonable computational execution time. The number of elements generated within the 3D geometry can be increased by changing the element concentration in the longitudinal direction and in the transverse plane as explained before (Section 4.2.2, under "Volume meshing"). The maximum peak systolic velocity was chosen to test this mesh independence. In addition, the wall shear rate at a specific timing of the cardiac cycle near the downstream of the bifurcation in the radial artery was also used to test the meshing independence.

The differences in maximum velocity and wall shear rate are provided in Table 4.1. The criteria for the optimum volume mesh was to have less than 4% difference in maximum velocity and wall shear rate from the previous and proceeding volume mesh (Wood et al. 2006; Cheng et al. 2010). Therefore, the meshing with 373435 nodes and 351288 elements was finally chosen. The quality of this meshing was assessed as 'good' by the mesh verification analytics in Abaqus, only 1.48% of the elements highlighted with warnings and no errors indicated.

One and a half cardiac cycles were simulated to thoroughly cover a complete cardiac cycle. To save simulation time, only the sections near insonating positions, as indicated as R and U in Figure 4.7, were chosen to generate a velocity field output. With the meshing of 373435 nodes and 351288 elements, the CFD simulation took 11 hours on a PC with 64-bit, 3.40 GHz Intel Core i7-3770 processor.

Table 4. 1. The meshing independence test results for maximum velocity and maximum WSR.

Nodes	**Elements**	**Maximum velocity** (m/s)	**Differences**	WSR(s^{-1})	**Differences**
41819	38376	0.6600		135.37	
			2.24%		-0.73%
158403	147600	0.6748		134.38	
			0.6%		8.1%
252137	236160	0.6788		145.28	
			0.2%		4.1%
311320	292740	0.6792		151.24	
			0.04%		-3.4%
373435	351288	0.6795		146.13	
			0.3%		-0.57%
450342	425088	0.6816		145.30	

Velocity related parameters extraction

As explained in chapter 3, the velocity measured by a clinical ultrasound scanner with PW Doppler mode is the maximum velocity waveform near the centreline. It is assumed that the maximum velocity is located at the centreline even though this is not

always the case for instance if there is reverse flow or when the vascular geometry is complex (Li et al. 1993a; Leguy et al. 2009a). The flow rate and wall shear rate are then derived based on the centerline maximum velocity and the vessel diameter using the Womersley theory. To allow comparison between the ultrasound measurements and the CFD reference values, three parameters need to be extracted from the CFD: centerline velocity, wall shear rate and vessel diameter.

Velocity from the element (marked as C in the Fig. 4.8) in the very centre in the transverse plane can be retrieved as the centreline velocity from the velocity field according to its element number. The velocity obtained from CFD is a 3D vector. With reference to this vector, velocity at any other direction could be calculated through the angular relationship.

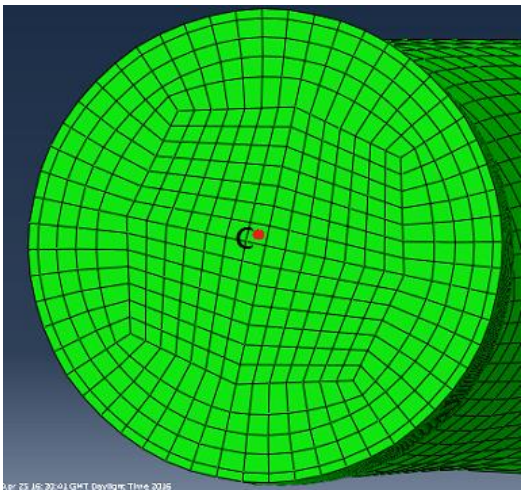

Fig. 4. 8. The central element from where the centreline maximum velocity was extracted.

The wall shear rate was defined as the velocity gradient at the vessel wall ($wsr = \partial v / \partial r |_{r=R}$, where v is velocity, r is radial position and R is vessel radius). In Abaqus, the velocity for each element represents the value at the centroid of the element. Based on this, the wall shear rate can be obtained from the wall element velocity divided by half of the element thickness. The thickness of the element and the vessel diameter were available for Abaqus.

4.2.3 Doppler ultrasound simulation

An ultrasound simulator (Field II) was chosen in this study to generate the simulated RF signals (Jensen and Svendsen 1992; Jensen 1996). This simulator allows arbitrary transducer settings and a realistic image scan sequence and has been widely used in the literature for over two decades. The underlying theories of Field II are spatial impulse response estimation which was proposed by Tupholme (1969) and Stepanis.Pr (1971), and the linear propagation of sound wave. With this Field II ultrasound simulator different kinds of linear imaging can be simulated for tissue and blood flow.

A synthetic computer-based phantom is required for generating RF data by introducing point scatterers to create flow images. Blood can, in this setting, be modelled as randomly distributed point scatterers with a suitable density. These point scatterers contain the amplitude and position information for reflecting the sound waves. Trajectories of these moving scatterers can either be described in an analytical way or obtained through 3D flow fields from CFD simulation. In this study, the analytically described computer phantom of a straight tube was used as a trial to evaluate Field II, and the computer phantom based on CFD flow fields was used for validating ultrasound measurements in the radial and ulnar arteries.

Transducer settings in Field II

A linear-array transducer was created in Field II for transmission and reception of the ultrasound waves. Parameters of this transducer are listed in Table 4.2. Each transducer element was divided into 4 rectangular elements in elevation. The pulse repetition frequency (PRF) varied from 3 kHz to 10 kHz according to the velocity in the vessels under different circumstances. Since an accurate acoustic field cannot be guaranteed in the near-field region of the simulated sound field in Field II (Jensen and Svendsen 1992), imaging depths were set between 4-50 mm to investigate its effects and to make sure that the sample volume was located in the far-field area while looking into other factors. Transmit focus was set to match the imaging depth. The scan positions in the radial and ulnar arteries are indicated as R and U in Figure 4.7. The length of the sample volume was set large enough (2.3 mm) to encompass the centreline area of the vessel where the maximum velocity normally occurs.

Table 4. 2. Linear array transducer settings in Field II.

Parameters	**Values**
Pulse central frequency (f_0)	5 MHz
Excitation pulse (P)	Sinusoid
Pulse cycles (n)	5
Sound velocity (c)	1540 m/s
RF data sampling frequency (f_s)	100 MHz
Element width (w)	Half a wavelength
Element height (h)	5 mm
Gap between elements (Kerf)	0.05 mm
Number of elements (N)	64
Pulse repetition frequency (PRF)	3-10 kHz
Transmit focus (F)	[0,0,4-50] mm

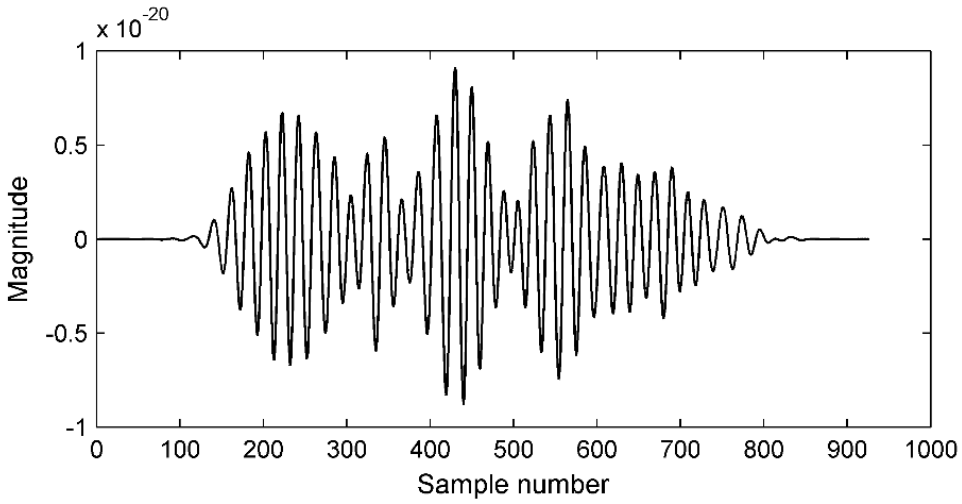

Fig. 4. 9. The RF data simulated in the Field II.

Velocity estimation with RF data

The RF data generated from the Field II was used for post signal processing to estimate the velocities of the moving scatterers in the sample volume. An example plot of the RF signal is shown in Figure 4.9.

After obtaining the RF signal, a series of signal processing steps were performed as shown in Figure 4.10. The number of RF signals is determined by the scanning time and the pulse repetition frequency (PRF). Firstly the product of each RF signal and the exponential function $e^{j\omega t}$ (ω is the central angular frequency of the transmitted sound wave) was generated, resulting in a complex signal with a length equal to the number of RF pulse in the sequence. Each sample of this complex signal comes from one reflected RF signal, and these samples were aligned based on the scan sequence. Then this complex signal was multiplied by a Hanning window before the fast Fourier transform (FFT) was used to estimate the amplitude of all of the frequencies existing within the Doppler signal.

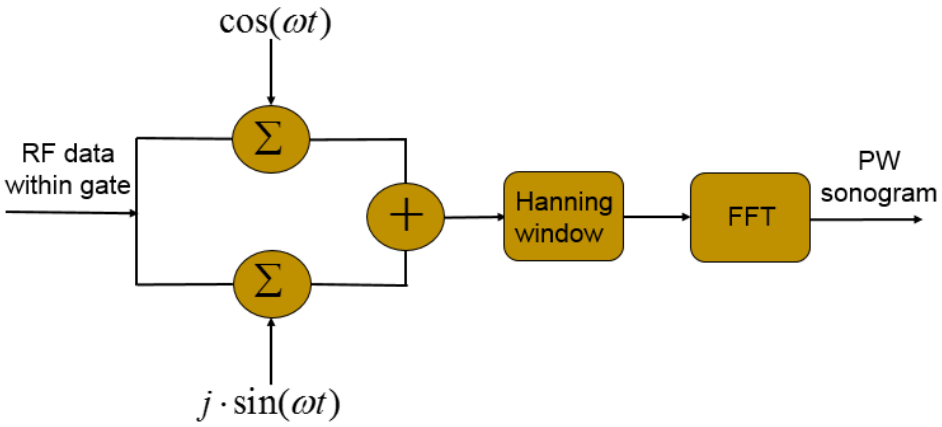

Fig. 4. 10. The signal processing for estimating Doppler velocity from the RF data.

When using the FFT algorithm, a complete Doppler spectrum was calculated on each of 256 consecutive samples. The time duration varied from 25.6 ms to 85.3 ms in accordance with a PRF from 3000 Hz to 10000 Hz. There is an overlap sweeping between two consecutive FFT calculations. If the segment from sample 1 to sample 256 were used for the first spectral estimation, then the second spectral estimation would be calculated based on the segment from sample 17 to sample 272, and so on for subsequent samples. In each estimated spectrum, the value of Doppler frequency corresponds to the velocity of moving scatterers within the sample volume. The relationship between Doppler frequency and velocity is given by the Doppler equation,

$$v = \frac{c \cdot f_d}{2 \cdot f_t \cdot \cos\theta} \tag{4.1}$$

where c is the sound speed, f_d is the Doppler shift, f_t is the central frequency of transmitted sound wave, and θ is the angle between sound beam and the direction of moving scatterers.

Aligning all the estimated spectra in a sequence forms the velocity waveform. The outline of the spectra represents the maximum velocity waveform within the sample volume.

FR and WSR estimation

The same Womersley theory explained in chapter 3 was used to derive the velocity profile within the vessel based on the maximum velocity at the centreline and the arterial diameter. The flow rate and wall shear rate can then be derived from the velocity profile. The diameter of the vessel within the beam can be easily measured according to the 3D geometry in Abaqus.

Validation of the Field II simulation

In order to evaluate the performance of this virtual transducer in Field II in detecting the centreline maximum velocity, a trial was conducted using an analytically-described synthetic straight tube-like flow phantom. The velocity field in the tube phantom was analytically described to act as input to drive the spatially and temporally moving scatterers for generating the simulated ultrasound signals with Field II. This allows the comparison between the ultrasound measured values and the analytically defined values in terms of the centreline maximum velocity.

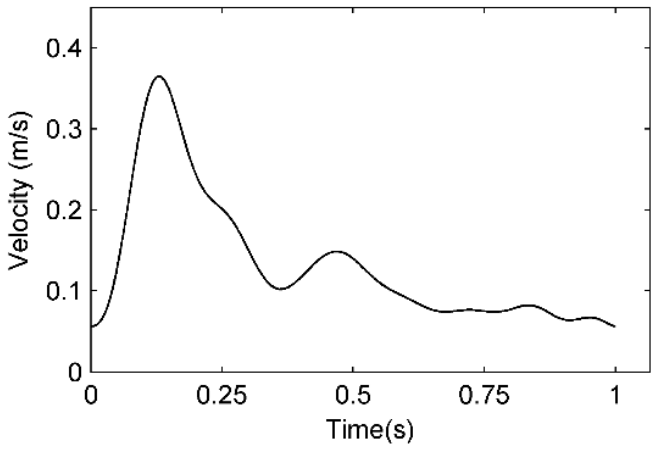

Fig. 4. 11. The assumed mean velocity waveform in a rigid tube.

To obtain the velocity field in this straight tube phantom, a method described by Evans (1982) for predicting velocity profiles in steady-state pulsatile flow was used. A cyclic mean flow waveform (Fig. 4.11) was assumed in a rigid tube-like geometry where the radius is 4.2 mm. According to Evan's description, the relation between the velocity profile and the mean volumetric flow waveform for one single sinusoidal component is given by,

$$v_k(r,t) = \frac{1}{\pi R^2} \cdot Q_k \cdot \left|\psi_k\left(r,\tau_k\right)\right| \cdot \cos(\omega_k t - \Phi_k + \chi_k)$$

$$\psi_k(r,\tau_k) = \frac{J_0(\tau_{k)} - J_0(r\cdot\tau_k)}{J_0\left(\tau_k\right) - 2J_1(\tau_k)/\tau_k}$$

$$\chi_k = \angle\psi_k(r,\tau_k)$$

$$\Phi_k = \angle Q_k$$

$$\tau_k = j^{3/2}\cdot\alpha_k$$

$$\alpha_k = R\cdot\sqrt{\frac{\rho}{\mu}\cdot\omega_k} \qquad (4.2)$$

The α_k in the above equations is the Womersley number which indicates how far the pulsatile flow is from the steady flow (A smaller value α means steadier flow condition). R represents the radius of the tube-like geometry, ρ is the fluid density, μ is the dynamic viscosity, Q_k and ω_k are the kth sinusoidal component of the flow rate waveform and the corresponding harmonic angular frequency, and j is the complex number. The volumetric flow rate is related to the mean spatial velocity $Q(t) = A\cdot v_{mean}(t)$. Assuming a Newtonian fluid allows linearly superimposition of the different sinusoidal components to obtain the time variation of the pulsatile flow. The individual sinusoidal components of a mean velocity waveform depicted in Figure 4.11 can be derived by Fourier decomposition,

$$V_{mean,k} = \frac{1}{T}\int_0^T v_{mean}(t)e^{-jkw_0 t}dt \qquad (4.3)$$

The spatial velocity is then obtained by superimposition of the first several orders of sinusoidal components. The first eight sinusoidal components were chosen in this study.

$$v_{mean}(t) = v_0 + \sum_{k=1}^{8} \left| V_{mean,k} \right| \cdot \cos(k\omega_0 t - \Phi_{mean,k})$$

$$\Phi_{mean,k} = \angle V_{mean,k} \tag{4.4}$$

Combing eqn. 4.2, eqn. 4.3 and eqn. 4.4, it is possible to reconstruct the time evolution of the velocity profile for the pulsatile flow.

$$v(r,t) = 2v_0(1-r^2) + \sum_{k=1}^{8} \left| V_{mean,k} \right| \cdot \left| \psi_k \right| \cdot \cos(k\omega_0 t - \Phi_{mean,k} + \chi_k) \tag{4.5}$$

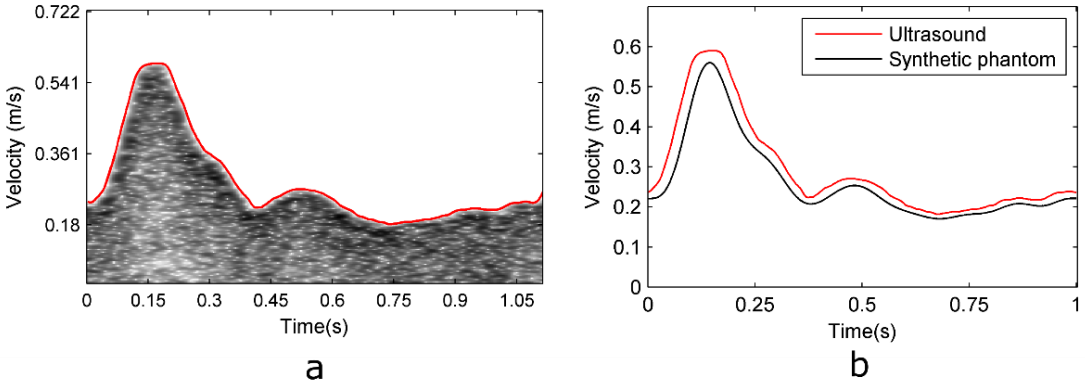

Fig. 4. 12. The simulation results from Field II based on an analytically-described flow phantom.

The moving scatterers in the tube-like synthetic flow phantom, driven by the velocity profile from eqn. 4.5, were virtually scanned by the transducer in Field II. Scanning parameters of the virtual transducer were the same as shown in the Table 4.2. The phantom was placed with an angle of 30^o to the sound beam. After obtaining the RF data, velocity sonogram was estimated according to the procedure (Fig. 4.10) in the velocity estimation section and the maximum velocity waveform was superimposed onto the sonogram by extracting its outline (Fig. 4.12a).

As shown in Figure 4.12b, the virtually estimated maximum velocity waveform by the Field II was compared with the original centreline velocity waveform which is analytically described by the eqn. 4.5. It was proved that this Field II simulator can estimate the centreline maximum velocity with a high accuracy. The overestimation of maximum velocity shown in Figure 4.12b was caused by the 30^o angle between the beam and vessel, and this issue is discussed later in this chapter.

4.2.4 Coupling the CFD data with US

Field II simulates the RF signal based on the moving point scatterers within the sample volume. In this thesis, the trajectory of these moving scatterers were determined by the flow velocity field from CFD. In order to couple the CFD flow field and the Field II simulator, a method proposed by Swillens et al. (2009b) was applied to regulate stepwise movement of the scatterers which are spatially and temporally fitted into the meshed 3D grid.

The concentration of these scatterers depends on the spatial cell resolution of the sound beam, normally 10 scatterers per cubic wavelength (Thijssen 2003; Swillens et al. 2009b). All these generated scatterers contain information of locations within a 3D coordinate, magnitudes and velocities (a 3D vector assigned based on the CFD velocity field in the 3D geometry together with spatial and temporal interpolation). Each single scatterer updates its location according to its velocity at the previous frame and the time gap (determined by the PW Doppler PRF) between the two consecutive frames as shown in Figure 4.13. After moving to the new location, all scatterers can obtain their new velocities from the CFD velocity field by spatial and temporal interpolation, and are ready to update their locations for the next frame. Scatterers, which "flee" away from the 3D geometry, were removed. At the inlet area, new scatterers were generated at each frame to feed downstream, like the red cells coming continuously from upstream area.

A virtualisation of this coupling method is shown in Figure. 4.14. This was accomplished by designing a graphic user interface (GUI) in MATLAB R2015a (The MathWorks, Natick, MA, USA) to automate this procedure. Within the GUI, the ultrasound transducer and the beam were demonstrated to show their relative positions with respect to the vascular vessels. Beam vessel angle, imaging depth and beam axis can be adjusted easily by changing their relative positions.

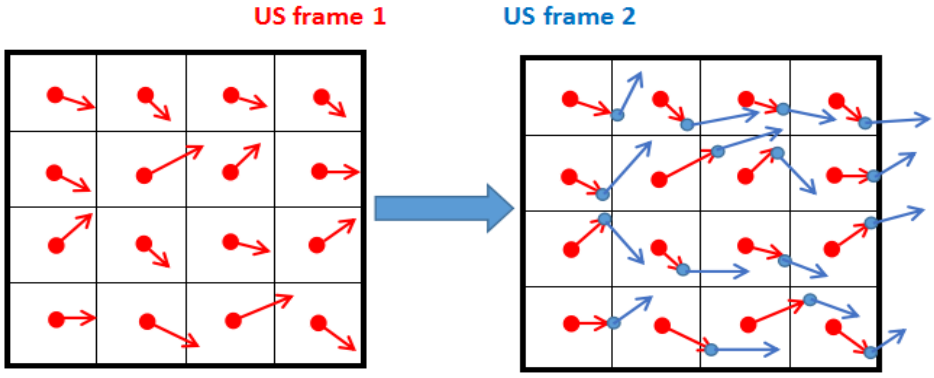

Fig. 4. 13. Illustration of the moving scatterers between two scan frames in simulation.

4.2.5 A straight tube trial

Based on the proposed coupling method, a straight tube was chosen to assess the feasibility of this simulation technique.

A rigid straight tube with a length of 40 mm and diameter of 2.5 mm was created as the 3D geometric domain. The mean velocity waveform shown in Figure 4.11 was used as the inlet boundary condition and a parabolic profile was assumed for this inlet. Zero-pressure was applied to the outlet and the tube wall was rigid. This 3D straight tube was created and meshed with hexahedral elements in Abaqus/CAE. Pyformex was not needed here because a straight tube is easily meshed with hexahedral elements in Abaqus/CAE. The number of element is 12525, with 14952 nodes. All other settings for this CFD simulation were the same as the descriptions in section 4.2.2. After deriving the CFD flow field, the proposed coupling method was applied to feed moving scatterers to the Field II simulator. The parameters of simulated transducer were the same as they are in the Table 4.2. The diagram of this scanning procedure is shown in Figure 4.15.

The beam axis was set to cross the axis of the tube with the sample volume encompassing the centreline. Within the beam-axis, the centreline velocity waveform estimated from the ultrasound simulation (based on the procedure in section 4.2.2) can be compared with the centreline velocity waveform in the CFD velocity field. The angle between the sound beam and the straight tube was set to 30 ^{o}. The estimated sonogram superimposed on the outline velocity waveform is shown in Figure 4.16a. The outline maximum velocity is compared with the CFD centreline velocity waveform in Figure 4.16b.

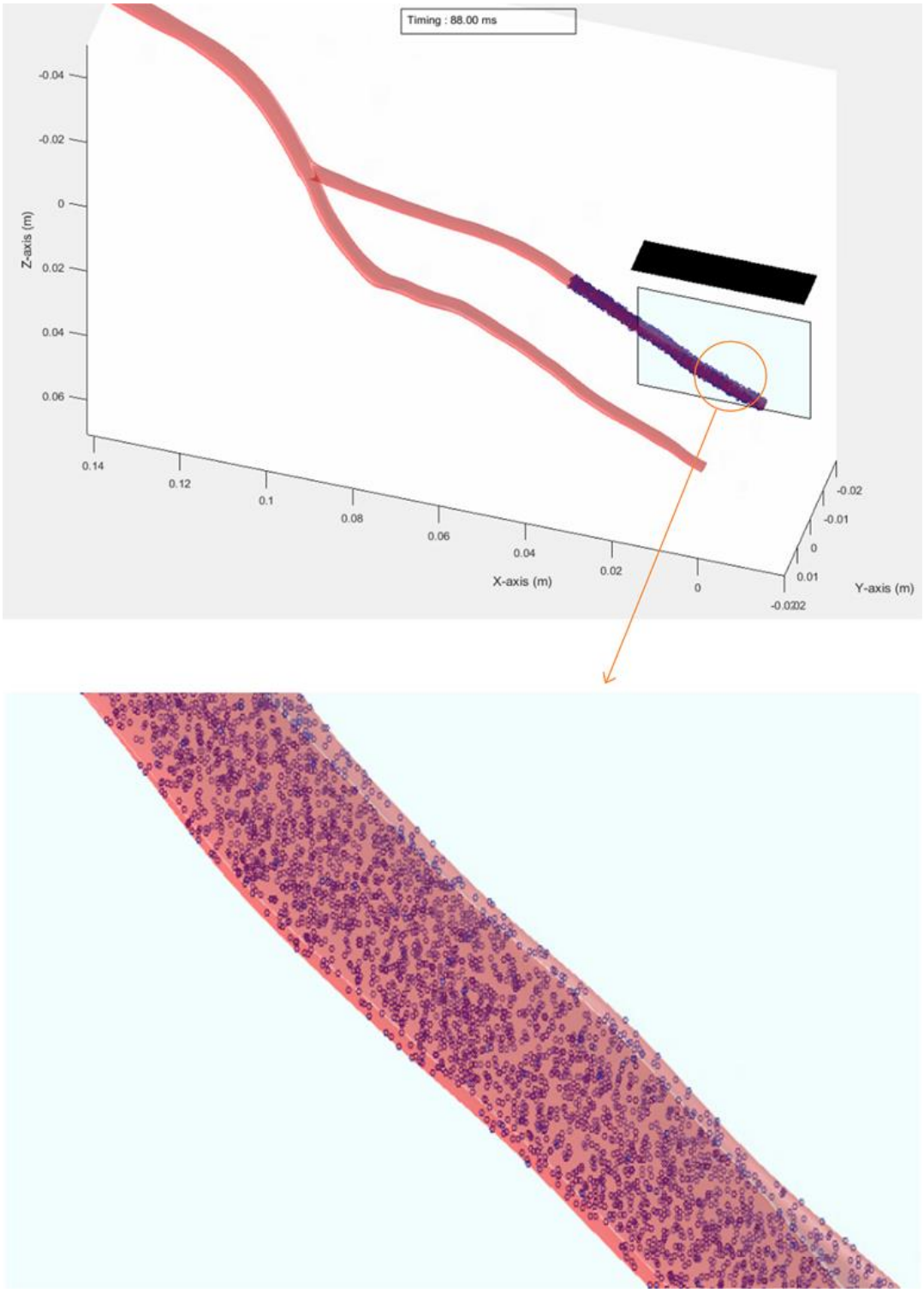

Fig. 4. 14. GUI visualisation of the ultrasound scanning procedure with scatterers moving according to the CFD velocity field.

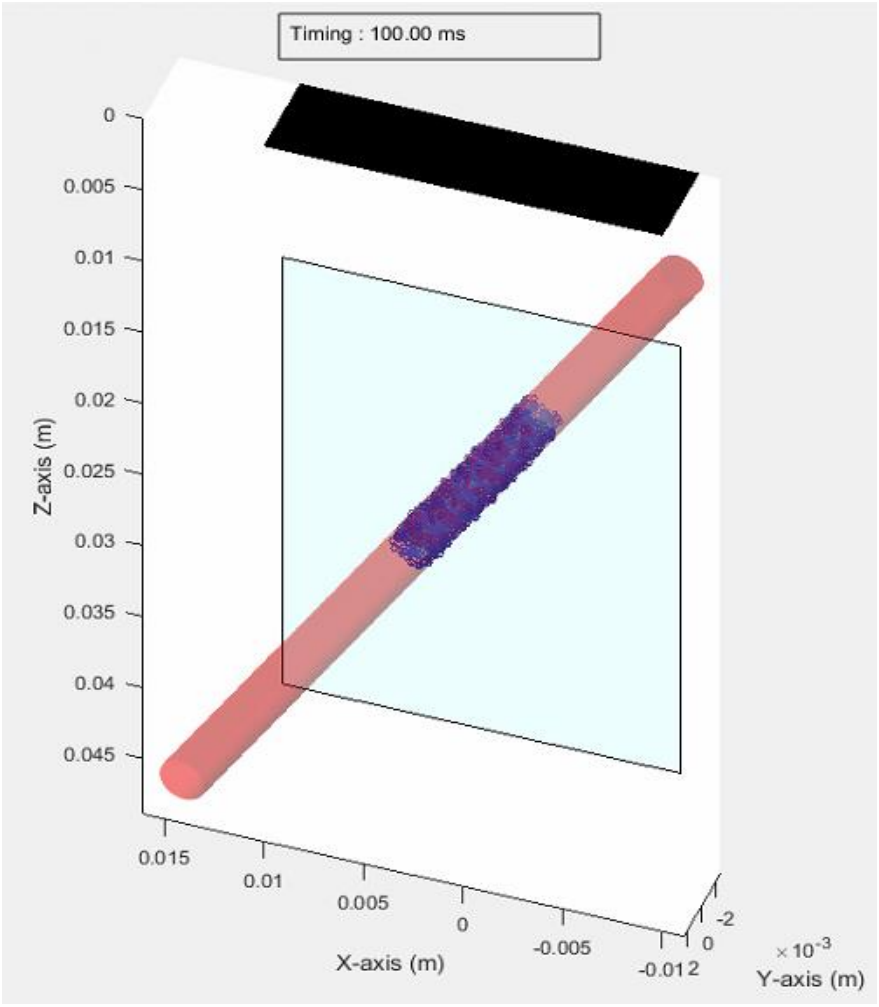

Fig. 4. 15. The scanning procedure of a straight tube.

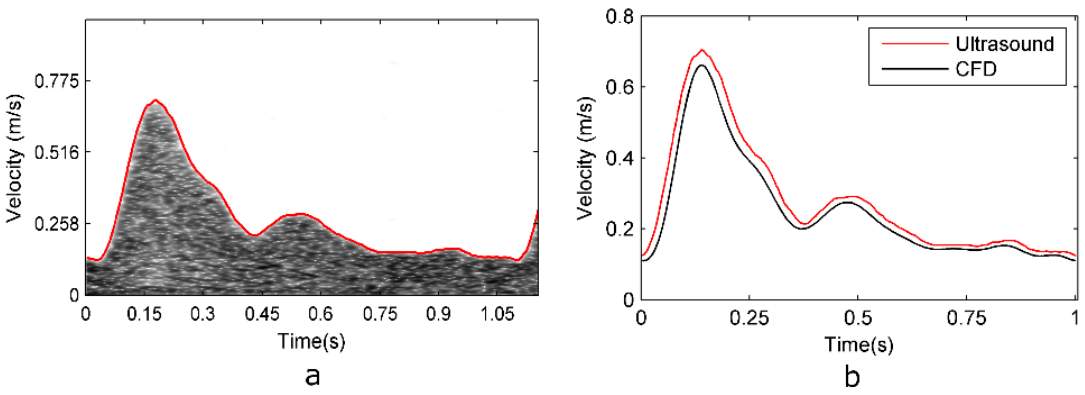

Fig. 4. 16. The simulation results from Field II for flow in a rigid straight tube.

As shown in the Figure 4.16b, the waveform estimated from Field II simulator is in good agreement with the CFD reference waveform in terms of phase and amplitude. This straight-tube trial justified the application of this simulation method. The overestimation

by ultrasound in Figure 4.16b was caused by the 30^{o} angle between the sound beam and the vessel as shown in Figure 4.15. This angle-caused issue is explained later in the discussion.

4.2.6 Overall simulation protocol

In order to investigate the effects caused by different factors, such as the scanning procedure or the flow condition itself, the detailed protocol for evaluating PW Doppler in estimating flow parameters in the radial and ulnar arteries by the proposed simulation method is explained in this section.

The accuracy of estimated flow velocity was investigated under beam-vessel angles of 30 ^{o}, 40 ^{o}, 50 ^{o}, 60 ^{o}, and 70^{o} by placing the synthetic vessel at the appropriate angle with respect to the sound beam propagation direction as shown in Figure 4.13. The flow rate in the blood vessel was set at different levels to investigate its effect on the ultrasound maximum velocity estimation, ranging from two thirds to twice the phase-contrast MRI measurement by changing the amplitude of the boundary conditions (flow rate waveforms in Fig. 4.6) during CFD simulation. To avoid the influence of near-field approximation in Field II, the imaging depth was set to 4 mm, 10 mm, 20 mm, 30 mm, 40 mm and 50 mm. The effect of the beam-vessel angle, the flow rate and the imaging depth were each investigated by adopting a standard set of criteria then varying each in turn. The standard criteria is 60 ^{o} for beam-vessel angle, MRI-measured value for flow rate and 40 mm for imaging depth, as they are indicated by the asterisks in Table 4.3. For example, flow rate and imaging depth would be fixed at MRI-measured value and 40 mm respectively when investigating beam-vessel angles from 30 ^{o} to 70 ^{o}.

Table 4. 3. Values of three variables investigated in the simulation.

Variable	**1**	**2**	**3**	**4**	**5**	**6**
Depth(mm)	4	10	20	30	40*	50
Angle (^{o})	30	40	50	60*	70	----
Flow rate (times of MRI value)	$\frac{2}{3}$	1*	$\frac{4}{3}$	$\frac{5}{3}$	2	----

Using the Field II ultrasound scanning was repeated five times in each case when measuring the maximum velocity, as such the mean values and standard deviations were obtained for these estimations. Maximum velocity waveform from five individual measurements was averaged to calculate flow rate and wall shear rate, with beam-vessel angle of 60^{o}, MRI-measured flow rate and imaging depth of 40 mm.

4.3 Results

4.3.1 Flow velocity

The velocity field at the peak systolic point of the cardiac cycle in the transverse plane where the beam axis passes through is shown in Figure 4.17. The sample volume positions in the PW Doppler ultrasound image are marked in the transverse plane with sample gate position shown. It can be seen that the velocity in the radial artery is higher than in the ulnar artery for this volunteer, with a peak systolic velocity of over 0.6 m.s^{-1}. The velocity profiles also differ.

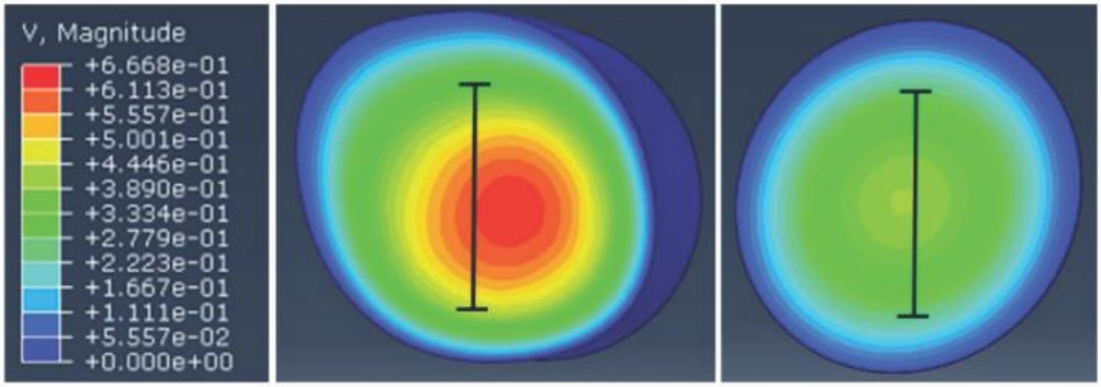

Fig. 4. 17. Contours of flow velocity in the cross-sectional plane.

The diameters of radial and ulnar arteries within the insonating area were measured as 3.22±0.02 mm and 2.82±0.02 mm respectively according to the 3D geometry in Abaqus. Simulated velocity spectral sonograms, based on the velocity field calculated from CFD, are shown in Figure 4.18. Maximum velocity waveforms were extracted and superposed onto the spectra.

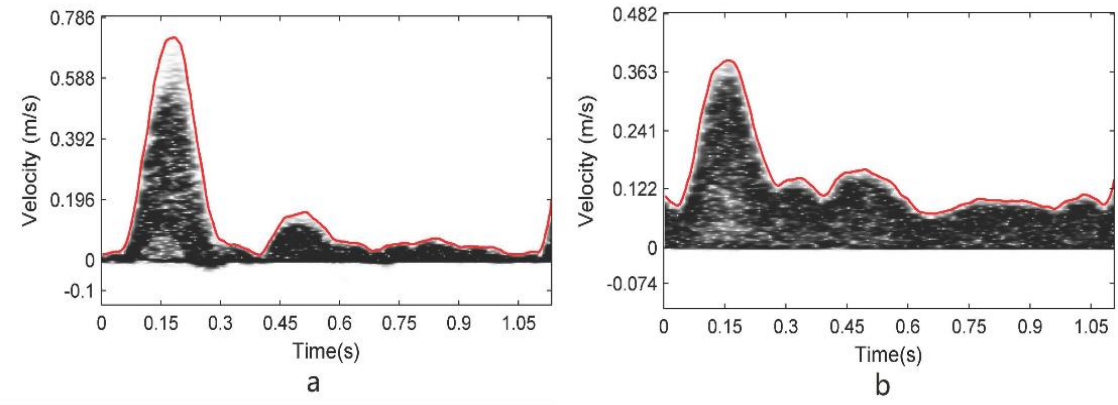

Fig. 4. 18. PW sonograms and the maximum velocity waveforms. (a) For the radial artery. (b) For the ulnar artery.

Ultrasound-measured maximum velocity waveforms were compared with the CFD maximum velocity waveforms in two different ways. Maximum velocity waveforms in the radial artery from CFD and ultrasound in the beam direction are compared in Figure 4.19a, with the beam-vessel angle at 60^o. The CFD maximum velocity waveforms in the direction parallel to the vessel axis are compared with ultrasound-measured waveforms in the direction of vessel axis calculated using the 60^o beam-vessel angle (Fig. 4.19b).

Similar comparisons for the ulnar artery are shown in Figure 4.19c and Figure 4.19d. In the radial artery the ultrasound overestimation of maximum velocity waveform in the beam direction (30.9% for systolic and 52.6% for time-averaged) was higher than that in the angle-corrected vessel direction (24.2% for systolic and 43.6% for time-averaged). This differences between beam direction and vessel direction are much smaller in the ulnar artery where they are 20.6% and 20.9% (Fig. 4.19c and Fig. 4.19d) for peak velocity, and 39.6% and 40.4% for time-averaged velocity.

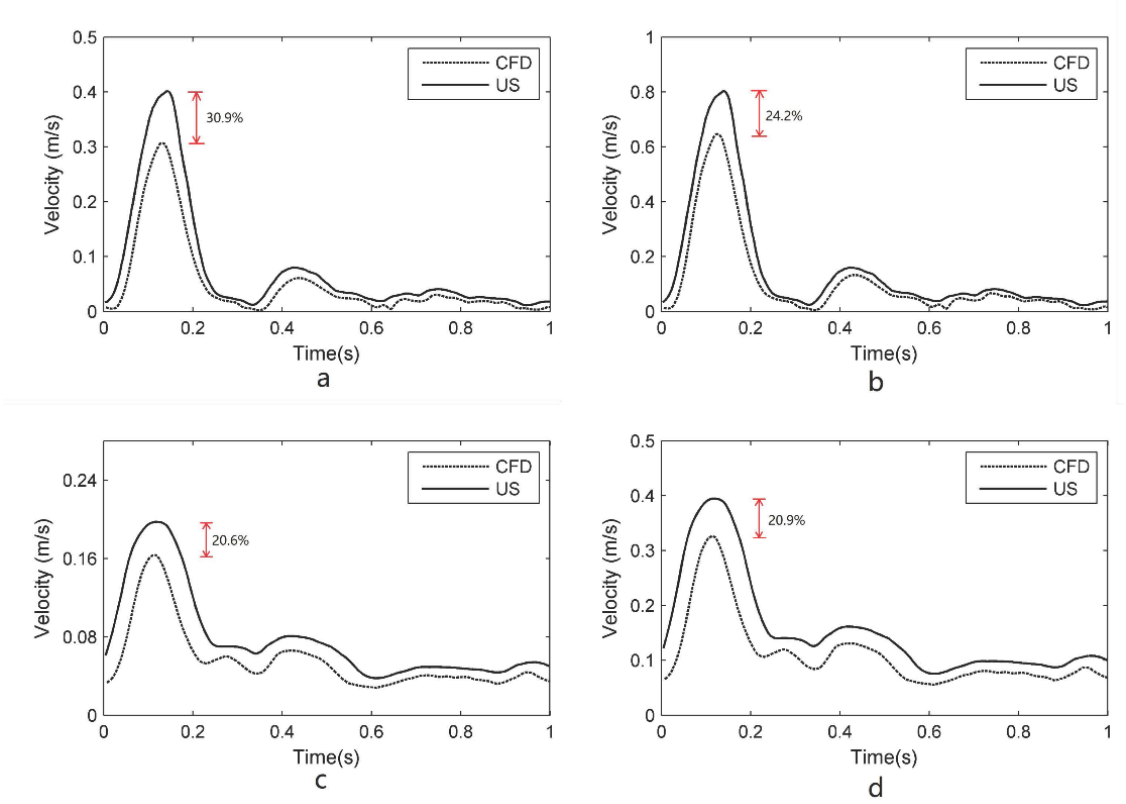

Fig. 4. 19. Maximum velocity estimated from the ultrasound simulation and the reference result from the CFD. (a) FV waveforms in beam direction in the radial artery. (b) FV waveforms in vessel axis direction in the radial artery. (c) FV waveforms in beam direction in the ulnar artery. (d) FV waveforms in vessel axis direction in the ulnar artery. FV=flow velocity, CFD=computational fluid dynamics, US=ultrasound.

Based on the reference maximum velocity waveforms in CFD, errors in the peak velocity and time-averaged velocity measured by ultrasound in the vessel direction are illustrated with different beam-vessel angles, flow rate and imaging depths (Fig. 4.20). While changing the flow rate in CFD from two thirds to twice of the MRI measured values, the error percentages in both arteries (Fig. 4.20a and Fig. 4.20b) are almost constant. However the beam-vessel angle does have an obvious effect on the maximum velocity estimation (Fig. 4.20c and Fig. 4.20d). In Figure 4.20e and Figure 4.20f, it is seen the imaging depth has no effect in the radial artery, but very large effect in the ulnar artery in estimation of the maximum velocity waveform. Statistical confidence of drawing these conclusion is demonstrated in Table 4.4 by the correlation coefficients between the ultrasound-measured parameters and the scanning factors. The corresponding p-values are also given in the Table 4.4.

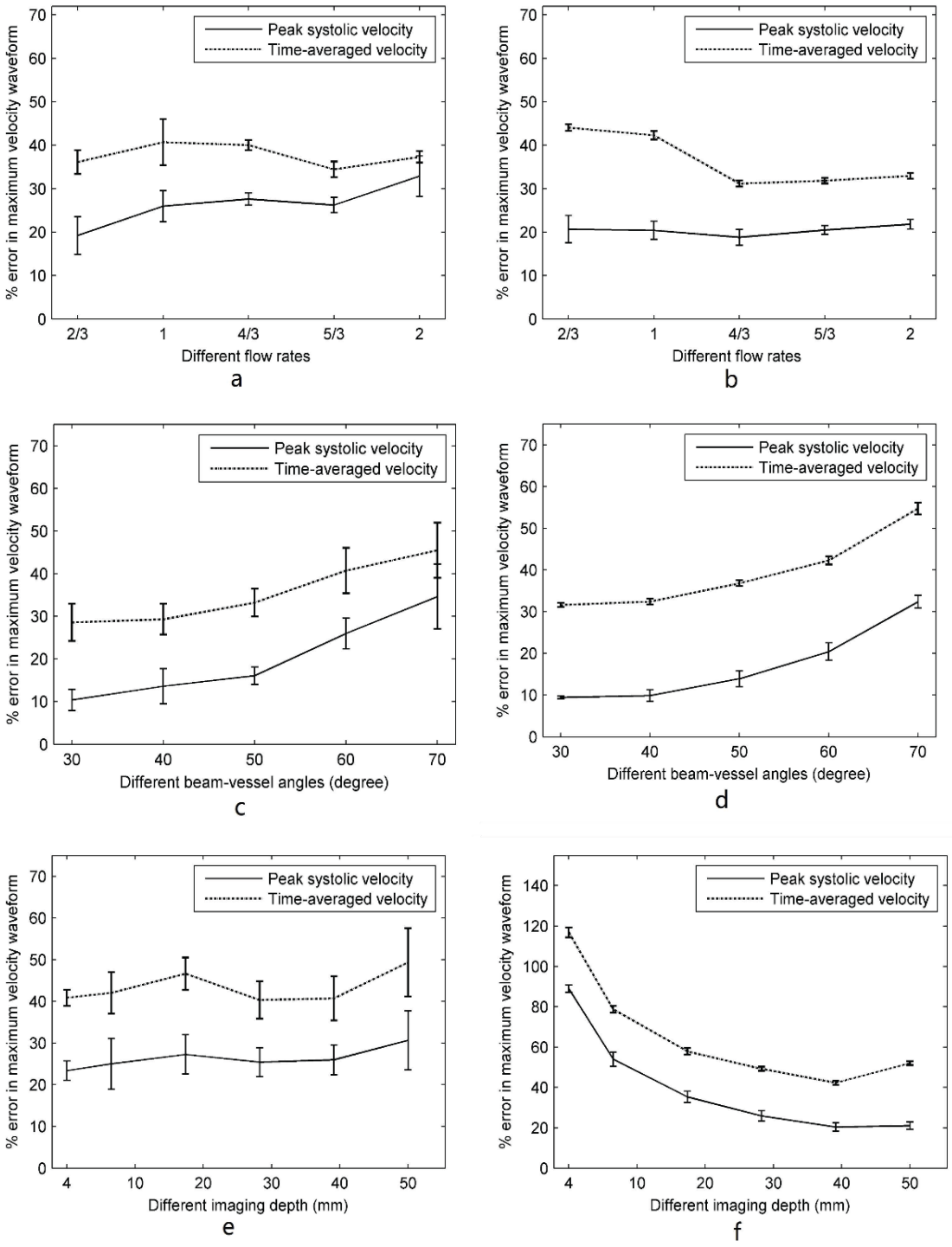

Fig. 4. 20. Percentage errors of peak systolic and time-averaged velocity with different flow rate amplitudes, beam-vessel angles and imaging depths. (a)-(c)-(e) for the radial artery and (b)-(d)-(f) for the ulnar artery.

Table 4. 4. Correlation and P-value between estimated velocity parameters and scanning factors

Artery	Scanning factor	Estimated Peak velocity	Estimated Mean velocity
Radial artery	Flow rate (Fig 4.20a)	Correlation: 0.92 P-value: 0.03	Correlation: -0.23 P-value: 0.71
	Beam-vessel angle (Fig 4.20c)	Correlation: 0.96 P-value: 0.008	Correlation: 0.97 P-value:0.007
	Vessel depth (Fig 4.20e)	Correlation: 0.31 P-value: 0.55	Correlation: 0.28 P-value: 0.59
Ulnar artery	Flow rate (Fig 4.20b)	Correlation: 0.34 P-value:0.58	Correlation: -0.84 P-value: 0.07
	Beam-vessel angle (Fig 4.20d)	Correlation: 0.93 P-value: 0.02	Correlation: 0.94 P-value: 0.019
	Vessel depth (Fig 4.20f)	Correlation: -0.88 P-value: 0.02	Correlation: -0.87 P-value: 0.02

4.3.2 Flow rate

Figure 4.21a presents flow rate waveforms derived from ultrasound-measured maximum velocity waveforms using Womersley equation. The estimated time-averaged flow rate from ultrasound is 37.9 $ml.min^{-1}$ in the radial artery and 29.2 $ml.min^{-1}$ in the ulnar artery. Since the time-averaged flow rate is 25.8 $ml.min^{-1}$ in the radial artery and 21.4 $ml.min^{-1}$ in the ulnar artery for boundary conditions in CFD, the ultrasound-estimated time-averaged flow rates were overestimated by 46.9% and 36.3% in the radial and ulnar arteries respectively. Flow rate waveforms derived from CFD maximum velocity waveforms using Womersley equation are given in Figure 4.22a. In this case, the time-averaged flow rates from Womesley equations are 26.3 $ml.min^{-1}$ for the radial artery and 20.8 $ml.min^{-1}$ for ulnar artery, indicating very small errors compared to the true value from CFD.

4.3.3 Wall shear rate

Wall shear rate was also analysed in two ways. The wall shear rate waveforms calculated from the ultrasound-measured maximum velocity waveforms and from the CFD maximum velocity waveforms were compared with that from the CFD references in the two arteries (Fig. 4.21b and Fig. 4.21c, Fig. 4.22b and Fig. 4.22c). The CFD reference wall shear rate waveforms at each meshed element (elements are shown in Figure 4.23 for the radial artery) around a circumference of the vessel wall on the axis of the sound beam were calculated. It can be seen that the wall shear rate values are not constant around the circumference. The average wall shear rate waveform was calculated around this circumference in each case to compare with Womersley-estimated wall shear rate waveform in terms of their systolic peak values and time-averaged values as shown in Table 4.4.

4.4 Discussion

Blood flow in arteries is complicated due to the characteristics of the cardiovascular system such as its geometry and pulsatile flow. In modern clinical ultrasound scanners, a dominant source of error in velocity estimation is the geometric spectral broadening which can lead to overestimation in velocity especially for maximum velocity. The error is dependent on the beam-flow angle (Hoskins 1996; Steinman et al. 2001). Within the sample volume of PW Doppler a lack of knowledge of the true beam-flow angle (the angle between the beam and moving target) could cause underestimation or overestimation of flow velocity when simply assuming the flow is parallel to the blood vessel (Hoskins 1999a; Van Canneyt et al. 2013). The bias in estimating flow velocity would cause errors in estimating the velocity related parameters, such as flow rate and wall shear rate.

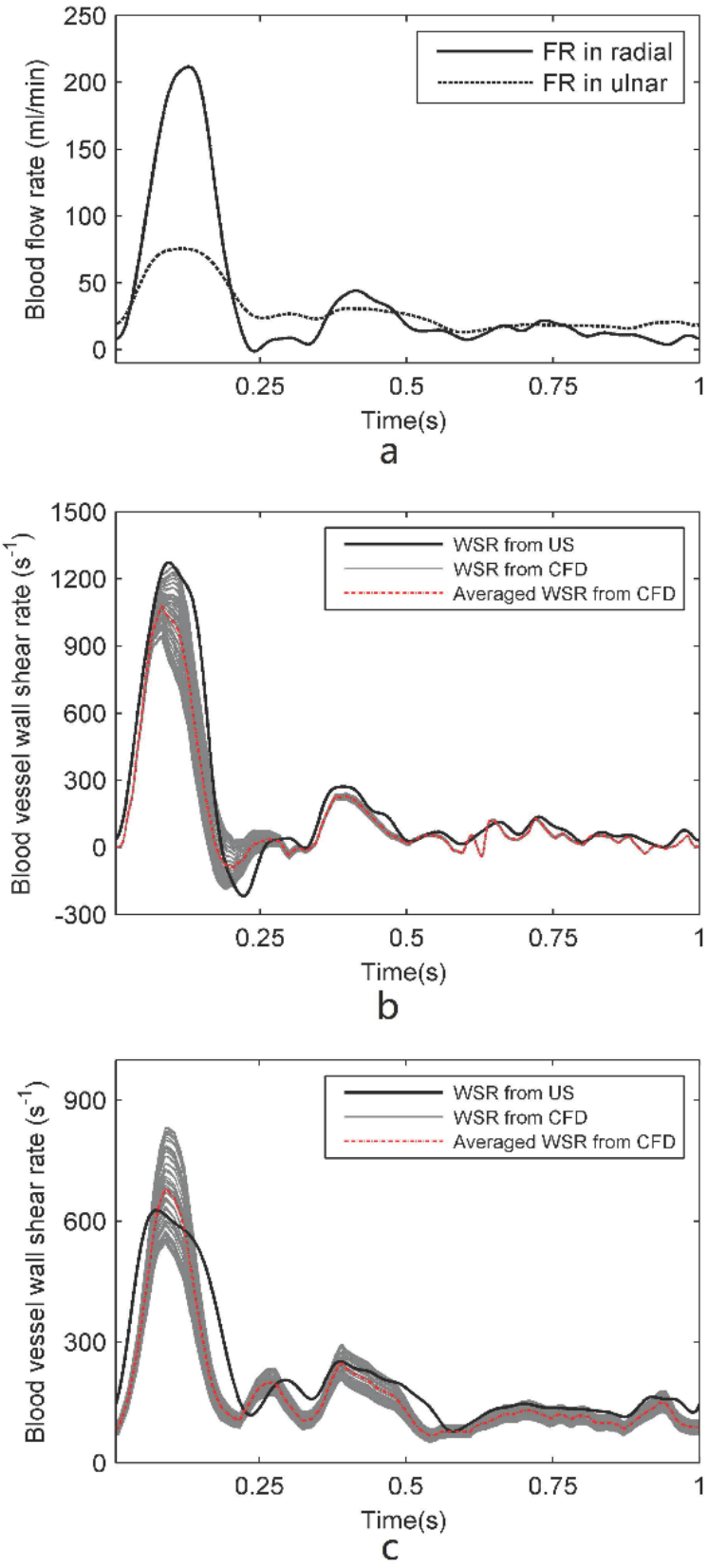

Fig. 4. 21. FR and WSR estimated from ultrasound and from the CFD. (a) FR waveforms estimated from ultrasound-measured maximum velocity waveforms; (b)-(c) the ultrasound-measured WSR waveform; the CFD reference WSR waveforms at different sites of a circumference; and the averaged WSR waveform in CFD along this circumference; (b) for the radial artery and (c) for the ulnar artery. FR=flow rate, WSR=wall shear rate, CFD=computational fluid dynamics, US=ultrasound.

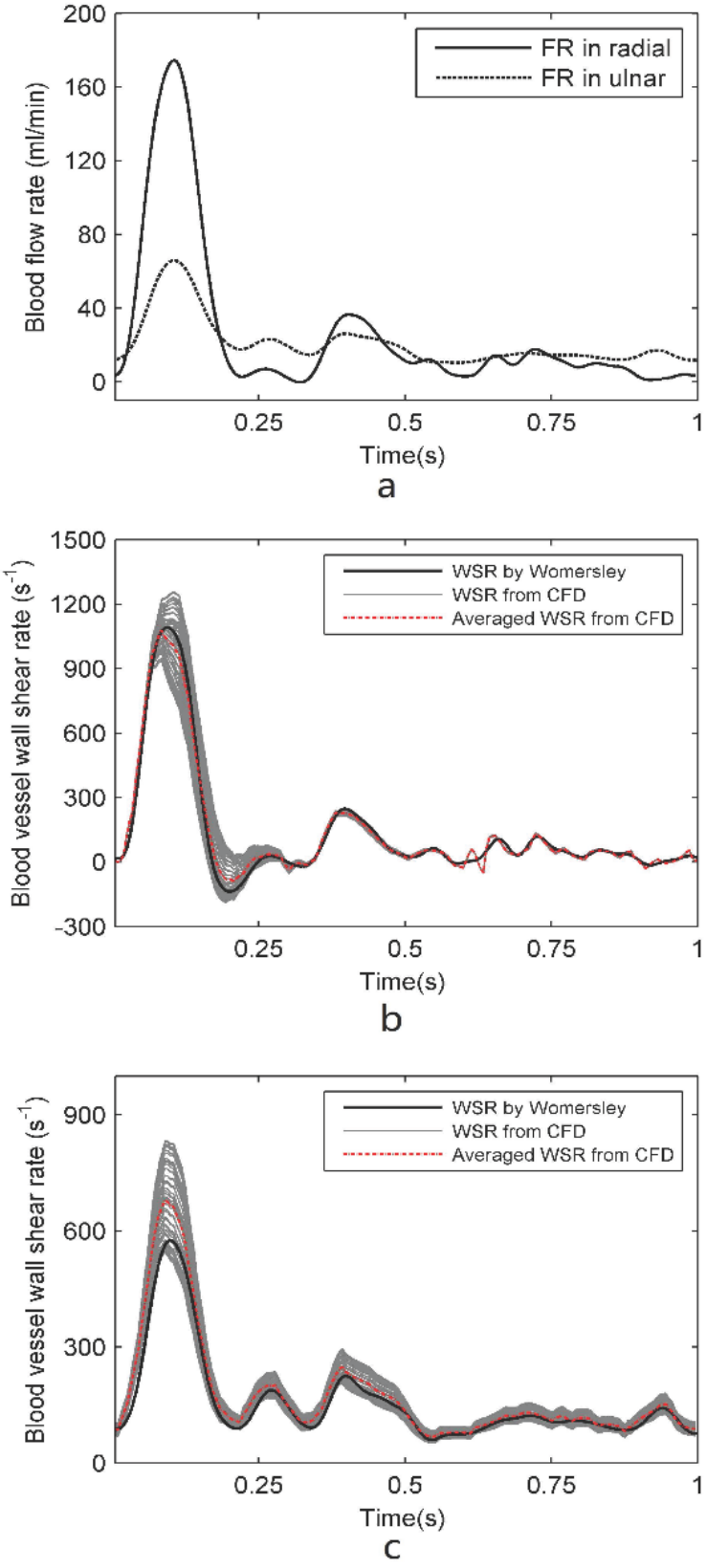

Fig. 4. 22. FR and WSR estimated from the CFD. (a) FR waveforms estimated from CFD maximum velocity waveforms. (b)-(c) the WSR waveform estimated from CFD maximum velocity waveform; the CFD reference WSR waveforms at different site of a circumference; and the averaged WSR waveform in CFD along this circumference; (b) for the radial artery and (c) for the ulnar artery. FR=flow rate, WSR=wall shear rate, CFD=computational fluid dynamics.

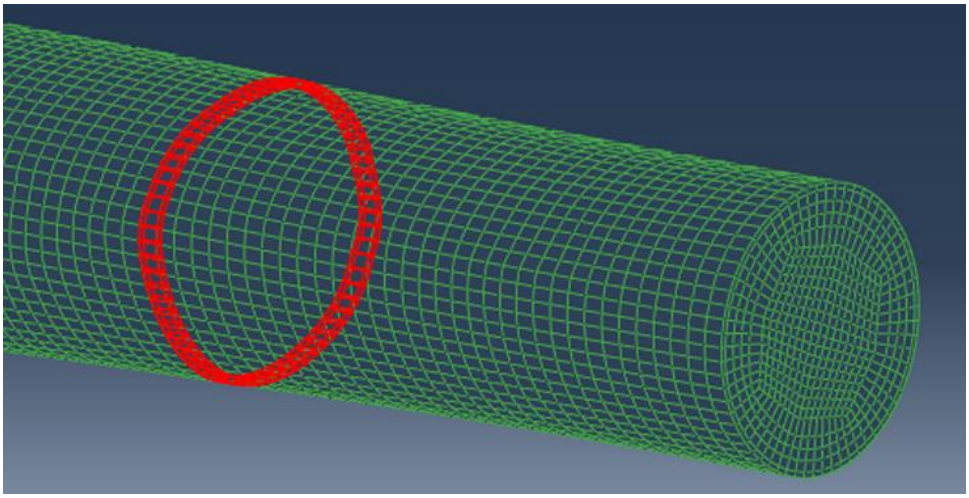

Fig. 4. 23. Elements chosen around a circumference for calculating wall shear rate.

4.4.1 Flow velocity

In Figure 4.17, the velocity contours in the transverse planes of these two arteries, where the sample volumes are located, showed that the flow conditions in the radial artery are more complicated and the velocity profile is not as symmetric as compared to that in the ulnar artery. This also showed that even a large sample volume could not guarantee the maximum velocity is included when the velocity profile is not symmetric.

Due to the asymmetric velocity profile, the overestimations in maximum velocity waveforms in the radial artery were quite different in the beam direction (30.9% for systolic and 52.64% for time-averaged) and in the blood vessel direction (24.2% for systolic and 40.38% for time-averaged) as shown in Figure 4.19a and Figure 4.19b. It should be noted that the velocity in the vessel direction from ultrasound was estimated based on the velocity in beam direction and the beam-vessel angle. The differences are caused by the inconsistency between the direction of blood flow and the direction parallel to the blood vessel. This more commonly occurs when flow is complex (Hoskins 1999a; Van Canneyt et al. 2013). The flow in the ulnar artery is more symmetric (Fig. 4.17), which keeps the overestimation differences very small between the beam direction (20.6% for systolic and 39.6% for time-averaged) and vessel direction (20.9% for systolic and 40.4% for time-averaged).

Compared to the error generated by the angle variation, the error caused by different beam-vessel angles is more severe. When changing the beam-vessel angle from 30^{o} to 70^{o}, overestimation of both the systolic peak velocity and the time-averaged velocity in the maximum velocity waveforms increased drastically from about 10% to 50% in both

arteries (Fig. 4.20c and Fig. 4.20d). Overestimation percentage errors in the time-averaged velocity were higher than that in the systolic peak velocity. This angle-dependent overestimation in maximum velocity by simulation in this study is in agreement with previous phantom and in *vivo* studies, and is believed to be caused by the geometric spectral broadening (Hoskins 1996; Tola and Yurdakul 2006; Hoskins et al. 2010b). It is noted that the critical angle in velocity overestimation caused by geometric spectral broadening is the angle between the beam and the true flow direction (Hoskins 1999a). In this study, this true beam-flow angle changes as a result of changing the beam-vessel angle.

From Figure 4.20a and 4.20b, it was found that the amplitude of flow rate in the vessel did not influence the ultrasound estimation of velocity. When the flow rate in the CFD was set from two thirds to twice the MRI measured value, the overestimation of flow velocity stays almost constant and governed by the 60^o beam-vessel angle. For the Field II simulator, it was stated that accuracy of the simulated acoustic field can only be guaranteed in the far-field region. The far-field region which is beyond about 1.3 mm in this study based on $l >> w_s^2/(4\lambda)$, where l is the distance to the field point, w_s is the largest dimension of the rectangle in element and λ is the wavelength (Jensen and Svendsen 1992). When the imaging depth in the ulnar artery was increased from 4 mm to 50 mm, the estimated systolic peak velocity and time-averaged velocity change markedly initially and then remain constant after 40 mm (Fig. 4.20f). Although the imaging depth did not affect the velocity estimation in the radial artery (Fig. 4.20e), it was set to a constant 40 mm in all the simulations in this study.

4.4.2 Flow rate

Compared to the time-averaged flow rate used in the boundary conditions for CFD simulation, there are obvious overestimations in the ultrasound-measured results. The 46.9% and 36.3% overestimation in time-averaged flow rates in the radial and ulnar arteries, calculated from the flow rate waveforms shown in Figure 4.21a, were caused by the overestimation in ultrasound-measured maximum velocity waveforms. In chapter 3, the overestimation in flow rate was assumed to be caused by the overestimation of maximum velocity waveform, for there was no true reference value of velocity available in the experimental flow phantoms. With CFD velocity field as true reference value, this assumption is confirmed by the simulation.

The time-averaged flow rate could be accurately estimated based on the maximum velocity waveform from CFD using the Womersley theory. In this case the time-averaged flow rates, calculated from the flow rate waveforms (Fig. 4.22a), are 26.3 $ml.min^{-1}$ in the radial artery and 20.8 $ml.min^{-1}$ in the ulnar artery, with very small differences compared to the CFD reference (boundary conditions for CFD simulation) where time-averaged flow rates are 25.8 $ml.min^{-1}$ and 21.4 $ml.min^{-1}$ in these two arteries respectively. Therefore, the Womersley theory is able to estimate the time-averaged flow rate in both arteries on condition that the maximum velocity waveforms are provided accurately.

4.4.3 Wall shear rate

The Womersley theory assumes that the blood vessel is an ideal tube and the flow profile is symmetric, meaning wall shear rate values would be the same around a circumference on the vessel wall. This assumption is not true in reality. The wall shear rate calculated from near-wall velocity gradient in CFD (true reference) in this study showed that wall shear rate values vary with positions around the vessel wall, especially during the systolic period of the cardiac cycle. Results in Table 4.5 show that the Womersley theory is able to estimate wall shear rate (averaged values around a circumference) in the radial artery in terms of the systolic peak and time-averaged values if the correct velocity waveform is used. Overestimations (peak: 1273 s^{-1} vs 1078.3 s^{-1}, time-averaged: 191.2 s^{-1} vs 135.6 s^{-1}) occur when the ultrasound estimated maximum velocity waveforms are used and there is only minor overestimation if maximum velocity waveform is taken from CFD.

That is not the case in the ulnar artery where the wall shear rate waveform was not overestimated as in the radial artery even though the overestimated maximum velocity waveform from ultrasound was used. The Womersley theory seems partly to compensate for the overestimate in velocity. When the maximum velocity waveform from CFD velocity field was used, both systolic peak and time-averaged wall shear rate were then underestimated by the Womersley theory.

It was shown that the performance of the Womersley theory in estimating wall shear rate is dependent on the flow condition in the arteries and it cannot be guaranteed the Womersley equation would perform better under a more symmetric flow. Actually it could be worse as it is in the ulnar artery here.

Table 4. 5. WSR (s^{-1}) calculated from ultrasound-based and CFD-based maximum velocity waveform.

	US-based estimations with WE		CFD-based estimations with WE		CFD near-wall velocity field reference values	
	Systolic peak	**Time-averaged**	**Systolic peak**	**Time-averaged**	**Systolic peak**	**Time-averaged**
Radial artery	1273.0	191.2	1103.2	132.4	1078.3	135.6
Ulnar artery	627.4	218.5	575.3	156.0	679.8	176.6

4.4.4 Limitations and advantages of simulation

This study was conducted by coupling the image-based CFD and ultrasound simulator. Limitations in these two procedures exert an influence on the estimations with this technique. For image-based CFD, the most notable limitations are the assumptions of rigid walls, Newtonian fluids, and fully developed flow boundary conditions (Steinman and Taylor 2005). Spatial resolution of MRI images, segmentation and smoothing possibly lead to loss of information in 3D vascular geometry. The limitations in CFD simulation will result in the discrepancies between simulated velocity field and the real velocity field. For example, the assumption of rigid walls in this study means the lumen domain does not change but, actually, the arterial wall moves with the pulsatile flow. Even though there are some limitations in the CFD model, the velocity field obtained by CFD in this chapter is still far more realistic than the flow simulated by experimental flow phantoms in chapter 3.

Limitations also exist in the Field II ultrasound simulator as explained by Swillens (Swillens et al. 2009b). For example, nonlinear wave propagation and multiple scatterering were not considered. The disc-shaped red blood cells were modelled as point scatterers and there was no tissue surrounding the blood vessel. Frequency dependent attenuation and focus in the elevation plane were also not added into the model in the current study. This simulation investigated the ultrasound-measured flow related parameters in the radial and ulnar arteries based on the MRI data of only one person. Further investigations are suggested on more cases. Besides, the received ultrasound signal in reality is mixed with noise components resulting from background and

electronic hardware, but the influences of noise signals have not been considered while post-processing the RF signals from the Field II ultrasound simulator in this study.

Even with those limitations, coupling CFD and Field II can still be very useful in investigating Doppler ultrasound imaging of flow characteristics in blood vessels, as it has proven in a series of studies (Swillens et al. 2009a; Swillens et al. 2009b; Swillens et al. 2010). Compared to the experimental flow phantom, simulation has the following advantages:

- Greater flexibility to change scan settings, such as flow rate, scan angle and imaging depth, than it is in the experimental flow phantoms.
- A more physiologically realistic flow condition is available from the image-based CFD.
- The parameters of interest are easily obtained from CFD results to allow comparisons between true CFD reference and ultrasound estimations. For example, the velocities from CFD flow field in all directions are available to be compared with the ultrasound-measured values.
- Velocities both in the beam direction and in the vessel direction were compared between CFD flow field and ultrasound-measured values in this chapter. However, the velocity information in the experimental flow phantoms was not available, only the time-averaged flow rate was measured through the time-collection method. In addition, the wall shear rate waveform in the CFD flow field is also available as a reference value while only the mean value can be derived in the flow phantoms.

4.5 Conclusion

With the flexible simulation platform, the flow velocity, flow rate and wall shear rate were investigated under realistic flow conditions in the radial and ulnar arteries. The errors in estimating maximum velocity waveforms using Doppler ultrasound due to different sources were confirmed by simulation for the first time. Furthermore, the performance of the Womersley theory was proved to vary under different flow conditions in these two arteries.

The results obtained from simulations in this chapter were in good agreement with the results from the flow phantoms in last chapter. It has been shown that the beam-vessel angle has an obvious effect on the Doppler velocity estimation in the radial and ulnar arteries based on the results both from flow phantoms and simulations. Other factors, such as the flow rate and imaging depth, did not affect the flow parameters estimation very much.

Since errors in those measurements can lead to misinterpretation, the simulation results should again raise the awareness of researchers and clinicians who need to use these measurements in these two arteries in clinical practice and clinical research.

Chapter 5

5. Estimation of wall motion in the radial artery using ultrasound

5.1 Introduction

As explained in chapter 2 the blood pressure waveform measured from the radial artery at the level of wrist is a useful clinical predictor for cardiovascular disease (Cohn et al. 1995; Chen 1997; O'Rourke et al. 2001; Duprez et al. 2004). Although applanation tonometry is currently used to capture the blood pressure waveform in the radial artery, it has been reported that this technology needs further improvement under some circumstances (Dueck et al. 2012; Greiwe et al. 2016), especially for obese patients. In recent years arterial wall motion in the vessel's radial direction measured by the ultrasonic echo-tracking has been used to derive the corresponding blood pressure waveform in the carotid artery (Papaioannou et al. 2009; Millasseau and Agnoletti 2015). This chapter aims to apply the ultrasonic method to measure the blood pressure waveform of the radial artery and evaluate its accuracy in various ways.

Estimating the arterial blood pressure waveform through its vessel wall motion in the radial direction is based on the high correlation between arterial cross-sectional area and pressure in a healthy artery (Hayashi et al. 1980). The underlying justification is that wall motion is actually caused by the variation in pressure. The most important thing to guarantee an accurate estimation of blood pressure waveform is to accurately measure the arterial wall motion in the first place. Motion amplitude in the radial artery (less than 100 μm in most cases) is much smaller than that in the carotid artery whose diameter changes by 500-600 μm during the cardiac cycle. This makes it harder to measure the waveform in the radial artery.

In practice, traditional clinical ultrasound B-mode scanning is not capable of detecting vessel wall motion due to limited spatial resolution (hundreds of micrometres for a 10 MHz transducer). The echo-tracking technique was therefore used to detect the wall motion waveform. This requires access to the RF data from the scanner. Two consecutive received RF signals are shifted both in time and phase domain. Capturing the shift in the time domain requires a high sampling frequency. Spatial resolution in the axial direction is only 19.25 μm for a 40 MHz sampling rate when the speed of sound is assumed to be 1540 $m.s^{-1}$. This is not sufficient to distinguish the wall motion of a few micrometres. Hence subsampling or interpolating techniques have to be applied (Moddemeijer 1991; Viola and Walker 2005; McCormick and Varghese 2013). In contrast, the shift in phase can derive the motion with displacements in the range of 1-10 μm. Therefore the phase shift is more commonly used to detect the arterial wall motion (Hoeks et al. 1990; Brands et al. 1997; Rabben et al. 2002b; Hasegawa and Kanai 2006; Bazan et al. 2014).

A commonly used auto-correlation algorithm was adopted to estimate the mean phase shift (also known as mean frequency shift) between two received RF signals. The spatial displacement of the vessel wall can then be derived. This auto-correlation technique was originally proposed to estimate the blood flow velocity with ultrasound by Kasai (1986), but was later adapted to estimate the motion in tissue in many studies (Hoeks et al. 1994; Rabben et al. 2002a; Hasegawa and Kanai 2006).

The aim of this chapter is to use the auto-correlation method to estimate the arterial wall motion in the radial artery. Tests to validate this method were done using a phantom, simulation and in *vivo*.

5.2 Methods

5.2.1 Overall

This chapter describes three studies to validate the auto-correlation method for measurement of wall motion in the radial artery:

- an experimental study using a flow phantom in which there is a comparison between wall motion measured using the auto-correlation method (with RF data from an Ultrasonix ultrasound system) and using a Phillips HDI 5000 ultrasound scanner(Bothell, USA);

- two computational methods using simulated RF data to estimate the wall motion, in which the estimated results can be compared with the pre-defined values;
- a study in volunteers to demonstrate feasibility.

5.2.2 Theory on wall motion estimation

The overall procedure to estimate the arterial wall motion is illustrated in Figure 5.1. The auto-correlation algorithm requires access to the RF data. With the RF signal $s_i(t)$, the quadrature method was used for demodulation, and the demodulated signal filtered with a low pass filter:

$$u_i(t) = LPF\left\{s_i(t)\cdot e^{-j2\pi f_{dem}t}\right\} \tag{5.1}$$

where LPF represents a low pass filter, i is the number of the ultrasound pulse sent by the transducer, $j=\sqrt{-1}$, f_{dem} represents the demodulation frequency and t is the time. Note that $u_i(t)$ is a complex signal after demodulation.

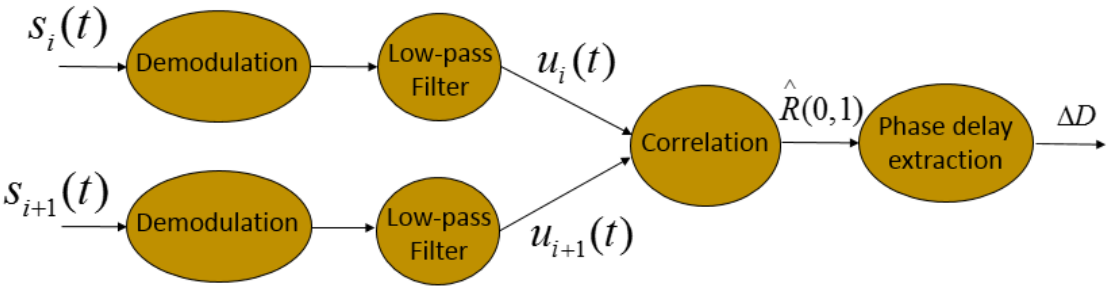

Fig. 5. 1. Schematic of the procedure to estimate the motion of the arterial wall.

According to the auto-correlation method (Kasai 1986), the phase delay between two consecutive transmitted pulses is estimated as:

$$\Delta\theta = \angle\hat{R}(0,1) = \angle\sum_{l=0}^{N-1} u_i^*(t_0+lT_s)\cdot u_{i+1}(t_0+lT_s) \tag{5.2}$$

where t_0 is the starting point of the correlation window, N the length of the correlation window, T_s the sampling period of the RF signal $s_i(t)$ and $\angle$ is the phase angle of the

complex signal. The displacement in the beam direction can be derived through the phase angle shift.

$$\Delta D = \frac{\Delta\theta}{2\pi f_{dem}} \cdot \frac{c}{2} \tag{5.3}$$

where ΔD is the spatially averaged displacement of tissue in the correlation window starting at the t_0 . The overall motion of the tissue during the cardiac cycle could then be obtained through the cumulative sum of these displacements over time.

In eqn. 5.3, it is the central frequency of the RF signal that should be used, rather than the demodulation frequency f_{dem} , especially for wide bandwidth signals (short pulses) where the RF centre frequency is shifted by attenuation. Therefore, in the modified auto-correlation method, the central frequency of the RF signals is estimated by:

$$f_c = f_{dem} + \frac{\angle \hat{R}(1,0)}{2\pi \cdot \triangle T} \tag{5.4}$$

where f_c represents the central frequency, $\angle \hat{R}(1,0)$ is the phase angle of the autocorrelation of the demodulated RF signal with one lag in beam direction (Loupas 1995; Rabben et al. 2002a). Replacing the f_{dem} in eqn. 5.1 and eqn. 5.3 with the f_c can improve the accuracy in estimation of the tissue motion. Rabben et al. (2002a) has shown the resolution of this method can be a few micrometres. This was also demonstrated by (Hasegawa and Kanai 2008).

In addition to the variation of the diameter caused by pulsatile blood flow, the baseline diameter also needs to be estimated. The baseline diameter was calculated from the RF signal at the frames corresponding to the minima of the wall motion waveform. The averaged baseline diameter was obtained from 3 cycles. The baseline diameter D_b was extracted from the RF signal by identifying the anterior and posterior vessel walls as it was done by Hoeks et al. (1990). The diameter waveform $DiaW(t)$ can be obtained from:

$$DiaW(t) = D_b + \Delta D_a(t) + \Delta D_p(t) \tag{5.5}$$

where ΔD_a represents the wall motion of the anterior wall and ΔD_p represents the wall motion of posterior wall. Both ΔD_a and ΔD_p were derived by eqn. 5.3.

5.2.3 Flow phantom

Although the modified auto-correlation method has already shown high precision Rabben et al. (2002a) and Hasegawa and Kanai (2008), evaluation of its performance is still important because it has never been applied to the radial artery whose wall motion amplitude is small compared to that in larger arteries. A flow phantom was used to evaluate the accuracy of this method.

Experimental setup

The flow phantom fabricated in chapter 3, which used mimicking materials with acoustic and mechanical properties equivalent to the blood vessel, blood and surrounding tissue, was used. This flow phantom can generate pulsatile motion in the PVA-c vessel wall by connecting it to a pump (Fig. 5.2). Since pure PVA-c does not contain ultrasound scatterers, 0.75% (by weight) of 400-grit silicon carbide particles were added during the manufacture of the PVA-c vessel mimic.

The diameter of the vessel was 2.60 mm. Flow rate was adjustable to create wall motion with physiological amplitudes (tens to a few hundred micrometres). The waveform of the signal to drive the pump (Fig. 5.2) was chosen by averaging centreline maximum velocity waveforms measured by PW ultrasound from 10 volunteers' radial arteries.

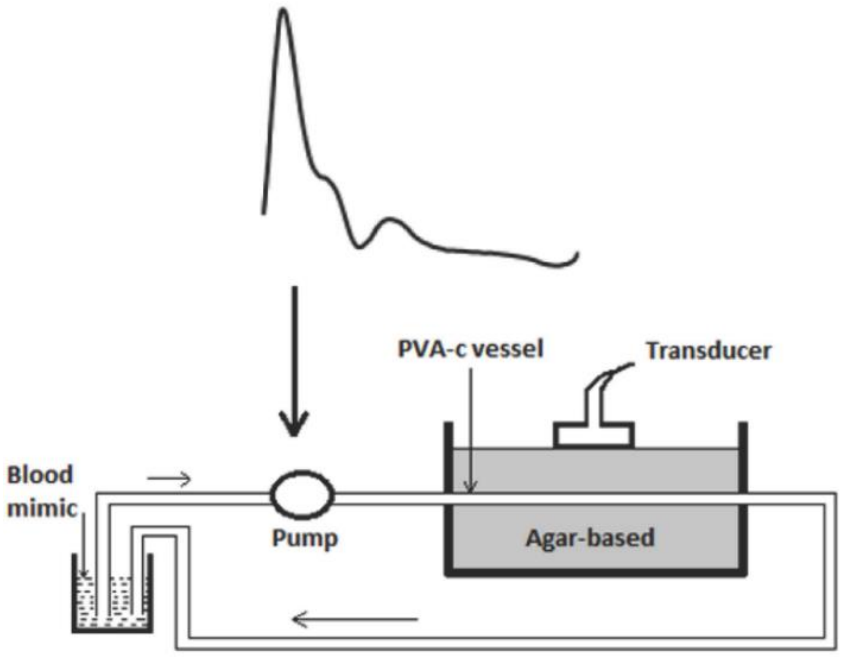

Fig. 5 2. The flow phantom to generate pulsatile vessel wall motion.

Data acquisition

Flow rates were set to three different levels to generate wall motion with different amplitudes. Under each flow rate, the HDI 5000 ultrasound scanner was used to measure the vessel wall motion, followed by the Ultrasonix Tablet at the same site. Reference marks on the flow phantom container and at the middle position of both transducers were used to help reposition the probes to ensure that scanning took place at the same location in the longitudinal orientation as shown in Figure 5.3.

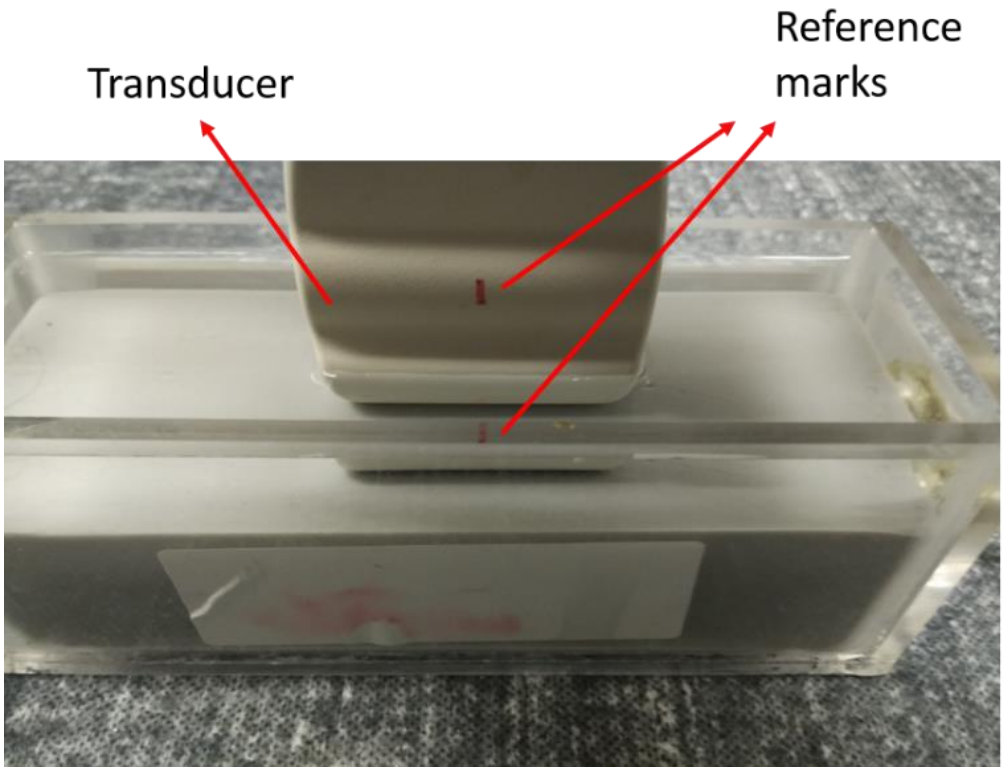

Fig. 5 3. Locating the transducer through two reference marks.

The Phillips HDI 5000 ultrasound scanner, which has a built-in functionality for measuring diameter distension under its research licence, was used here as the reference to evaluate the proposed auto-correlation method. This built-in functionality, which is specifically designed for analysing the carotid artery distension, is based on the technique called Tissue Doppler Imaging (TDI). The details of this TDI technique were reported by Bonnefous et al. (2000). An L12-5 transducer that supports the TDI image acquisition was used to do the scanning on the flow phantom. This TDI imaging mode works together with the colour Doppler mode which must be turned on before using the TDI imaging mode. The parameters used listed in Table 5.1.

Table 5. 1. The parameters in the HDI 5000 for TDI imaging acquisition.

Parameters	Values	Parameters	Values
2D Optimise parameter	Pen	Colour mode	On
TDI imaging	On	Tissue Opt	GEN
Colour mode Line density	A	Sensitivity	Medium
Smoothing	OFF	DMD	OFF
Persistence	OFF	Colour mode Gain	Saturated (>85%)

During the data acquisition by HDI 5000 scanner, the TDI region of interest (ROI) was placed perpendicular to the main axis of the image. The velocity scale was set to maintain a frame rate higher than 30 Hz to capture the motion of the vessel wall. The velocity scale was set to avoid aliasing. It was necessary to resize the ROI box to achieve the desired frame rate and velocity scale setting. The transducer was positioned to make sure the imaging plane transverses the central plane of the vessel in the longitudinal orientation. The 2D gain was adjusted to allow the vessel walls to be clearly defined in the image, as shown in Figure 5.4. A cine loop of 3-5 cardiac cycles was stored in the scan buffer and transferred to a PC for post processing.

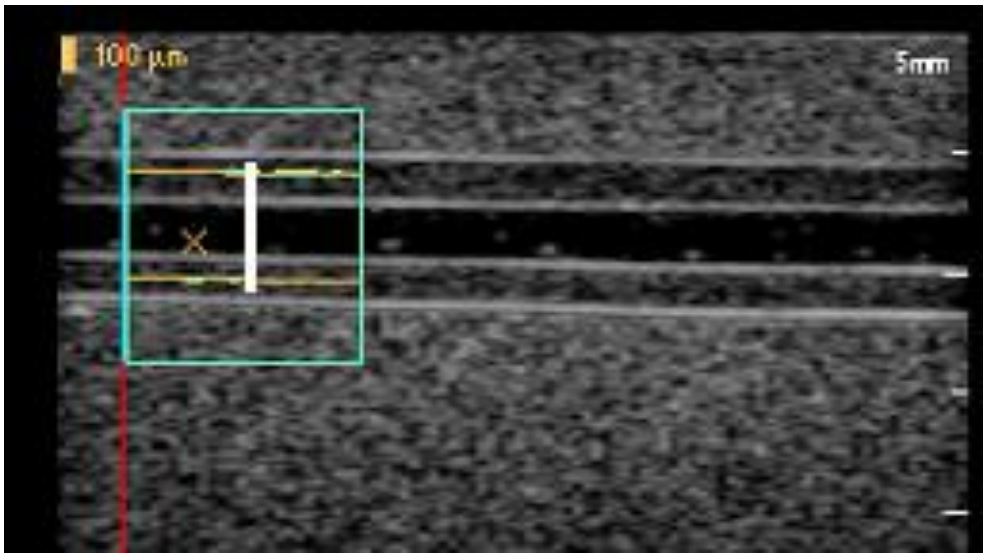

Fig. 5 4. The TDI imaging acquisition with the HDI 5000 scanner.

With the Ultrasonix Tablet, RF data was acquired using the transducer L14-5/38, imaging the flow phantom in B-mode. The transducer was placed onto the flow phantom to scan the same area as for the HDI 5000 and the best view of the blood vessel in the longitudinal orientation was obtained. The acquired image and the scan parameters are shown in Figure 5.5. The scan element group was reduced to 50% to give a higher frame rate (130Hz). 3-5 cycles of RF data were stored in the cine loop and transferred to a PC for post processing.

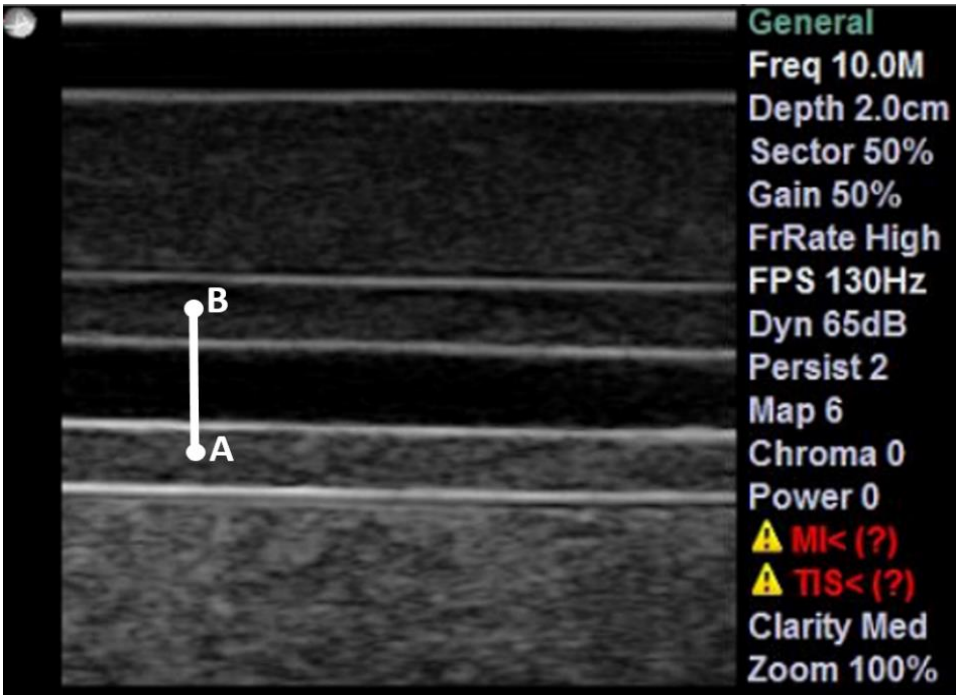

Fig. 5 5. B-mode scanning by Ultrasonix to record RF data.

Data processing

The Phillips arterial wall motion (AWM) software, which comes with the research functionalities of the HDI 5000, was installed on a computer to extract the wall motions from the stored TDI data. In AWM, the TDI technique recognised the vessel walls in the places indicated by the yellow lines within the ROI box (Fig. 5.4) as the arterial wall baseline reference points for TDI evaluation. It is the diameter dilation waveforms along these yellow lines that were extracted. The number of waveforms along the yellow lines depended on the line density and the width of the ROI box. The diameter waveform from the site (the white line in the middle of the ROI box indicated in Fig. 5.4), offset 10 mm to left of the middle reference mark, was extracted from the AWM software into a

spreadsheet file. This was compared with the waveform estimated by the RF data from the Ultrasonix Tablet.

For the Ultrasonix Tablet, it was the RF data from the B-mode scanning that was used to estimate the wall motions. The number of scan lines forming one 2D image depended on the transducer setting. Only 50% of the element group was used to ensure a higher frame rate. The RF data from the scanning line (indicated by the white line in Fig. 5.5), 10 mm to the left of the reference mark, was chosen to compare the results from the HDI 5000.

The auto-correlation method requires a segment of samples from each RF signal to estimate the phase delay between two consecutive frames. Two segments of data, each with a length of 40 sample points, starting from A and B marked in the middle place of posterior wall and anterior wall respectively (Fig. 5.5), were used for calculating the motion waveform. The sampling rate for the digital RF data was 40 MHz in the Ultraosnix Tablet. The 40 samples therefore represent 1 μs time period or a 0.75 mm spatial segment when the speed of sound is assumed to be 1540 $m.s^{-1}$. The reason that the interfaces between the lumen and blood vessel were not used for estimating the wall motions was to ensure consistency with measurements made by the HDI 5000 where the vessel walls were recognised roughly in the middle of the walls. The motion of the anterior and posterior wall were both estimated, and their absolute magnitudes were added to produce the diameter distension waveform.

5.2.4 Simulation

The proposed wall motion detection method was also validated by simulation. Two types of simulation were adopted according to the ways of generating the RF data, one is the simple analytical model, and the other is Field II ultrasound simulation.

A simple model method

A simple model proposed by Hasegawa and Kanai (2006) for validating a vessel motion detection algorithm was used to evaluate the performance of the auto-correlation method. The simulated ultrasound RF signal $rf_i(n)$ from an interface or a point scatterer of the i^{th} frame at a time $t = nT_s$ (n=1, 2, 3, ... ; T_s is the sampling interval) was defined by a sinusoidal wave and an overall envelope. The central angular frequency of the

sinusoidal wave ($\omega_m = 2\pi f_m$) is the same as the transmitted wave, and the envelope $env_i(n)$ is given in eqn. 5.6.

$$rf_i(n) = env_i(n) \cdot \sin\left\{\omega_m (nT_s - \tau_i\right\} = env_i(n) \frac{e^{j\omega_m (nT_s - \tau_i)} - e^{-j\omega_m (nT_s - \tau_i)}}{2j}$$

$$env_i(n) = \begin{cases} 0.5\left\{1 - \dfrac{e^{j2\pi \frac{nT_s - \tau_i}{\Delta T_p}} + e^{-j2\pi \frac{nT_s - \tau_i}{\Delta T_p}}}{2}\right\} & \left(\tau_i \le nT_s \le \tau_i + \Delta T_p\right), \\ 0 & else \end{cases} \tag{5.6}$$

where ΔT_p represents the pulse length, and τ_i represents the time delay at the ith frame from the origin of the signal as shown in Figure 5.6.

The number of points in the simulated RF signals was 40, with a sampling rate (f_s) of 40 MHz ($T_s = 1/f_s$) and central frequency of 10 MHz. The time delay between the ith frame and the (i+1)th frame $\Delta\tau_i$ was set to a series of values, ranging from 1 to 65 ns to test the capabilities of the proposed method under different motion amplitudes. In addition, a uniformly distributed random noise in the range from -0.2 to 0.2 (normalised according to the RF signal) was added into the generated RF signal to test the robustness of this vessel motion detection method. The eqn. 5.3 was used to estimate the motion-caused time delay of the RF signals between two consecutive frames.

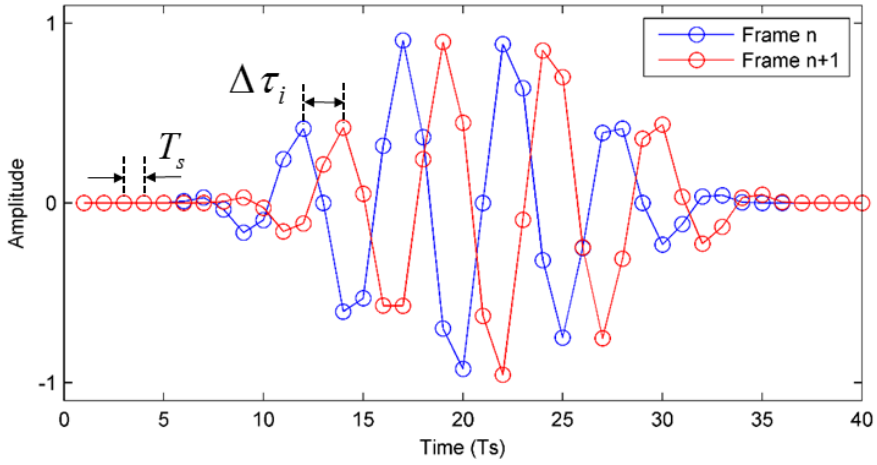

Fig. 5 6. Two consecutive frames of simulated RF signal from the analytical model.

RF data from Field II simulator

It has been shown in last chapter that the linear ultrasound simulator Field II can be used to simulate the RF data by representing the scanned objects in a form of point scatterers. Those point scatterers contain the position and scattering amplitude information which determine the simulated RF data from the Field II simulator in the similar way as the real ultrasound scanning takes place. In this section, a synthetic tube-like vessel phantom was created to evaluate the proposed wall motion method.

The settings of the transducer in Field II are given in Table 5.2. A linear array transducer focused in elevation was used to provide an improved resolution near the vessel wall. To be consistent with previous experiments, the central frequency of transmitted pulse was set to 10 MHz. The foci in the elevation and axial directions were both set to 50 mm (where the vessel central axis was located). Receive focusing was adopted to improve spatial resolution.

Table 5. 2. Linear array transducer settings in Field II.

Parameters	**Values**
Pulse central frequency (f0)	10 MHz
Excitation pulse (P)	Sinusoid
Pulse cycles (n)	2
Sound velocity (c)	1540 m/s
RF data sampling frequency (fs)	100 MHz
Element width (w)	Half a wavelength
Element height (h)	5 mm
Gap between elements (Kerf)	0.05 mm
Number of elements (N)	192
Active elements	64
Pulse repetition frequency (PRF)	130 Hz
Transmit focus (F)	50 mm
Dynamic receiving	On

The simulated synthetic vessel phantom was 20 mm in length, with a diameter of 2.5 mm and wall thickness of 1 mm. The diagram of this tube and its simulated B-mode image from the Field II are shown in Figure 5.7. The limited spatial resolution in the elevation plane in the Field II simulation led to a failure to clearly virtualise the hollow lumen area. Neither soft tissue outside the vessel and flowing blood within were simulated. The vessel wall dilated in the radial direction through changing the positions of all scatterers within the vessel wall. This was accomplished in the polar coordinate system where the distances between the individual scatterers and the central axis were adjusted all together by adding the motion components to their baseline (initial) position. The temporal motion component, described by eqn. 5.7, for all those point scatterers is given in Figure 5.8.

$$W_{motion} = A_{motion} \sin(2\pi f_{motion} t) \tag{5.7}$$

In the eqn. 5.7, A_m is the amplitude of the motion waveform, f_{motion} represents the frequency and t is the time. Only the first half of one complete sinusoidal wave with 130 samples was used as the motion waveform when the frequency f_{motion} was set to 0.5 Hz. The 130 samples within a one-second period are in accord with the ultrasound scan frame rate set in the Field II transducer (Table 5.2). The amplitude A_{motion} of the motion waveform was varied from 10 to 2000 um, in order to evaluate the vessel wall motion detection method over the full range of motions which might be expected physiologically. The motion estimated from the Field II RF signals can then be compared with the pre-set motion in the synthetic vessel phantom.

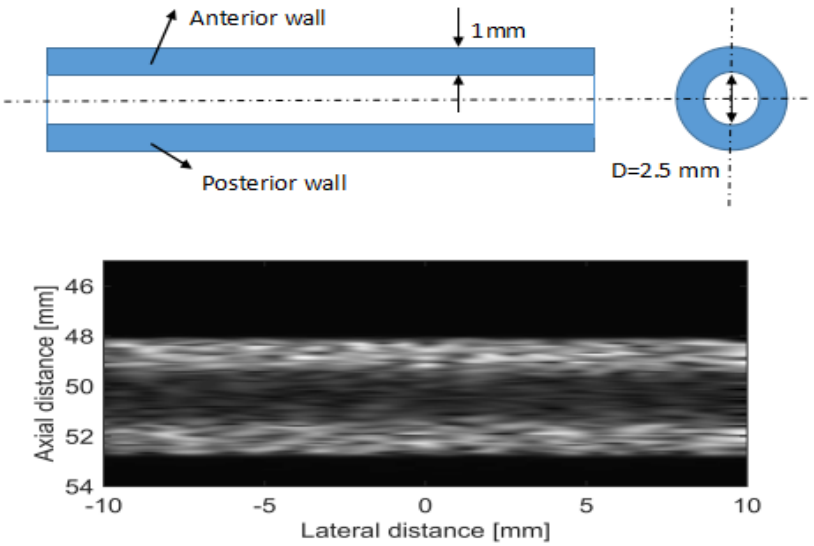

Fig. 5 7. The diagram of the vessel phantom and its simulated B-mode image.

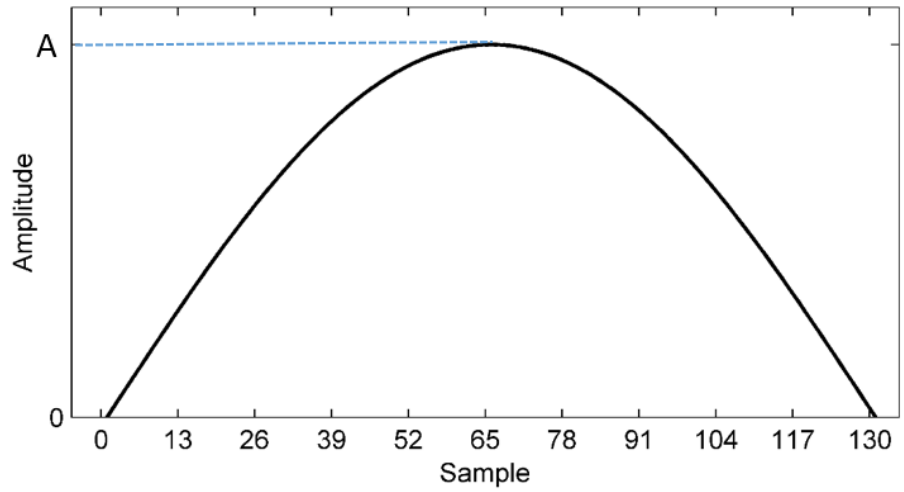

Fig. 5 8. The vessel wall motion waveform for the synthetic phantom in the Field II.

5.2.5 Initial experience in volunteers

The auto-correlation method was established to estimate the arterial wall motion in the radial artery. In addition to the above experiments conducted to validate this method, it is important to apply this method *in vivo*. 14 healthy volunteers were recruited to test this wall motion detection method.

The protocol for acquiring data from volunteers was reviewed and approved by the Research Ethics Committee of Dundee University. All volunteers who participated gave their written informed consent before the experiment.

Data acquisition

As for the flow phantom, the same ultrasound scanner Ultrasonix Tablet with the transducer L14-5/38 was set up to collect the data. The volunteers were asked to sit down for five minutes to calm down and rest their left arm comfortably on a desk. The ultrasound transducer was fixed by a flexible clamp which enabled easy adjustment of the transducer orientation and secured fixation. The scanning setup is shown in Figure 5.9.

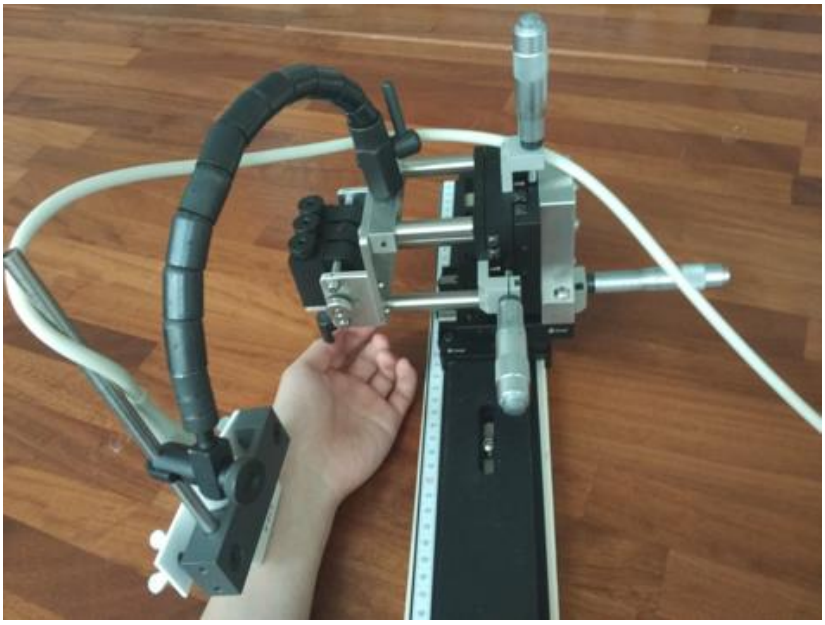

Fig. 5 9. The setup for scanning volunteers' radial artery.

During the scanning, the volunteer was asked to keep their arm as still as possible. Firstly the colour Doppler mode was turned on to help locate the radial artery by achieving the strongest colour signal within the blood vessel (Fig. 5.10). The clamp platform was used to tune the position of the transducer by adjusting three stages in x, y and z directions. Once the best orientation was obtained, the colour mode was turned off. The ultrasound settings for the scanning were similar to that in experiments on flow phantoms. The transmit focus was set near the middle of the lumen, allowing good resolution at both anterior and posterior walls. 3-5 seconds of RF data from the B-mode were stored in the cine loop and transferred to a PC for post processing. The scanning of each volunteer was repeated three times.

Data processing

The processing of RF data from the Ultrasonix Tablet for estimating the wall motion in volunteers' radial artery was similar to that for the flow phantom in section 5.2.3. The motion of two interfaces (anterior and posterior) between the vessel walls and the lumen were detected, rather than the motion from the middle of the vessel wall as in the flow phantom. 40 samples from each arterial wall (marked by the white dot A and B in Fig. 5.10) were fed into the equations explained in the 5.2.2 to estimate the motion from both wall-lumen interfaces. The absolute motion of both walls, coming from the same scan line, were added to produce the diameter waveform.

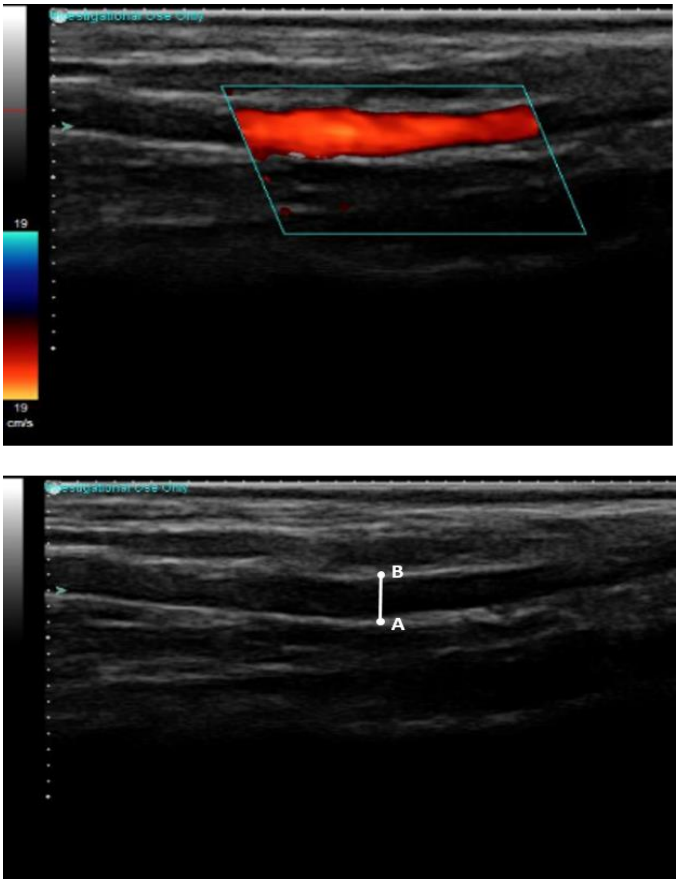

Fig. 5 10. Locating the radial artery under Colour Doppler and grey scale.

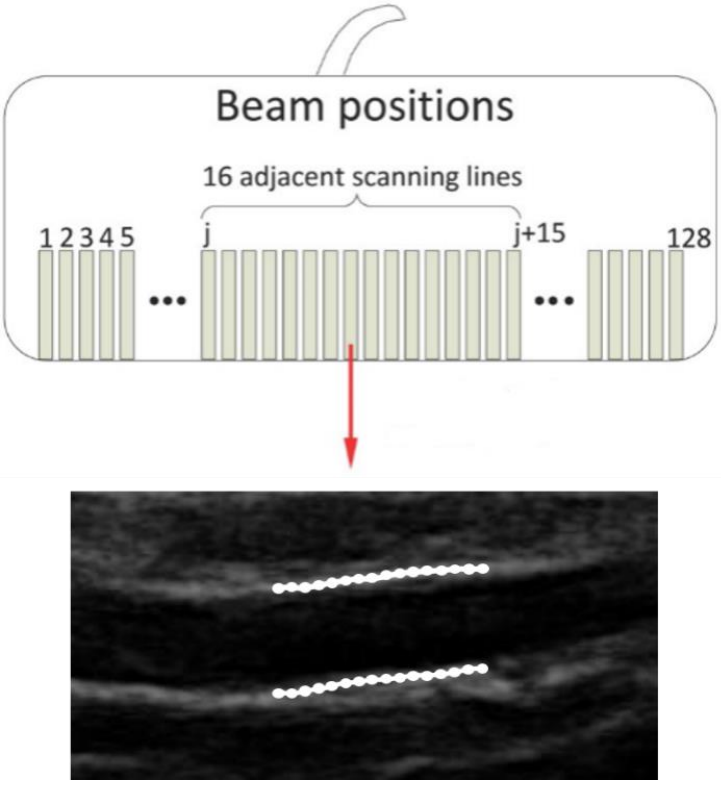

Fig. 5 11. Estimation of the radial artery's diameter waveform from 16 consecutive scan lines.

Since the situation in *vivo* is much more complicated than in the phantom or in simulation, an averaging method was adopted. The wall motion along a segment of about 4.75 mm from 16 consecutive scan lines were estimated (Fig. 5.11). Diameter waveforms estimated from those 16 consecutive scan lines were averaged. The baseline (minimum) diameter was determined by averaging the diameters from these 16 scanning lines as well.

5.2.6 A trial estimating blood pressure waveform

Although the scope of this chapter is to measure the radial artery wall motion, it is noted that the purpose of estimating this to derive the corresponding blood pressure waveform. It is the pressure waveform that is of clinical value. It has been reported that there is a high correlation between the variation in arterial cross-section area and the blood pressure for healthy arteries (Hayashi et al. 1980; Millasseau and Agnoletti 2015). Initially, experience of estimation of pressure from wall motion in the radial artery was gained on a single volunteer. Applanation tonometry, which is the gold standard for non-invasively measuring the blood pressure waveform in the radial artery, was used to compare against the pressure waveform derived from the ultrasound-measured diameter waveform.

Theory

Using the arterial diameter waveform obtained from ultrasound, the arterial cross-section as function of time $A(t)$, can be calculated by assuming the artery is rotationally symmetrical,

$$A(t) = \frac{\pi \cdot D^2(t)}{4} \tag{5.8}$$

where $D(t)$ is the arterial diameter waveform. An exponential relationship between the blood pressure waveform and cross-section waveform is given by

$$p(t) = p_d \cdot e^{\beta(\frac{A(t)}{A_d}-1)} \tag{5.9}$$

$$\beta = \frac{A_d \cdot \ln(\frac{p_s}{p_d})}{A_s - A_d} \tag{5.10}$$

where p_d is the end diastolic blood pressure, p_s the systolic blood pressure, A_d the end diastolic arterial cross-section, A_s the systolic arterial cross-section and β the wall

rigidity coefficient. In order to give the pressure waveform $p(t)$ in eqn. 5.9, the coefficient β has to be estimated via the eqn. 5.10 where the p_s and p_d are unknowns.

β can be estimated through iteration based on the assumption that the diastolic and mean blood pressures do not change significantly throughout the arterial tree (Meinders and Hoeks 2004; Nichols 2005). The systolic and diastolic blood pressures measured by a automatic pressure recorder from the brachial artery can be used in eqn. 5.10 to get an initial value of coefficient β. With this coefficient β, the blood pressure $p(t)$ in eqn. 5.9 can be obtained. If the mean pressure calculated from $p(t)$ is significantly different from the mean pressure obtained in the brachial artery, the coefficient β is changed by

$$\beta_{new} = \frac{p_{m,Brachial}}{p_{m,radial}} \beta_{old} \tag{5.11}$$

where β_{old} is the previously estimated coefficient; β_{new} is the updated coefficient for next iteration; $p_{m,Brachial}$ is the mean blood pressure from the brachial artery and $p_{m,Radial}$ the previously estimated mean radial artery blood pressure from the eqn. 5.9. The iteration stopped if the absolute difference between $p_{m,Brachial}$ and $p_{m,Radial}$ was less than 0.01 mmHg.

This iteration method was used by Meinders and Hoeks (2004) to derive the blood pressure waveform from the carotid artery, and validated on a large number of human subjects by Zimlichman (2005) and Vermeersch et al. (2008). As it was proved that those wall rigidity-related coefficients β are pressure-independent over a large pressure range (Van Loon 1977; Hayashi et al. 1980), this is a justification for using the iteration method for the radial artery data of the current study.

Data acquisition

Measurements were performed in a room where temperature was around 25^{o}C and the volunteer was asked to take a rest for five minutes. The blood pressure at the brachial artery was measured and recorded with an automated, calibrated blood pressure monitor (SureTemp,Welch Allyn, UK) three times with a five-minute gap between each, from which the systolic and diastolic blood pressure in the brachial artery were obtained. Mean blood pressure was calculated from the systolic and diastolic pressure values

($Mean = (Systole + 2 \cdot Diastole)/3$). These pressure values from the brachial artery were used to calibrate the pressure values in the radial artery for both methods.

Before collecting data with the ultrasound scanner, the volunteer took a further five-minute rest. The Ultrasonix Tablet with transducer L14-5/38 was positioned longitudinally above the volunteer's radial artery at the position where the pulse could be felt by finger tips. This scanning procedure was similar to that described in section 5.2.5 as shown in Figure 5.9. The transducer was oriented to have the best view of the radial artery walls, as it was done in the section 5.2.5 where the Colour Doppler was used to help locate the radial artery. Three to five cardiac cycles of data were saved in the cine loop of the scanner for post processing.

The SphygmoCor tonometry (SphygmoCor XCEL PWA, AtCor Medical Pty Ltd, USA), as used in section 4.2.2, was used to measure the blood pressure waveform from the wrist (over the radial artery) again where the pulse could be sensed by fingertips.

Data processing

The SphygmoCor tonometry is able to provide the calibrated blood pressure waveform when the systolic and diastolic blood pressures from the brachial artery are input into the associated data processing software.

The ultrasound data was firstly processed using the methods described in section 5.2.5 to estimate the arterial diameter waveform. The radial artery diameter waveform was obtained by temporally averaging a 3-4 cycles into one single cycle and spatially averaging 16 waveforms from 16 consecutive scan lines along a segment of 4.75 mm (as illustrated in Fig. 5.11). This refined diameter waveforms was used to derive the blood pressure waveform. It should be noted that pressure values from the brachial artery were required to use the iteration method (eqn. 5.11). The blood pressure waveforms from the two methods were then compared.

5.3 Results

5.3.1 Validation on a flow phantom

The vessel diameter variations caused by the pulsatile flow in the phantom are shown in Figure 5.12, 5.13 and 5.14. The motion estimated from the HDI 5000 scanner and by the auto-correlation method were compared at three different amplitudes. It is seen that

the amplitudes estimated from the auto-correlation method are larger than they are from the TDI. The peak value from auto-correlation is 40.6% higher than that from the HDI 5000 in Figure 5.12. This discrepancy goes down to around 15% in Figure 5.13. In Figure 5.14 it shows the motion waveforms measured from two methods are quite different.

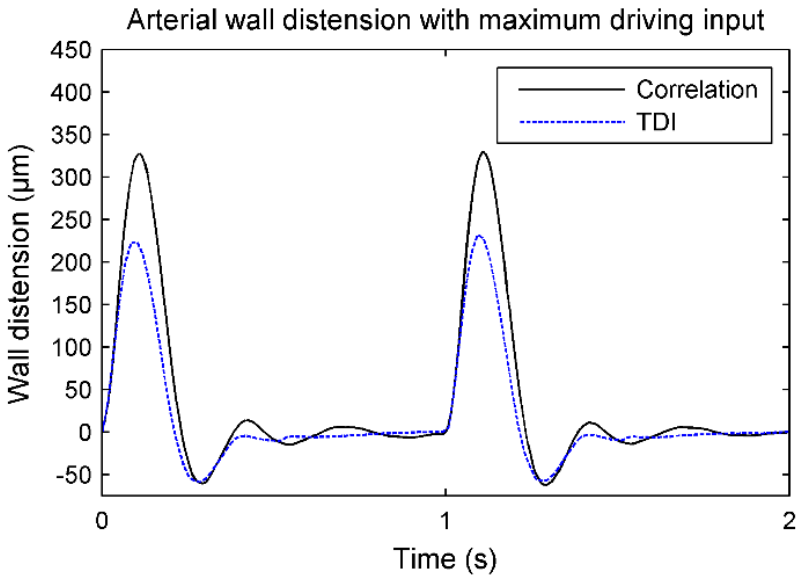

Fig. 5 12. Flow phantom vessel diameter variation estimated from both methods under maximum flow rate.

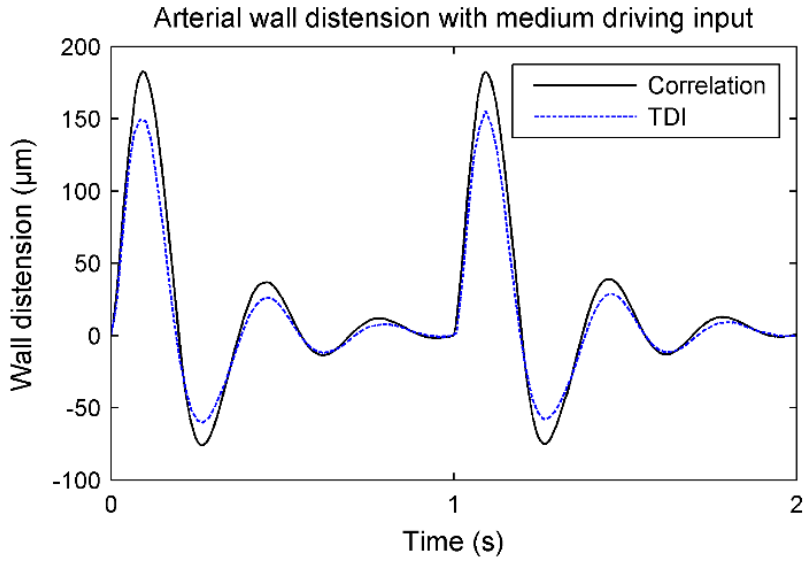

Fig. 5 13. Flow phantom vessel diameter variation estimated from both methods under medium flow rate.

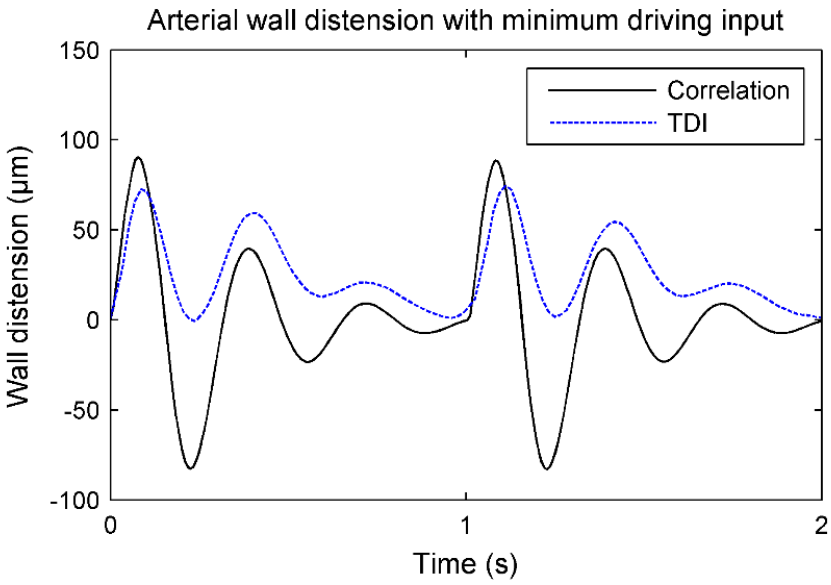

Fig. 5 14. Flow phantom vessel diameter variation estimated from both methods under minimum flow rate.

5.3.2 Validation by simulation

The estimated time delays between analytically-simulated RF signals from two consecutive frames are listed in Table 5.3, compared with the pre-defined time delays in each case. The results include the situation with and without added noise. The proposed method proved robust to noise. However, it failed to estimate correctly the time delay over 55 ns. The reason is explained in the discussion.

Table 5. 3. Data from simulations: comparison between the defined time delay values and the estimated values with and without the added noise.

Pre-defined values (ns)	**Estimated values** (ns)	**Estimated values with noise** (ns)
1	0.999	0.952
15	15	14.359
25	25	25.171
35	35	35.674
45	45	45.791
55	-45	-45.318
65	-35	-35.119

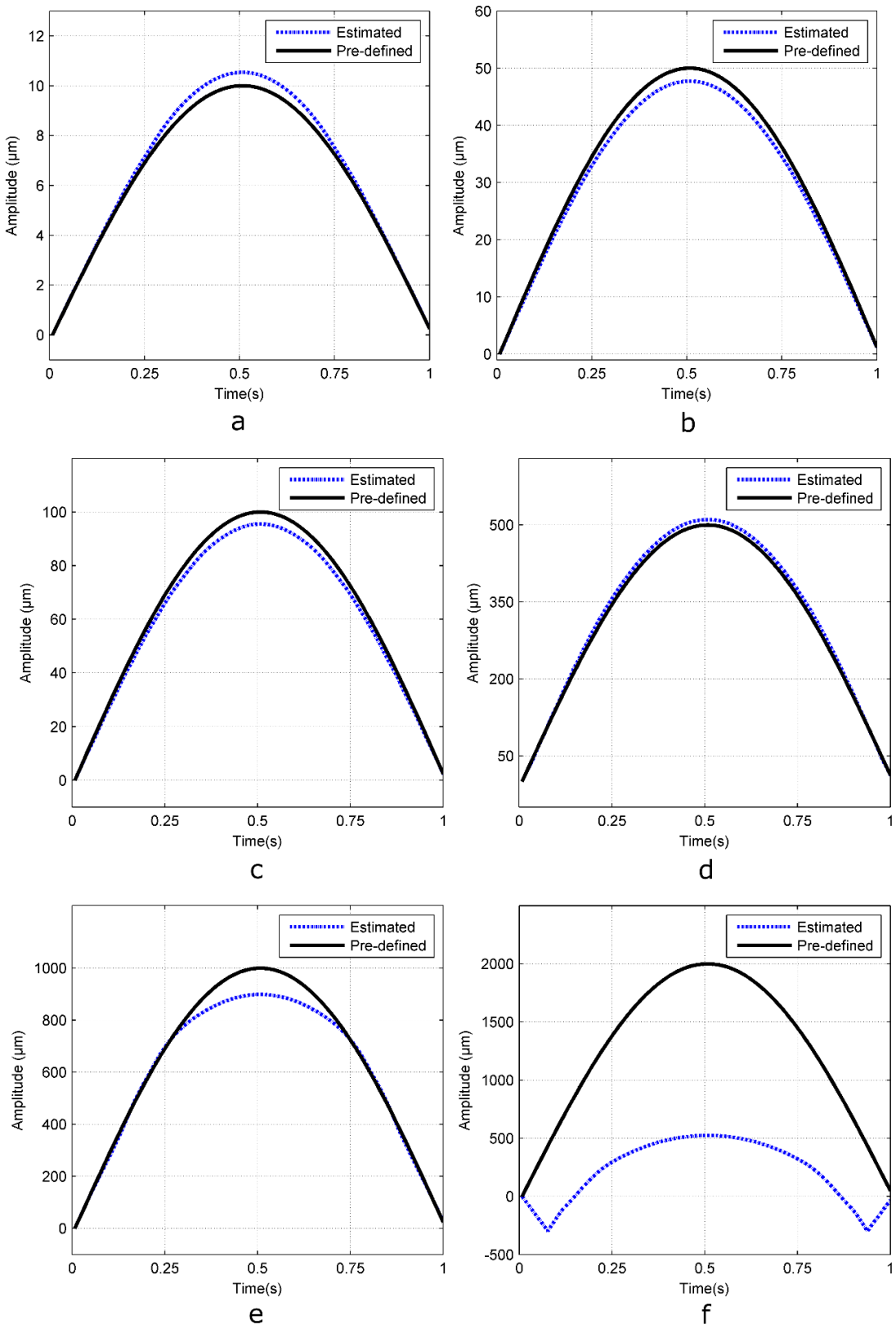

Fig. 5 15. Data from simulations: comparisons between pre-defined and estimated vessel wall motions under different amplitudes. (a) 5.39% overestimation at peak point; (b) 4.53% underestimation at peak point; (c) 4.47% underestimation at peak point; (d) 2.14% overestimation at peak point; (e) 10.1% underestimation at peak; (f) aliasing occurring.

For the Field II simulation, the defined motions of the vessel wall in the synthetic phantom and the estimated motion from the simulated RF signals are compared in Figure 5.15. The comparisons between the defined waveforms and the estimated waveforms range from 2000 µm down to 10 µm in waveform amplitude. The proposed method is able to detect the motion with very high resolution (less than 1 µm between consecutive frames) in this simulation. However, it failed to give a correct estimation when the amplitude was too large, due to aliasing as explained in the discussion.

5.3.3 Diameter variation of volunteer's radial artery

The posterior and anterior wall motion and the diameter variation of one of the volunteers are given in Figure 5.16. Results from this volunteer's data show that diameter variation waveforms of the radial artery can be estimated accurately by the auto-correlation method. The results from all 14 recruited volunteers are shown in Figures 5.17, 5.18 and 5.19. As can been seen, the diameter variation can be measured very clearly and repeatedly waveform in most cases, except for volunteer 4, 5 and 14. The magnitudes of the variation ranges from about 30 um to over 100 um. The large amplitudes tend to be detected better.

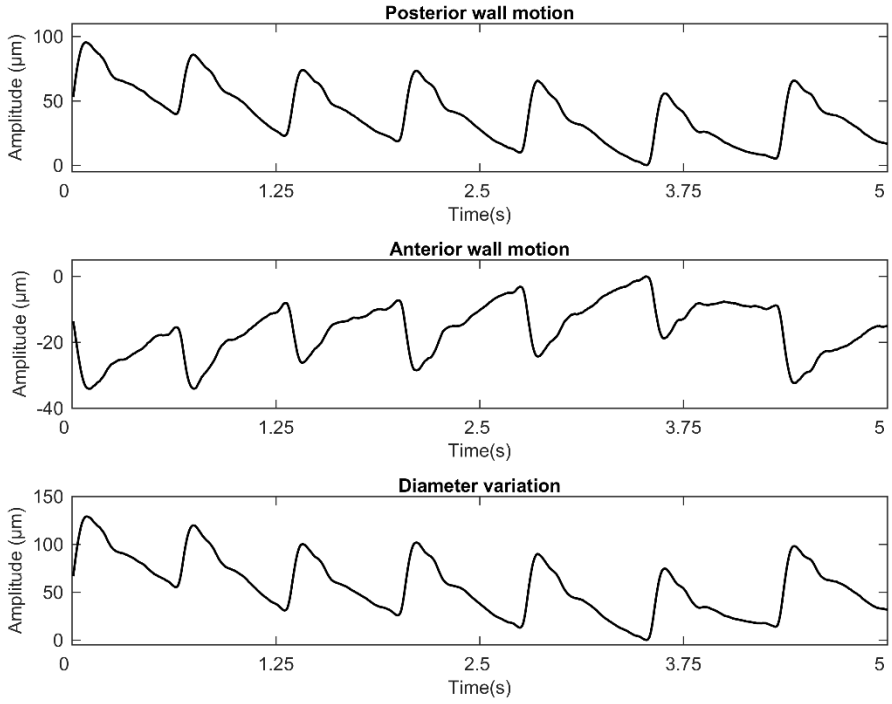

Fig. 5 16. Wall motion and diameter variation of the radial artery of volunteer 1.

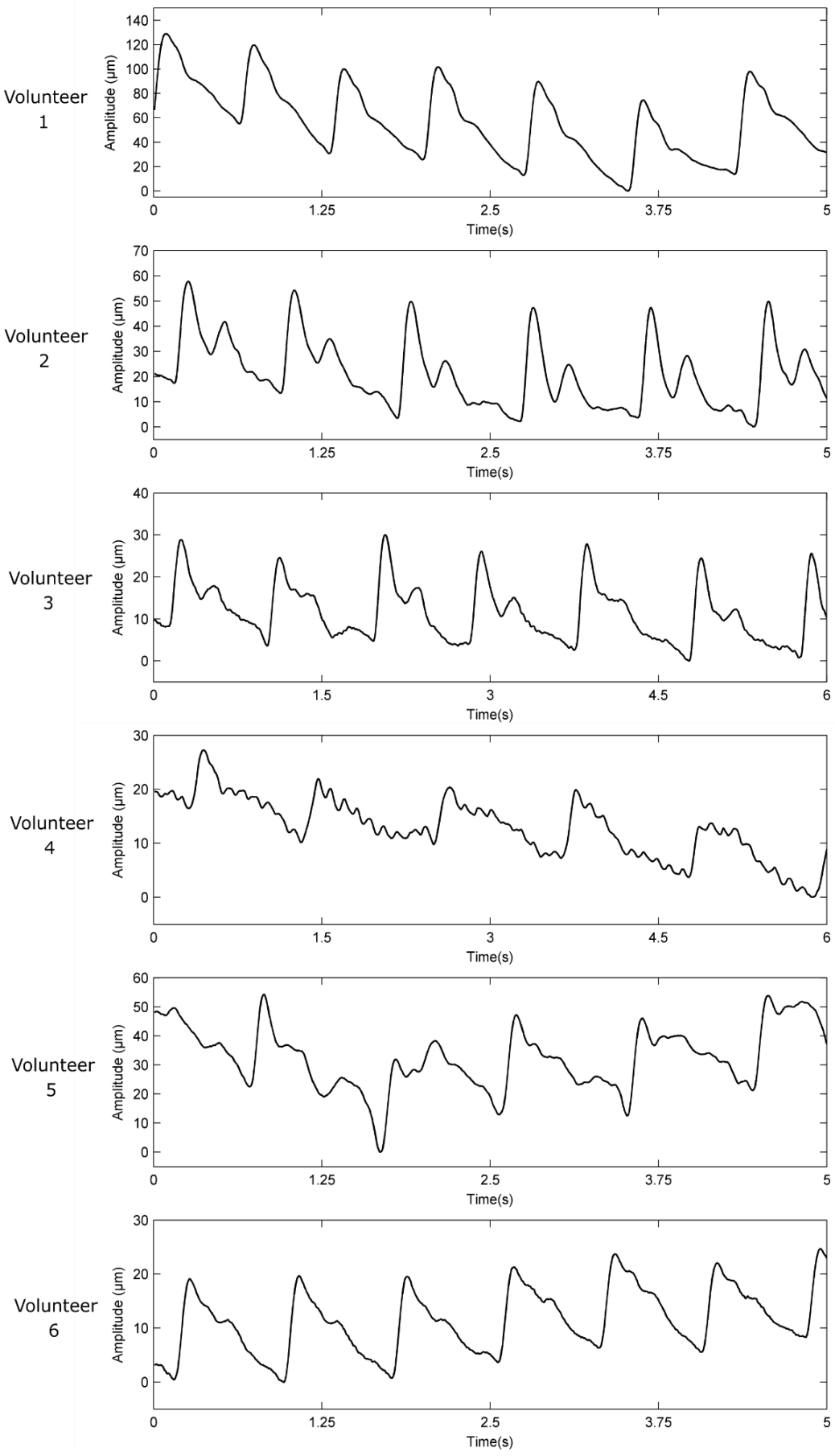

Fig. 5 17. Radial artery diameter variations of the volunteers 1-6.

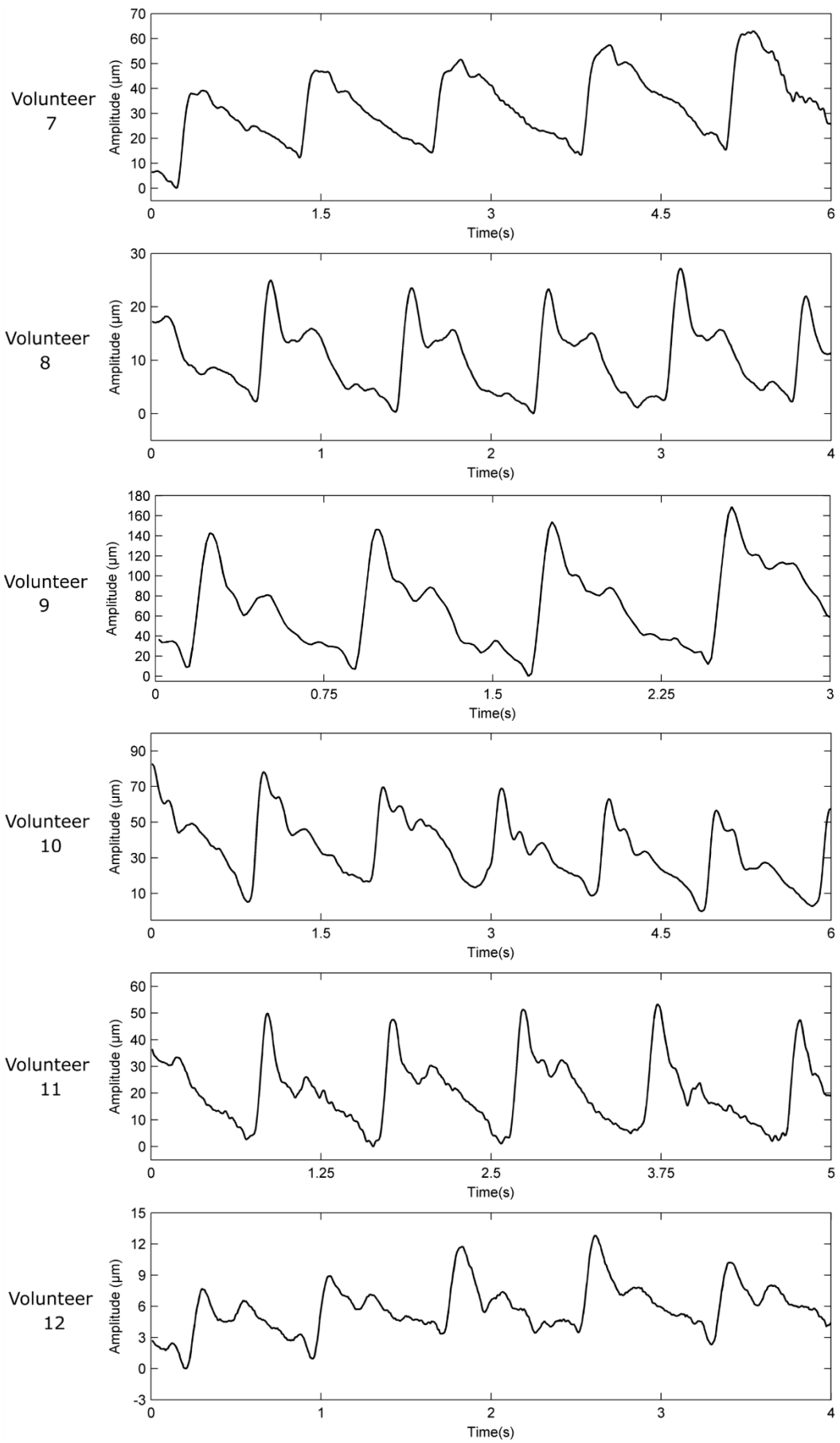

Fig. 5 18. Radial artery diameter variations of the volunteers 7-12.

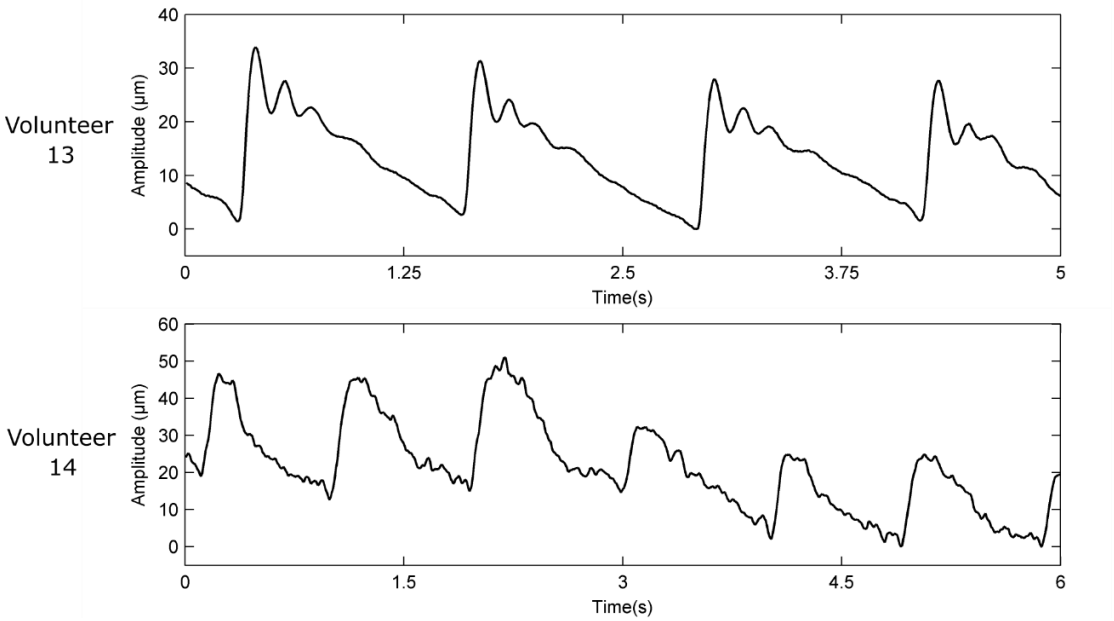

Fig. 5 19. Radial artery diameter variations of the volunteers 13-14.

5.3.4 Blood pressure waveform trial

The blood pressure waveform in the radial artery of one volunteer estimated by ultrasound-measured wall motion was compared with the reference waveform obtained from the tonometry as shown in Figure 5.20. The shape of these two waveforms are very high similar. Both were calibrated using the blood pressure values measured from the volunteer's brachial artery.

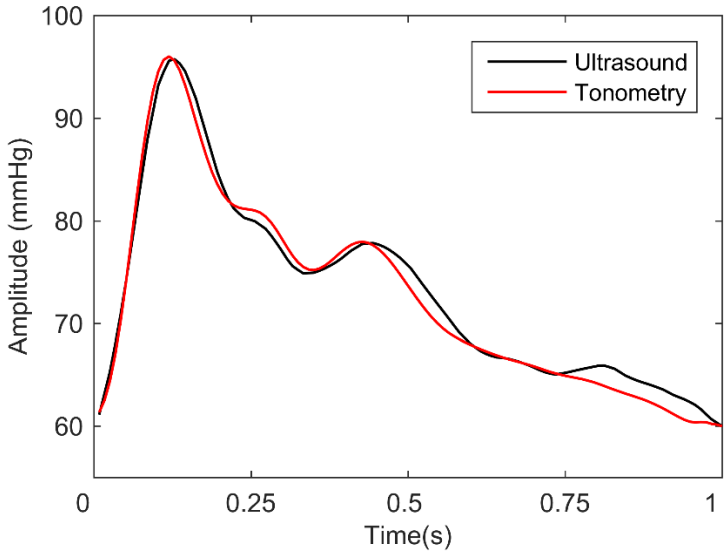

Fig. 5 20. Blood pressure waveforms in the volunteer's radial artery estimated by two different methods.

5.4 Discussion

As the pressure waveform is derived from the wall motion waveform, accuracy of the arterial wall motion measured through the ultrasound RF data will directly affect the estimated pressure waveform. The results in evaluating the wall motion detection are discussed here in detail.

5.4.1 Flow phantom

For the vessel wall motion in the flow phantom, the motion waveforms detected by the TDI mode in the HDI 5000 scanner and by the proposed auto-correlation method are very similar as shown in Figures 5.12 and 5.13. It can be seen that the amplitude of the motion estimated by the auto-correlation method is higher than that of the TDI method. This result agrees with the published study where it stated that the TDI in the HDI 5000 scanner tended to underestimate the arterial motion amplitude by 10% to 20% (Hammer et al. 2007). In Hammer's study, a wall motion test phantom, which was able to simulate physiological wall motion measured independently by a laser vibrometer, was created to evaluate the TDI tool in HDI 5000.

It can also be seen that the waveform shapes from these two methods during the diastolic period do not match very well when the flow rate was set to maximum level. In this case, the motion amplitude during the diastolic period is so small that the TDI method failed to capture the waveform details. By comparison, the auto-correlation method is still able to obtain detailed information about the waveform shape even when the motion amplitude is small during this diastolic period.

Compared to the amplitude at maximum flow rate, the wall motion amplitude at medium or minimum flow rate is larger during the diastolic period. This increased amplitude might be caused by the inertia of the vessel wall. This phenomenon happens more readily at lower flow rates (as shown in Fig. 5.13 and 5.14) because the high flow rate could prevent the vessel wall moving backward due to fluid in the lumen.

When the peak amplitude is less than 100 μm, the TDI method is not able to provide an acceptable result. This is demonstrated by its failure to detect the motion during the diastolic period in Figure 5.14.

The wall motion generated in the flow phantom is easier to detect than real arterial wall motion which is much more complicated. It was difficult even to locate the radial

artery's wall boundaries in *vivo* in some cases. The flow phantom can at least prove that the proposed auto-correlation method performs better than the TDI method in the HDI 5000 scanner. The HDI 5000 scanner can only detect motion with large amplitudes, but the correlation method is capable of detecting smaller amplitudes and providing more detailed information about the waveform.

5.4.2 Simulation

In the validation by simulation with a simple analytical model, the auto-correlation method performed very well, with the ability to detect accurately the time delay down to 1 ns between two consecutive frames as shown in Table 5.3. Assuming the sound velocity as 1540 m.s^{-1}, the time delay of 1 ns represents a spatial resolution of 0.77 μm. However, when the pre-defined time delay was set as 55 or 65 ns, the estimated time delay was totally wrong, having a negative value. This was caused by the aliasing which happened when the time delay between two consecutive frames was too big (Kanai et al. 1996). This auto-correlation method has a limitation on detecting the motion with very large displacement between two frames or high velocity. Theoretically, the absolute magnitude of the phase difference ($\Delta\theta$) between two frames (time interval T_s) must be less than π based on the sampling theorem, which means

$$\Delta\theta = 2\pi \cdot f_t \cdot \Delta t = 2\pi \cdot f_t \cdot \frac{2\Delta D}{c} < \pi \tag{5.12}$$

where f_t is the central frequency of the transmitted ultrasonic wave; Δt is the time delay between two consecutive frames; ΔD is the displacement between two frames and c is the velocity of sound. According to eqn. 5.12, the time delay Δt and displacement ΔD between two frames must meet the following conditions in eqn. 5.13

$$\Delta t < \frac{1}{2 f_t} \quad or \quad \Delta D < \frac{c}{4 f_t} \tag{5.13}$$

In this study the central frequency (f_t) is 10 MHz and speed of sound (c) is assumed to be 1540 m.s^{-1}. Based on this theorem, the longest time delay Δt that this method can detect is 50 ns. This means the aliasing will happen when the time delay is any larger than this. That is why in Table 5.3 the time delay was estimated as negative when the Δt was pre-defined to 55 ns or 60 ns. Additional measures might be able to deal with this aliasing issue but they are not covered in this study. Within this limitation, this correlation method

can estimate the time delay with high accuracy even if a uniformly distributed random noise was added to the analytically-produced RF signals.

In the synthetic phantom simulated by the Field II, the auto-correlation method can successfully estimate the simulated sinusoidal motion in most cases. The errors between the estimated waveform and the pre-defined waveform were very small with respect to the peak of the motion, except when the amplitude is too big as shown in Figure 5.15f. The abnormal motion waveform estimated by the correlation method in Figure 5.15f was again caused by the aliasing. If the absence of aliasing, the peak point errors were less than 10% in most cases.

From the results in Figure 5.15, it appears that this method performed worse when the motion had a large amplitude, with the error of 10.1% when the amplitude of the sinusoidal motion was 1 mm even though there was no aliasing. However, such large amplitudes do not occur in the peripheral arteries, especially not in the radial artery where the motion amplitude varies from tens of micrometres to a few hundred micrometres.

5.4.3 In vivo

Motion waveforms in Figures 5.17, 5.18 and 5.19 show that the auto-correlation method can derive repeatable, high quality motion information of the radial artery wall in most cases. It did not work very well only for volunteer 4, 5 and 14, and this was caused by one of two reasons below. The first reason is that this method is based on the B-mode scanning of the radial artery. If the volunteer's radial artery is too small (less than 2.0 mm), the clinical ultrasound scanner used with the frequency range of 2-15 MHz has inadequate spatial resolution to distinguish clearly between the arterial walls and this directly reduces the ability of this method to estimate the wall motion. The other reason is that the wall motion amplitude of some volunteers' radial artery is too small even though its diameter is over 2.0 mm. This was the case for volunteers 4 and 5. These two reasons could combine, leading to inaccuracies in estimating the wall motion.

As shown previously, the TDI technique in HDI 5000 is only able to detect vessel motion with amplitudes over 100 μm in the flow phantom. Although it is known that this TDI technique was designed for the carotid artery and not suitable for smaller arteries, there is a need to directly prove this in the radial artery and justify the development of the auto-correlation method. The limitation of TDI method was again demonstrated here by applying it to the radial artery of the volunteer 9 as shown in Figure 5.21. It shows that

the build-in TDI technique in the HDI 5000 is not able to detect the wall motion in this case, and thus it cannot be used to estimate the arterial wall motion in the radial artery.

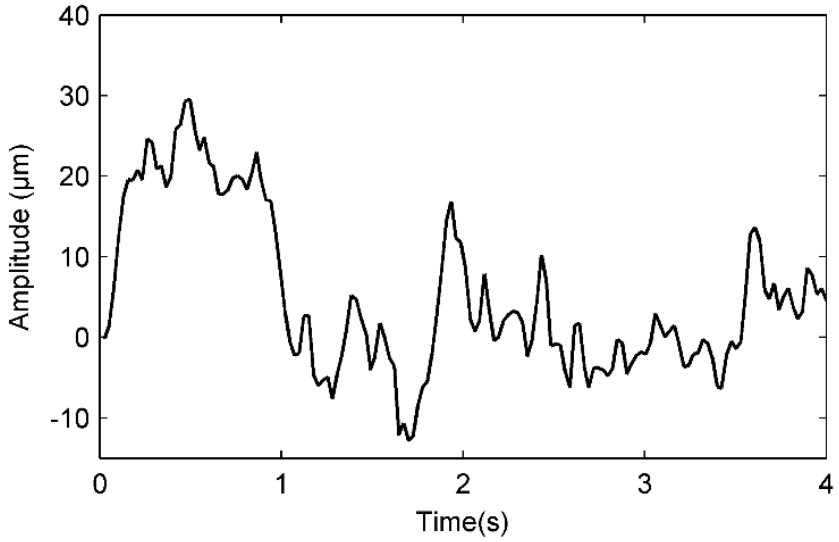

Fig. 5 21. The radial artery diameter variation measured by TDI from the volunteer 9.

5.4.4 Trial on blood pressure

The comparison of measured blood pressure waveforms between the tonometry and the ultrasound, shown in Figure 5.20, indicates that the two methods can give very similar motion waveforms. The slight difference occurs mostly during the diastolic period where the arterial wall motion has a small amplitude. As discussed above, small motion amplitude could affect the accuracy of motion estimation. Despite this slight difference, the overall similarity is high. It is therefore concluded that the blood pressure waveform in the radial artery can be estimated from the arterial wall motion using ultrasound.

5.4.5 Limitations

Although the proposed auto-correlation method was tested in various ways, by the flow phantom comparison, the simple model, the Field II simulation and in *vivo* trial, it has not been compared with direct measurements of wall motion. The HDI 5000 used on the flow phantom only gave an indirect comparison, assuming that the HDI 5000 is absolutely correct when the motion amplitude is over 100 μm. It would be best if a direct motion of the vessel wall in the flow phantom could be measured as an ultimate reference. However it is extremely difficult to achieve this since the vessel wall in the flow phantom was totally embedded in the surrounding tissue mimic material.

Only 14 volunteers were recruited to test this correlation method in the radial artery and one volunteer was used as a trial to validate the derivation of blood pressure waveform. More volunteers should be recruited to further test the reliability of this correlation method and the exponential relationship between the arterial cross-sectional area and blood pressure.

5.5 Conclusions

The auto-correlation method has proved able to detect the motion of the arterial wall with high resolution. As long as the arterial wall can be visualised clearly in the B-mode and aliasing does not occur, the smallest displacement of the wall it can capture goes down to a few micrometres. This technique is the preferred one to measure the arterial wall motion for most cases in *vivo*. The blood pressure waveform in the radial artery, which is useful in clinical practice research, can be derived from this arterial wall motion.

Chapter 6

6. A case study: Correlation between flow related parameters and hand perfusion in healthy human

6.1 Introduction

As explained in previous chapters, the flow related parameters in the radial and ulnar arteries, such as the flow rate (FR) and wall shear rate (WSR), can be estimated using a clinical scanner and the accuracies were evaluated through flow phantom and simulation. In this chapter the previously established methodology is applied to healthy volunteers to measure the flow and wall shear rates in their radial and ulnar arteries, as a case study to further investigate this ultrasound-based method *in-vivo*.

Additionally, this case study also provides a chance to investigate the correlation between the flow related parameters in wrist arteries and the hand perfusion in digits, which may be used as a clue for studying a perfusion-related disease in hand, the Raynaud's phenomenon. As explained in section 2.2.1 of chapter 2, Raynaud's phenomenon (RP), is characterized by transient cessation of blood flow to the digits of the extremities, such as fingers and toes (Cooke et al. 1996). RP can be categorized into the primary RP and the secondary RP. Both types of RP are believed to be the direct result of vasospasms that decrease blood supply to the affected areas. It is important to diagnose the types of RP before applying any clinical management. The distinction between primary and secondary RP is critical because patients with the latter require further medical evaluation and surveillance (Spencer-Green 1998; Herrick 2013).

Most studies aiming to understand the RPs were focused on the blood flow in hand arteries (i.e., radial and ulnar arteries) (Krause et al. 2002; Toprak et al. 2011), nail fold capillaries (Kim et al. 2008) or digital arteries (Schmidt et al. 2008), using magnetic resonance angiography (MRA) or Doppler ultrasound. Laser Doppler skin perfusion has also been used to study the RP (Kanetaka et al. 2004). Although many different techniques were used to diagnose these two types of RP, there is still no single method which can ideally make reliable diagnosis (Wigley 2002) .

Investigation of the correlation between flow related parameters and hand perfusion in this case study attempts to explore a new way to study the RP, which may provide possible value for clinics. The flow and wall shear rates in the wrist arteries of volunteers will be measured with a clinical ultrasound scanner, and at the same time the blood perfusion at the digits is recorded through a non-invasive, non-contact full field laser perfusion imager.

The aim of this chapter is to test the established methodology in chapter 3 and 4 for estimating flow and wall shear rates *in-vivo*, and to study the correlation between the flow related parameters in wrist arteries and blood perfusion in hand digits among healthy volunteers. It should be noted that this case study is just to try the established methodology so only the healthy volunteers are recruited. The same study protocol can be further used to investigate the RP for patients.

6.2 Methods

6.2.1 Overall

In order to study the correlation between flow parameters in wrist arteries and the blood perfusion in the hand digits, all these parameters must be measured simultaneously. The measuring procedure is illustrated in Figure 6.1. The ultrasound scanner was used for estimating the flow and wall shear rates in the radial or ulnar artery. The laser perfusion imager was for concurrently recording the blood perfusion from five digits. The estimated flow and wall shear rates were used to calculate the correlation with the blood perfusion magnitude from each of these digits individually.

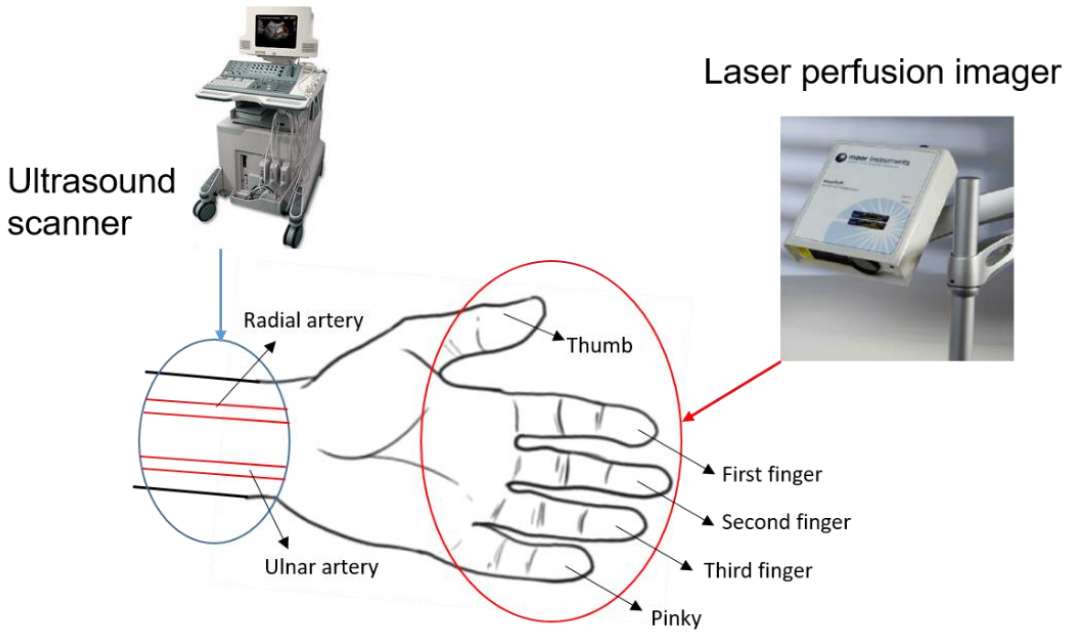

Fig. 6 1. The diagram to conceptualize the overall experimental design. Ultrasound transducer is for measuring FR and WSR in the radial and ulnar arteries. The laser perfusion imager is for measuring blood perfusion at five digits.

6.2.2 Experimental setup

The same ultrasound scanner as used in chapter 3 and 5 (Phillip HDI 5000 with the L12-5 transducer) was used to collect the ultrasound data from volunteer's radial and ulnar arteries and a MoorFLPI full-field laser perfusion imager (Moor Instruments, London, UK) was used to record the blood perfusion.

Moor FLPI is a commercial instrument designed for the measurement of blood flow within the microvasculature system by using infrared laser speckle contrast analysis (Fig. 6.2). Using software on a computer, this can record and measure changes in blood flow in real-time. The maximum depth that the MoorFLPI can reach is approximately 1mm into skin. The parameter that this MoorFLPI provides is tissue blood perfusion, also called 'Flux', which is related to the product of average speed and concentration of moving red blood cells in the tissue sample volume.

Fig. 6 2. The MoorFLPI full-field perfusion imager for recording the blood perfusion in digits.

In this MoorFLPI, the unit for flow measurement 'Flux' is arbitrary. Due to the nature of the flow in capillaries and connecting small blood vessels and the effect of varying skin colour and structure, it is not appropriate to use absolute units such as $ml.min^{-1}$. This is generally agreed by researchers and manufacturers, and this MoorFLPI has been calibrated by the manufacturer using the arbitrary unit for the 'Flux' (MoorInstrument 2010).

The devices were set up, as illustrated in Figure 6.3, to allow the volunteer to be conveniently scanned both by the HDI 5000 and by the Moor FLPI. In the reactive hyperaemia procedure, a manual inflatable cuff was used for occluding the brachial artery. A cushion was also provided under the volunteer's arm to help the volunteer stay comfortable so that they could keep still for over 5 minutes that each scan took. The Moor FLPI was connected to a laptop where the associated software was installed. The HDI 5000 was connected to another PC with the crossover cable through the Ethernet interface to transfer ultrasound data as necessary during the procedure.

Fig. 6 3. The experimental setup for collecting data from volunteer.

6.2.3 Data acquisition

16 healthy volunteers aged between 18 and 30 years were recruited, with 8 females and 8 males. The experiment for each volunteer was arranged at around 10 am in the morning, and the volunteer was asked to have breakfast earlier than 8:00 am, and not to drink alcohol, coffee or any other stimulants within 2 hours before the experiment as food or stimulants could affect the flow pattern in the cardiovascular system. The experiment protocol in this study was reviewed and approved by the Dundee University Research Ethics Committee.

The experiment was conducted in a room with temperature around 25^{o}C. Before data acquisition, the volunteer rested for 5 minutes, then blood pressure in the brachial artery was measured by an automatic pressure recorder. During the procedure, the volunteer was seated comfortably and place his or her left arm on a table as shown in Figure 6.3. The height of the chair was adjusted to make the volunteer's left arm level with the heart. A manual inflatable cuff was fitted on the upper arm but left in the deflated condition for the reactive hyperaemia later. The ultrasound transducer was placed on the wrist to firstly locate the radial artery and obtain the best view of the arterial walls (posterior and

anterior). The colour mode could be turned on to help locate the artery. Once the position of the transducer was fixed, the MoorFLPI scan head was placed above the palm and height adjusted to give a clear view of the outstretched digits shown in the software on a laptop. Five ROIs (region of interest) were used and carefully placed on each digit (Fig. 6.4).

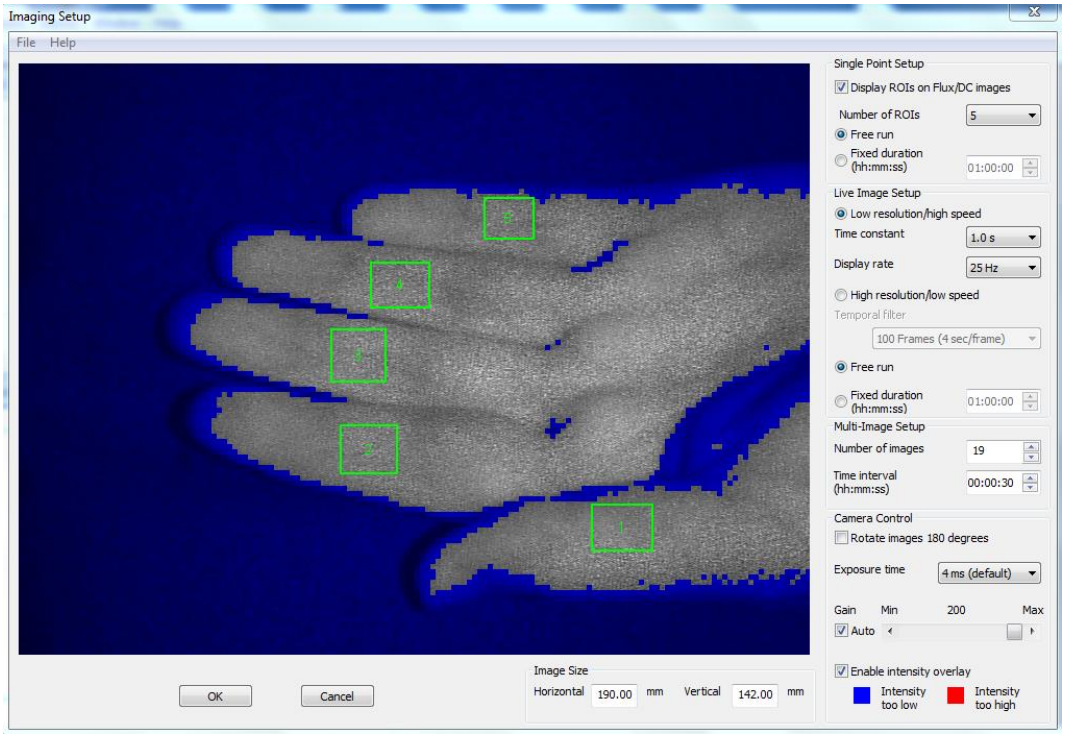

Fig. 6 4. The imaging setup used in MoorFLPI.

The volunteer was asked to keep as still as possible as both the ultrasound scanning and the MoorFLPI are very sensitive to movement. A large movement of the volunteer's arm could lead to losing the radial artery in the ultrasound image, or cause sharp spikes in the data collected from MoorFLPI.

The diameter of the radial artery was measured by the ultrasound in B-mode. Then, the ultrasound was changed into the PW mode to measure the centreline velocity in the radial artery. Both the ultrasound and MoorFLPI were left running and a timer was set to record the time. During the first two minutes, the baseline data was collected. The parameters for the ultrasound scanning were adjusted to obtain a clear spectrum with a proper velocity scale. After two minutes, the cuff was inflated to about 200 mmHg to occlude the blood flow through the lower arm arteries. The ultrasound scanning was

frozen and about 45 seconds of data stored in the cine loop was downloaded to the PC through the Ethernet.

The occlusion was maintained for five minutes and there was no blood going through the radial artery and no Doppler signal was detected. During this period, the volunteer was asked to continue to stay still, for any movements can cause failure of this scanning. At an elapsed time of seven minutes, the cuff was released. This released a huge blood flow downstream. Both the ultrasound scanner and the MoorFLPI were running to record the flow related parameters and blood perfusion.

The HDI 5000 can only store about 45 seconds of data, limited by the memory of the cine loop. However, the MoorFLPI has a much bigger memory to record the data during the whole procedure. An example of data collected from ultrasound and MoorFLPI are shown in Figure 6.5.

Since the ultrasound scanner can only collect the data from one artery at a time, the procedure had to be repeated for the ulnar artery. Before this, the volunteer rested and a gap over 10 minutes must be guaranteed to avoid occluding the upper arteries for the second time too soon. The procedure for the ulnar artery was exactly the same as the radial artery, except that the ultrasound transducer should be repositioned to locate the ulnar artery.

6.2.4 Data processing

As indicated in Figure 6.5, the temporal waveforms of the maximum velocity from the wrist arteries and the blood perfusion 'Flux' from digits are both available. Using the method explained in chapter 3, the blood flow and wall shear rate waveforms can be derived based on the arterial diameter and the maximum velocity waveform using the Womersley theory. Peak and mean values from these waveforms were calculated for analysis. These flow and wall shear rate values were used individually to do the correlation analysis with the 'Flux' values from the five different digits using the correlation coefficients and P values for each situation. The data was analysed by category as detailed below.

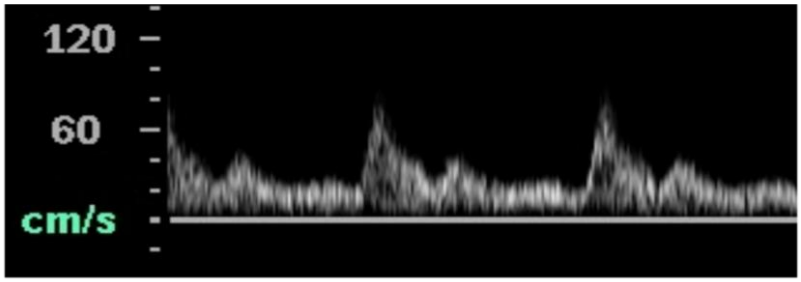

a

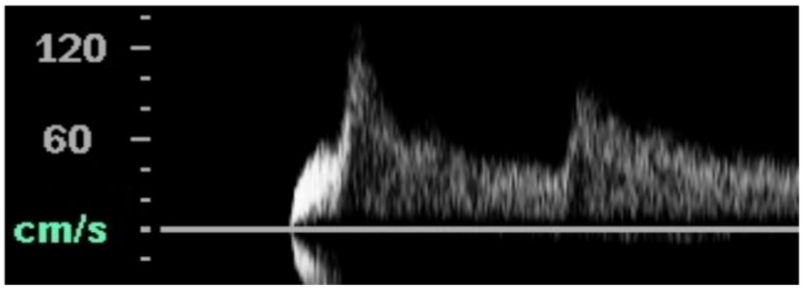

b

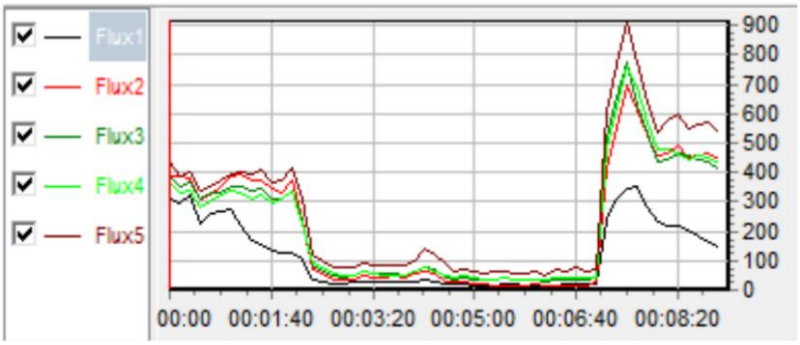

c

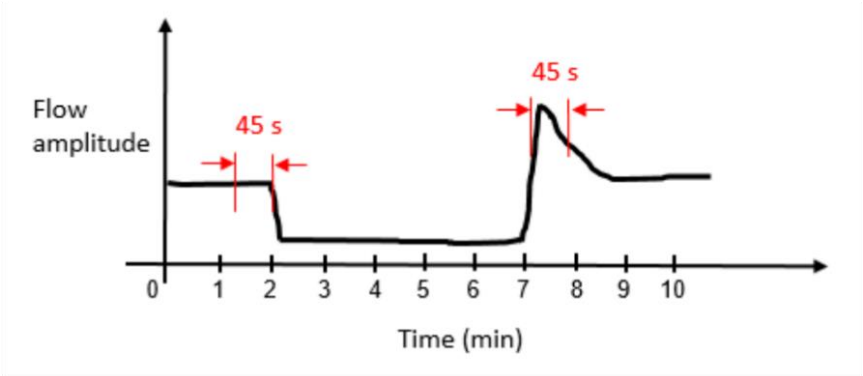

d

Fig. 6 5. Example of data collected from a volunteer. (a) The baseline centreline velocity from the ultrasound PW mode; (b) The centreline velocity from the PW mode after releasing the cuff; (c) The blood perfusion flux recorded by the MoorFLPI from five digits; (d) An illustration of timeline during the procedure. Ultrasound data was collected only within two 45-second periods as indicated. Data from MoorFLPI is available during the whole procedure.

Gender

Since RP is more prevalent in females, gender was considered while processing these volunteer data. Firstly, the data from both genders were mixed to do the correlation analysis. After that, the correlation analysis was separated for female and male volunteers.

Arteries

The correlation analysis between wrist arteries and hand digits was conducted separately for the radial artery and the ulnar artery.

Different digits

In order to study the relationship between the flow related parameters (FR and WSR) and blood perfusion in different digits, data from five different digits were analysed individually.

Timeline

Data from the baseline condition and the procedure of reactive hyperaemia were also analysed separately. The time periods chosen for the calculations are illustrated in Figure 6.5d.

Data type

For the baseline data, mean values within the 45 seconds were applied to do the correlation analysis. For the data from the reactive hyperaemia procedure, both the peak values and the mean values were used.

6.3 Results

6.3.1 FR and WSR values

The flow and wall shear rate waveforms, at baseline and after releasing the cuff from one of the volunteers' radial artery, are shown in Figure 6.6. It shows the great increase in flow and wall shear rate values after the pressure cuff was released in the brachial artery. Based on these waveforms, the peak value and mean value over the 45s measurement time can be calculated for the correlation analysis.

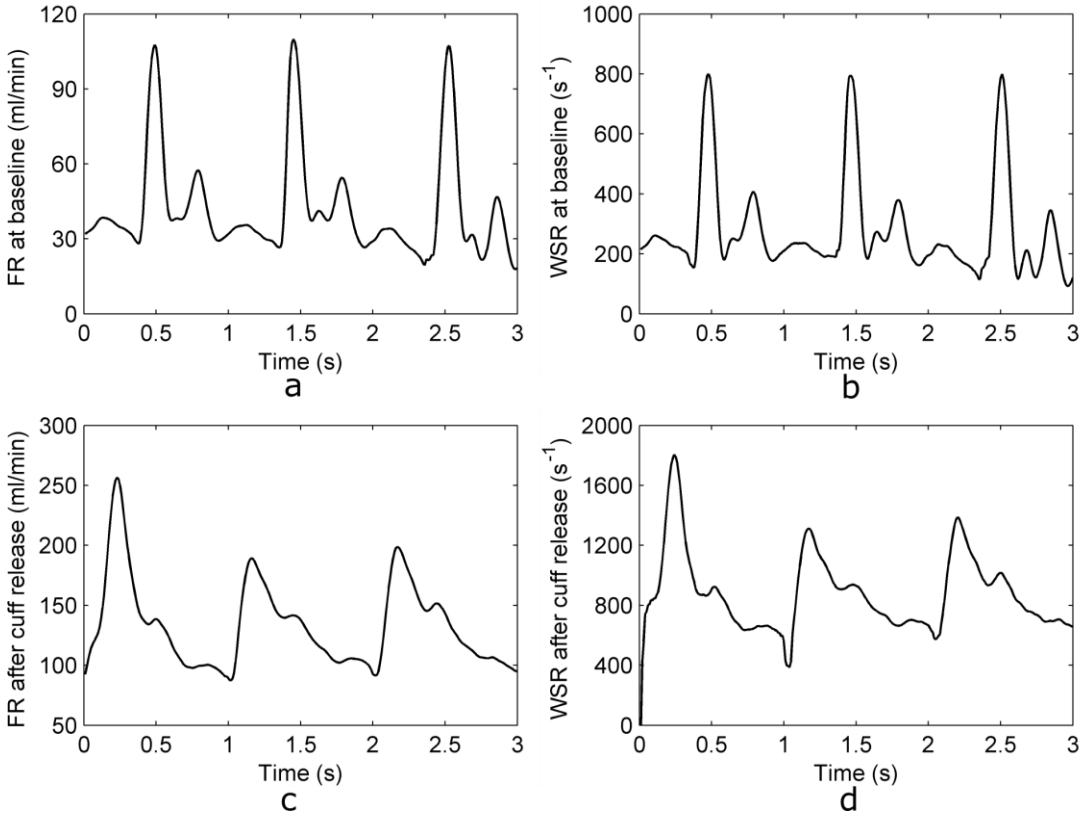

Fig. 6 6. FR and WSR waveforms from one volunteer's radial artery. (a) FR waveform at baseline. (b) WSR waveform at baseline. (c) FR waveform after the pressure cuff was released. (d) WSR waveform after the pressure cuff was released.

The baseline mean flow and wall shear rate values over time in the radial and ulnar artery from all 16 volunteers are illustrated in Figure 6.7. The flow rate ranges from 2.8 $ml.min^{-1}$ to 73.1 $ml.min^{-1}$ in the radial artery, and 2.1 $ml.min^{-1}$ to 61.3 $ml.min^{-1}$ in the ulnar artery. The wall shear rate is 50.4 s^{-1} to 583.2 s^{-1} in the radial artery, and 49.4 s^{-1} to 428.9 s^{-1} in the ulnar artery. By assuming the typical dynamic viscosity of blood fluid in these arteries as 3.5 mPa.s and the blood fluid is Newtonian (Papaioannou and Stefanadis 2005), the wall shear stress (WSS) in these two arteries nearly range from 0.2 Pa to 2.0 Pa.

6.3.2 Mixed correlation

For the data from volunteers of both genders, the correlation results (correlation coefficient R and P value) in both arteries are listed in Table 6.1 for the values at baseline, Table 6.2 for the mean values over 45s after the cuff release and Table 6.3 for the peak values after the cuff release. Two instances of the correlation result from Table 6.1 between the flow rate and blood perfusion 'Flux' are presented through the bivariate plot as shown in Figure 6.8.

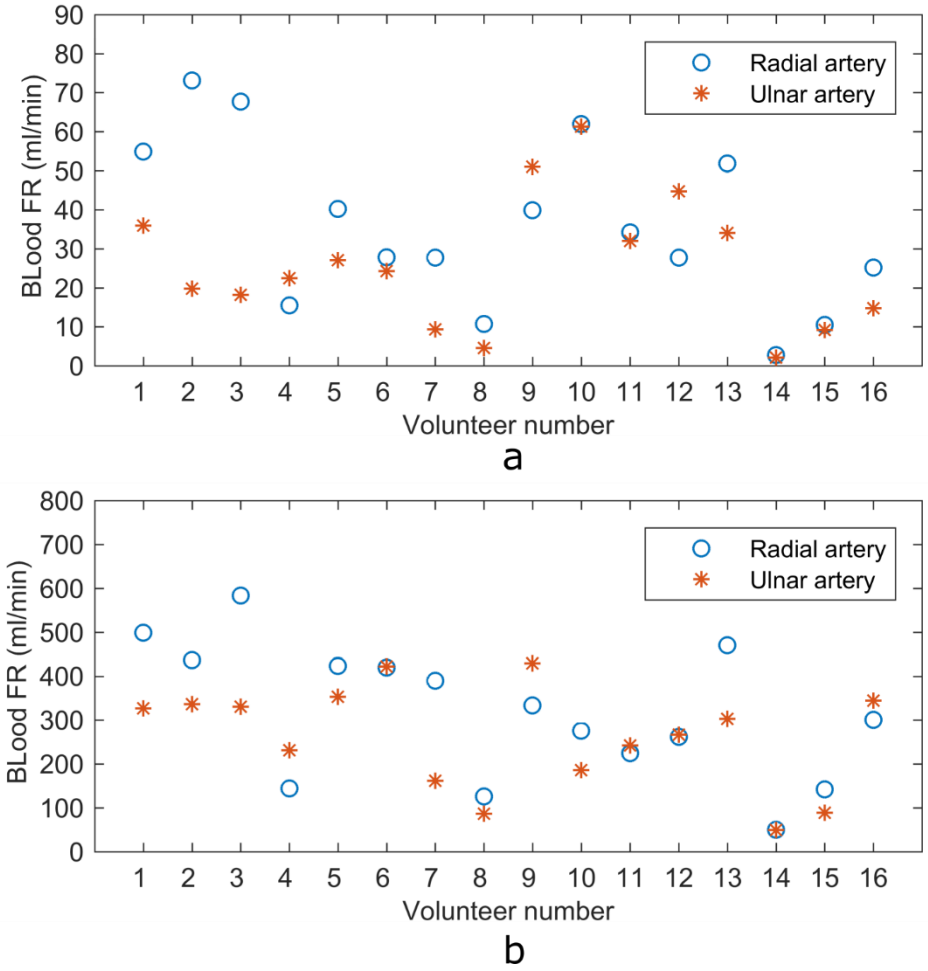

Fig. 6 7. The baseline mean FR and WSR over time from 16 volunteers' hand arteries. (a) The FR in hand arteries. (b) The WSR in hand arteries.

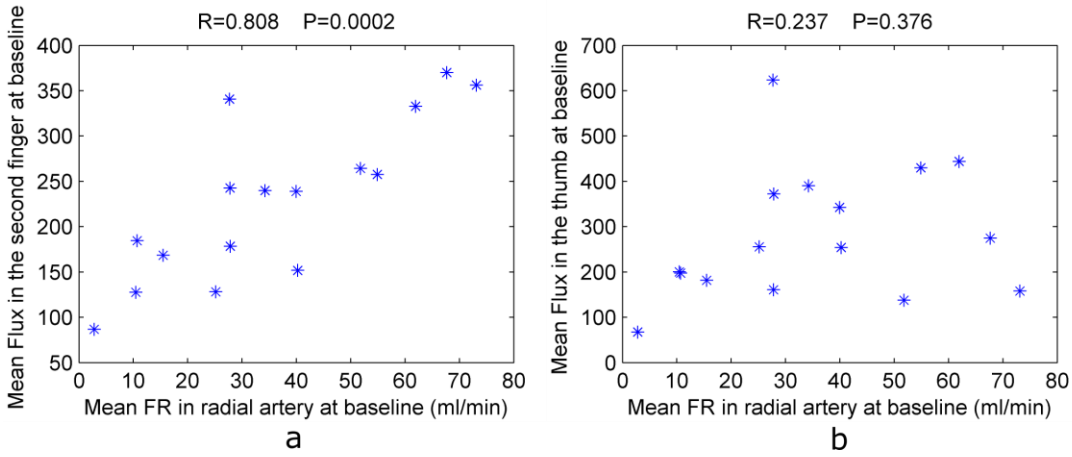

Fig. 6 8. The example bivariate plots for the correlation results with maximum R and minimum R in Table 6.1. (a) The values of flow rate in the radial artery and 'Flux' values in the second finger of the 16 volunteers. (b) The values of flow rate in the radial artery and 'Flux' values in the thumb of the 16 volunteers.

Table 6. 1. Correlation coefficient and P value between mean flow related parameters in wrist arteries and mean 'Flux' values in digits for all volunteers at baseline.

FLPI / Ultrasound	'Flux' from thumb	'Flux' from first finger	'Flux' from second finger	'Flux' from third finger	'Flux' from pinky
FR in the radial artery	R= 0.237 P=0.376	R= 0.681 P=0.004	R= 0.808 P=0.0002	R= 0.705 P=0.002	R= 0.712 P=0.002
WSR in the radial artery	R= 0.350 P=0.184	R= 0.655 P=0.006	R= 0.635 P=0.008	R= 0.514 P=0.042	R= 0.526 P=0.037
FR in the ulnar artery	R= 0.798 P=0.0002	R= 0.514 P=0.042	R= 0.717 P=0.002	R= 0.728 P=0.001	R= 0.763 P=0.001
WSR in the ulnar artery	R= 0.387 P=0.139	R= 0.408 P=0.117	R= 0.396 P=0.129	R= 0.390 P=0.136	R= 0.497 P=0.050

Table 6. 2. Correlation coefficient and P value between mean flow related parameters in wrist arteries and mean 'Flux' values in digits for all volunteers after cuff release.

FLPI / Ultrasound	'Flux' from thumb	'Flux' from first finger	'Flux' from second finger	'Flux' from third finger	'Flux' from pinky
FR in the radial artery	R= 0.205 P=0.446	R= 0.235 P=0.381	R= 0.483 P=0.058	R= 0.605 P=0.013	R= 0.519 P=0.039
WSR in the radial artery	R= 0.314 P=0.236	R= 0.194 P=0.047	R= 0.378 P=0.149	R= 0.413 P=0.112	R= 0.454 P=0.077
FR in the ulnar artery	R= 0.309 P=0.244	R= 0.191 P=0.478	R= 0.430 P=0.097	R= 0.414 P=0.111	R= 0.442 P=0.087
WSR in the ulnar artery	R= 0.317 P=0.232	R= 0.044 P=0.873	R= 0.070 P=0.796	R= 0.129 P=0.634	R= 0.179 P=0.507

Table 6. 3. Correlation coefficient and P value between peak flow related parameters in wrist arteries and peak 'Flux' values in digits for all volunteers after cuff release.

FLPI / Ultrasound	'Flux' from thumb	'Flux' from first finger	'Flux' from second finger	'Flux' from third finger	'Flux' from pinky finger
FR in the radial artery	R= -0.101 P=0.711	R= -0.115 P=0.671	R= 0.124 P=0.646	R= 0.212 P=0.431	R= 0.263 P=0.324
WSR in the radial artery	R= 0.06 P=0.825	R= -0.194 P=0.472	R= 0.114 P=0.673	R= 0.146 P=0.589	R= 0.177 P=0.513
FR in the ulnar artery	R= 0.336 P=0.204	R= 0.218 P=0.416	R= 0.371 P=0.157	R= 0.364 P=0.166	R= 0.468 P=0.067
WSR in the ulnar artery	R= 0.431 P=0.096	R= -0.011 P=0.968	R= -0.033 P=0.903	R= 0.122 P=0.653	R= 0.173 P=0.521

6.3.3 Correlation between male volunteers

For the data from male volunteers, the correlation results (correlation coefficient R and P value) for arteries are listed in Table 6.4 for the values at baseline, Table 6.5 for the mean values after the cuff release and Table 6.6 for the peak values after cuff release.

Table 6. 4. Correlation coefficient and P value between mean flow related parameters in wrist arteries and mean 'Flux' values in digits at baseline for male volunteers.

FLPI / Ultrasound	'Flux' from thumb	'Flux' from first finger	'Flux' from second finger	'Flux' from third finger	'Flux' from pinky
FR in the radial artery	R= 0.187 P=0.658	R= 0.984 P=0.0001	R= 0.932 P=0.001	R= 0.839 P=0.009	R= 0.606 P=0.111
WSR in the radial artery	R= -0.013 P=0.976	R= 0.714 P=0.046	R= 0.512 P=0.194	R= 0.303 P=0.466	R= 0.167 P=0.693
FR in the ulnar artery	R= 0.704 P=0.051	R= 0.437 P=0.279	R= 0.618 P=0.102	R= 0.643 P=0.086	R= 0.581 P=0.131
WSR in the ulnar artery	R= -0.006 P=0.989	R= 0.086 P=0.840	R= -0.067 P=0.875	R= 0.073 P=0.863	R= 0.144 P=0.733

Table 6. 5. Correlation coefficient and P value between mean flow related parameters in wrist arteries and mean 'Flux' values in digits after cuff release for male volunteers.

FLPI / Ultrasound	'Flux' from thumb	'Flux' from first finger	'Flux' from second finger	'Flux' from third finger	'Flux' from pinky
FR in the radial artery	R= 0.410 P=0.313	R= 0.853 P=0.007	R= 0.847 P=0.008	R= 0.858 P=0.006	R= 0.839 P=0.009
WSR in the radial artery	R= 0.316 P=0.446	R= 0.684 P=0.061	R= 0.495 P=0.213	R= 0.427 P=0.291	R= 0.574 P=0.137
FR in the ulnar artery	R= 0.452 P=0.261	R= 0.411 P=0.312	R= 0.6 P=0.116	R= 0.596 P=0.119	R= 0.538 P=0.169
WSR in the ulnar artery	R= -0.169 P=0.688	R= -0.341 P=0.408	R= -0.344 P=0.404	R= -0.152 P=0.720	R= -0.282 P=0.498

Table 6. 6. Correlation coefficient and P value between peak flow related parameters in wrist arteries and peak 'Flux' values in digits after cuff release for male volunteers.

FLPI / Ultrasound	'Flux' from thumb	'Flux' from first finger	'Flux' from second finger	'Flux' from third finger	'Flux' from pinky
FR in the radial artery	R= 0.321 P=0.439	R= 0.475 P=0.234	R= 0.525 P=0.181	R= 0.534 P=0.173	R= 0.513 P=0.193
WSR in the radial artery	R= 0.309 P=0.456	R= 0.563 P=0.146	R= 0.514 P=0.193	R= 0.520 P=0.187	R= 0.507 P=0.200
FR in the ulnar artery	R= 0.545 P=0.163	R= 0.523 P=0.183	R= 0.806 P=0.016	R= 0.701 P=0.053	R= 0.694 P=0.056
WSR in the ulnar artery	R= 0.725 P=0.042	R= 0.559 P=0.150	R= 0.523 P=0.183	R= 0.651 P=0.081	R= 0.620 P=0.101

6.3.4 Correlation between female volunteers

For the data from female volunteers, the correlation results (correlation coefficient R and P value) for both arteries are listed in Table 6.7 for values at baseline, Table 6.8 for the mean values after the cuff release and Table 6.9 for the peak values after cuff release.

Table 6. 7. Correlation coefficient and P value between mean flow related parameters in wrist arteries and mean 'Flux' values in digits at baseline for female volunteers.

FLPI / Ultrasound	'Flux' from thumb	'Flux' from first finger	'Flux' from second finger	'Flux' from third finger	'Flux' from fourth finger
FR in the radial artery	R= 0.325 P=0.433	R= 0.621 P=0.100	R= 0.717 P=0.045	R= 0.606 P=0.111	R= 0.735 P=0.038
WSR in the radial artery	R= 0.559 P=0.150	R= 0.541 P=0.166	R= 0.714 P=0.047	R= 0.598 P=0.117	R= 0.167 P=0.693
FR in the ulnar artery	R= 0.523 P=0.183	R= 0.437 P=0.279	R= 0.671 P=0.069	R= 0.626 P=0.152	R= 0.820 P=0.013
WSR in the ulnar artery	R= 0.632 P=0.093	R= 0.512 P=0.194	R= 0.660 P=0.075	R= 0.562 P=0.147	R= 0.815 P=0.014

Table 6. 8. Correlation coefficient and P value between mean flow related parameters in wrist arteries and mean 'Flux' values in digits after cuff release for female volunteers.

FLPI / Ultrasound	'Flux' from thumb	'Flux' from first finger	'Flux' from second finger	'Flux' from third finger	'Flux' from fourth finger
FR in the radial artery	R= 0.682 P=0.062	R= 0.474 P=0.236	R= 0.498 P=0.209	R= 0.614 P=0.105	R= 0.664 P=0.073
WSR in the radial artery	R= 0.619 P=0.101	R= 0.195 P=0.644	R= 0.310 P=0.454	R= 0.345 P=0.403	R= 0.421 P=0.298
FR in the ulnar artery	R= 0.272 P=0.514	R= 0.382 P=0.350	R= 0.413 P=0.309	R= 0.466 P=0.244	R= 0.590 P=0.124
WSR in the ulnar artery	R= 0.489 P=0.219	R= 0.214 P=0.610	R= 0.339 P=0.411	R= 0.417 P=0.304	R= 0.593 P=0.122

Table 6. 9. Correlation coefficient and P value between peak flow related parameters in wrist arteries and peak 'Flux' values in digits after cuff release for female volunteers.

Ultrasound \ FLPI	'Flux' from thumb	'Flux' from first finger	'Flux' from second finger	'Flux' from third finger	'Flux' from fourth finger
FR in the radial artery	R=0.282 P=0.498	R=-0.307 P=0.460	R=-0.27 P=0.519	R=-0.153 P=0.718	R=0.090 P=0.831
WSR in the radial artery	R=0.386 P=0.345	R=-0.45 P=0.264	R=-0.124 P=0.770	R=-0.181 P=0.669	R=-0.129 P=0.761
FR in the ulnar artery	R=-0.016 P=0.970	R=0.322 P=0.437	R=0.253 P=0.545	R=0.174 P=0.681	R=0.253 P=0.545
WSR in the ulnar artery	R=0.190 P=0.652	R=-0.416 P=0.306	R=-0.501 P=0.206	R=-0.378 P=0.356	R=-0.493 P=0.215

6.4 Discussion

6.4.1 FR and WSR estimations

The method for estimating flow and wall shear rate waveforms using a clinical ultrasound scanner was explained in chapter 3 where the maximum velocity waveform and the arterial diameter were used in the Womersley equations. Based on the experimental and computational validations in chapter 3 and 4 respectively, it was concluded that these flow and wall shear rate values were overestimated up to 50% in the radial and ulnar artery, many due to beam-vessel angle. Therefore, it is high likely that these two parameters measured *in-vivo* in this chapter were also overestimated but this should not influence the correlation analysis because the overestimation of flow parameters will happen in all volunteers.

As reported in the literature, the mean flow rate value over time estimated both by ultrasound (Manabe et al. 2005; Ozcan et al. 2011) and MRI (Van Canneyt et al. 2013) in the radial and ulnar arteries is typically near the range of 10 $ml.min^{-1}$ to 120 $ml.min^{-1}$. The mean flow rate values (2.8 $ml.min^{-1}$ to 73.1 $ml.min^{-1}$ in the radial artery, and 2.1 $ml.min^{-1}$ to 61.3 $ml.min^{-1}$ in the ulnar artery) measured in this study are in good agreement with the published data. The extremely low flow rate values (2.8 $ml.min^{-1}$ in the radial artery and 2.1 $ml.min^{-1}$ in the ulnar artery) measured in the volunteer 14 should not be taken as true measurements, and were actually governed by the waveforms of spectrum.

The spectrum of volunteer 14 (Fig. 6.9) showed there was reverse flow and the ultrasound scanner failed to detect the extremely low flow velocities during the diastolic period. The flow velocities during this period were assumed to be zero. This kind of extremely low and reverse flow was only detected in two of the 16 volunteers. Most volunteers did not have reverse flow in their radial and ulnar arteries.

The typical value of wall shear stress (WSS) in the cardiovascular system for a healthy human varies at different sites (Reneman et al. 2009). WSS at conduit arteries ranges between approximately 0.1 and 7 Pa (Malek et al. 1999; Nichols 2005; Papaioannou and Stefanadis 2005). The measured WSS values (0.2 Pa to 2.0 Pa) from the wrist arteries of 16 volunteers in this study are consistent with this published data. The waveform of the volunteer 14 illustrated in Figure 6.9 can cause the underestimation of the corresponding WSS which is the lowest (0.2 Pa) within these volunteers. The volunteer 14 is a 26-year-old young female and she provided information on her experience with cold hand and fingers when exposed under cold weather. This might indicate that blood velocity information in the wrist arteries from people with or without hand circulation issues could be used as a biomarker for diagnosing and studying the RP.

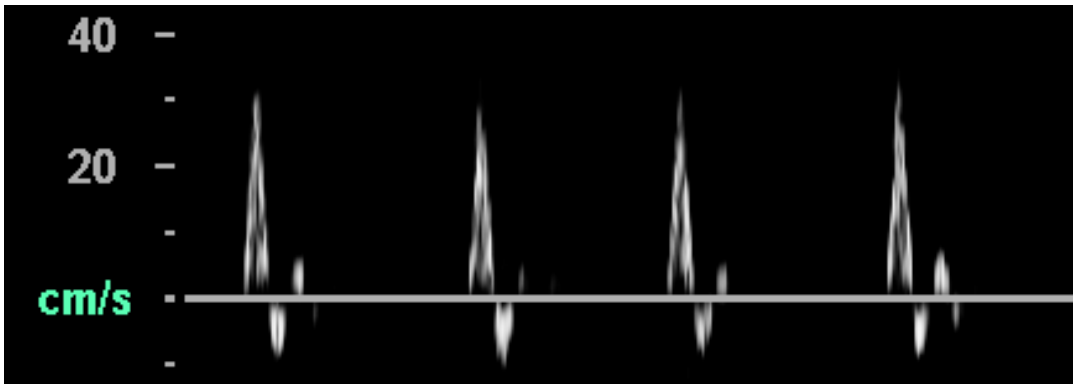

Fig. 6 9. The spectral sonogram from the volunteer 14.

6.4.2 Correlations

The results from those 16 healthy volunteers indicate that the correlation between flow related parameters in wrist arteries and hand perfusion in digits is not high but there are still some clues that can be derived. For example, the flow rate by all means seems to be more related to the hand perfusion in digits than the wall shear rate among healthy volunteers. In all cases correlations between flow related parameters and hand perfusion

in digits are higher at baseline than in the hyperaemia procedure. Besides, the correlations among female volunteers are much lower than that among the male volunteers. Also, the correlation coefficients between wrist arteries and the thumb are higher in the ulnar arteries than that in the radial artery.

Since there are only results from the healthy volunteers, their roles in studying the RP are not clear from the current work. However, these results would be useful references if further data from RP patients are obtained in the future. For example, if the correlation result is different among RP patients, these flow related parameters flow rate and wall shear rate should be studied to help understand the mechanism of the vasospasm that causes the RP. Furthermore, these correlation coefficients may also be used to distinguish the primary RP and the secondary RP if the data from both types of RP patients are available.

6.4.3 Limitations

As mentioned before, the capability of proposed method for estimating flow and wall shear rates could be affected by the undetected low velocities during the diastolic period. Assuming the undetected velocities as zero could lead to the underestimation of flow and wall shear rates, which can influence the correlation analysis.

The arterial diameter is required for estimating flow and wall shear rates and the Womersley-based method is very sensitive to error in the arterial diameter (Leguy et al. 2009a). The clinical ultrasound B-mode has limitations estimating the diameter accurately due to its spatial resolution. Although the arterial wall would dilate after releasing the occlusion cuff and the arterial diameter should be larger than the baseline value, the baseline diameter value was still used to estimate the flow and wall shear rates after cuff release due to the difficulty of measuring the dilated diameter. This bias in diameter could lead to errors in estimations of flow and wall shear rates. Another limitation is the assumptions made within the Womersley theory that the artery is considered a rigid cylinder tube. The blood is also considered as a Newtonian fluid and the flow is at a steady-state pulsatile condition (well-developed). These assumptions could also introduce errors in estimating the flow and wall shear rates.

Only 16 volunteers were recruited. It would be better to have more data. As the aim to do the correlation analysis between flow parameters in wrist arteries and blood perfusion in the hand digits is to study the RP. It would be better to test this analysis

method on the patients with RP and then compare the correlation results with the healthy volunteers.

6.5 Conclusions

From the results in *vivo* experiment, the proposed methodology in this thesis was able to provide a way to estimate the flow and wall shear rates in the radial and ulnar arteries with an acceptable accuracy. The measured flow and wall shear rate values agreed with the published data in the literature.

For the correlation analysis among healthy volunteers, it seemed that the correlation between flow related parameters in wrist arteries and hand perfusion in digits is not high. However, correlation results between healthy controls and patients with RP can be compared if the data from patients is available in the future. It is high likely that the correlation results among patients with RP would be different with the proposed correlation analysis in this chapter. Therefore, this study may provide a potential way to understand the RP in clinical practice and research.

Chapter 7

7. Conclusion and future work

7.1 Conclusion

Blood flow related parameters in the radial and ulnar arteries, such as flow velocity (FV), flow rate (FR), wall shear rate (WSR), arterial wall motion (AWM) and blood pressure waveform, are being used in clinical practice and clinical research in preoperative assessment of adequacy of the collateral ulnar circulation for coronary bypass surgery, in evaluation of the radial artery remodelling after creation of arteriovenous fistula for haemodialysis access, and to study the flow characteristics in the two arteries of patients with Raynaud's syndrome. Ultrasound imaging is the most commonly used imaging modality to estimate those flow related parameters but there are some inevitable errors in those estimations.

This thesis established methodologies for estimating those flow related parameters in these two arteries using ultrasound. Most importantly, evaluations of these estimations were conducted by flow phantom, simulation and *in-vivo*.

With the flow phantoms (chapter 3), it was concluded that the overestimations of FR and WSR were mainly caused by the beam-vessel angle during the procedure of pulsed wave Doppler ultrasound scanning. The arterial diameter appeared to affect the estimations of FR and WSR as well, while other factors such as imaging depth, flow rate, flow waveform did not. By simulation (chapter 4), the main observation was that the overestimations of FR and WSR were actually caused by the overestimation of maximum velocity from the Doppler ultrasound. The fact that beam-vessel angle can cause overestimation in maximum velocity was again proved in simulation. The performance of Womersley theory was also evaluated during the simulation and it showed that its

accuracy in estimating FR and WSR was dependent on the flow conditions within the blood vessel. The results of the investigation about these two parameters should raise the awareness of researchers and clinicians who need to use these measurements in these two arteries.

After being tested in the experimental flow phantom, by simulation and through *in-vivo* trial, the auto-correlation algorithm with ultrasound RF data was proven as an appropriate method to detect the arterial wall motion in the radial artery where the motion amplitude is between tens of micrometres to less than 200 μm. The method showed its capabilities in detecting arterial wall motion *in-vivo* in most cases as long as the arterial vessel walls could be viewed clearly in the B-mode ultrasound. Furthermore, the exponential relationship between arterial diameter variation and the blood pressure waveform was also validated in the radial artery of a healthy volunteer.

The case study (chapter 6) showed that the values of estimated FR and WSR were in good agreement with the published data *in-vivo*. The correlation between flow parameters in wrist arteries and blood perfusion in fingers among healthy volunteers have been studied and it is believed the correlation results would be different among patients with Raynaud's phenomenon. The correlation method proposed in this chapter could be used for studying RP if the data from RP patients are available in the future, and it may provide a potential way to understand the RP in clinical practice and research.

The aims of this thesis (section 1.3) were well addressed in chapter 3-6. Contributions of this study can be concluded as follows:

- Firstly, this thesis evaluated the errors in those ultrasound-measured flow related parameters. Clinicians and researchers who need to use those flow related parameters should be aware of the error sources and their ranges pointed out in this thesis; and necessary considerations should be taken to help make the correct decisions in clinical management.
- After evaluations through phantom, simulation and *in-vivo* data, it can be concluded that the conventional Doppler ultrasound is prone to bias in estimating flow velocity; Biasness in estimations of other flow parameters, such as the flow rate and the wall shear rate, also existed resulting from the biasness in estimated flow velocity and the angle-dependent limitation of conventional Doppler ultrasound.

- The statistical correlation analysis in chapter 6 provided a potential method for studying the hand perfusion which is associated with diseases occurring at hand such as the Raynaud's phenomenon.
- Soundly-designed experimental flow phantoms and simulation methods applied in this study can be useful for investigating the flow related parameters with Doppler ultrasound in other arterial applications;
- Validation of the auto-correlation method's capability of estimating the arterial wall motion in the radial artery provided the potential of deriving the blood pressure waveform in this arterial site with ultrasound scanner in clinical practice.

7.2 Future work

Future work should be focused in the following aspects:

1. The structure of the flow phantoms used in chapter 3 should be more realistic. In this thesis, a straight tube made of PVA-c was used to mimic the blood vessel. If a 3D realistic vessel mimic could be manufactured in the flow phantom, it would simulate more realistic flow condition similar to the hand arteries. This could improve the reliability when using the flow phantom to validate the FR and WSR measurements.
2. In the simulation in chapter 4, a rigid wall was assumed in the CFD, which could influence the accuracy of the simulated flow field, especially for the flow near the vessel wall. The extension of this would be using fluid structure interaction (FSI) to simulate the flow field.
3. Blood was assumed to be Newtonian both in the flow phantoms and in CFD simulation. Numerical studies have suggested that the assumption of Newtonian blood fluid can significantly affect the flow phenomena (Tu and Deville 1996; O'Callaghan et al. 2006). It would be better to use non-Newtonian blood fluid mimic in the flow phantoms and model the blood as non-Newtonian in the future work.
4. An important extension of this work would be the validation of the auto-correlation method for estimating the arterial wall motion in chapter 5. An experimental way of comparing the ultrasound auto-correlation method with

a direct measurement of the motion should be applied. The current study only compared the auto-correlation method with the TDI tool in the Phillip HDI 5000, which was an indirect comparison and was based on the assumption that the motion detected by TDI tool was reliable.

5. The volunteer numbers recruited in chapter 5 and 6 were not enough to draw a general conclusion, especially for the correlation analysis in chapter 6 where more volunteers should be recruited in the future work.
6. Patients with Raynaud's phenomenon should be recruited to study the differences of flow characteristics between patients and healthy controls, and also to look into the correlations between flow parameters in the wrist arteries and blood perfusion in the fingers among patients.

Publications

Journal papers:

Zhou X, Xia C, Khan F, Corner GA, Huang Z, Hoskins PR. Investigation of Ultrasound-Measured Flow Rate and Wall Shear Rate in Wrist Arteries Using Flow Phantoms (Journal). Ultrasound in Medicine & Biology 2016; 42:815-23.

Zhou X, Kenwright D, Wang S, John H, Hoskins P. Fabrication of two flow phantoms for Doppler ultrasound imaging. Transactions on Ultrasonics, Ferroelectrics, and Frequency Control 2017; 64(1):1-13.

Zhou X, Xia C, Stephen G, Khan F, Corner GA, Hoskins PR, Huang Z. Investigation of ultrasound-measured flow velocity, flow rate and wall shear rate in radial and ulnar arteries using simulation. Ultrasound in Medicine & Biology (in press).

Presentations in conferences:

Jin B, Evans A, Zhou X, Cochran S, Skerl K. Simulation and evaluation of anisotropy on 2D shear wave elastography in a phantom study (conference proceedings). International Tissue Elasticity Conference 2015, September 21-24, Verona, Italy.

Zhou X, Kan F, Corner G, Huang Z, Hoskins PR. Measuring hemodynamics in radial and ulnar arteries (Oral presentation). 17th Artimino ultrasound conference 2015, June 7-10, Helsinborg, Sweden.

APPENDIX

Appendix I

The LABVIEW programme for outputting the arbitrary voltage signal to drive the pump in the flow phantom.

The Front Panel of the main programme:

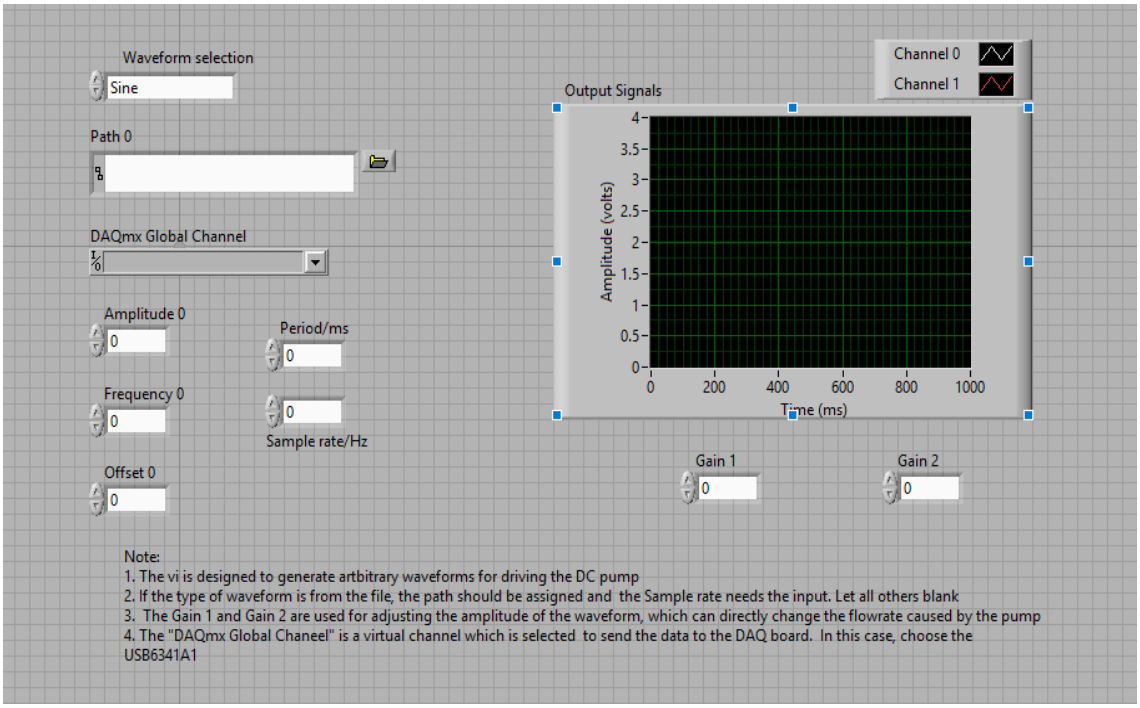

The Block Diagram of the main programme:

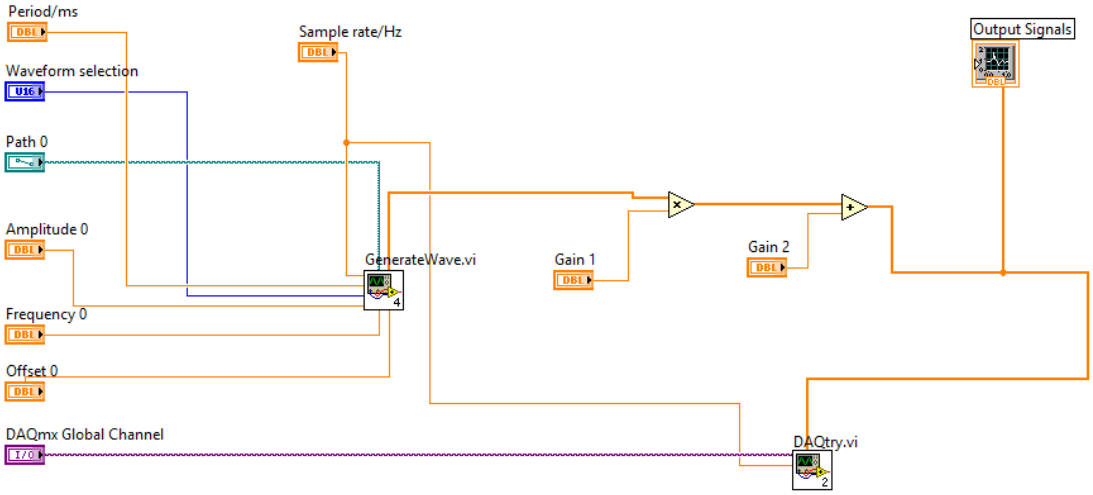

The Block Diagram of the sub vi “GenerateWave.vi” in the main programme:

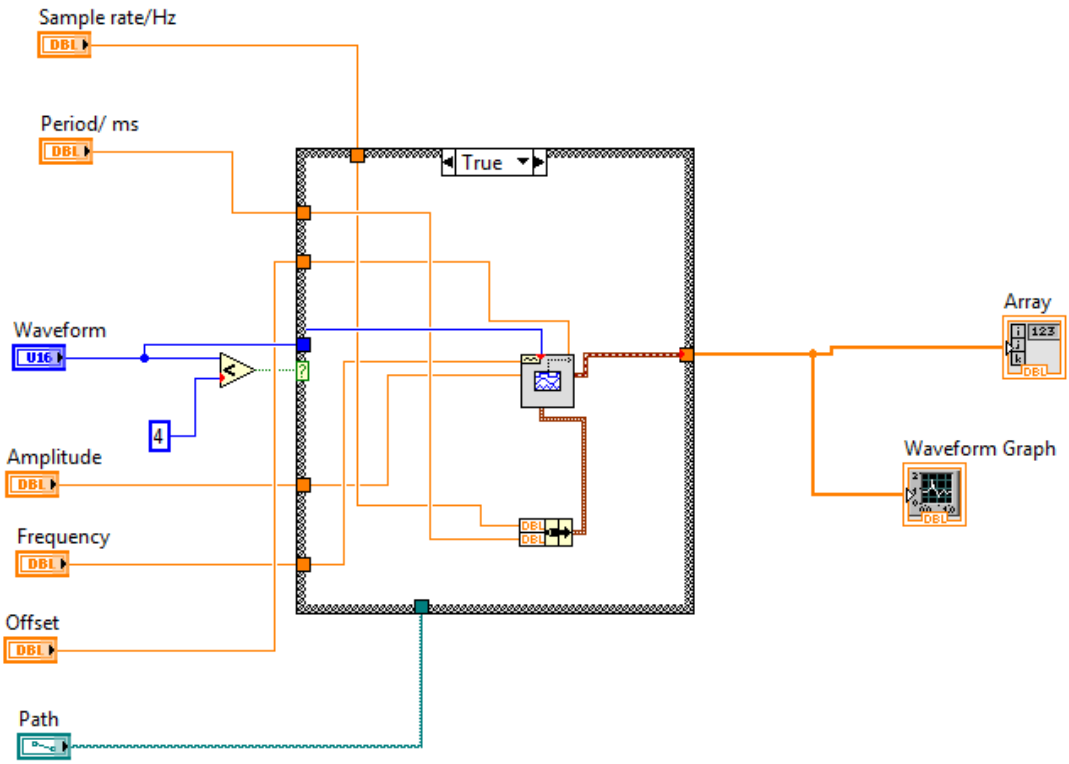

The Block Diagram of the sub vi “DAQtry.vi” in the main programme:

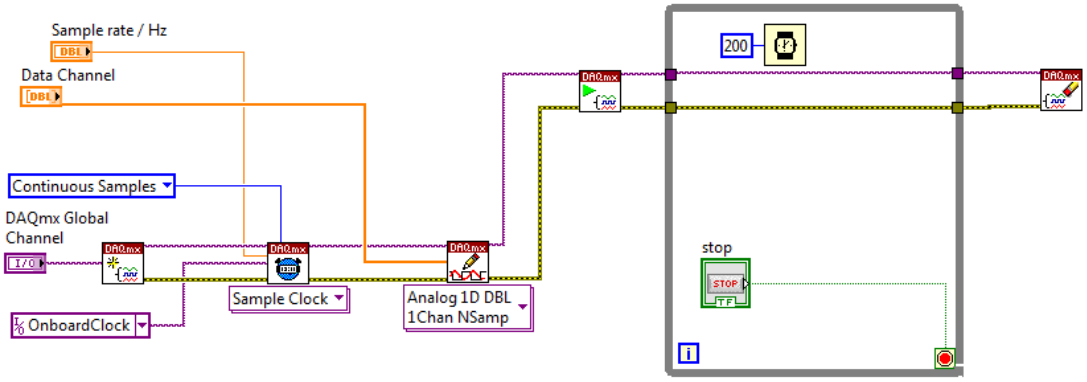

References

Abu-Omar Y, Mussa S, Anastasiadis K, Steel S, Hands L, Taggart DP. Duplex ultrasonography predicts safety of radial artery harvest in the presence of an abnormal Allen test. Ann Thorac Surg 2004;77:116-9.

Achouh P, Isselmou KO, Boutekadjirt R, D'Alessandro C, Pagny JY, Fouquet R, Fabiani JN, Acar C. Reappraisal of a 20-year experience with the radial artery as a conduit for coronary bypass grafting. Eur J Cardio-Thorac 2012;41:87-92.

Agrifoglio M, Dainese L, Pasotti S, Galanti A, Cannata A, Roberto M, Parolari A, Biglioli P. Preoperative assessment of the radial artery for coronary artery bypass grafting: Is the clinical Allen test adequate? Ann Thorac Surg 2005;79:570-2.

Ali SN, Srivastava S. Study of ulnar and radial arteries at wrist level in smokers. Scand J Plast Recons 2008;42:320-4.

Appis AW, Tracy MJ, Feinstein SB. Update on the safety and efficacy of commercial ultrasound contrast agents in cardiac applications. Echo Res Pract 2015;2:R55-62.

Bazan I, Negreira C, Ramos A, Brum J, Ramirez A. A new high-resolution spectral approach to noninvasively evaluate wall deformations in arteries. Computational and mathematical methods in medicine 2014;2014:606202.

Beulen BW, Bijnens N, Koutsouridis GG, Brands PJ, Rutten MC, van de Vosse FN. Toward noninvasive blood pressure assessment in arteries by using ultrasound. Ultrasound in Medicine & Biology 2011;37:788-97.

Blake JR, Meagher S, Fraser KH, Easson WJ, Hoskins PR. A method to estimate wall shear rate with a clinical ultrasound scanner. Ultrasound in Medicine & Biology 2008;34:760-74.

Bohs LN, Geiman BJ, Anderson ME, Gebhart SC, Trahey GE. Speckle tracking for multi-dimensional flow estimation. Ultrasonics 2000;38:369-75.

Bonnefous O, Criton A, Germond L, Denis E. New TDI developments for vascular and cardiac applications. 2000 Ieee Ultrasonics Symposium Proceedings, Vols 1 and 2 2000;1285-90.

Brahmbhatt A, Remuzzi A, Franzoni M, Misra S. The molecular mechanisms of hemodialysis vascular access failure. Kidney Int 2016;89:303-16.

Brands PJ, Hoeks AP, Ledoux LA, Reneman RS. A radio frequency domain complex cross-correlation model to estimate blood flow velocity and tissue motion by means of ultrasound. Ultrasound Med Biol 1997;23:911-20.

Brum J. Arterial diameter measurement using high resolution ultrasonography: In vitro validation. 2011;

Chen H. Estimation of central aortic pressure waveform by mathematical transformation of radial tonometry. Circulation 1997;95:1827-36.

Cheng Z, Tan FP, Riga CV, Bicknell CD, Hamady MS, Gibbs RG, Wood NB, Xu XY. Analysis of flow patterns in a patient-specific aortic dissection model. Journal of biomechanical engineering 2010;132:051007.

Chikui T, Izumi M, Eguchi K, Kawabe Y, Nakamura T. Doppler spectral waveform analysis of arteries of the hand in patients with Raynaud's phenomenon as compared with healthy subjects. Am J Roentgenol 1999;172:1605-9.

Cohn JN, Finkelstein S, McVeigh G, Morgan D, LeMay L, Robinson J, Mock J. Noninvasive pulse wave analysis for the early detection of vascular disease. Hypertension 1995;26:503-8.

Cooke JP, Dzau VJ. The pathophysiology of vasospasm. Boston: 1996.

Cooke JP, Marshall JM. Mechanisms of Raynaud's disease. Vasc Med 2005;10:293-307.

Couser WG, Remuzzi G, Mendis S, Tonelli M. The contribution of chronic kidney disease to the global burden of major noncommunicable diseases. Kidney Int 2011;80:1258-70.

Davidson PM, Phillips JL, Dennison-Himmelfarb C, Thompson SC, Luckett T, Currow DC. Providing palliative care for cardiovascular disease from a perspective of sociocultural diversity: a global view. Curr Opin Support Pa 2016;10:11-7.

Davies PF. Flow-mediated endothelial mechanotransduction. Physiol Rev 1995;75:519-60.

De Santis G, De Beule M, Segers P, Verdonck P, Verhegghe B. Patient-specific computational haemodynamics: generation of structured and conformal hexahedral meshes from triangulated surfaces of vascular bifurcations. Comput Method Biomec 2011a;14:797-802.

De Santis G, De Beule M, Van Canneyt K, Segers P, Verdonck P, Verhegghe B. Full-hexahedral structured meshing for image-based computational vascular modeling. Med Eng Phys 2011b;33:1318-25.

Deane CR, Markus HS. Colour velocity flow measurement: in vitro validation and application to human carotid arteries. Ultrasound Med Biol 1997;23:447-52.

Dineley J, Meagher S, Poepping TL, McDicken WN, Hoskins PR. Design and characterisation of a wall motion phantom. Ultrasound in Medicine & Biology 2006;32:1349-57.

Dineley JA, McDicken WN, Hoskins PR. Factors affecting the arterial distension waveform derived from tissue Doppler imaging (TDI): an in vitro study on precision. Ultrasound in Medicine & Biology 2007;33:1123-31.

Dodge JT, Jr., Brown BG, Bolson EL, Dodge HT. Lumen diameter of normal human coronary arteries. Influence of age, sex, anatomic variation, and left ventricular hypertrophy or dilation. Circulation 1992;86:232-46.

Doucette JW, Corl PD, Payne HM, Flynn AE, Goto M, Nassi M, Segal J. Validation of a Doppler guide wire for intravascular measurement of coronary artery flow velocity. Circulation 1992;85:1899-911.

Dueck R, Goedje O, Clopton P. Noninvasive continuous beat-to-beat radial artery pressure via TL-200 applanation tonometry. J Clin Monit Comput 2012;26:75-83.

Dunmire B, Beach KW, Labs K, Plett M, Strandness DE, Jr. Cross-beam vector Doppler ultrasound for angle-independent velocity measurements. Ultrasound Med Biol 2000;26:1213-35.

Duprez DA, Kaiser DR, Whitwam W, Finkelstein S, Belalcazar A, Patterson R, Glasser S, Cohn JN. Determinants of radial artery pulse wave analysis in asymptomatic individuals. Am J Hypertens 2004;17:647-53.

Eklund C FP, Gan LM. High-resolution radial artery intima-media thickness and cardiovascular risk factors in patients with suspected coronary artery disease--comparison with common carotid artery intima-media thickness. 2012;

Ekroll IK, Torp H, Lovstakken L, Swillens A, Segers P. Simultaneous quantification of flow and tissue velocities based on multi-angle plane wave imaging with an extended velocity range. 2011 Ieee International Ultrasonics Symposium (Ius) 2012;438-41.

Ene-Iordache B, Mosconi L, Antiga L, Bruno S, Anghileri A, Remuzzi G, Remuzzi A. Radial artery remodeling in response to shear stress increase within arteriovenous fistula for hemodialysis access. Endothelium-New York 2003;10:95-102.

Ene-Iordache B, Remuzzi A. Disturbed flow in radial-cephalic arteriovenous fistulae for haemodialysis: low and oscillating shear stress locates the sites of stenosis. Nephrol Dial Transplant 2012;27:358-68.

Ene-lordache B. Radial artery remodeling in response to shear stress increase within arteriovenous fistula for hemodialysisaccess. 2003;

Evans DH. Some Aspects of the Relationship between Instantaneous Volumetric Blood-Flow and Continuous Wave Doppler Ultrasound Recordings .3. The Calculation of Doppler Power Spectra from Mean Velocity Waveforms, and the Results of Processing These Spectra with Maximum, Mean, and Rms Frequency Processors. Ultrasound Med Biol 1982;8:617-23.

Ferrari M, Werner GS, Bahrmann P, Richartz BM, Figulla HR. Turbulent flow as a cause for underestimating coronary flow reserve measured by Doppler guide wire. Cardiovasc Ultrasound 2006;4:14.

Fillinger MF, Baker RJ, Jr., Zwolak RM, Musson A, Lenz JE, Mott J, Bech FR, Walsh DB, Cronenwett JL. Carotid duplex criteria for a 60% or greater angiographic stenosis: variation according to equipment. J Vasc Surg 1996;24:856-64.

Fraser KH, Meagher S, Blake JR, Easson WJ, Hoskins PR. Characterization of an abdominal aortic velocity waveform in patients with abdominal aortic aneurysm. Ultrasound in Medicine & Biology 2008;34:73-80.

Garcia D, del Alamo JC, Tanne D, Yotti R, Cortina C, Bertrand E, Antoranz JC, Perez-David E, Rieu R, Fernandez-Aviles F, Bermejo J. Two-Dimensional Intraventricular Flow Mapping by Digital Processing Conventional Color-Doppler Echocardiography Images. IEEE Trans Med Imaging 2010;29:1701-13.

Gaudino M, Crea F, Cammertoni F, Massetti M. The radial artery: a forgotten conduit. Ann Thorac Surg 2015;99:1479-85.

Gemignani V, Faita F, Ghiadoni L, Poggianti E, Demi M. A system for real-time measurement of the brachial artery diameter in B-mode ultrasound images. IEEE Trans Med Imaging 2007;26:393-404.

Gibyeli Genek D, Tuncer Altay C, Unek T, Sifil A, Secil M, Camsari T. Can primary failure of arteriovenous fistulas be anticipated? Hemodial Int 2015;19:296-305.

Gill RW. Measurement of blood flow by ultrasound: accuracy and sources of error. Ultrasound Med Biol 1985;11:625-41.

Girerd X, London G, Boutouyrie P, Mourad JJ, Safar M, Laurent S. Remodeling of the radial artery in response to a chronic increase in shear stress. Hypertension 1996;27:799-803.

Gnasso A, Carallo C, Irace C, De Franceschi MS, Mattioli PL, Motti C, Cortese C. Association between wall shear stress and flow-mediated vasodilation in healthy men. Atherosclerosis 2001;156:171-6.

Gnasso A, Carallo C, Irace C, Spagnuolo V, DeNovara G, Mattioli PL, Pujia A. Association between intima-media thickness and wall shear stress in common carotid arteries in healthy male subjects. Circulation 1996;94:3257-62.

Grant EG, Benson CB, Moneta GL, Alexandrov AV, Baker JD, Bluth EI, Carroll BA, Eliasziw M, Gocke J, Hertzberg BS, Katanick S, Needleman L, Pellerito J, Polak JF, Rholl KS, Wooster DL, Zierler RE. Carotid artery stenosis: gray-scale and Doppler US diagnosis--Society of Radiologists in Ultrasound Consensus Conference. Radiology 2003;229:340-6.

Greiwe G, Tariparast PA, Behem C, Petzoldt M, Herich L, Trepte CJ, Reuter DA, Haas SA. Is applanation tonometry a reliable method for monitoring blood pressure in morbidly obese patients undergoing bariatric surgery? Br J Anaesth 2016;116:790-6.

Habib J, Baetz L, Satiani B. Assessment of collateral circulation to the hand prior to radial artery harvest. Vasc Med 2012;17:352-61.

Haluska BA, Jeffriess L, Mottram PM, Carlier SG, Marwick TH. A new technique for assessing arterial pressure wave forms and central pressure with tissue Doppler. Cardiovascular Ultrasound 2007;5:6.

Hammer SJ, Dineley J, Easson WJ, Hoskins PR. An arterial wall motion test phantom for the evaluation of wall motion software. Ultrasound in Medicine & Biology 2007;33:1504-11.

Hasegawa H, Kanai H. Improving accuracy in estimation of artery-wall displacement by referring to center frequency of RF echo. IEEE Trans Ultrason Ferroelectr Freq Control 2006;53:52-63.

Hasegawa H, Kanai H. Reduction of influence of variation in center frequencies of RF echoes on estimation of artery-wall strain. IEEE Trans Ultrason Ferroelectr Freq Control 2008;55:1921-34.

Hayashi K, Handa H, Nagasawa S, Okumura A, Moritake K. Stiffness and elastic behavior of human intracranial and extracranial arteries. J Biomech 1980;13:175-84.

Heiberg E, Sjogren J, Ugander M, Carlsson M, Engblom H, Arheden H. Design and validation of Segment--freely available software for cardiovascular image analysis. BMC Med Imaging 2010;10:1.

Hergum T, Langeland S, Remme EW, Torp H. Fast ultrasound imaging simulation in K-space. IEEE Trans Ultrason Ferroelectr Freq Control 2009;56:1159-67.

Heron M. Deaths: leading causes for 2008. Natl Vital Stat Rep 2012;60:1-94.

Herrick AL. Management of Raynaud's phenomenon and digital ischemia. Curr Rheumatol Rep 2013;15:303.

Hoeks AP, Brands PJ, Arts TG, Reneman RS. Subsample volume processing of Doppler ultrasound signals. Ultrasound Med Biol 1994;20:953-65.

Hoeks APG, Brands PJ, Smeets FAM, Reneman RS. Assessment of the Distensibility of Superficial Arteries. Ultrasound Med Biol 1990;16:121-8.

Hoeks APG, Samijo SK, Brands PJ, Reneman RS. Noninvasive Determination of Shear-Rate Distribution across the Arterial Lumen. Hypertension 1995;26:26-33.

Holdsworth DW, Norley CJD, Frayne R, Steinman DA, Rutt BK. Characterization of common carotid artery blood-flow waveforms in normal human subjects. Physiol Meas 1999;20:219-40.

Hope SA, Tay DB, Meredith IT, Cameron JD. Comparison of generalized and gender-specific transfer functions for the derivation of aortic waveforms. Am J Physiol Heart Circ Physiol 2002;283:H1150-6.

Hoskins PR. Accuracy of maximum velocity estimates made using Doppler ultrasound systems. Brit J Radiol 1996;69:172-7.

Hoskins PR. Peak velocity estimation in arterial stenosis models using colour vector Doppler. Ultrasound Med Biol 1997;23:889-97.

Hoskins PR. A comparison of single- and dual-beam methods for maximum velocity estimation. Ultrasound Med Biol 1999a;25:583-92.

Hoskins PR. A Review of the Measurement of Blood Velocity and Related Quantities Using Doppler Ultrasound. 1999b;

Hoskins PR. Simulation and Validation of Arterial Ultrasound Imaging and Blood Flow. Ultrasound in Medicine & Biology 2008;34:693-717.

Hoskins PR. Estimation of blood velocity, volumetric flow and wall shear rate using Doppler ultrasound. Ultrasound 2011;19:120-9.

Hoskins PR, Fish PJ, McDicken WN, Moran C. Developments in cardiovascular ultrasound. Part 2: Arterial applications. Med Biol Eng Comput 1998;36:259-69.

Hoskins PR, Hardman D. Three-dimensional imaging and computational modelling for estimation of wall stresses in arteries. Brit J Radiol 2009;82:S3-S17.

Hoskins PR, Martin K, Thrush A. Diagnostic ultrasound physics and equipment. Cambridge University Press, 2010a.

Hoskins PR, Soldan M, Fortune S, Inglis S, Anderson T, Plevris J. Validation of Endoscopic Ultrasound Measured Flow Rate in the Azygos Vein Using a Flow Phantom. Ultrasound Med Biol 2010b;36:1957-64.

Humphrey JD. Cardiovascular solid mechanics: cells, tissues, and organs. New York: Springer-Verlag, 2002.

Iaco AL, Teodori G, Di Giammarco G, Di Mauro M, Storto L, Mazzei V, Vitolla G, Mostafa B, Calafiore AM. Radial artery for myocardial revascularization: Long-term clinical and angiographic results. Ann Thorac Surg 2001;72:464-8.

Jensen JA. Field: A program for simulating ultrasound systems. Med Biol Eng Comput 1996;34:351-3.

Jensen JA. Improved Vector Velocity Estimation using Directional Transverse Oscillation. Ieee Int Ultra Sym 2015;

Jensen JA, Munk P. Computer phantoms for simulating ultrasound B-mode and CFM images. Acoust Imag 1997;23:75-80.

Jensen JA, Nikolov SI. Directional synthetic aperture flow imaging. Ieee T Ultrason Ferr 2004;51:1107-18.

Jensen JA, Nikolov SI, Gammelmark KL, Pedersen MH. Synthetic aperture ultrasound imaging. Ultrasonics 2006;44:E5-E15.

Jensen JA, Nikolov SI, Yu AC, Garcia D. Ultrasound Vector Flow Imaging-Part I: Sequential Systems. IEEE Trans Ultrason Ferroelectr Freq Control 2016a;63:1704-21.

Jensen JA, Nikolov SI, Yu AC, Garcia D. Ultrasound Vector Flow Imaging-Part II: Parallel Systems. IEEE Trans Ultrason Ferroelectr Freq Control 2016b;63:1722-32.

Jensen JA, Svendsen NB. Calculation of pressure fields from arbitrarily shaped, apodized, and excited ultrasound transducers. IEEE Trans Ultrason Ferroelectr Freq Control 1992;39:262-7.

Kanai H, Sato M, Koiwa Y, Chubachi N. Transcutaneous measurement and spectrum analysis of heart wall vibrations. Ieee T Ultrason Ferr 1996;43:791-810.

Kanetaka T, Komiyama T, Onozuka A, Miyata T, Shigematsu H. Laser Doppler skin perfusion pressure in the assessment of Raynaud's phenomenon. European journal of vascular and endovascular surgery : the official journal of the European Society for Vascular Surgery 2004;27:414-6.

Kasai C. Real-Time Two-Dimensional Blood-Flow Imaging Using an Autocorrelation Technique. Ieee T Ultrason Ferr 1986;33:94-.

Kehrer M, Goelz R, Krageloh-Mann I, Schoning M. Measurement of volume of cerebral blood flow in healthy preterm and term neonates with ultrasound. Lancet 2002;360:1749-50.

Kelly R, Hayward C, Avolio A, O'Rourke M. Noninvasive determination of age-related changes in the human arterial pulse. Circulation 1989;80:1652-9.

Kerr AT, Hunt JW. A method for computer simulation of ultrasound Doppler color flow images--I. Theory and numerical method. Ultrasound Med Biol 1992;18:861-72.

Kharboutly Z, Deplano V, Bertrand E, Legallais C. Numerical and experimental study of blood flow through a patient-specific arteriovenous fistula used for hemodialysis. Medical Engineering & Physics 2010;32:111-8.

Khimdas S, Harding S, Bonner A, Zummer B, Baron M, Pope J, Canadian Scleroderma Research G. Associations with digital ulcers in a large cohort of systemic sclerosis: results from the Canadian Scleroderma Research Group registry. Arthritis Care Res (Hoboken) 2011;63:142-9.

Kim SH, Kim HO, Jeong YG, Lee SY, Yoo WH, Choi TH, Lee SI. The diagnostic accuracy of power Doppler ultrasonography for differentiating secondary from primary Raynaud's phenomenon in undifferentiated connective tissue disease. Clin Rheumatol 2008;27:783-6.

King DM, Fagan AJ, Moran CM, Browne JE. Comparative imaging study in ultrasound, MRI, CT, and DSA using a multimodality renal artery phantom. Med Phys 2011;38:565-73.

King DM, Ring M, Moran CM, Browne JE. Development of a range of anatomically realistic renal artery flow phantoms. Ultrasound Med Biol 2010;36:1135-44.

Kirpalani A, Park H, Butany J, Johnston KW, Ojha M. Velocity and wall shear stress patterns in the human right coronary artery. J Biomech Eng-T Asme 1999;121:370-5.

Krause U, Pabst T, Kenn W, Hahn D. High resolution contrast enhanced MR-angiography of the hand arteries: preliminary experiences. Vasa 2002;31:179-84.

Kumwenda M. Clinical practice guideline: vascular access for hemodialysis. 2015;

Lally EV. Raynaud's phenomenon. Current Opinion in Rheumatology 1992;4:

Lee SI, Lee SY, Yoo WH. The usefulness of power Doppler ultrasonography in differentiating primary and secondary Raynaud's phenomenon. Clin Rheumatol 2006;25:814-8.

Leguy CA, Bosboom EM, Hoeks AP, van de Vosse FN. Assessment of blood volume flow in slightly curved arteries from a single velocity profile. J Biomech 2009a;42:1664-72.

Leguy CA, Bosboom EM, Hoeks AP, van de Vosse FN. Model-based assessment of dynamic arterial blood volume flow from ultrasound measurements. Med Biol Eng Comput 2009b;47:641-8.

Leow CH, Bazigou E, Eckersley RJ, Yu ACH, Weinberg PD, Tang MX. Flow Velocity Mapping Using Contrast Enhanced High-Frame-Rate Plane Wave Ultrasound and

Image Tracking: Methods and Initial in Vitro and in Vivo Evaluation. Ultrasound Med Biol 2015a;41:2913-25.

Leow CH, Iori F, Corbett R, Duncan N, Caro C, Vincent P, Tang MX. Microbubble Void Imaging: A Non-Invasive Technique for Flow Visualisation and Quantification of Mixing in Large Vessels Using Plane Wave Ultrasound and Controlled Microbubble Contrast Agent Destruction. Ultrasound Med Biol 2015b;41:2926-37.

Levi F, Chatenoud L, Bertuccio P, Lucchini F, Negri E, La Vecchia C. Mortality from cardiovascular and cerebrovascular diseases in Europe and other areas of the world: an update. Eur J Cardiovasc Prev Rehabil 2009;16:333-50.

Li S, Hoskins PR, Anderson T, McDicken WN. Measurement of mean velocity during pulsatile flow using time-averaged maximum frequency of doppler ultrasound waveforms. Ultrasound in Medicine & Biology 1993a;19:105-13.

Li S, Mcdicken WN, Hoskins PR. Blood-Vessel Diameter Measurement by Ultrasound. Physiol Meas 1993b;14:291-7.

Logason K, Barlin T, Jonsson ML, Bostrom A, Hardemark HG, Karacagil S. The importance of Doppler angle of insonation on differentiation between 50-69% and 70-99% carotid artery stenosis. Eur J Vasc Endovasc 2001;21:311-3.

Longest PW, Vinchurkar S. Effects of mesh style and grid convergence on particle deposition in bifurcating airway models with comparisons to experimental data. Medical Engineering & Physics 2007;29:350-66.

Loupas T. <An axial velocity estimator for ultrasound blood flow imaging, based on a full evaluation of the Doppler equation by means of a two-dimensional autocorrelation approach.pdf>. Ieee T Ultrason Ferr 1995;

Lui EYL, Steinman AH, Cobbold RSC, Johnston KW. Human factors as a source of error in peak Doppler velocity measurement. J Vasc Surg 2005;42:972-9.

Ma J, Xu CS, Gao F, Chen M, Li F, Du LF. Diagnostic and therapeutic research on ultrasound microbubble/nanobubble contrast agents (Review). Molecular Medicine Reports 2015;12:4022-8.

Maier SE, Meier D, Boesiger P, Moser UT, Vieli A. Human abdominal aorta: comparative measurements of blood flow with MR imaging and multigated Doppler US. Radiology 1989;171:487-92.

Malek AM, Alper SL, Izumo S. Hemodynamic shear stress and its role in atherosclerosis. JAMA 1999;282:2035-42.

Malkawi AH, Hinchliffe RJ, Xu Y, Holt PJ, Loftus IM, Thompson MM. Patient-specific biomechanical profiling in abdominal aortic aneurysm development and rupture. J Vasc Surg 2010;52:480-8.

Malovrh M. Native arteriovenous fistula: preoperative evaluation. Am J Kidney Dis 2002;39:1218-25.

Manabe S, Tabuchi N, Tanaka H, Arai H, Sunamori M. Hand circulation after radial artery harvest for coronary artery bypass grafting. J Med Dent Sci 2005;52:101-7.

Manabe S, Tabuchi N, Toyama M, Kuriu K, Mizuno T, Sunamori M. Measurement of ulnar flow is helpful in predicting ischemia after radial artery harvest. Thorac Cardiov Surg 2002;50:325-8.

Manini S, Passera K, Huberts W, Botti L, Antiga L, Remuzzi A. Computational model for simulation of vascular adaptation following vascular access surgery in haemodialysis patients. Comput Methods Biomech Biomed Engin 2014;17:1358-67.

Masengu A, McDaid J, Maxwell AP, Hanko JB. Preoperative radial artery volume flow is predictive of arteriovenous fistula outcomes. J Vasc Surg 2016;63:429-35.

McCormick MM, Varghese T. An approach to unbiased subsample interpolation for motion tracking. Ultrason Imaging 2013;35:76-87.

Mcilory MB. Doppler ultrasonic investigation of Raynaud's phenomenon: effect of tempearture on blood velocity. 1985;

Meagher S, Poepping TL, Ramnarine KV, Black RA, Hoskins PR. Anatomical flow phantoms of the nonplanar carotid bifurcation, part II: experimental validation with Doppler ultrasound. Ultrasound Med Biol 2007;33:303-10.

Meinders JM, Hoeks AP. Simultaneous assessment of diameter and pressure waveforms in the carotid artery. Ultrasound in Medicine & Biology 2004;30:147-54.

Mendis S, Puska P, Norrving B. Global atlas on cardiovascular disease prevention and control. World Healthy Organization 2011;3-18.

Millasseau S, Agnoletti D. Non-invasive Estimation of Aortic Blood Pressures: A Close Look at Current Devices and Methods. Curr Pharm Design 2015;21:709-18.

Milner JS, Moore JA, Rutt BK, Steinman DA. Hemodynamics of human carotid artery bifurcations: computational studies with models reconstructed from magnetic resonance imaging of normal subjects. J Vasc Surg 1998;28:143-56.

Moddemeijer R. On the determination of the position of extrema of sampled correlators. Ieee T Signal Proces 1991;39:216-9.

MoorInstrument. MoorFLPI user manual software version 3.0. 2010;

Mynard JP, Wasserman BA, Steinman DA. Errors in the estimation of wall shear stress by maximum Doppler velocity. Atherosclerosis 2013;227:259-66.

Nassar GM. Endovascular management of the "failing to mature" arteriovenous fistula. Tech Vasc Interv Radiol 2008;11:175-80.

Nichols WW, O'Rourke, M. F. McDonald's blood flow in arteries. Theoretical, experimental and clinical principles, fifth edition. London: Arnold, 2005.

Nietert PJ, Shaftman SR, Silver RM, Wolf BJ, Egan BM, Hunt KJ, Smith EA. Raynaud phenomenon and mortality: 20+ years of follow-up of the Charleston Heart Study cohort. Clin Epidemiol 2015;7:161-8.

O'Callaghan S, Walsh M, McGloughlin T. Numerical modelling of Newtonian and non-Newtonian representation of blood in a distal end-to-side vascular bypass graft anastomosis. Med Eng Phys 2006;28:70-4.

O'Rourke MF, Pauca A, Jiang X-J. Pulse wave analysis. British Journal of Clinical Pharmacology 2001;51:507-22.

Ozcan HN, Kara M, Ozcan F, Bostanoglu S, Karademir MA, Erkin G, Ozcakar L. Dynamic Doppler evaluation of the radial and ulnar arteries in patients with carpal tunnel syndrome. AJR Am J Roentgenol 2011;197:W817-20.

Papaioannou TG, Protogerou AD, Stamatelopoulos KS, Vavuranakis M, Stefanadis C. Non-Invasive Methods and Techniques for Central Blood Pressure Estimation: Procedures, Validation, Reproducibility and Limitations. Curr Pharm Design 2009;15:245-53.

Papaioannou TG, Stefanadis C. Vascular wall shear stress: basic principles and methods. Hellenic J Cardiol 2005;46:9-15.

Poelma C. Ultrasound Imaging Velocimetry: a review. Experiments in Fluids 2017;58:

Poepping TL, Nikolov HN, Thorne ML, Holdsworth DW. A thin-walled carotid vessel phantom for Doppler ultrasound flow studies. Ultrasound Med Biol 2004;30:1067-78.

Ponzini R, Vergara C, Rizzo G, Veneziani A, Roghi A, Vanzulli A, Parodi O, Redaelli A. Womersley number-based estimates of blood flow rate in Doppler analysis: in vivo validation by means of phase-contrast MRI. IEEE transactions on bio-medical engineering 2010;57:1807-15.

Prakash S, Ethier CR. Requirements for mesh resolution in 3D computational hemodynamics. Journal of biomechanical engineering 2001;123:134-44.

Rabben SI, Baerum S, Sorhus V, Torp H. Ultrasound-based vessel wall tracking: an auto-correlation technique with RF center frequency estimation. Ultrasound Med Biol 2002a;28:507-17.

Rabben SI, Segers P, de Backer J, de Sutter J, Verdonck P, Gillebert TC. Vessel wall tracking based on the modified autocorrelation estimator. 2002 Ieee Ultrasonics Symposium Proceedings, Vols 1 and 2 2002b;1787-90.

Ramnarine KV, Nassiri DK, Hoskins PR, Lubbers J. Validation of a new blood-mimicking fluid for use in Doppler flow test objects. Ultrasound Med Biol 1998;24:451-9.

Remuzzi A, Ene-Iordache B, Remuzzi G. Radial artery wall shear stress evaluation in patients with arteriovenous fistula for hemodialysis access. 2003;

Reneman RS, Vink H, Hoeks APG. Wall shear stress revisited. Artery Res 2009;3:73-8.

Rodriguez E, Ormont ML, Lambert EH, Needleman L, Halpern EJ, Diehl JT, Edie RN, Mannion JD. The role of preoperative radial artery ultrasound and digital plethysmography prior to coronary artery bypass grafting. Eur J Cardiothorac Surg 2001;19:135-9.

Roman MJ, Devereux RB, Kizer JR, Lee ET, Galloway JM, Ali T, Umans JG, Howard BV. Central pressure more strongly relates to vascular disease and outcome than does brachial pressure - The strong heart study. Hypertension 2007;50:197-203.

Royse AG, Chang GS, Nicholas DM, Royse CF. No late ulnar artery atheroma after radial artery harvest for coronary artery bypass surgery. Ann Thorac Surg 2008;85:891-5.

Safar ME, Blacher J, Pannier B, Guerin AP, Marchais SJ, Guyonvarc'h PM, London GM. Central pulse pressure and mortality in end-stage renal disease. Hypertension 2002;39:735-8.

Samady H, Eshtehardi P, McDaniel MC, Suo J, Dhawan SS, Maynard C, Timmins LH, Quyyumi AA, Giddens DP. Coronary Artery Wall Shear Stress Is Associated With Progression and Transformation of Atherosclerotic Plaque and Arterial Remodeling in Patients With Coronary Artery Disease. Circulation 2011;124:779-88.

Samijo SK, Willigers JM, Brands PJ, Barkhuysen R, Reneman RS, Kitslaar PJ, Hoeks AP. Reproducibility of shear rate and shear stress assessment by means of ultrasound in the common carotid artery of young human males and females. Ultrasound Med Biol 1997;23:583-90.

Savader SJ, Lund GB, Osterman FA. Volumetric evaluation of blood flow in normal renal arteries with a Doppler flow wire: A feasibility study. J Vasc Interv Radiol 1997;8:209-14.

Schlichting H. Boundary-layer theory, 7th edition. New York: McGraw-Hill, 1987.

Schmidt WA, Krause A, Schicke B, Wernicke D. Color Doppler ultrasonography of hand and finger arteries to differentiate primary from secondary forms of Raynaud's phenomenon. The Journal of rheumatology 2008;35:1591-8.

Silman A, Holligan S, Brennan P, Maddison P. Prevalence of symptoms of Raynaud's phenomenon in general practice. BMJ 1990;301:590-2.

Spencer-Green G. Outcomes in primary Raynaud phenomenon: a meta-analysis of the frequency, rates, and predictors of transition to secondary diseases. Arch Intern Med 1998;158:595-600.

Spring S, van der Loo B, Krieger E, Amann-Vesti BR, Rousson V, Koppensteiner R. Decreased wall shear stress in the common carotid artery of patients with peripheral arterial disease or abdominal aortic aneurysm: relation to blood rheology, vascular risk factors, and intima-media thickness. J Vasc Surg 2006;43:56-63; discussion

Steinman AH, Tavakkoli J, Myers JG, Cobbold RSC, Johnston KW. Sources of error in maximum velocity estimation using linear phased-array Doppler systems with steady flow. Ultrasound Med Biol 2001;27:655-64.

Steinman DA. Image-based computational fluid dynamics modeling in realistic arterial geometries. Annals of biomedical engineering 2002;30:483-97.

Steinman DA, Taylor CA. Flow imaging and computing: Large artery hemodynamics. Annals of biomedical engineering 2005;33:1704-9.

Stepanis.Pr. Transient Radiation from Pistons in an Infinite Planar Baffle. J Acoust Soc Am 1971;49:1629-&.

Stewart SFC, Paterson EG, Burgreen GW, Hariharan P, Giarra M, Reddy V, Day SW, Manning KB, Deutsch S, Berman MR, Myers MR, Malinauskas RA. Assessment of CFD Performance in Simulations of an Idealized Medical Device: Results of FDA's First Computational Interlaboratory Study. Cardiovascular Engineering and Technology 2012;3:139-60.

Stride E, Saffari N. Microbubble ultrasound contrast agents: a review. Proc Inst Mech Eng H 2003;217:429-47.

Stroev PV, Hoskins PR, Easson WJ. Distribution of wall shear rate throughout the arterial tree: A case study. Atherosclerosis 2007;191:276-80.

Struijk PC, Stewart PA, Fernando KL, Mathews VJ, Loupas T, Steegers EA, Wladimiroff JW. Wall shear stress and related hemodynamic parameters in the fetal descending aorta derived from color Doppler velocity profiles. Ultrasound Med Biol 2005;31:1441-50.

Sui B, Gao P, Lin Y, Jing L, Sun S, Qin H. Hemodynamic parameters distribution of upstream, stenosis center, and downstream sides of plaques in carotid artery with different stenosis: a MRI and CFD study. Acta Radiol 2015;56:347-54.

Swillens A. A combined speckle tracking and phase-shift estimation approach for 2D blood flow imaging in the carotid bifurcation. 2010;

Swillens A, De Schryver T, Lovstakken L, Torp H, Segers P. Assessment of numerical simulation strategies for ultrasonic color blood flow imaging, based on a computer and experimental model of the carotid artery. Annals of biomedical engineering 2009a;37:2188-99.

Swillens A, Degroote J, Vierendeels J, Lovstakken L, Segers P. A simulation environment for validating ultrasonic blood flow and vessel wall imaging based on fluid-structure interaction simulations: ultrasonic assessment of arterial distension and wall shear rate. Med Phys 2010;37:4318-30.

Swillens A, Lovstakken L, Kips J, Torp H, Segers P. Ultrasound simulation of complex flow velocity fields based on computational fluid dynamics. IEEE Trans Ultrason Ferroelectr Freq Control 2009b;56:546-56.

Taggart DP. The radial artery as a conduit for coronary artery bypass grafting. Heart 1999;82:409-10.

Tang MX, Mulvana H, Gauthier T, Lim AK, Cosgrove DO, Eckersley RJ, Stride E. Quantitative contrast-enhanced ultrasound imaging: a review of sources of variability. Interface Focus 2011a;1:520-39.

Tang MX, Mulvana H, Gauthier T, Lim AKP, Cosgrove DO, Eckersley RJ, Stride E. Quantitative contrast-enhanced ultrasound imaging: a review of sources of variability. Interface Focus 2011b;1:520-39.

Taylor CA, Figueroa CA. Patient-Specific Modeling of Cardiovascular Mechanics. Annual Review of Biomedical Engineering 2009;11:109-34.

Teirlinck CJPM, Bezemer RA, Kollmann C, Lubbers J, Hoskins PR, Fish P, Fredfeldt KE, Schaarschmidt UG. Development of an example flow test object and comparison of five of these test objects, constructed in various laboratories. Ultrasonics 1998;36:653-60.

Thijssen JM. Ultrasonic speckle formation, analysis and processing applied to tissue characterization. Pattern Recogn Lett 2003;24:659-75.

Thorne ML, Poepping TL, Nikolov HN, Rankin RN, Steinman DA, Holdsworth DW. In vitro Doppler ultrasound investigation of turbulence intensity in pulsatile flow with simulated cardiac variability. Ultrasound Med Biol 2009;35:120-8.

Tiev KP, Diot E, Clerson P, Dupuis-Simeon F, Hachulla E, Hatron PY, Constans J, Cirstea D, Farge-Bancel D, Carpentier PH. Clinical features of scleroderma patients with or without prior or current ischemic digital ulcers: post-hoc analysis of a nationwide multicenter cohort (ItinerAIR-Sclerodermie). The Journal of rheumatology 2009;36:1470-6.

Tiftik T, Kara M, Ozcan HN, Turkkan C, Ural FG, Ekiz T, Akkus S, Ozcakar L. Doppler ultrasonographic evaluation of the radial and ulnar arteries in hemiparetic patients after stroke. J Clin Ultrasound 2014;

Tola M, Yurdakul M. Effect of Doppler angle in diagnosis of internal carotid artery stenosis. J Ultrasound Med 2006;25:1187-92.

Toprak U, Hayretci M, Erhuner Z, Tascilar K, Ates A, Karaaslan Y, Karademir MA. Dynamic Doppler Evaluation of the Hand Arteries to Distinguish Between Primary and Secondary Raynaud Phenomenon. Am J Roentgenol 2011;197:W175-W80.

Toprak U, Selvi NA, Ates A, Erhuner Z, Bostanoglu S, Karademir MA, Karaaslan Y. Dynamic Doppler evaluation of the hand arteries of the patients with Raynaud's disease. Clin Rheumatol 2009;28:679-83.

Tordoir J, Canaud B, Haage P, Konner K, Basci A, Fouque D, Kooman J, Martin-Malo A, Pedrini L, Pizzarelli F, Tattersall J, Vennegoor M, Wanner C, ter Wee P, Vanholder R. EBPG on Vascular Access. Nephrology Dialysis Transplantation 2007;22:ii88-ii117.

Tu C, Deville M. Pulsatile flow of non-newtonian fluids through arterial stenoses. J Biomech 1996;29:899-908.

Tupholme GE. Generation of Acoustic Pulses by Baffled Plane Pistons. Mathematika 1969;16:209-&.

Udesen J, Gran F, Jensen JA. Fast color flow mode imaging using plane wave excitation and temporal encoding. Medical Imaging 2005: Ultrasonic Imaging and Signal Processing 2005;5750:427-36.

Van Canneyt K, Swillens A, Lovstakken L, Antiga L, Verdonck P, Segers P. The accuracy of ultrasound volume flow measurements in the complex flow setting of a forearm vascular access. J Vasc Access 2013;14:281-90.

Van Loon P. Length-force and volume-pressure relationships of arteries. Biorheology 1977;14:181-201.

Van Tricht I, De Wachter D, Tordoir J, Verdonck P. Hemodynamics and complications encountered with arteriovenous fistulas and grafts as vascular access for hemodialysis: A review. Annals of biomedical engineering 2005;33:1142-57.

Varray F, Basset O, Tortoli P, Cachard C. CREANUIS: a non-linear radiofrequency ultrasound image simulator. Ultrasound Med Biol 2013;39:1915-24.

Velasco A, Ono C, Nugent K, Tarwater P, Kumar A. Ultrasonic Evaluation of the Radial Artery Diameter in a Local Population From Texas. Journal of Invasive Cardiology 2012;24:339-41.

Vergara C, Ponzini R, Veneziani A, Redaelli A, Neglia D, Parodi O. Womersley number-based estimation of flow rate with Doppler ultrasound: sensitivity analysis and first clinical application. Comput Methods Programs Biomed 2010;98:151-60.

Verma S, Szmitko PE, Weisel RD, Bonneau D, Latter D, Errett L, LeClerc Y, Fremes SE. Should radial arteries be used routinely for coronary artery bypass grafting? Circulation 2004;110:E40-E6.

Vermeersch SJ, Rietzschel ER, De Buyzere ML, De Bacquer D, De Backer G, Van Bortel LM, Gillebert TC, Verdonck PR, Segers P. Determining carotid artery pressure from scaled diameter waveforms: comparison and validation of calibration techniques in 2026 subjects. Physiol Meas 2008;29:1267-80.

Viceconti M, Bellingeri L, Cristofolini L, Toni A. A comparative study on different methods of automatic mesh generation of human femurs. Medical Engineering & Physics 1998;20:1-10.

Viola F, Walker WF. A spline-based algorithm for continuous time-delay estimation using sampled data. Ieee T Ultrason Ferr 2005;52:80-93.

Watanabe H, Kawai M, Sibata T, Hara M, Furuhata H, Mochizuki S. Noninvasive measurement of aortic pressure waveform by ultrasound. Heart Vessels 1998;13:79-86.

Wigley FM. Clinical practice. Raynaud's Phenomenon. N Engl J Med 2002;347:1001-8.

Wilkinson IB, Cockcroft JR, Webb DJ. Pulse wave analysis and arterial stiffness. J Cardiovasc Pharmacol 1998;32 Suppl 3:S33-7.

Womersley JR. Method for the Calculation of Velocity, Rate of Flow and Viscous Drag in Arteries When the Pressure Gradient Is Known. J Physiol-London 1955;127:553-63.

Wong V, Ward R, Taylor J, Selvakumar S, How TV, Bakran A. Reprinted article "Factors associated with early failure of arteriovenous fistulae for haemodialysis access". European journal of vascular and endovascular surgery : the official journal of the European Society for Vascular Surgery 2011;42 Suppl 1:S48-54.

Wood NB, Zhao SZ, Zambanini A, Jackson M, Gedroyc W, Thom SA, Hughes AD, Xu XY. Curvature and tortuosity of the superficial femoral artery: a possible risk factor for peripheral arterial disease. J Appl Physiol (1985) 2006;101:1412-8.

Xiang J, Siddiqui AH, Meng H. The effect of inlet waveforms on computational hemodynamics of patient-specific intracranial aneurysms. J Biomech 2014;47:3882-90.

Yerdel MA, Kesenci M, Yazicioglu KM, Doseyen Z, Turkcapar AG, Anadol E. Effect of haemodynamic variables on surgically created arteriovenous fistula flow. Nephrol Dial Transplant 1997;12:1684-8.

Yusuf S, Reddy S, Ounpuu S, Anand S. Global burden of cardiovascular diseases - Part I: General considerations, the epidemiologic transition, risk factors, and impact of urbanization. Circulation 2001;104:2746-53.

Zell K, Sperl JI, Vogel MW, Niessner R, Haisch C. Acoustical properties of selected tissue phantom materials for ultrasound imaging. Phys Med Biol 2007;52:N475-84.

Zimlichman R. Determination of Arterial compliance using blood pressure waveform analysis with the CR-2000 system. 2005;